PHOTON INTERACTION COEFFICIENTS FOR ELEMENTS OF LOW ATOMIC NUMBER IN THE ENERGY RANGE FROM 4 TO 25 KEV

ROBERT H. MILLAR, B.A.

THESIS PRESENTED FOR THE DEGREE OF DOCTOR OF PHILOSOPHY OF THE UNIVERSITY OF EDINBURGH, JULY 1973.

"It is seen, therefore, that some agent is capable of penetrating black cardboard, which is quite opaque to ultra-violet light, sunlight, or arc-light. It is therefore of interest to investigate how far other bodies can be penetrated by the same agent"

Wilhelm Conrad Röntgen
(Nature, 53, 1896)

C O N T E N T S

ABSTRACT

A survey of the literature on mass attenuation coefficients for low atomic number materials reveals certain deficiencies in currently available data. Accurate experimental work below 25 keV is scarce for all elements except aluminium, and for many it is non-existent; recently published theoretical results claiming high precision have not been tested adequately against experimental data; and the proliferation of semi-empirical and compiled data has led to considerable confusion as to the best available values.

Consequently accurate mass attenuation coefficients for air, nitrogen, oxygen, neon, argon, ethylene, carbon tetrafluoride, carbon dioxide, hydrogen sulphide, hydrogen chloride, magnesium, aluminium, silicon dioxide and tri-ethyl phosphate have been measured, enabling values for all the elements from $Z = 6$ to $Z = 18$, with the exception of sodium, to be calculated directly. Measurements were carried out at 15 energies between 4.508 keV and 25.192 keV for all elements except silicon and phosphorus where the ranges covered were 8.041 keV to 25.192 keV and 11.210 keV to 25.192 keV respectively.

The apparatus used consisted of a Machlett constant-potential X-ray tube with a beryllium window. The primary radiation excited a secondary fluorescent source. This radiation was then collimated, passed through the absorbing sample, and the $K\alpha$ component was detected using a single-crystal spectrometer and a Xe-filled gas proportional counter. The amplified pulses from the counter were counted using a multichannel analysis system. In the case of gaseous absorbers, a double tube-interchange system was developed permitting a series of attenuation readings to be quickly taken. The apparatus criteria

necessary to permit precise measurement of mass attenuation coefficients to be carried out are fully discussed.

A set of mass attenuation coefficients and total attenuation cross-sections for the elements considered is obtained. Experimental checks indicate the internal consistency of these values to be satisfactory. A set of photoelectric cross-sections is derived, making use of published scattering cross-sections. The functional relationship between photoelectric cross-section and energy is considered and is shown to be adequately described by a cubic polynomial on log-log scales. The coefficients for these polynomials are derived, and smoothed and interpolated values of photoelectric cross-sections are presented. Similar work on the total cross-section is also carried out. The uncertainties on such smoothed or interpolated values are shown to be approximately $\pm$ 1% (99% confidence limits).

It is shown that the functional relationship between photoelectric cross-section and atomic number is not smooth, in contrast to the relationship with energy. The observed irregularities are in qualitative (and in certain cases, quantitative) agreement with theoretical predictions. This is the first attempt to obtain experimental evidence about these theoretical results. The problems of interpolation at other atomic numbers are discussed.

Finally the measured values of total attenuation cross-section are compared with the most reliable results of previous experimental work and with the best compilations. The results are shown to be in excellent agreement with the theoretical compiled results of Storm and Israel (1970) and provide strong evidence in support of their work. A coherent data-setfor the elements Z = 6 to 18 in the energy range from 4 to 25 keV is recommended. This data-set is

more comprehensive and has greater accuracy than any experimental data previously published in the same energy range.

CHAPTER 1

THE INTERACTION OF PHOTONS WITH MATTER

1.1 TOTAL INTERACTION CROSS-SECTION AND MASS ATTENUATION COEFFICIENT

The applications of X rays and gamma rays in the fields of medicine and biology depend fundamentally on one of two properties which the rays possess, either on their differing ability to penetrate different types of tissue or on their ability to deposit energy within a body on which they are incident. Both of these properties depend, in turn, on the strength of the interaction between the individual X-ray photons and the atoms or molecules of the material through which they are passing. This "strength of interaction" finds quantitative expression in the concept of an interaction cross-section. A cross-section is a convenient means of visualising an interaction probability as an effective area presented by a target particle (in this case, an atom or molecule of an attenuating material) to the bombarding particles (the X-ray photons). The probability of an interaction occurring can then be calculated on a purely geometrical basis.

Hence (see Figure 1.1) if a beam of photons is incident normally on a thin target of thickness dx, which contains N attenuating particles per unit volume, the probability of any photon undergoing a reaction within the target is related to the cross-section σ for that reaction by the relationship:

$$\text{Probability of interaction} = N\sigma\, dx \qquad .....(1.1)$$

The cross-section is a function of the photon energy, E, and the atomic number, Z, of the attenuating medium.

In the particular case of the interaction of photons with matter, several different reactions may occur, for each of which there exists a

Figure 1.1 CROSS-SECTION

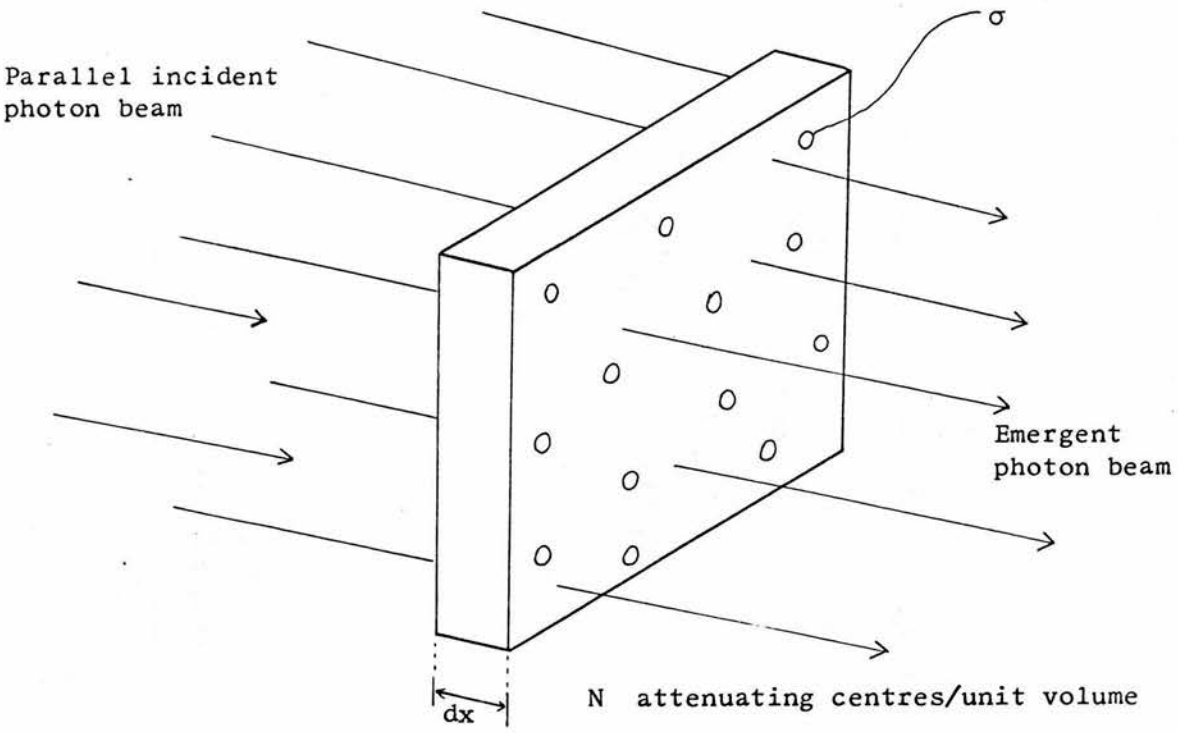

Figure 1.2 ATTENUATION COEFFICIENT

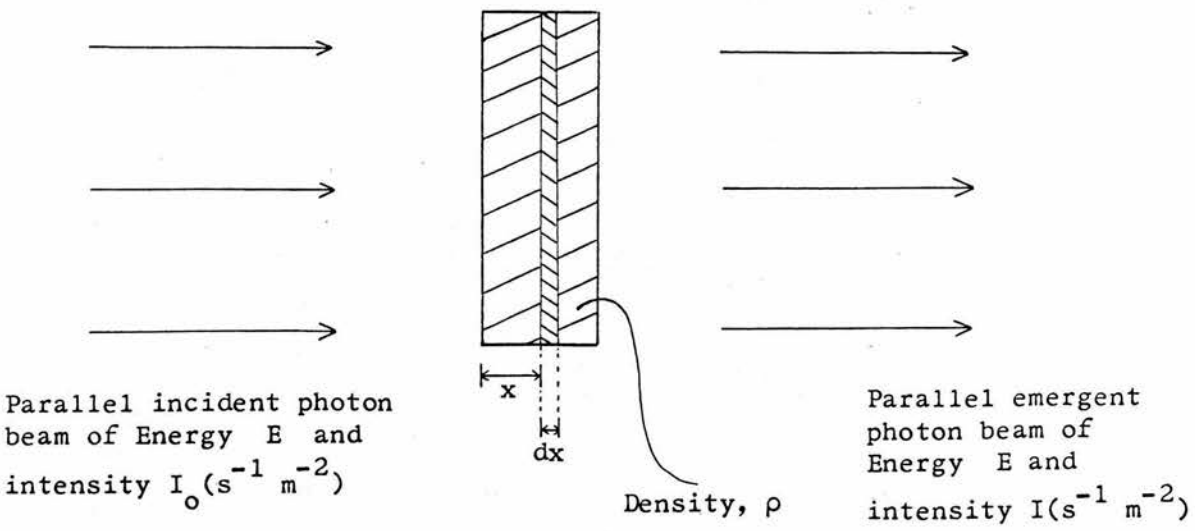

separate cross-section defined as above. This project is concerned with the interaction between low energy ($\leqslant 30$ keV) photons and materials of low atomic number ($Z \leqslant 18$). In this region the important reactions are photoelectric absorption, Compton (or incoherent) scattering, and Rayleigh (or coherent) scattering. Other minor interactions with a much lower probability of occurrence are possible, involving the interaction of the photons with the nuclei of the absorber atoms, or with the electric field around charged particles in the atom. The most important of this last type of interaction, namely electron-positron pair production, is, however, forbidden below 1.02 MeV by energy-momentum conservation requirements. For all practical purposes the other minor interactions can also be disregarded.

Photoelectric absorption is an interaction between a photon and an entire atom. It involves the absorption of the photon, and the ejection of an electron from the atom. The ejected electron carries away the energy of the incident photon, minus its own former binding energy in the atom. Compton scattering, on the other hand, is a photon-electron process. A photon collides with an electron, loses some energy to the electron, and is deflected from its original direction of motion. Rayleigh scattering is an interaction between photons and bound atomic electrons. Neither is the atom ionized or excited by the collision, nor does the photon lose energy in the process. From a wave-mechanical point of view, this can be regarded as "coherent" reflection of a photon from the different parts of the atomic charge distribution, and contrasts with the "incoherent" nature of the Compton scattering process.

The total photon attenuation cross-section, σ_{tot}, is then given by the sum of the photoelectric cross-section τ_{pe}, the Compton cross-section σ_c, and the Rayleigh cross-section σ_R.

$$\sigma_{tot} = \tau_{pe} + \sigma_c + \sigma_R \qquad \text{.....(1.2)}$$

This cross-section governs the probability of a photon undergoing any interaction in the attenuating material.

The interaction between photons and matter can, however, be quantified using a different parameter, the attenuation coefficient. This is defined in terms of a hypothetical experiment (see Figure 1.2).

Consider a perfectly parallel beam of monoenergetic photons of energy E of intensity $I_o(m^{-2}\ s^{-1})$ incident on a macroscopically thick target. The radiation is detected by a perfectly collimated detector which records only those photons of energy E which are travelling in the same direction as the incident beam. Hence any photon which undergoes an absorption or a scattering process within the target will not be detected. Let us then consider the reduction in intensity in a layer of thickness δx at a depth x from the front face of the target. This layer is assumed to be macroscopically thin and to be homogeneous. Then, if the interaction is weak, so that the intensity is essentially constant within the layer, the reduction of intensity in transit, δI, will be proportional to the local intensity I, and to the layer thickness

$$\delta I \quad \alpha \quad I\,\delta x \qquad \text{.....(1.3)}$$

$$\delta I \quad = \quad -\mu I\,\delta x \qquad \text{.....(1.4)}$$

The constant of proportionality, μ, is called the linear attenuation coefficient.

Further, if the quotient $\frac{\delta I}{\delta x}$ tends to a stable limit (as δx tends to zero) while δx is still sufficiently large relative to atomic dimensions to satisfy the requirements of absorber homogeneity, then equation 1.4 can be integrated to give the result.

$$I(x) = I_o e^{-\mu x} \qquad .....(1.5)$$

The dimensions of μ are $\left[\text{length}\right]^{-1}$. The linear attenuation coefficient suffers from the drawback that it is not uniquely defined for a given material, but is proportional to the density, ρ, of the material, and is therefore dependent on the physical state of the material. For this reason, it is customary to remove the density dependence and use the mass attenuation coefficient, $\frac{\mu}{\rho}$. The dimensions of this quantity are $\left[\text{length}\right]^2 \left[\text{mass}\right]^{-1}$, and hence its units in the M.K.S. system are $m^2 kg^{-1}$.

The mass attenuation coefficient defines, in macroscopic terms, the same property as is microscopically defined by the total attenuation cross-section per atom, σ_{tot}.

Differentiating equation 1.5 it follows that

$$-\frac{dI}{I} = \mu\, dx \qquad .....(1.6)$$

Hence the linear attenuation coefficient μ is the fractional attenuation of a beam per unit distance travelled in a thin absorber. Since the quantity $-\frac{dI}{I}$ is simply the probability of an interaction occurring within a layer of thickness dx, its value must be identical with that of equation 1.1, since the experimental conditions are identical. Hence the total attenuation cross-section is directly proportional to the linear attenuation coefficient, the constant of proportionality being the number of attenuating centres per unit volume in the target. The mass attenuation coefficient is similarly related to the total attenuation coefficient by the number of attenuating centres per unit mass. For elementary absorbers the relationship is:

$$\frac{\mu}{\rho}\left[m^2\ kg^{-1}\right] = \sigma_{tot}\left[m^2\ atom^{-1}\right] \frac{N_A\left[atoms\ mol^{-1}\right]}{M\left[kg\ mol^{-1}\right]} \qquad .....(1.7)$$

where N_A is the Avogadro constant, and M is the molar mass of the attenuating substance. The conventional units of σ_{tot} are barns/atom, 1 barn being defined as 10^{-28} m^2. In these units the relation becomes

$$\frac{\mu}{\rho}\left[m^2\ kg^{-1}\right] = \sigma_{tot}\left[b\ .\ atom^{-1}\right]\ \frac{N_A}{M}\ 10^{-28} \qquad .....(1.8)$$

If the attenuating material is a compound, an analogous cross-section per molecule can be defined. It is, however, usually more convenient to regard the attenuation coefficient of a compound or a mixture as made up of the sum of contributions from its constituent atoms, according to the "mixture rule"

$$\frac{\mu}{\rho} = \sum_i \omega_i\ \frac{\mu_i}{\rho_i} \qquad .....(1.9)$$

where ω_i is the proportion by weight of the i^{th} constituent, and $\frac{\mu_i}{\rho_i}$ is its mass attenuation coefficient. In the case of compounds, the mixture rule neglects any changes in attenuation which may result from changes in atomic wave-functions due to chemical composition. Very little experimental information has been published on deviations from the mixture rule. Deslattes (1969) reports that such deviations are likely to be less than one percent above 10 keV except in the neighbourhood of an absorption edge of one constituent element. Since only a minority of elements can be obtained in a stable, pure, and homogeneous form suitable for experimental studies of attenuation, it is necessary to make use of the mixture rule to extend the range of available elements. If precautions are taken to ensure that measurements are not being made in a region where the mixture rule might be expected to break down, then any deviations from the rule are likely to be insignificant sources of error in the experiment, even down to 1 keV.

In the foregoing discussion a distinction has been made between

attenuation and absorption of photons. Attenuation includes all scattering and absorption processes, and is more simply determined experimentally than either the scattering or absorption fractions separately. Many important uses of X radiation are related to the energy deposition in an irradiated medium, and many dosimetric techniques (e.g. calorimetry, chemical dosimetry) depend on measurement of this energy deposition. It is, therefore, useful to have a direct measure of energy deposition, and this is done using the mass energy-absorption coefficient, $\left(\frac{\mu}{\rho}\right)_{en}$ defined as:

$$\left(\frac{\mu}{\rho}\right)_{en} = \left(\frac{\mu}{\rho}\right)_{\tau} f_{\tau} + \left(\frac{\mu}{\rho}\right)_{c} f_{c} \qquad \text{.....(1.10)}$$

where $\left(\frac{\mu}{\rho}\right)_{\tau}$ and $\left(\frac{\mu}{\rho}\right)_{c}$ are the components of the mass attenuation coefficient due to photoelectric absorption and Compton scattering respectively, and f_{τ} and f_{c} are fractions which indicate, for the photoelectric and Compton processes, the average fraction of the incident photon energy which is eventually converted into kinetic energy within the volume of interest. This takes account of the escape of Compton-scattered, fluorescence, and secondary bremsstrahlung photons. Rayleigh scattering does not contribute, since no energy is transferred to the medium. The factors f_{τ} and f_{c} have been calculated and tabulated by Berger (1961) for air, water and fifteen elements over the energy range 10 keV $\leqslant$ E $\leqslant$ 10 MeV and by Allison (1961) for air, water and seven elements over the range 10 keV $\leqslant$ E $\leqslant$ 100 MeV.

1.2 AIMS OF THE PROJECT

The primary aim of the project is to measure the mass attenuation coefficients of low atomic number elements for low energy X rays, paying particular attention to elements of biological interest. This is an

area in which the uncertainty in previous experimental and theoretical data is believed to be large. In a recent review of mass attenuation data, Hubbell (1969) concludes that uncertainties of 5 - 10% are present in values below 30 keV for the elements from hydrogen (Z = 1) to oxygen (Z = 8). There is also an almost complete absence of any experimental data on the elements from fluorine (Z = 9) to argon (Z = 18) with the exception of the two noble gases, neon and argon, and the stable metals magnesium and aluminium for which measurements have been made. To fill these gaps in the attenuation data, the mass attenuation coefficient was measured for each of the elements, carbon, nitrogen, oxygen, fluorine, neon, magnesium, aluminium, sulphur, chlorine and argon at fifteen energy points in the range 4 to 26 keV, for silicon at eleven energy points in the range 8 to 26 keV, and for phosphorus at eight energy points in the range 11 to 26 keV. The accuracy of existing data in this atomic number and energy range was also improved on.

1.3 USEFULNESS OF MORE ACCURATE DATA

The present uncertainty in our knowledge of such a basic physical parameter as the mass attenuation coefficient is inherently unsatisfactory. In the absence of sufficiently accurate experimental data over the whole range of energy and atomic number, various groups of workers have attempted to synthesise critical data sets from a variety of experimental results, theories of the various attenuating processes, and semi-empirical interpolation and extrapolation techniques. This has inevitably led to a profusion of "best" values, and considerable confusion among workers in any field where attenuation coefficients are used as to which values are the most reliable.

For this reason, it is valuable on two counts to measure accurate attenuation coefficients over a range of energies and atomic numbers. Apart from the new data provided directly from such a project, the opportunity is also presented to carry out a reasonably extensive comparison of measured values with the most recent theoretical figures, and may increase confidence in the theory. In that case the value of the experimental measurements extends greatly beyond the ranges of energy and atomic number in which they were made.

More accurate data on the elements which occur most frequently in biological materials is of direct interest to workers in radiation dosimetry.

Another field in which accurate work is hampered by the inaccuracy of present attenuation coefficients is electron microprobe analysis. This is a potentially accurate method of assaying the composition of materials by bombarding them with an electron beam and observing the fluorescent radiation produced. Better attenuation values will greatly improve the accuracy of the technique.

Finally, the need for accurate values of attenuation coefficient in crystal structure analysis should be mentioned. Many structure determinations, particularly those of highly complex molecules like proteins and nucleic acids, depend on the measurements of relative intensities of the spots in the diffraction pattern. The observed intensities must, however, be corrected for attenuation of the diffracted beams within the diffracting sample. The accuracy to which mass attenuation coefficients are known sets a limit to the accuracy to which these relative intensities may be specified.

CHAPTER 2

SURVEY OF THE LITERATURE

2.1 EXPERIMENTAL

The varying ability of different materials to attenuate a beam of X rays has been known as long as the rays themselves. In Röntgen's preliminary report to the President of the Physical Medical Society of Würzburg on December 28, 1895, he states:

"It is seen, therefore, that some agent is capable of penetrating black cardboard which is quite opaque to ultra-violet light, sunlight or arc-light. It is therefore of interest to investigate how far other bodies can be penetrated by the same agent.

Paper is very transparent: ..... a single card does not visibly diminish the brilliancy of the light ..... a single thickness of tinfoil hardly casts a shadow on the screen ..... thick blocks of wood are still transparent ..... a piece of sheet aluminium 15 mm thick still allowed the rays to pass, but greatly reduced the fluorescence ..... lead 1.5 mm thick is practically opaque."

Röntgen and many other early workers experimented on the thicknesses of various materials required to produce the same weakening of an X-ray beam, and during this early period the "hardness" of X radiation was measured by its half-value thickness of aluminium, i.e. the thickness of aluminium which reduced the beam intensity to half its unattenuated value.

Secondary fluorescence was also discovered, and fluorescent radiation from various elements was used by Barkla and Sadler (1909) in a series of experiments in which they measured the attenuation coefficient of aluminium in absolute terms, and of several other metals

Figure 2.1 TRENDS IN $\frac{\mu}{\rho}$ VALUES

X-ray energy: Cu Kα (8.041 keV)

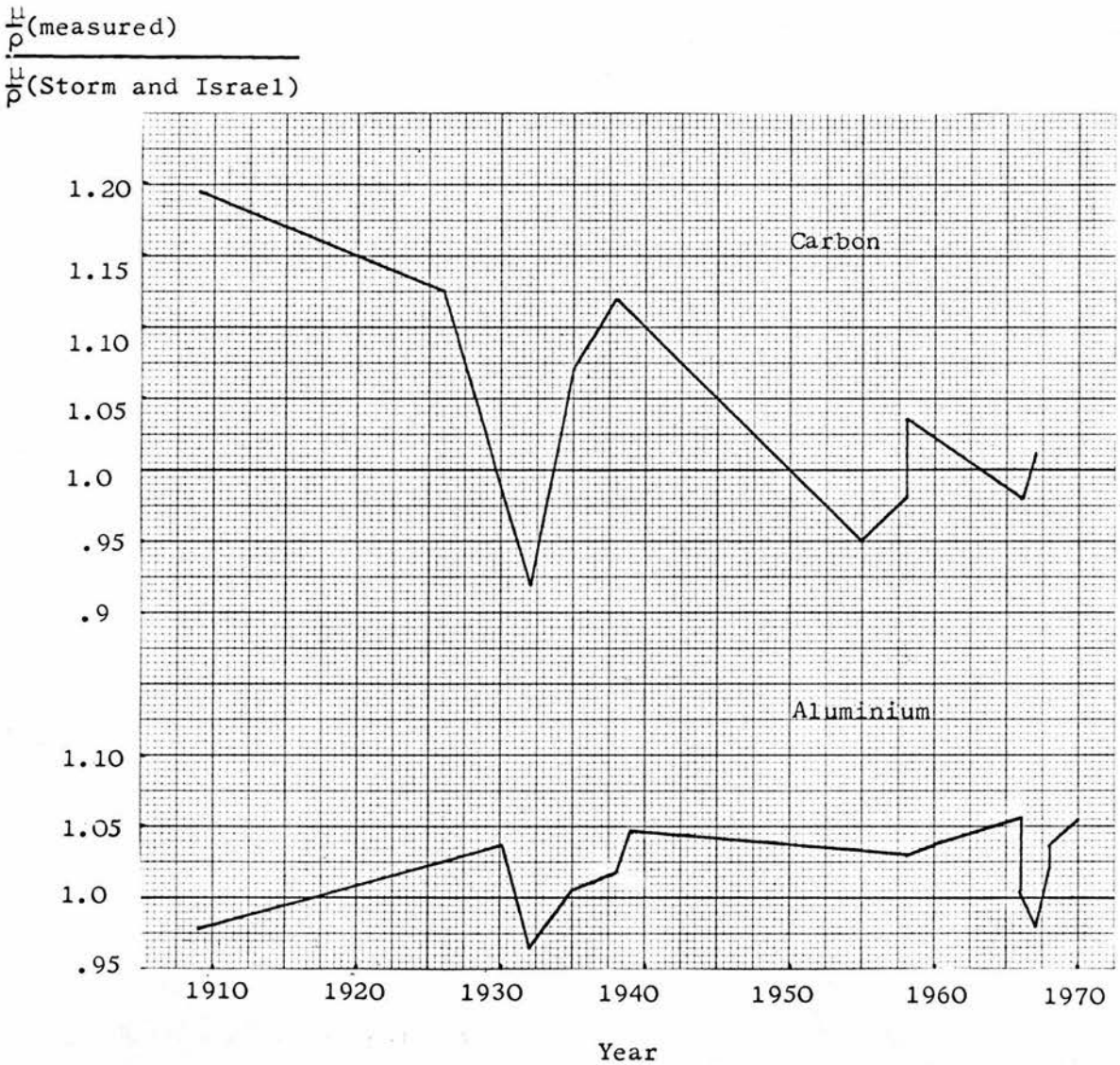

and non-metals (C, Mg, Fe, Ni, Cu, Zn, Ag, Sn, Pt, Au), relative to aluminium.

This work was carried out in the absence of any real understanding of the physical nature of the rays. With the verification of the wave-nature of X rays by Friedrich, Knipping and von Laue (1913) and W. H. and W. L. Bragg (1913), wavelength emerged as a true quantitative measure of the quality and homogeneity of an X-ray beam. The Bragg crystal spectrometer also provided a means of generating a much more monochromatic beam than was previously possible.

During the sixty years since the introduction of the crystal spectrometer the only really significant improvement in the instrumentation of X-ray attenuation coefficient measuring techniques has been the more recent development of gas proportional counters, scintillation counters, and doped semiconductors as detectors, in place of the ionization chambers used by earlier workers. This is, of course, no mean improvement, and the extra sensitivity of the modern counters, combined with the extra reliability of energy-discriminating detectors in general, increases confidence in more recent work. It might also be expected that improvements over the past fifty years in such technologies as the production and handling of very high purity gas, liquid and solid samples (and, in the case of solids, the production of foils of uniform thickness) would have helped to produce a gradual and steady improvement in attenuation data. That this has not always been the case may be seen from Figure 2.1. The ratios of values published between 1909 and 1970 for the mass attenuation coefficients of carbon and aluminium for copper K_{α} radiation, relative to recent critical values of Storm and Israel (1970), show some tendency to converge asymptotically towards an accepted value but the

convergence is far from being smooth and monotonic. It is, therefore, not possible to reject the results of older work solely on account of its age.

The total volume of experimental data on photon attenuation coefficients is now so large that a comprehensive bibliography containing upwards of three hundred references has recently been published to assist workers in the field (Hubbell, 1971). Despite this, there is not a single comprehensive experimental data set by any author covering the elements below Z = 18 in the energy range from 4 - 30 keV. The materials most commonly chosen as absorbers are those which are readily available in a pure and easily manageable form. Hence, in the atomic number range of interest, almost half of the total published work is on aluminium. It is to rectify this imbalance, by filling some of the gaps, and to obtain a single experimental data set thereby enabling variations with energy and atomic number to be investigated over the entire range of interest, that the work described in this thesis has been undertaken.

There are several sets of results which lie either completely or partially within the range of interest of this work. Bearden (1959, 1966) has measured the total attenuation coefficients of H_2, He, Be, C, N_2, O_2, Ne, Al, A, Cu, Sn between 0.852 and 8.048 keV (with an extension to 40 keV for Al, Cu, Sn). He used three different source techniques within the range: at very low energy a single crystal spectrometer was used to monochromate characteristic secondary fluorescence radiation; at intermediate energies the characteristic radiation was analysed by a double-crystal monochromator; whilst above 10 keV, the double-crystal technique was used to select narrow energy bands from the tube continuum. Detection was by either a scintillation counter or a proportional counter depending on the energy of the radiation, and

pulse-height analysis techniques were used to eliminate any high order diffraction effects and to reduce background. An accuracy of 1 - 2% is claimed for the published results.

An exact statement of precisely what the author means by this uncertainty is not made. This is generally true of the published work. The statements of accuracy of the results of the different workers referred to in this chapter are those of the workers themselves. In general, I have regarded them as corresponding roughly to 68% confidence limits, i.e. one standard error of the mean.

Another comprehensive recent measurement is that of McCrary et al. (1967), who measured attenuation coefficients for Be, C, Mg, Al, S and 19 other metallic elements from Ti to U. The energy range was 25 - 130 keV, so only a few values fall within the energy range considered here. McCrary used a single-crystal spectrometer to reflect parts of the tube continuum. The degree of collimation used in such a method determines the monochromaticity of the radiation. The smaller the solid angle subtended by the collimator at the source, the purer the energy spectrum of the radiation obtained, but also, unfortunately, the less intense the beam. Bragg reflection of the continuum has the advantage of permitting any energy to be used, but it omits to take advantage of the great usefulness of secondary fluorescence, viz. that of concentrating an appreciable fraction of the total beam intensity into a single energy (or group of energies). McCrary and his co-workers claim an uncertainty in their energies of around 0.1% and in the measured attenuation coefficients of 1 - 2%.

Two other recent publications by McCrary and others are also noteworthy. Using filtered isotope sources and a scintillation counter sealed within a leak-free pipe, attenuation coefficients of

Air, Ne, A, Kr and Xe were measured at four energies from 4.508 keV to 27.380 keV by McCrary, Looney, Constanten and Atwater (1970). The same apparatus was also used by McCrary, Looney and Atwater (1970) to measure the attenuation of H_2 and He at 5.895 keV, with estimated accuracy of around 5%. There are many problems associated with measurements for these gases, notably the large effect produced by trace amounts of other impurities (which must, of necessity, have relatively large atomic numbers), and the large pressure or sample length required to produce accurately measurable attenuation of the beam.

Most of the experimental data on low atomic number gases dates from a much earlier period. Colvert (1930) carried out measurements on Ne, SO_2, Cl_2 and A (as well as Al) in the energy range from 5.419 keV to 25.00 keV; Spencer (1932) published data on Air, O_2 and A between 1.778 keV and 8.068 keV; and Hewlett (1921) worked on liquid oxygen, as well as water, lithium, carbon and aluminium. All these workers used secondary fluorescent radiation with crystal monochromatisation as a source of X rays, and ionization chambers as detectors. A modification of this technique was used by Crowther and Orton (1930, 1932). They used a null method involving the balancing of two ionization detectors placed before and after the absorbing sample. Varying air pressure within one such detector led to a linear variation in the observed charge, and the air pressure required to balance the electroscopes provided a direct measure of the absorption in the sample. Using this method Crowther and Orton measured the attenuation of Air, N_2, O_2, CO_2, C_2H_4 and H_2S for copper Kα radiation (8.041 keV) and later repeated this with copper and iron Kα radiations (8.041 and 6.400 keV) using the above absorbers plus several organic halides, an aluminium

Figure 2.2 ROSS FILTERS

a) Mass attenuation coefficients for elements of adjacent atomic number

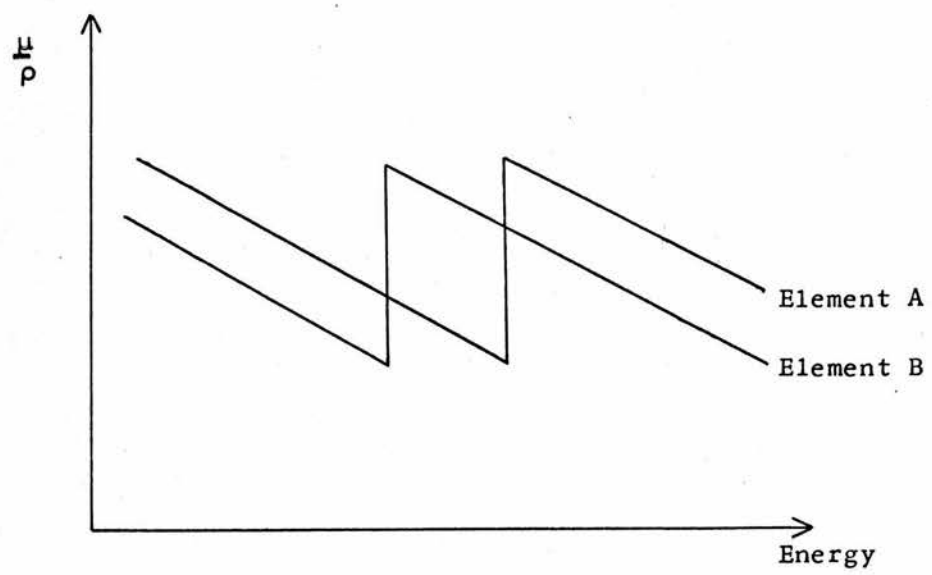

b) Effect of Ross filters on an X-ray spectrum

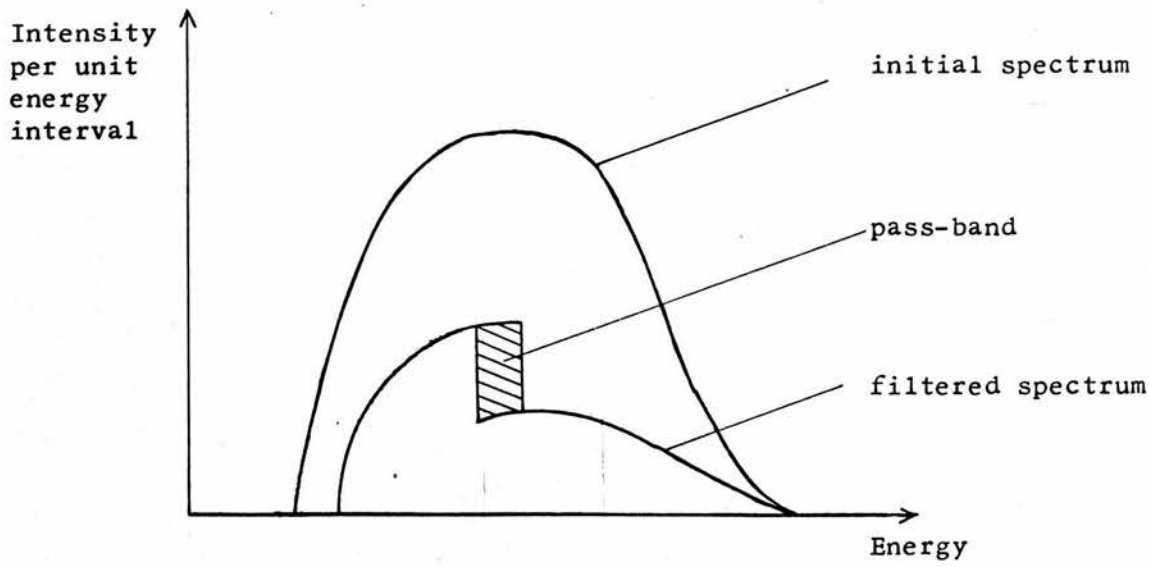

sample, and a paraffin wax $(CH_2)_n$. It is also worth mentioning another similar null technique which Woernle (1930) used for experiments on Air, N_2, O_2 Ne, A, SO_2, C_5H_{12}, CCl_4 at energies from 5.411 keV downwards.

The results of all these experiments carried out in the twenties and early thirties are of comparable reliability. Comparison with more recent work shows a tendency for older values to be systematically higher than the currently favoured data. The most plausible explanation for this is sample impurity in the case of low atomic number absorbers. Other sources of error in the early work are likely to be due to lack of constancy of X-ray tube output; imperfect collimation and rejection of scattered radiation; and the sensitivity limitations and absence of energy discrimination of ionization chamber detectors.

Lack of sensitivity of ionization chambers becomes a major problem when dealing with highly monoenergetic radiation since, in general, the degree of monochromaticity of the radiation is inversely proportional to its intensity. The inevitable intensity losses due to collimation of fluorescent radiation, and reflection from a crystal, result in a beam which, although spectrally very pure, is much weaker than that which might be optimally detected by ionization techniques. This situation led several workers to seek an alternative means of monochromatisation which would still permit high intensity beams to be used. One such alternative is the use of balanced filters (or Ross filters). This depends on the similarity of the variation with energy of the attenuation coefficient of elements of adjacent atomic number, except in the region near an absorption edge. The attenuation coefficients of two such elements, and their effects as filters on a

Figure 2.3 KÜSTNER FILTERING METHOD

a) Alternative filter positions

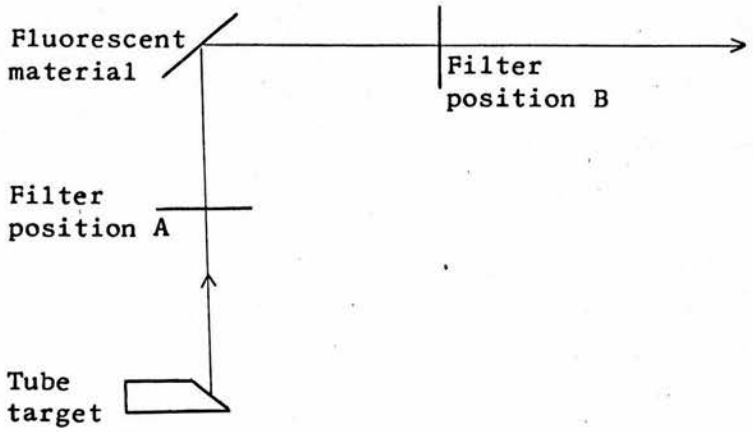

b) Unfiltered and filtered tube continuum spectra

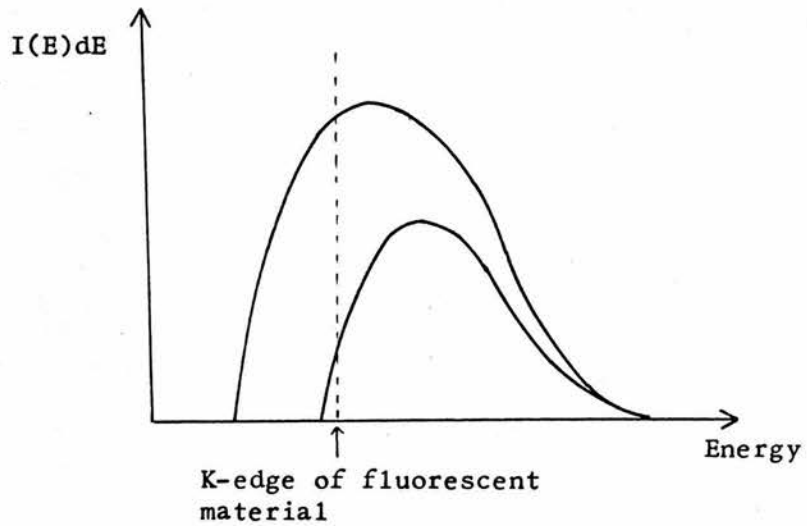

c) Final spectra using filter positions A and B respectively

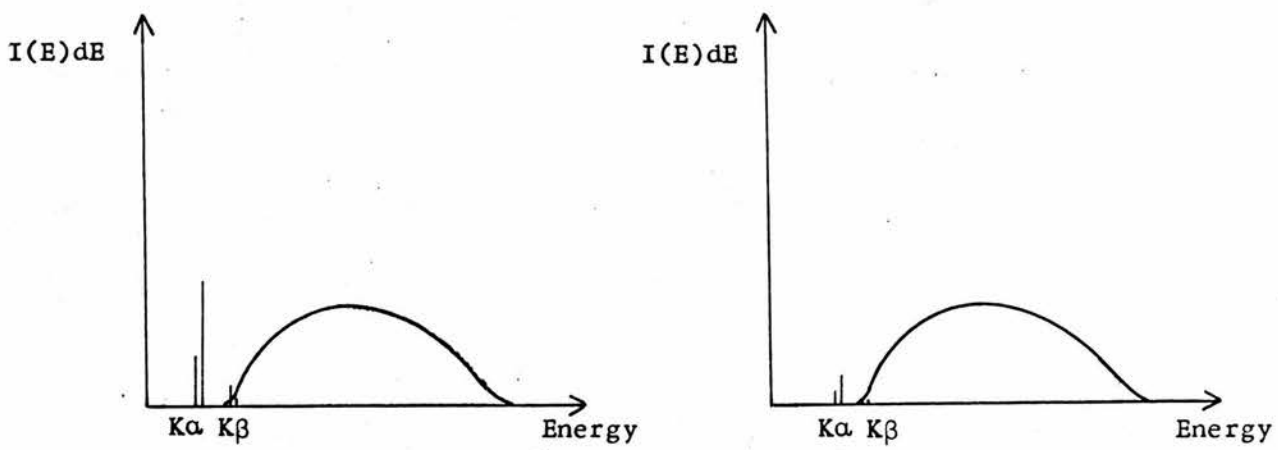

continuous spectrum are illustrated schematically in figure 2.2. If the filter thicknesses are correctly chosen, the transmitted spectra will be identical at all energies except those in a narrow band between the absorption edges of the two materials. Hence, the difference in observed intensities with each filter separately placed in the beam will be due to energies in this pass-band. A choice of filters can be made such that a fluorescent peak (due either to the target itself, or to a secondary fluorescent source) lies within the pass-band. This technique was used by Callisen (1937) to measure the absorption of K_α radiation from Fe, Ni, Cu, Zn, and Sn (6.400 keV - 25.192 keV) in gaseous oxygen samples.

Another differential filtering technique is that due to Küstner (1931). In this method a secondary fluorescent source, whose K_α energy is approximately known, is used. An aluminium or copper filter is made of such a thickness that it attenuates this fluorescent radiation quite strongly (i.e. only 1 - 2% of the intensity is transmitted). Then Küstner states that, depending on whether the filter is placed before or after the fluorescent material, the resultant spectrum will contain a greater or lesser amount of characteristic radiation superimposed on an identical continuous background (see figure 2.3). By subtracting the observed intensities obtained with the two filter positions, the resultant difference can be attributed to the characteristic radiation of the secondary fluorescent source only. A further filter with a suitably chosen absorption edge can then be used to isolate the K_α from the K_β component.

This method of producing monochromatic radiation was subsequently used by a group of workers under Küstner in Göttingen to obtain a very

comprehensive set of attenuation coefficients over a wide range of energies and atomic numbers. Several of these measurements fall within our range of interest. Grosskurth (1934) measured attenuation coefficients for carbon, aluminium and sulphur (as well as many higher atomic number elements) spanning the energy range from 5.411 keV to 30.85 keV. Biermann (1936) extended these measurements on aluminium down to 3.312 keV. Hansen (1939) worked on liquid and gaseous samples of CS_2, CH_2Cl_2, C_2H_5Br, and CH_3I, deducing values for sulphur, chlorine, bromine and iodine, from 6.400 keV to 25.195 keV. Finally, Wrede (1939) carried out a very extensive series of determinations which included results for C, F, Mg, Al, S, and Cl from 8.631 keV to 25.192 keV. (N.B. The fluorine and chlorine measurements were carried out on powdered LiF and NH_4Cl samples respectively).

The same criticism can be levelled at both these filtration techniques, and attenuation data derived from them, viz. that high intensity has been achieved at too great a price in terms of monochromaticity. This is particularly true of the Ross method which allows all energies within a band of appreciable width to pass. The Küstner technique is better but the spectral purity of the radiation band selected is inferior to that produced by crystal diffraction. Küstner's contention that the continuous spectrum is identical in both cases is true only if Compton scattering can be disregarded. A further drawback of filtering techniques is the degree of collimation attained. Crystal diffraction produces a highly collimated monoenergetic beam. To impose the same degree of collimation on a filtered beam by means of slits or aperture collimators would produce such a weakening of the beam that the intensity advantages gained by the filtering method would be lost in collimation. If, on the other hand, collimation

is not so stringent, then the possibility of scattered radiation being detected is correspondingly greater. Both filtering methods can also be criticised from the point of view that they rely on a measurement of the difference between two large quantities - a method which produces large uncertainties.

The resolution to the problem of detector sensitivity lies not in the attempt to produce intense beams at the expense of monochromaticity, but in the development of more sensitive detection techniques. The introduction of the Geiger counter, and subsequently gas proportional counters and scintillation counters, provides a considerable improvement in detector sensitivity. The Geiger counter can be regarded merely as a more sensitive substitute for the ionization chamber, but the proportional and scintillation counters have the further advantages of energy-dependent response. Output pulses are proportional to input photon energy and by the use of gating techniques it is possible to count only those photons in the energy range desired. This enables efficient rejection of diffuse scattering and higher-order crystal diffraction effects, something which is quite impossible with an ion chamber.

The work of Bearden, and McCrary et al., which is described previously, uses these detection methods. Much recent experimental work, however, has been solely on metallic absorbers, especially aluminium, the elements of the transition series, and the noble metals. Hopkins (1959) obtained $\frac{\mu}{\rho}$ values for Al, Cr, Co, Ni, Cu, Zn from 6 - 40 keV; Ehrenfried and Dodds (1960) worked with Al, Fe, Ni, Cu, Ag, Ti, Zn, Zr, Sn, Pt, Mo and some plastics in the 1.49 keV to 11.9 keV range; Cooper (1965) published results for Al, Ti, V, Cr, Mn, Fe, Co, Ni and Cu from 5.411 keV to 22.2 keV; Heinrich (1966)

quotes values for Al, Nb, Ta and Mylar in the soft X-ray region below 8.041 keV; Hughes, Woodhouse and Bucklow (1968) also made measurements in this energy region for Al, Ti, Ni, Cu, Zr, Nb, Pd, Ag, Ta, Au; and finally Lublin, Cukor and Jaworowski (1970) performed experiments on very thin aluminium foils, also at energies below 8.041 keV. All these experiments used a single-crystal monochromator with fluorescent radiation as source, and an energy-sensitive detector, and the results are expected to be reliable to around 3% in all cases. The main inaccuracies stem from considerations of foil purity and uniformity, and the inevitable difficulties of fluctuation in beam intensity which are unavoidable with X-ray tube sources.

Finally, on metallic absorbers, the very important work of Deslattes (1958) must be considered. Using a double crystal spectrometer for very rigorous monochromatisation, he measured attenuation coefficients of Mg, Al, Ti, Fe, Ni, Cu, Zn, Mo, Pd, Ag, Cd, Sn, W, Pt and Au. A proportional counter with pulse-height analyser was used, and the entire system was automated in such a way that the entire course of the experiment could be controlled by a programmed computer. The results are claimed to be accurate to better than 1%. Deslattes considers the theoretical implications of specifying the coefficients to better than 1% and his conclusions regarding small angle scattering and statistics will be considered in greater detail when the instrumentation for this work is discussed.

Unfortunately, there is no corresponding wealth of experimental data on the low atomic number non-metals. Apart from the measurements of Bearden (1959, 1966) and McCrary et al. (1967, 1970, 1970) mentioned earlier, the only other major publications on gas absorption are those of Wuilleumier (1969) and Chipman and Jennings (1963). Wuilleumier

measured the absorption spectra of Ne, A, Kr and Xe from 1.5 Å (8.267 keV) to 15 Å (0.8267 keV) at intervals of 0.05 Å between 1.5 and 8 Å and at intervals of 0.1 Å from 8 Å to 15 Å, using single-crystal diffraction of the tube continuum radiation as source, and a photographic detection technique. His very detailed work is therefore greatly reduced in value due to the combined effects of less complete monochromaticity and a rather doubtful and insensitive detection method. Wuilleumier only claims an accuracy of between 3 and 6% for his values.

Chipman and Jennings measured the attenuation coefficients of Ne, A, Kr and Xe using molybdenum K_α radiation. They used a single-crystal diffractometer to produce monochromatic radiation and a proportional counter as detector. The results are believed accurate to about 1%, but unfortunately only two data points within our region of interest have been measured.

Some experimental work has also been published on carbon. Chipman (1955) suggested that results for graphite using copper K_α radiation under very stringent collimation conditions deviated from the expected value due to a small-angle scattering phenomenon caused by the long-range structure of graphite. He suggests measuring the attenuation coefficient of graphite by using variable slit width and extrapolating to zero width. This method is claimed to agree better with measurements on non-crystalline carbon compounds.

Another measurement at the same energy by Ergun and Tiensuu (1958) employed a transmission and reflection technique on an oblique graphite sample. The method was designed to overcome the difficulties of small angle scatter and its result agreed with that of Chipman. In general,

the difficulties associated with measurements on graphite due to its crystalline structure constitute a very strong reason for obtaining data on carbon using non-crystalline organic materials as absorbers.

As regards the other elements between carbon (Z = 6) and argon (Z = 18) there is no reliable recent measurement on fluorine, sodium, silicon, phosphorus, sulphur or chlorine, or any of their compounds. While some information can be deduced by interpolation from elements of adjacent atomic number, it would clearly be of value to make direct measurements on many of the elements in the low atomic number range.

2.2 THEORETICAL

In the energy region of interest and for low -Z materials only three processes contribute significantly to the total photon cross-section; these are the photoelectric effect, Compton (or incoherent) scattering, and Rayleigh (or coherent) scattering.

2.2.1 Photoelectric effect

Exact calculations of theoretical photoelectric cross-sections in closed form are not possible. The principles involved in such a calculation are, however, well understood, but systematic calculations are complicated. Various approximations can be used, but these must be applied with care. Until recently, the difficulties were so great that uncertainties in theoretical photoeffect cross-sections were large, and information was more accurately derived indirectly from total cross-section data by subtraction of the scattered contribution. Recent improvements have made the accuracies of theoretical and experimental values comparable.

Most calculations neglect radiative effects, and treat the problem by time-dependent perturbation theory, i.e. the incoming photon is

regarded as a perturbation causing transition of an electron from an initial bound state ψ_B to a final state in the continuum ψ_p.

The cross-section is then proportional to the transition probability, which depends on the matrix element between the initial and final states and the Hamiltonian of the perturbation.

$$M \propto \int d^3\underline{r} \quad \psi_p \quad \underline{\alpha} \cdot e^{\underline{ik}\cdot\underline{r}} \quad \psi_B \qquad \ldots\ldots(2.1)$$

where $\underline{\alpha}$ is the Dirac matrix, $\underline{k}$ is the k-vector of the incident radiation ($|\underline{k}| = \frac{2\pi}{\lambda}$), and $\underline{e}$ is a vector of magnitude e (= 2.71...) in the direction of polarisation of the incident photon.

ψ_B is normally taken as a bound-state solution of either the Schrödinger equation or the Dirac equation, which for the K-shell is a hydrogen-like wave-function. For L- and higher shells some form of screening must be taken into account. ψ_p is also a solution of the Schrödinger or Dirac equation in a Coulomb field. This can be treated as an expansion in partial waves, in which case truncated series, of validity at one extreme of E or Z only, can be managed computationally. Alternatively one can establish ψ_p in successive Born approximations, or using a technique involving Sommerfeld - Maue - Furry wave-functions to obtain results in the high-energy limit. The handling of the final wavefunction is the chief difficulty in all theoretical approaches, and improvements come through more quickly convergent iteration techniques which make summations to higher terms feasible. This has extended the range of theoretical data considerably within the last few years. The treatment of the screening effect due to the inner electrons is another aspect of the calculation in which considerable improvements have recently been made.

A calculation using exact non-relativistic hydrogen-like wave-

functions was done by Stobbe (1930) and a relativistic calculation using the Dirac equation was carried out by Sauter (1931). This turns out to be a series in $\frac{Z\alpha}{E}$ (Z = atomic number of absorber; α = fine structure constant $\doteqdot \frac{1}{137}$; E = ingoing photon energy). Sauter's calculation is correct to first order in $\frac{Z\alpha}{E}$. This result, and a similar high-energy approximation due to Hall (1934), tally well with a numerical calculation performed by Hulme et al. (1935).

Interest in these calculations has recently revived. Information on the K-shell component has been published by Bethe and Salpeter (1957), Erber (1959), Gavrila (1959), Pratt (1960), Nagel (1960), Hultberg et al. (1961), Pratt et al. (1964), Hall and Sullivan (1966), Forssner (1968) and Hultberg et al. (1968). Most of these consist of successive improvements of computational technique enabling the E and Z range within manageable limits to be greatly extended to include high Z and lower energies. Except Hall and Sullivan, who used a screened Coulomb potential on the Fermi-Thomas model, all the calculations use an unscreened Coulomb potential for calculation of ψ_B. This work has extended the range of such calculations to cover all elements, although only energies from 800 keV upwards are manageable for uranium, and other high -Z elements.

Analogous calculations for the L-shell photoeffect have also been carried out by Pratt (1960), Gavrila (1961), Alling and Johnson (1965) and Matese and Johnson (1965). The first three authors used an unscreened Coulomb potential to obtain ψ_B and Sommerfeld - Maue - Furry wave-functions, the Born approximation and partial waves respectively, to calculate ψ_p. Matese and Johnson developed the work of Alling and Johnson by using a screened potential for calculating the wave-functions.

Recently results for all shells incorporating some screening model have appeared. Schmickley and Pratt (1967) have calculated cross-sections up to the M_V level contribution for Fe, Sn and U and by a normalisation approach corrected their results for electron screening. Their values cover Z = 13 to 92 from 10 - 3000 keV. Rakavy and Ron (1967) used Shalitin's modification of the Fermi-Amaldi potential to derive cross-sections in the energy range 1 - 2000 keV for Z = 13, 26, 50, 74, and the Thomas-Fermi potential for Z = 92. Finally Brysk and Zerby (1968) calculated cross-sections for Z = 13 from 1 - 150 keV using bound state wave-functions derived by Liberman, Cromer and Waber (1965). These are based on a solution of the Dirac equation in a Coulomb field using Slater's density approximation to represent the exchange potentials experienced by a given electron.

Brysk and Zerby (1967) also published the computer programme used to obtain their results. This was modified by Cromer, who used experimental rather than theoretical binding energies, and made extensive calculations from 1 to 100 keV. Further calculations by Atwater and by Israel, and interpolation methods, have enabled a complete table of photoeffect cross-sections from 1 to 1000 keV for Z = 1 to 100 to be derived. This work is published by Storm and Israel (1970).

Some low energy non-relativistic calculations have also recently been carried out. Manson and Cooper (1968) derive results for Z = 13 from 5 to 30 keV using the Hartree-Fock potential with Slater's density approximation (the so-called Herman-Skillman (1963) potential). McGuire (1968) has also used this potential to calculate cross-sections for Z = 2 to 54 from 0.006 keV to 60 keV.

2.2.2 Incoherent and coherent scattering

The Klein Nishina formula describes the Compton scattering process:

$$\frac{d\sigma_c^{KN}(\theta)}{d\Omega} = \frac{1}{2} r_e^2 \left[1 + k(1 - \cos\theta)\right]^{-2} \left[1 + \cos^2\theta + \frac{k^2(1 - \cos\theta)^2}{1 + k(1 - \cos\theta)}\right]$$

$$m^2 \text{ electron}^{-1} \text{ sr}^{-1} \qquad \ldots\ldots(2.2)$$

$$\sigma_c^{KN} = 2\pi r_e^2 \left\{\frac{1 + k}{k^2}\left[\frac{2(1 + k)}{1 + 2k} - \frac{\ln(1 + 2k)}{k}\right] + \frac{\ln(1 + 2k)}{2k} - \frac{1 + 3k}{(1 + 2k)^2}\right\} m^2 \text{ electron}^{-1} \qquad \ldots\ldots(2.3)$$

where σ_c^{KN} and $\frac{d\sigma_c^{KN}(\theta)}{d\Omega}$ are the total and differential Klein-Nishina cross-sections; r_e is the classical electron radius; and k is the incident photon Compton wavelength ($k = \frac{1}{\lambda}$).

These formulae apply to the scattering of a photon by a free electron. When the electron is bound in an atom, the binding effects must be considered, especially in the limit of low energy transfer. The binding is treated using an incoherent scattering function S(q, Z) which represents the probability that an atom be raised to any excited or ionized state as a result of an impulse which imparts recoil momentum q, to an atomic electron

$$\frac{d\sigma_c^{bd}(\theta)}{d\Omega} = S(q,Z) \frac{d\sigma_c^{KN}(\theta)}{d\Omega} \; m^2 \text{ atom}^{-1} \text{ sr}^{-1} \qquad \ldots\ldots(2.4)$$

S(q,Z) can be calculated for any atom, once the electronic wave-functions of the atom have been obtained. Hence it is known analytically for hydrogen, and approximately for other elements.

Early results by Heisenberg (1931), and Bewilogua (1931) used the Thomas-Fermi model to calculate atomic wave-functions. Although

values of S(q,Z) from Hartree-Fock wave-functions were calculated for some atoms and ions by Milbert and Brailsford (1958) and Freeman (1959), it is only recently that a comprehensive calculation for all elements has been attempted. In 1967, Mann obtained Hartree-Fock wave-functions for all the atoms. Then by comparing the values of Herman and Skillman (1963) who used Slater's density approximation on the Hartree-Fock model, with those of Liberman, Cromer and Waber (1965) who used the same approximation with the Dirac equation, he was able to estimate the relativistic corrections to his Hartree-Fock wave-functions. These results were used by Cromer and Mann (1967) to calculate S(q,Z) for the thirty-nine spherically symmetric free atoms, and subsequently by Cromer (1969) for the remaining aspherical atoms.

Recently Brown (1970a, b) has used 2-, 3- and 4-electron wave-functions to derive exact values of S(q,Z) for He, Li, and Be.

Similar methods are used to deal with the effects of atomic binding on coherent scattering. The differential Rayleigh cross-section is modified by an atomic form factor F(q,Z) to take binding into account:

$$\frac{d\sigma_R(\theta)}{d\Omega} = \frac{r_e^2}{2}(1 + \cos^2\theta)\left[F(q,Z)\right]^2 \qquad .....(2.5)$$

As with S(q,Z), the earlier values of F(q,Z) are based on the Thomas-Fermi potential. More recent work uses the Hartree-Fock model. Using the Herman-Skillman wave-functions derived on the Hartree-Fock-Slater model, Hanson et al. (1964) have derived F(q,Z) for Z = 2 to 100. Cromer, Larson and Waber (1964) also published F(q,Z) values based on the Hartree model for Z = 37 to 98. A complete set of values based on Slater's density approximation in conjunction with the Dirac

equation was published in 1965 by Cromer and Waber.

2.3 SEMI-EMPIRICAL

At an early stage in the study of X-ray attenuation ~~it was~~ it was noticed that the variation of attenuation coefficient with photon wavelength for a given element followed a smooth curve, as did the variation with absorber atomic number for the same wavelength of radiation. On a log-log scale, both these relationships are, to a first approximation, linear. From their experimental observations Bragg and Pierce (1914) deduced a power law of the form:

$$\sigma_{tot} = CZ^4 \lambda^{5/2} \qquad .....(2.6)$$

where σ_{tot} is the total attenuation cross-section, and C is a constant over large ranges of Z and λ, between absorption edges. A similar result was obtained by Owen (1918) and a power law of the kind

$$\frac{\mu}{\rho} = CZ^a \lambda^b \qquad .....(2.7)$$

is generally referred to in this context as a Bragg-Owen law.

There is, however, little physical justification for expecting the total attenuation coefficient, which is a compound of several processes, to be described by a simple power law. A more reasonable suggestion is that of Hall and Rice (1916) who separate $\frac{\mu}{\rho}$ into a photoelectric and a scattering component. For each element they propose a third-power law in λ to describe photoelectric absorption, the multiplicative constant varying from element to element. For the short wavelength radiation used they proposed a constant scattering factor.

This still leaves a lot to be desired, but is a physically more realistic situation. It is also backed up by the results of various

workers who attempted to produce theoretical derivations of power law behaviour. A classical model used by Sir J. J. Thomson (1906) leads to a λ^3 law; using quantum theory Compton (1919), de Broglie (1922) and Kramers (1923) independently arrived at the same power law:

$$\tau_{pe} = CZ^4 \lambda^3 \qquad .....(2.8)$$

where τ_{pe} is the photoelectric cross-section, but they disagreed on their values of the constant C.

Because of the relationship between cross-section and attenuation coefficient (equation 1.8) this implies a relationship of the form:

$$\frac{\mu}{\rho} = C Z^3 \lambda^3 + \frac{\sigma}{\rho} \qquad .....(2.9)$$

During the twenties and thirties most experimenters tried to fit their results to a Bragg-Owen law. There was considerable disagreement on the values of the coefficients a and b (equation 2.7) which best fitted their data. In general, however, they observed a deviation from integral values for both coefficients. Part of the reason for the lack of agreement between experimenters is pointed out by Allen (1926). Although opting for a power law

$$\sigma_{tot} = C\lambda^{2.92} Z^4 + \sigma_{scattering} \qquad .....(2.10)$$

he states that the scattering contribution is too inaccurately known to allow any real distinction between the various empirical formulae to be made.

Recently, interest in this kind of simple semi-empirical fitting has been revived. Leroux (1961) proposed a self-consistent set of mass absorption coefficients using the relationship:

$$\frac{\mu}{\rho} = C\lambda^n \qquad .....(2.11)$$

Values of C and n vary from one element to the next. Heinrich (1966) tabulates figures for C and n for each element, different values being used between the various absorption discontinuities.

However, the graph of $\log \frac{\mu}{\rho}$ (or $\log \sigma_{tot}$) against $\log \lambda$ (or $\log E$) is not perfectly linear, especially on the short wavelength (or high energy) side of a discontinuity. There are two possible means of handling this deviation. The authors of the recent compilations (McMaster et al. (1969); Veigele et al. (1970); see section 2.4) fitted the $\ln \tau_{pe} / \ln E$ curve by a cubic polynomial between absorption discontinuities:

$$\log_e \tau_{pe} = \sum_{i=0}^{3} C_i (\log_e E)^i \qquad .....(2.12)$$

A somewhat less obvious modification of the basic Bragg-Owen relation was proposed earlier by Victoreen (1943, 1948, 1949). From available experimental data Victoreen suggested:

$$\frac{\tau}{\rho} = \alpha Z^2 \lambda^3 \left(\frac{2Z}{A}\right) - \beta Z^5 \lambda^4 \left(\frac{2Z}{A}\right) \qquad .....(2.13)$$

where A is the atomic ~~number~~ mass, and α and β are functions of Z, which change at each critical wavelength.

Then

$$\frac{\mu}{\rho} = \frac{\tau}{\rho} + \sigma_c^{KN} \cdot N_A \cdot \frac{Z}{A} \qquad .....(2.14)$$

where σ_c^{KN} is the Klein-Nishina total cross-section, and N_A is the Avogadro constant.

Victoreen published values of the coefficients in all the functions quoted, for the elements Z = 1 to 92. In his later papers, he extended the range of applicability of his formulae.

2.4 COMPILATION

Because of the possibility of fairly accurate semi-empirical fitting of data, and the improving accuracy of theoretical work, there has been a tendency recently for compilations of "best-values" of cross-sections to proliferate. Various authors have attempted a critical assessment of the data available to them, either from experimental or theoretical work, or from both, in order to synthesize a single table of values for a wide range of energies and atomic numbers. Unfortunately, there is considerable disagreement between the publications, even the most recent, with the result that confusion as to the most reliable set is as great as ever.

In 1952, the first modern compilation was published by White. This publication gave photon cross-sections for nineteen elements from 10 keV to 100 MeV and was based primarily on theoretical calculations, experimental data serving merely as a check. These tables, in revised form, were published by Grodstein (née White) in 1957. The K-shell photoeffect cross-sections were calculated from the Sauter-Stobbe formula in the low-energy range, and empirical correction factors obtained by comparison with experimental data were applied to these theoretical results. The incoherent scattering contribution was calculated from the Klein-Nishina formula. The author estimates the uncertainties to be possibly as large as 10% below 50 keV, but even this figure seems optimistic.

A revision of this work, published by McGinnies in 1959 in the light of new experimental data claims, again somewhat optimistically, to reduce these errors to 3 - 5%.

The compilation published by Davisson (1965) is a further updating of this work using new theoretical photoeffect values of Hultberg et al. (1961) and Pratt et al. (1964).

In these three compilations the best available values of S(q,Z) and F(q,Z), which were used to calculate incoherent and coherent scattering cross-sections, were derived from the Thomas-Fermi model. The authors tabulate the sum ($\sigma_c^{bd} + \sigma_R$), which is less sensitive to errors in the atomic model than is either of the two contributions taken separately. Since 1967, five major compilations have been published by Storm and Israel (1967, 1970); McMaster et al. (1969); Hubbell (1969); and Veigele et al. (1971). In their earlier 1967 version, Storm and Israel derive their photoeffect cross-sections from experiment and from recent theoretical values such as those of Schmickley and Pratt (1967), Rakavy and Ron (1967) and Hultberg et al. (1968). The data were graphically smoothed on a log-log scale against E (for constant Z) and Z (for constant E) to synthesize the tables. It is worth noting that recent theoretical work, notably that of McGuire (1968) and Manson and Cooper (1968) has suggested that smoothing against Z, at constant E, may be erroneous, as the theory suggests that the function is not a smooth one, especially at energies below 10 keV. Such smoothing is, however, a feature of most compilations. For scattering cross-section calculations, Storm and Israel used the S(q,Z) data of Cromer and Mann (1967) with some pre-publication data from Cromer (1969). As σ_c^{bd} is not a smooth function of Z they freely concede that interpolated values for those elements not yet calculated by Cromer may be up to 5% in error. Their σ_R is based on calculations of F(q,Z) by Hanson et al. (1964). Hence the coherent cross-sections are based on the Herman-Skillman wave-functions derived on the Hartree-Fock-Slater model, whereas the incoherent cross-sections are derived from data using a relativistic correction to the same wave-functions.

The scope of Storm and Israel's tabulation is from 1 keV to 100 MeV for Z = 1 to 100.

Hubbell's compilation is really a revision of the Grodstein-McGinnies-Davisson work, taking account of the recent theoretical photoeffect work and also more recent experimental values. The coherent and incoherent scattering cross-sections are obtained by methods identical to those of Storm and Israel (1967). Figures are given for a selection of elements between Z = 1 and 92 from 10 keV to 100 GeV.

The best available critical tables of experimental cross-section data are those of McMaster et al. (1969) and Veigele et al. (1971). Both publications use the scattering factors of Cromer and Mann (1967), and Cromer and Waber (1965) based on a relativistic correction to the Herman-Skillman wave-functions. Using these scattering cross-sections both sets of authors calculate photoelectric cross-sections from extensive bibliographies of experimental total cross-section measurements. In both cases, the resultant photoelectric cross-sections are assigned a subjective weighting factor dependent on the apparent reliability of the original experiments. McMaster then smoothes the photoelectric data using a single cubic fit on a log-log scale between each absorption edge before re-incorporating the scattering values to synthesize the total cross-section. Interpolation with Z is used to obtain results for elements where experimental information is scanty or non-existent.

Veigele, on the other hand, first performs a log-log cubic fit with energy for each element. He then uses points from these analytical fits to construct graphs of $\log \tau_{pe}$ against $\log Z$. A second cubic log-log fit is then made to this data. The process is then repeated using values from this $\log \tau_{pe}/\log Z$ fit as well as the

original data. After five repeats of this cycle of operations, the smoothed values of τ_{pe}, the photoelectric cross-section, are obtained. The scattering contributions are then added to give values of σ_{tot}, the total cross-section.

Both these approaches can be criticised on several counts. Firstly, the theoretical basis for smoothing against Z may be questioned. At low energies deviations are likely to occur. On the other hand, there is no other way to deduce data for elements for which little or no experimental information is available. It would appear that the McMaster approach with its emphasis on smoothing against E is more defensible from this point of view than the method of Veigele which over-stresses the Z dependence. The other major drawback in experimental compilations is the subjectivity involved in assigning weights to different experiments.

In contrast to both these compilations the 1970 publication by Storm and Israel is based entirely on theoretical information. Their photoeffect data from 1 to 200 keV are based on the Brysk-Zerby programme (see Section 2.2.1). Extensive use of this programme by Cromer, Atwater and Israel using a modification due to Cromer, provided a complete table for Z = 1 to 100 and E = 1 to 1000 keV. Above 200 keV their values are obtained from the Schmickley-Pratt (1967) and Rakavy-Ron (1967) results. The work of Cromer and Mann (1967), and Cromer (1969), using the relativistic Herman-Skillman potential, is used to calculate incoherent cross-sections and that of Cromer (1970) and Hanson et al. (1964) using the same potential was used for the coherent cross-sections. The results of Brown (1970) on low atomic number elements were also used. These represent the best available values for the cross-sections of all three attenuating

processes, and the report itself is the only really reliable volume of theoretical data in existence.

2.5 COMMENTS

The lack of agreement between the authors of the various experimentally-based compilations is a reflection of the unsatisfactory state of experimental knowledge itself. The McMaster tabulation can probably be regarded as the best data set based on experiment, and the results of the present work will be compared with his published values.

It will be of greater interest and value, however, to compare these experimental results with the theoretical values of Storm and Israel (1970). No previous experimental work has provided sufficient data for a thorough check of the new theoretical results at low energy and atomic number.

There has also been no previous attempt to provide experimental evidence for or against the theoretical hypothesis of McGuire (1968) and Manson and Cooper (1968) that "bumps" may occur in the log τ_{pe} versus log Z curve at low energies. The results of this work will provide evidence about such irregularities.

Finally, it is hoped that a reliable data set covering the low atomic number elements over the energy range from 4 - 25 keV will be synthesized which will supersede the values in this range quoted for use in radiation dosimetry work by the International Commission on Radiation Units and Measurements (ICRU Report 17, 1970).

CHAPTER 3

DESIGN OF THE APPARATUS

3.1 INTRODUCTION

At the outset this project was envisaged as an accurate measurement of total mass attenuation coefficients of low atomic number elements using gaseous absorbers. Several factors contributed to the choice of gases as absorbers. Between carbon and argon there are six elements (nitrogen, oxygen, fluorine, neon, chlorine and argon) which exist as gases at room temperature and pressure, and many gaseous compounds of these elements, and of others in the atomic number range (e.g. carbon, sulphur), are easily obtainable. The homogeneity, purity, and manageability of gases make them attractive absorbing materials, as well as the important fact that in the energy range of interest (4 to 25 keV) the length of gas column required to produce reasonable attenuation falls in a range which is easily measurable. This contrasts with the situation for solid absorbers, where very thin foils are required at the lower energy end of the range. These points are considered at length in subsequent sections of this chapter. However, in general terms, the measurements on gases constitute the main part of the work undertaken, and the apparatus, although easily adapted to deal with solid and liquid absorbers, was originally developed with gaseous absorbers in mind.

Work on solids and liquids was prompted by the need for data on some of the intervening elements (particularly magnesium, silicon, and phosphorus), and in order to make possible an investigation of the variation with atomic number of the photoelectric cross-section. Since the elements for which gaseous absorbers were not available fall in a

group from Z = 11 to 15 inclusive, the absence of any measurements on all of these materials would have prevented any such investigation being made.

3.2 CRITERIA OF APPARATUS DESIGN

The mass attenuation coefficient is defined by the relationship

$$I = I_o e^{-\frac{\mu}{\rho}\rho x} \qquad .....(3.1)$$

on the basis of a hypothetical experiment carried out under very carefully specified conditions (see Section 1.1). The validity and accuracy of any experimental determination of $\frac{\mu}{\rho}$ is governed by the extent to which the apparatus used fulfils the requirements implied in the derivation of equation 3.1.

These requirements may be enumerated as follows (see Section 1.1):

(a) the incident beam is perfectly collimated;

(b) the transmitted beam is also perfectly collimated;

(c) the incident photons are monoenergetic, of energy, E;

(d) the detected photons are monoenergetic, also of energy, E;

(e) the absorbing material is homogeneous; or, at least, the quotient $\frac{\delta I}{\delta x}$ which is the intensity loss in a thin layer, tends to a stable limit (as δx tends to zero) while δx is still sufficiently large to satisfy the requirement of absorber homogeneity;

(f) the interaction is sufficiently weak that the intensity is essentially constant within a thin layer, of sufficient thickness, δx, to satisfy requirement (e).

These conditions must be satisfied (or deviations from them be of such a kind that they can be shown to produce a negligible effect on

Figure 3.1 APPARATUS FOR GASEOUS ABSORPTION MEASUREMENTS (SCHEMATIC)

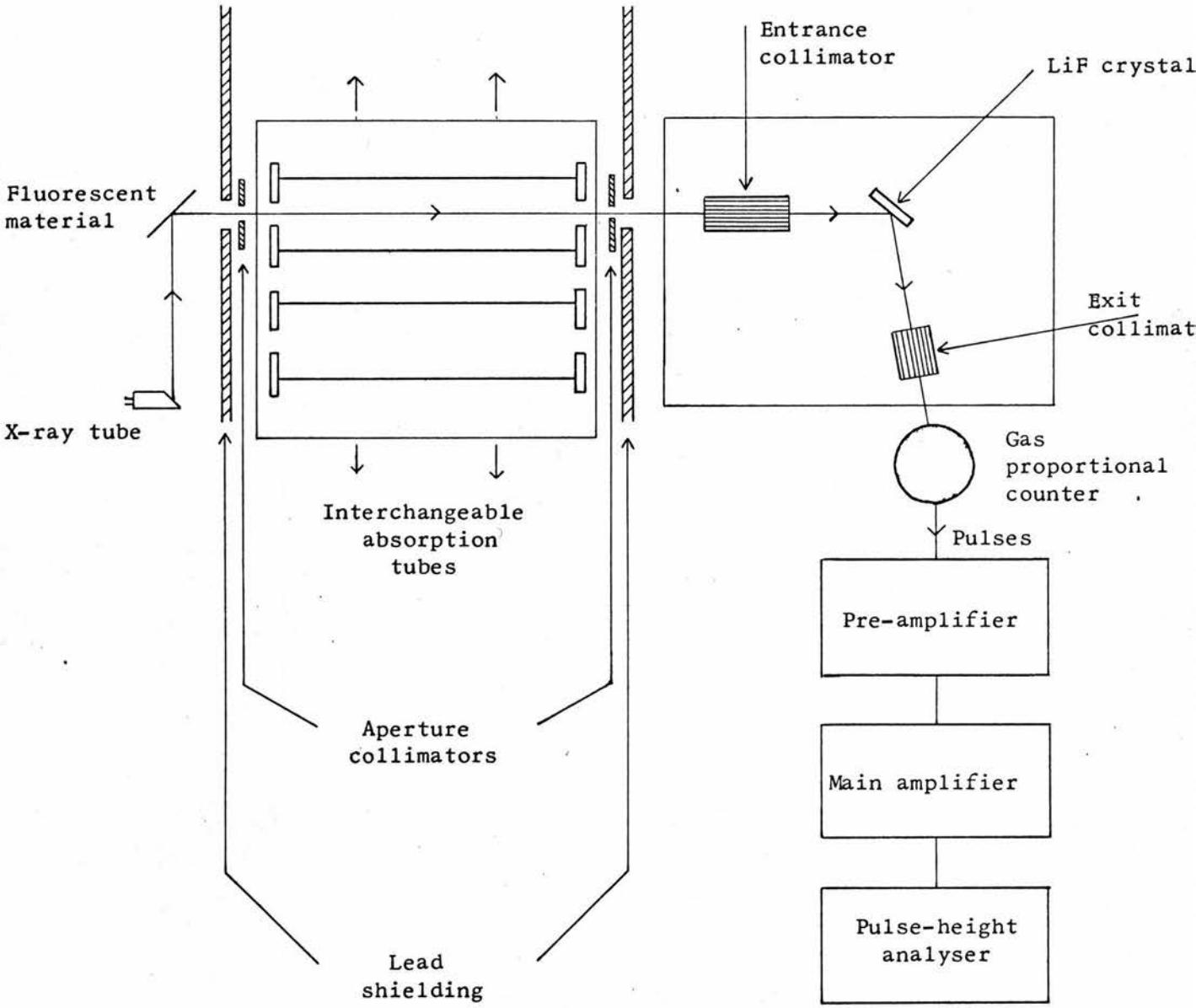

Figure 3.2 APPARATUS USED FOR MEASUREMENTS ON GASEOUS ABSORBERS

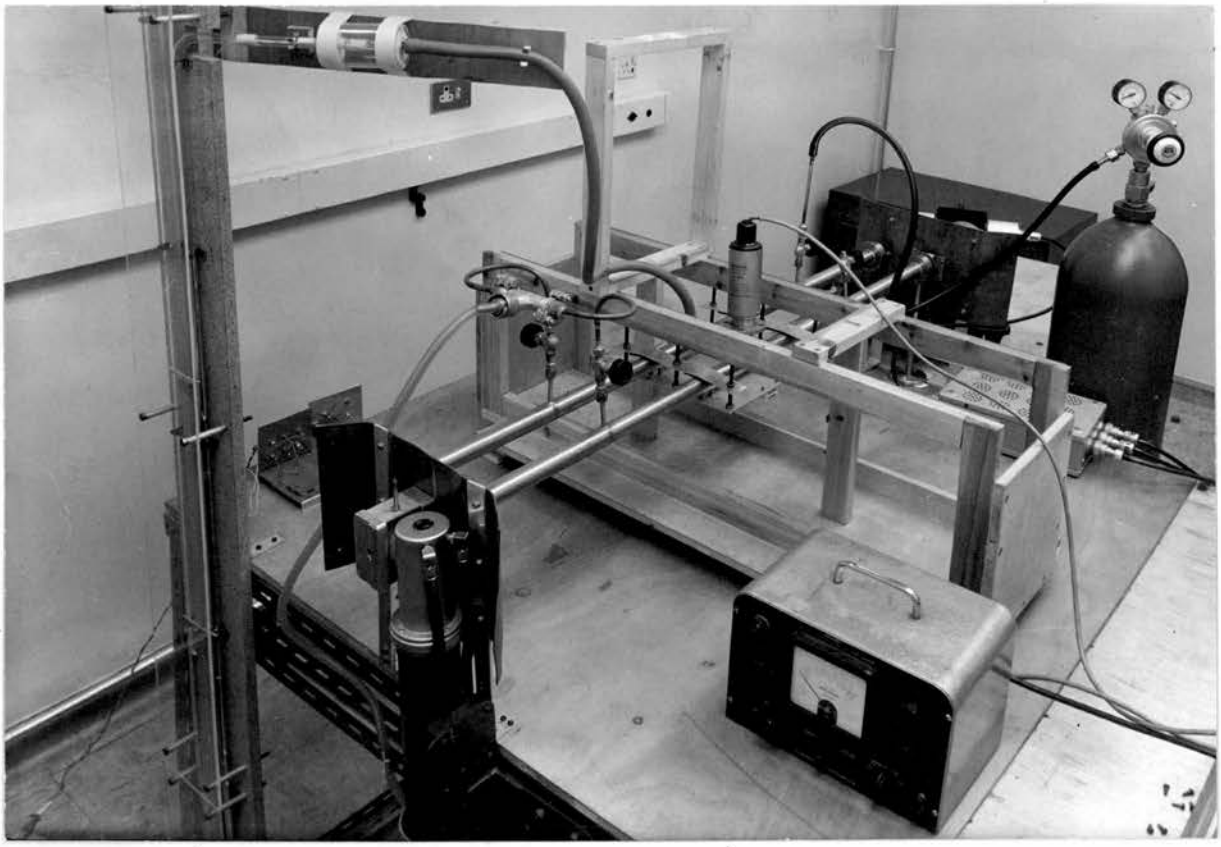

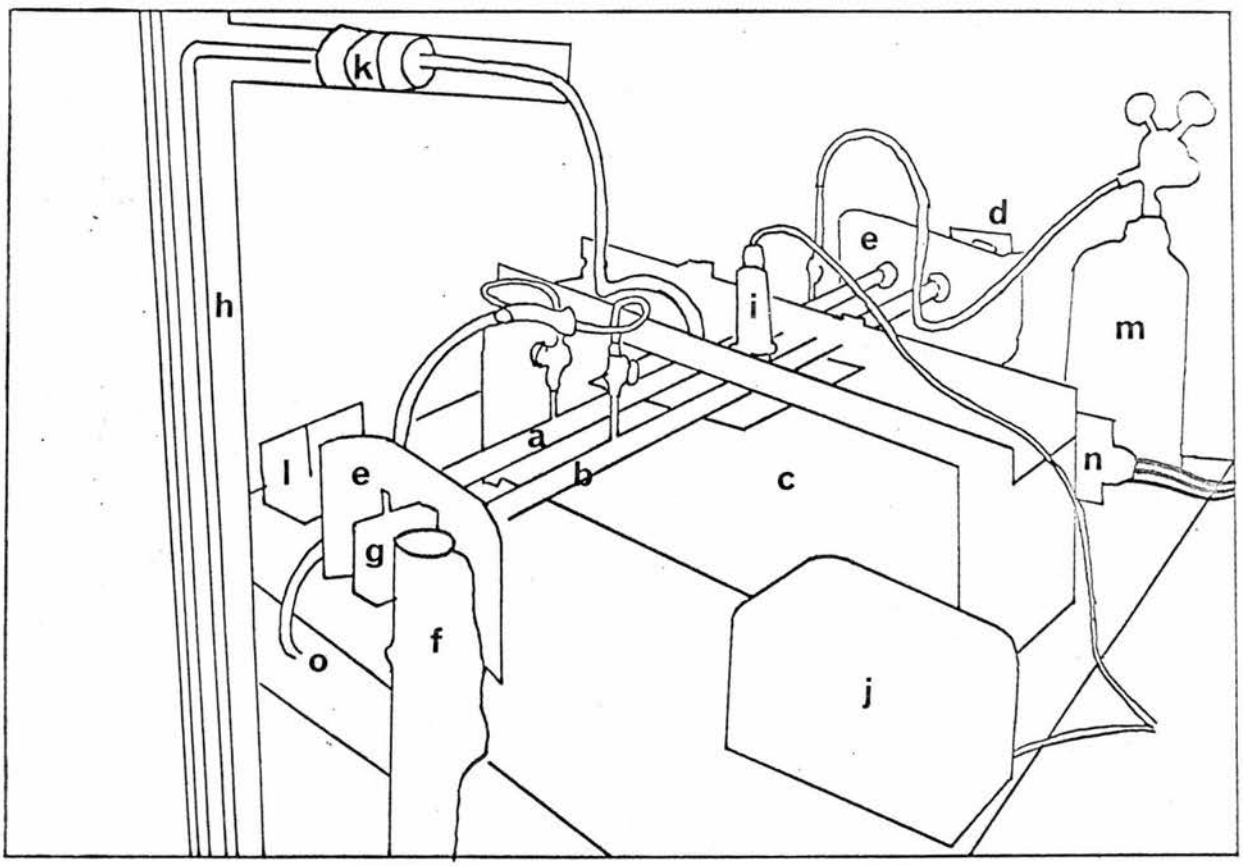

a - Gas tube; b - Vacuum tube; c - Tube interchange device; d - Spectrometer; e - Lead shielding; f - X-ray tube; g - Fluorescent foil holder; h - Manometer; i - Penning gauge head; j - Penning gauge; k - Thermistor protective housing; l - Thermistor bridge circuitry; m - Gas cylinder; n - Pulse pre-amplifier; o - To vacuum pump.

the values of attenuation coefficient observed) in order that the attenuation coefficient be well-defined. It then remains necessary to choose the apparatus parameters in such a way that the quantities $\ln \frac{Io}{I}$ and ρx may be determined to a sufficient accuracy to permit the attenuation coefficient $\frac{\mu}{\rho}$ defined by:

$$\frac{\mu}{\rho} = \frac{1}{\rho x} \ln \frac{Io}{I} \qquad .....(3.2)$$

to be obtained to the required accuracy.

3.3 DESIGN OF THE APPARATUS

3.3.1 General Layout of Apparatus

Before discussing individual aspects of the apparatus in the light of the preceding section, a general description of the apparatus layout is desirable. A schematic diagram of the layout is shown in figure 3.1.

Primary X rays are used to excite secondary fluorescence radiation. This passes through one or other of the two identical interchangeable absorption tubes before being collimated by the entrance Soller slit of the single-crystal goniometer. A lithium fluoride crystal is set to diffract radiation of the Kα characteristic energy of the fluorescent element used. After passing through a second collimator the radiation is detected by a system consisting of a gas proportional counter with a pulse amplifier and a multichannel analyser.

Figure 3.1 illustrates the arrangement for a gaseous absorber. The actual layout during the course of a measurement using a gaseous absorber is shown in figure 3.2.

When solid or liquid absorbers were used, the apparatus was unchanged except for the addition of a Soller slit collimator placed between the fluorescent material and the absorber. The purpose of

Figure 3.3 APPARATUS FOR SOLID AND LIQUID ABSORPTION MEASUREMENTS (SCHEMATIC)

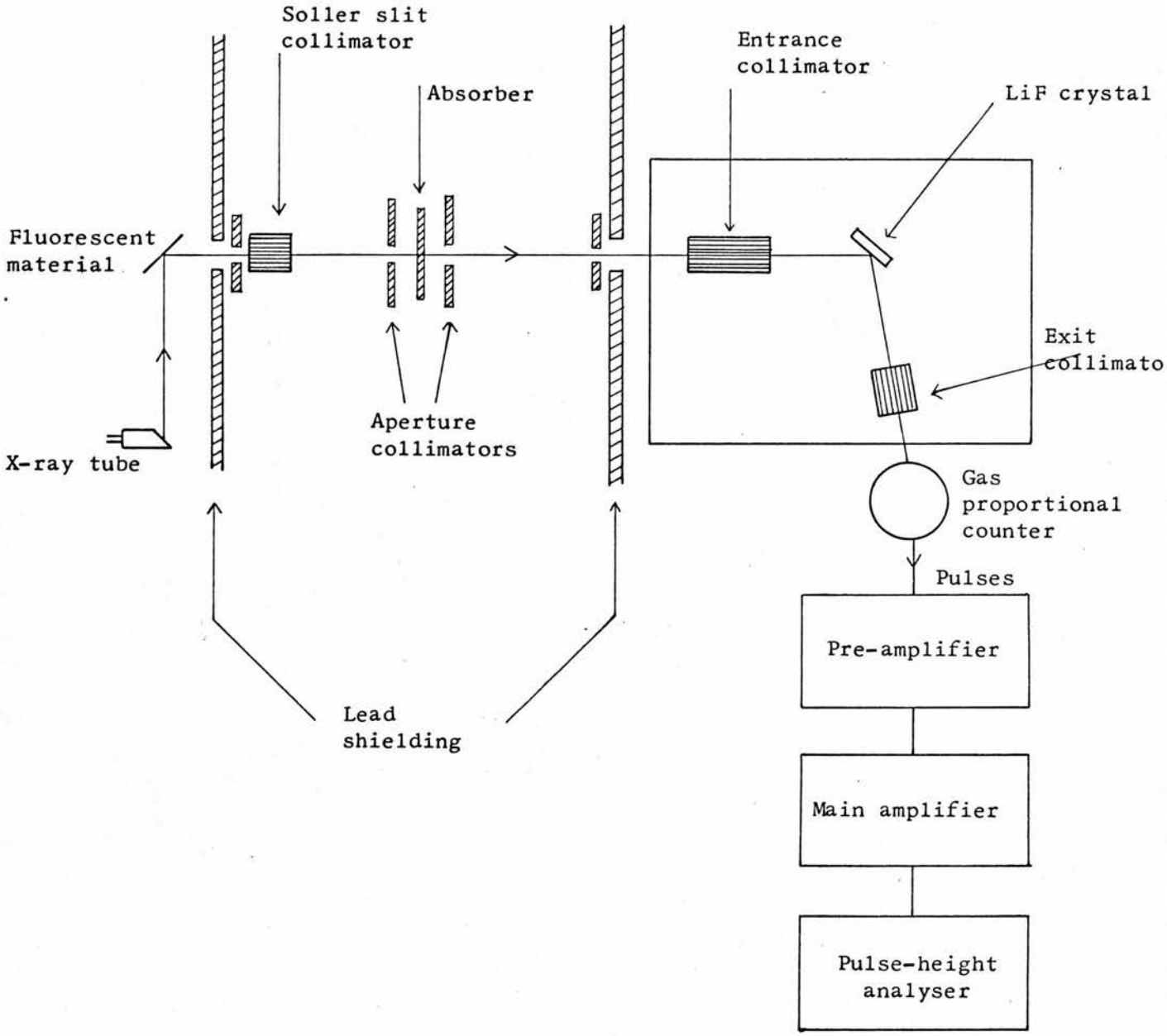

this was to provide good parallelism of the incident beam. A schematic diagram of the apparatus as used for measurements on solid and liquid absorbers is shown in figure 3.3.

3.3.2 Source

The X-ray tube used was a Machlett OEG-50-A with a tungsten target. The window is made of beryllium (1 mm thick), which permits high intensities of low energy radiation to be produced. The tube is operated at constant potential, the kilovoltage being continuously variable from 0 to 50 kV and the tube current from 0 to 30 mA provided that the maximum power dissipation does not exceed 800 watts. The kilovoltage is measured by a "Scalamp" mirror galvanometer which measures the current through a high resistance leak across the tube. The leakage resistance has been chosen such that the resultant sensitivity on the galvanometer scale is 0.5 kV mm^{-1}. The tube current is measured by a milliammeter calibrated in units of 1 mA from 0 to 30 mA.

For the purposes of the experiment a precise knowledge of the tube kilovoltage and current is not essential, i.e. accuracy in the kilovoltage and milliamperage meters is not required. However, the constancy and reproducibility of tube output at any fixed setting of kilovoltage and current is of paramount importance. It is necessary, therefore, to consider the merits of a beam monitoring system. This is discussed in section 3.3.8.

3.3.3 Secondary Fluorescence

The direct radiation from a tungsten target tube consists of a continuum spectrum distributed in energy up to that corresponding to the peak voltage applied externally to the tube. This spectrum

has a broad peak at an energy approximately equal to half of that corresponding to the peak applied voltage. Superimposed on this continuum are several characteristic lines of tungsten, notably the L-series which occurs around 10 keV and consists of three main lines and several subsidiaries. Clearly, it would be possible to produce pseudo-monochromatic radiation from the primary tube radiation using a crystal spectrometer and a collimation system. However, the monochromaticity depends on the degree of collimation and the total intensity in the pass-band is also dependent on the collimation. The more monochromatic the radiation, the lower the intensity. This conflict of criteria is not simply a practical one but is a necessary consequence of picking a narrow energy band from a continuous spectrum; the narrower the band chosen, the fewer photons in the continuum which will lie within. It would, however, be unfair to imply that a high degree of monochromaticity was an essential criterion for accurate attenuation measurements. The errors introduced by the finite width of the pass-band are of a non-critical nature unless the pass-band is very wide. This question is discussed fully in section 3.4.1.2.

A very real problem in any system relying on crystal monochromatisation of the continuum is the extent of the uncertainty in the value of the central energy in the pass-band. Knowledge of this value will depend on readings of the goniometer vernier scales and on information about the 2d spacing of the diffracting crystal used. The former is subject to uncertainties arising from any play in the goniometer bearings, and from any mechanical effects causing irreproducibilities of setting, whilst the latter is dependent on ambient temperature, since small thermal expansions can be important

Table 3.1 FLUORESCENT MATERIALS USED AND THE CORRESPONDING $\overline{K\alpha}$ ENERGIES

Element	$\overline{K\alpha}$ Energy (keV)	Fluorescent material used
Ti	4.508	Ti sheet
Cr	5.411	Cr powder
Fe	6.400	Fe sheet
Ni	7.472	Ni foil
Cu	8.041	Cu sheet
Zn	8.631	Zn sheet
Ge	9.876	Ge powder
Se	11.210	Se powder
Rb	13.375	$RbCO_3$ powder
Zr	15.746	Zr sheet
Mo	17.443	Mo sheet
Ru	19.235	Ru powder
Pd	21.122	Pd foil
Cd	23.108	Cd sheet
Sn	25.192	Sn sheet

at the level of accuracy sought.

The use of secondary fluorescence radiation assists in overcoming these objections. Since all photons in the primary beam, of energy greater than the K edge of the secondary source which is being used, are capable of exciting secondary fluorescence, an appreciable fraction of the primary beam energy is concentrated within a very narrow energy band, viz. within the natural widths of the characteristic lines. The energy resolution obtained by the apparatus is discussed in a subsequent section. For present purposes, it may be stated that the single-crystal spectrometer enabled the Kα and Kβ lines of all the elements used to be resolved but did not resolve $K\alpha_1$ and $K\alpha_2$, or $K\beta_1$ and $K\beta_2$, for any element. Consequently, the higher intensity Kα lines were used. The elements chosen as secondary sources are listed in table 3.1. These were selected to provide even spacing in energy throughout the range 4 - 26 keV. The values of energy tabulated are taken from data presented by Storm and Israel (1970). These are quoted as $\overline{K\alpha}$ energies, i.e. a weighted mean of $K\alpha_1$ and $K\alpha_2$. From data on the $K\alpha_1$ and $K\alpha_2$ energies presented in the same publication it is possible to arrive at an estimate of the effective resolving power of the spectrometer when used with secondary fluorescence radiation.

For example, the Ti $K\alpha_1$ energy is quoted as 4.510 keV, whilst the Ti $K\alpha_2$ energy is given as 4.504 keV. If it is assumed that the separation of the two characteristic lines is much greater than the natural width of either line then half the separation, 0.003 keV, is an estimate of the effective energy half-width of the unresolved Kα peak.

Figure 3.4 FLUORESCENCE MEASUREMENTS

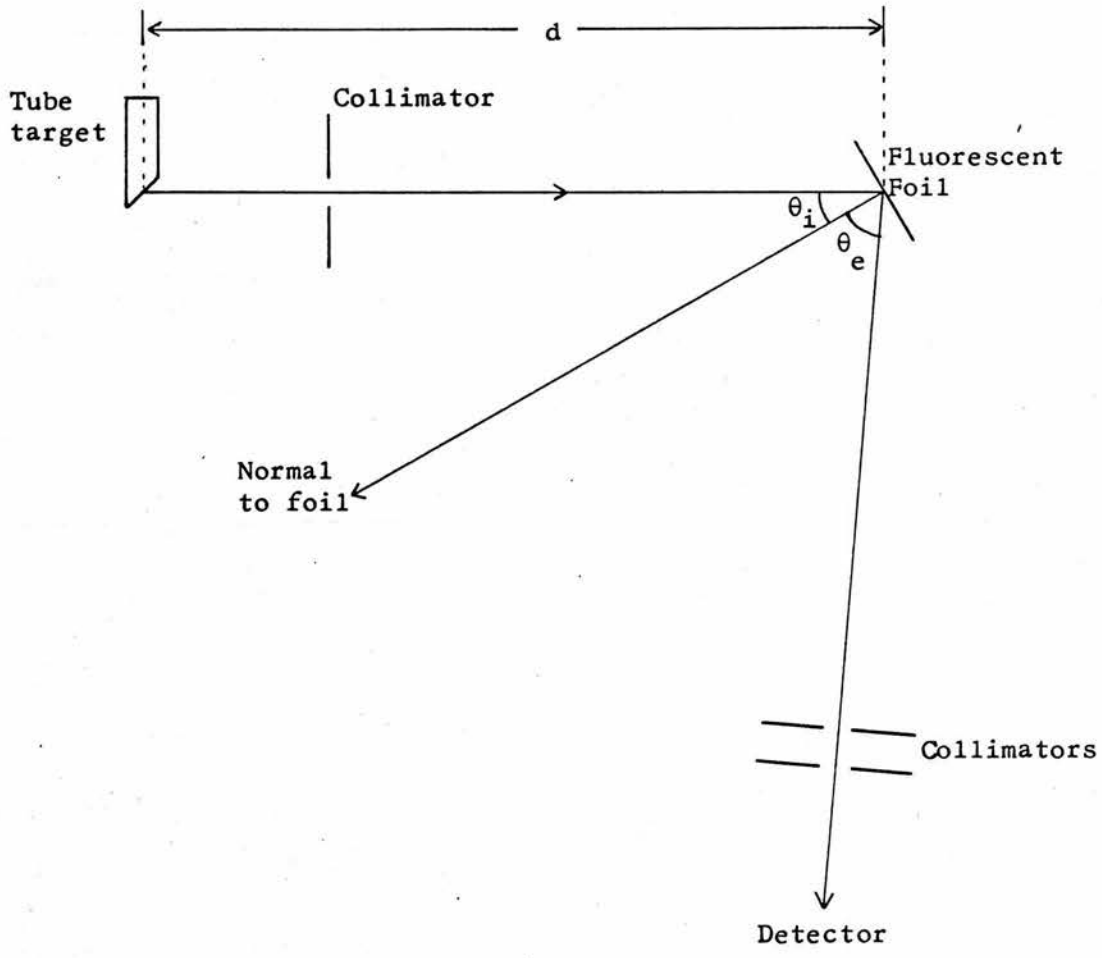

Figure 3.5 VARIATION OF FLUORESCENT RADIATION INTENSITY WITH SECONDARY SOURCE GEOMETRY

a) $\theta_i + \theta_e = 90^o$

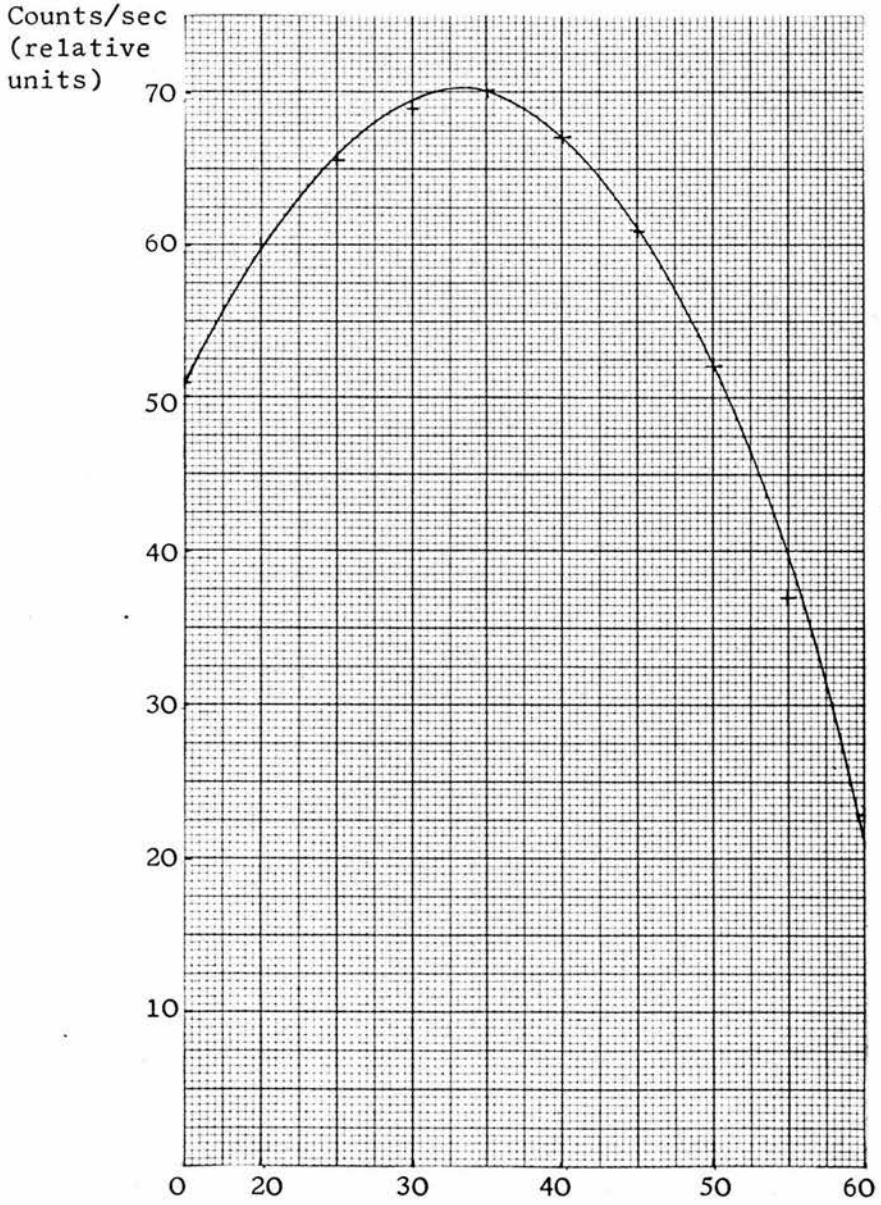

b) $\theta_i = \theta_e$

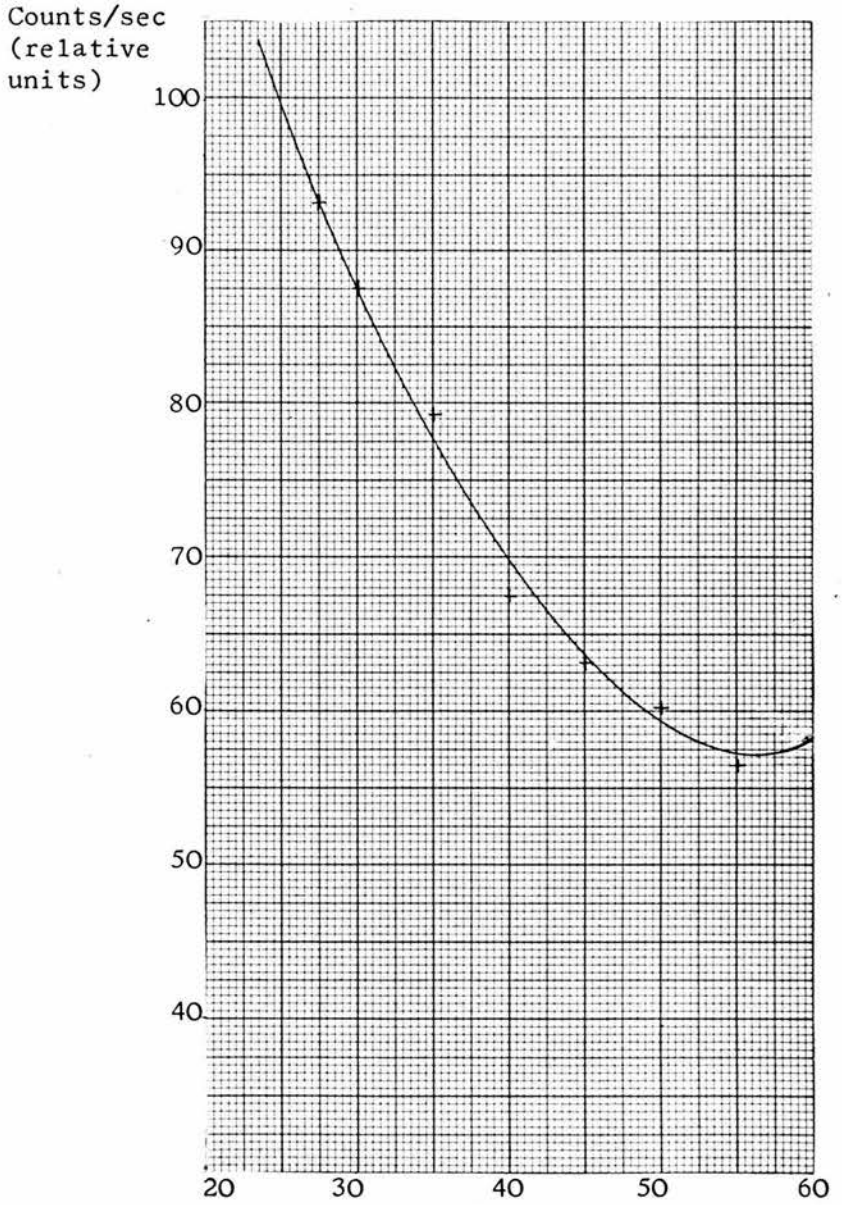

The resolving power, R, defined as E_o/σ where E_o is the peak energy and σ the energy half-width, has then a value of approximately 1500 for Ti $\overline{K\alpha}$ radiation.

At the other end of the energy range, the resolving power of the spectrometer for Sn $\overline{K\alpha}$ radiation is approximately 220.

The implications of these resolving powers on observed values of $\frac{\mu}{\rho}$ are discussed in section 3.4.1.2.

From a practical point of view it was necessary to design the apparatus in such a way as to produce the maximum intensity of secondary fluorescent radiation. A schematic diagram of the basic arrangement for the production of secondary fluorescence is shown (figure 3.4). The intensity of secondary fluorescence was investigated experimentally under three sets of conditions:

(i) d constant; $\theta_i + \theta_e = 90^o$; vary θ_i

(ii) d constant; $\theta_i = \theta_e$; vary θ_i

(iii) θ_i; θ_e constant; vary d

In all three experiments a molybdenum sheet was used as the source of fluorescent radiation (Mo $\overline{K\alpha}$ = 17.443 keV). There seems no reason to suppose that this essentially geometric effect will be in any way energy dependent. The tube kilovoltage was maintained at 30 kV, and the tube current at 8 mA. The detector used was a scintillation counter consisting of a 1" diameter NaI(Tl) crystal mounted on a 1" E.M.I. 9524 KA photomultiplier tube. Pinhole-type collimators were used. The output pulses were amplified and counted on a multichannel analyser, which enabled the molybdenum Kα peak intensity to be integrated.

The results were as follows:

(i) Observed count rate is maximum for $\theta_i \triangleq 35^o$; $\theta_e \triangleq 55^o$

with symmetric fall off on either side of this maximum. See figure 3.5(a).

(ii) The count rate increases monotonically as θ_i and θ_e tend to smaller angles. For reasons of the actual physical geometry of the tube it was impossible to work below $\theta_i = 28^o$. The relationship is shown in figure 3.5(b).

(iii) For varying d, it was expected that an inverse square law would hold, breaking down at short distances where the assumption of a point source is invalid. The angular geometry of the foil was held constant at $\theta_i \simeq 35^o$; $\theta_e \simeq 55^o$. As d is measured from the focal spot of the tube which is inaccessible, the distance, x, from the tube window was plotted against (count rate)$^{-\frac{1}{2}}$.

The relationship was observed to be linear at large distances, and the count-rate increases in general as d becomes smaller.

On the basis of these experimental results it was decided that the fluorescent substance should be placed as close as possible to the tube window. This necessitated using $\theta_i + \theta_e = 90^o$ in order to avoid obstruction of the beam by the tube head. Hence an angular setting of $\theta_i = 35^o$ was adopted.

The metallic sources were in the form of 5.08 cm x 5.08 cm sheets or foils. Each was mounted on a backing of 6.38 cm x 5.08 cm x 0.0635 cm Perspex sheet. The powder sources were contained in a cylindrical Perspex sided cell of 2.54 cm internal diameter and 0.635 cm thickness. The ends of the cell were of 0.00635 mm "Melinex" film in order that neither the incident nor the fluorescent

Figure 3.6 FLUORESCENT FOIL HOLDER: TOP AND SIDE PROJECTIONS

Scale 1x

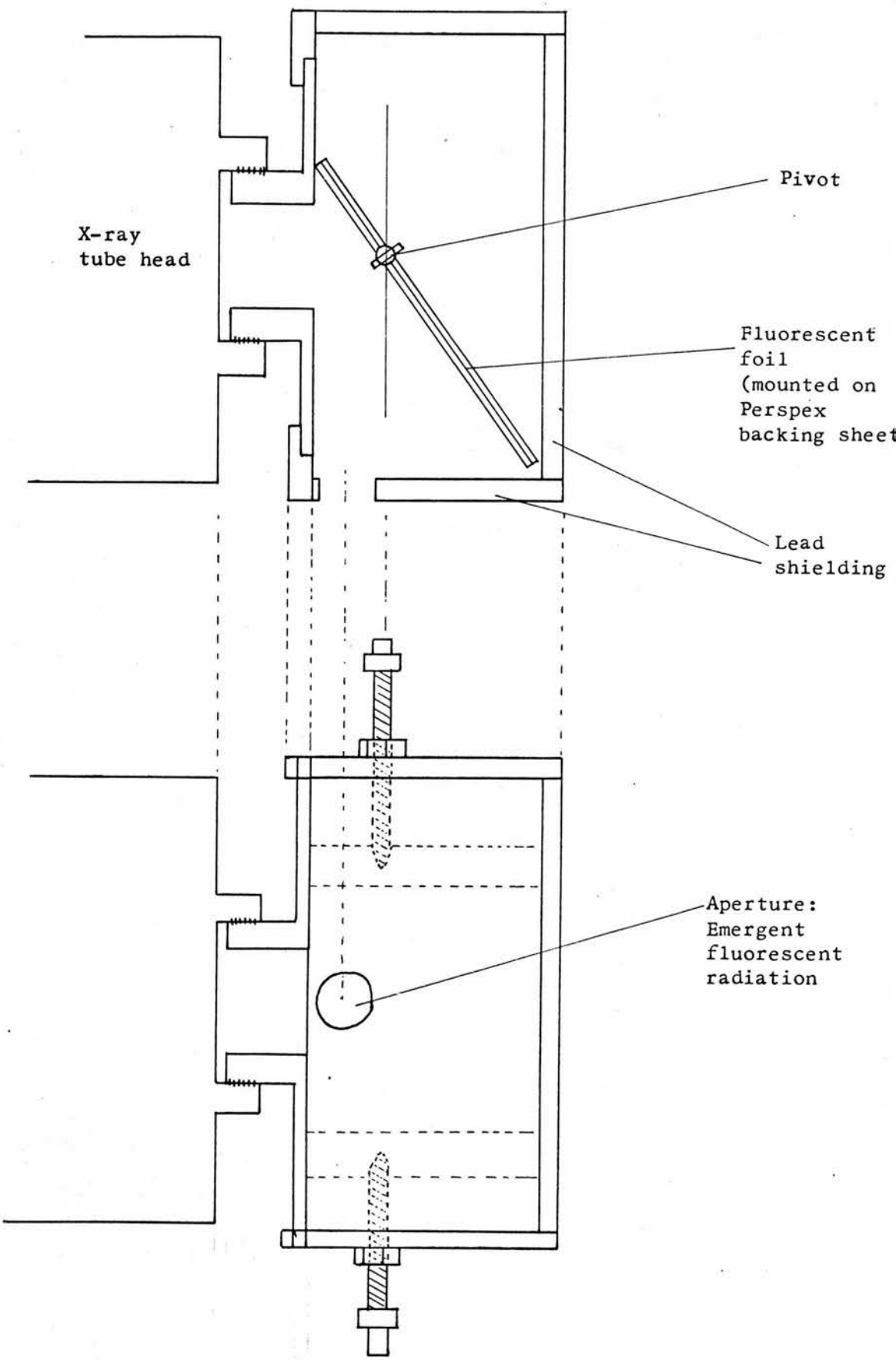

radiation be attenuated significantly by the material of the containing cell. The cell, in turn, was mounted on a 6.38 cm x 5.08 cm x 0.0635 cm Perspex sheet.

Both types of absorber were capable of being inserted in a holder, which was designed to be attached to the tube head. The design of the holder is shown in figure 3.6. The fluorescent source is held in the direct beam very close to the tube window, and may easily be adjusted to the desired incident angle. No other solid material (except the thin Perspex backing sheet) is within the direct beam, so that unwanted fluorescence and scattering are minimised. The entire assembly is lined with 3.17 mm lead sheet, the only aperture being a 1 cm diameter port to allow the emergent fluorescent radiation to pass into the attenuation apparatus proper. This minimises the level of diffuse scattered radiation within the room and reduces the X-ray background level.

The intensity levels produced by this arrangement were satisfactory for use with the collimation and detection systems adopted.

3.3.4 Absorber

3.3.4.1 Gases

In a measurement of attenuation coefficients for low atomic number materials, the usefulness of gaseous absorbers is considerable, especially for low energy radiation. For reasons which are discussed fully in chapter 4, it is desirable to have the ratio $\frac{I_o}{I}$ lying in the range 1.5 to 8 if this is practicable, with an optimum around $\frac{I_o}{I} = 5$. If solid absorbers are used this implies optimum thicknesses at 5 keV of 0.038 cm for carbon; 0.003 cm for aluminium; 0.0022 cm for sulphur.

At the same energy, however, a 41 cm column of nitrogen, or a 24 cm column of oxygen at s.t.p. will produce optimum absorption. In general, for the energy range from 4 to 26 keV, using gas pressures between 50 mm Hg and 2300 mm Hg with absorber tube lengths of 40 cm and 120 cm, an absorption ratio within the desired range can almost always be achieved. Consequently, it is a simple matter to measure the tube length to such an accuracy that it contributes insignificantly to the total uncertainty. This is not such a simple matter when very thin solid films are used.

Further, there is no problem about uniformity of thickness or homogeneity of the gas sample. Co-operative scattering effects caused by long-range order in certain solid scatterers like those observed by Chipman (1955) using graphite cannot be present when gases are used.

The absorption tubes used in the experiments were made of stainless steel, and the lengths chosen were 40 cm and 120 cm (nominal). Two tubes of each length were made; one was designed to hold the gas under investigation; the other to be evacuated. The exact lengths of the tubes used were measured by a travelling microscope. The measurement was repeated five times for each tube to randomise the uncertainty. The lengths were found to be:

(i) Short gas tube: 39.96 ± 0.01 cm

(ii) Short vacuum tube: 40.07 ± 0.01 cm

(iii) Long gas tube: 120.08 ± 0.01 cm

(iv) Long vacuum tube: 120.04 ± 0.01 cm

The uncertainties are, in each case, the standard error of the mean (SEOM) with four degrees of freedom.

In operation the two tubes were mounted on a sliding cradle. The axes were aligned parallel and horizontal by means of adjusting screws, and were at a horizontal separation of 4 cm. The sliding

cradle was capable of being moved between two stops (where it was held by magnetic catches) through a distance of 4 cm, i.e. in moving from one extreme position to the other, the axis of one tube moved into the previous position of the other. This arrangement enabled either tube to be placed in the beam in a reproducible position, and allowed successive readings of attenuated (passage through the gas) and unattenuated (passage through a vacuum of the same length) beam intensities to be quickly and easily made without appreciable time lag. This technique has been widely used by previous experimenters on solid absorbers but no record of the previous use of an interchange method for gases has been found in the literature on experimental attenuation coefficient measurement. With the short tubes, the end windows themselves formed the aperture collimators which limited the beam cross-section, and hence the count-rate. The mechanical stability of the tube interchange system was such that this method gave entirely reproducible results. With the long tubes, however, it was found necessary to add fixed aperture collimators at either end of the gas tube to define the beam cross-section. For the 120 cm tubes this led to an appreciable improvement in stability, and reproducibility, but it necessarily reduced the intensity, and somewhat longer counting times were required. In practice it was found necessary to calibrate the system by measuring the transmission through the two tubes under identical conditions. Differences due to the impossibility of obtaining perfect alignment in practice (for short tubes), slightly different lengths of tube, different window transmissions, and the possible presence of mercury vapour in the tube connected to the manometer, necessitated corrections of up to 0.5% in the $\frac{I_o}{I}$ ratio.

Figure 3.7 ABSORPTION TUBES USED IN MEASUREMENTS ON GASES

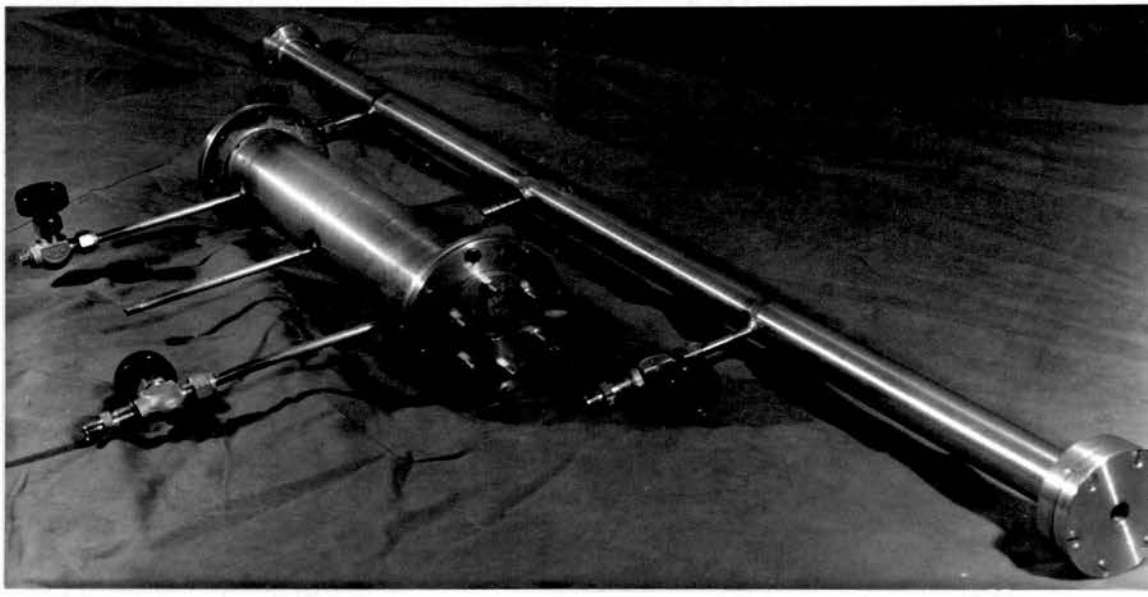

The correction was, however, constant and reproducible for any one fluorescent source and could, therefore, be obtained by measuring a calibration ratio for both tubes under identical vacuum conditions, (or by calculation from theoretical considerations (see Chapter 5)).

Although the interchange method thus necessitated the taking of rather more readings for each data point, it had advantages which more than compensated. Firstly, it enabled a series of twenty or more pairs of attenuated/unattenuated intensity and calibration measurements to be made on a single gas sample, thus saving time on repeated evacuation and refilling of the system, and economising on gas. By permitting short time lags between measurements of attenuated and unattenuated intensities, the method reduces the influence of medium and long-term fluctuations in primary beam intensity. Also, since the economic restraints on apparatus design prohibited the use of an enclosed vacuum spectrometer, the possibility of the observed intensity at the detector fluctuating with ambient temperature and pressure fluctuations in the room must be considered. Although it must be admitted that the possibility of a 3 K temperature fluctuation or a 7.6 mm Hg pressure fluctuation (or any combination of the two which would produce a 1% variation in air attenuation) is remote, the interchange method should reduce the effects of smaller temperature and pressure fluctuations on the observed count-rates.

The two gas tubes are shown in figure 3.7. The vacuum tubes are identical except that the central outlet is designed to fit an Edwards model 6 Penning gauge head. Stainless steel was chosen as the tube material to avoid the possibility of reaction between the gas and the tube itself when the more reactive gases (e.g. H_2S, HCl)

Figure 3.8 ABSORPTION TUBES: END WINDOW ASSEMBLIES

Scale 1x

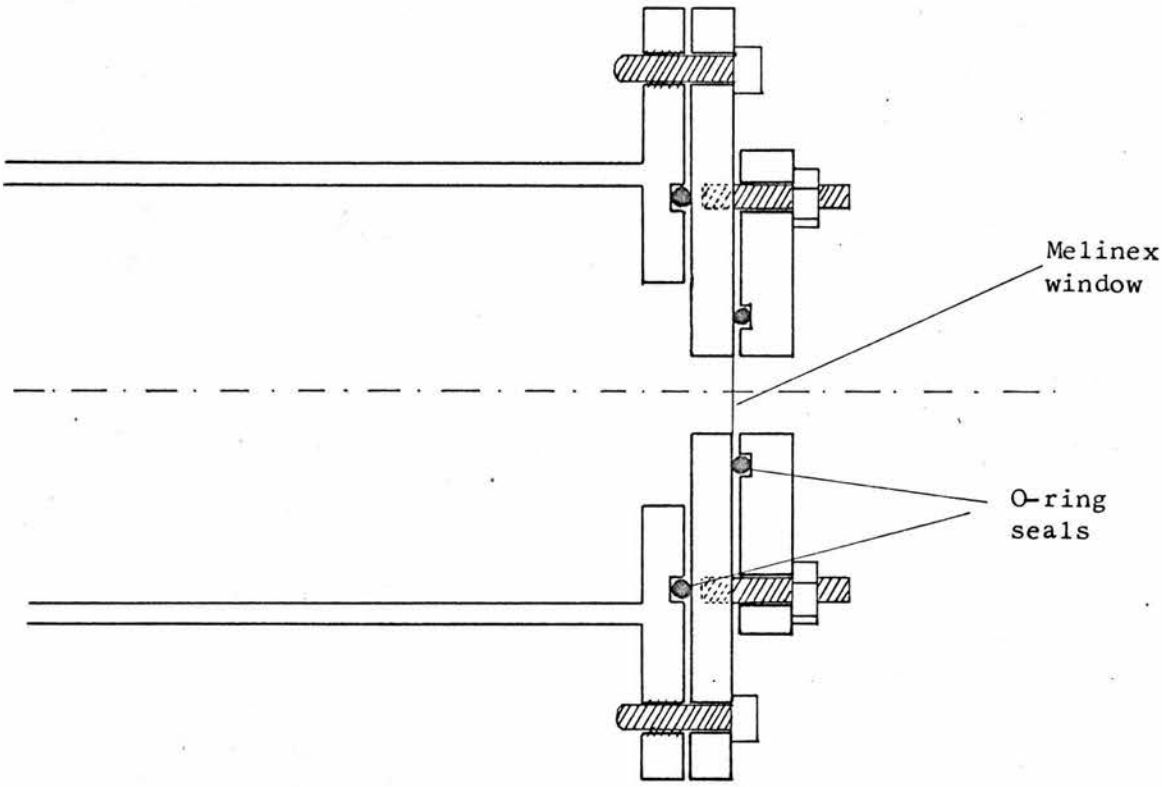

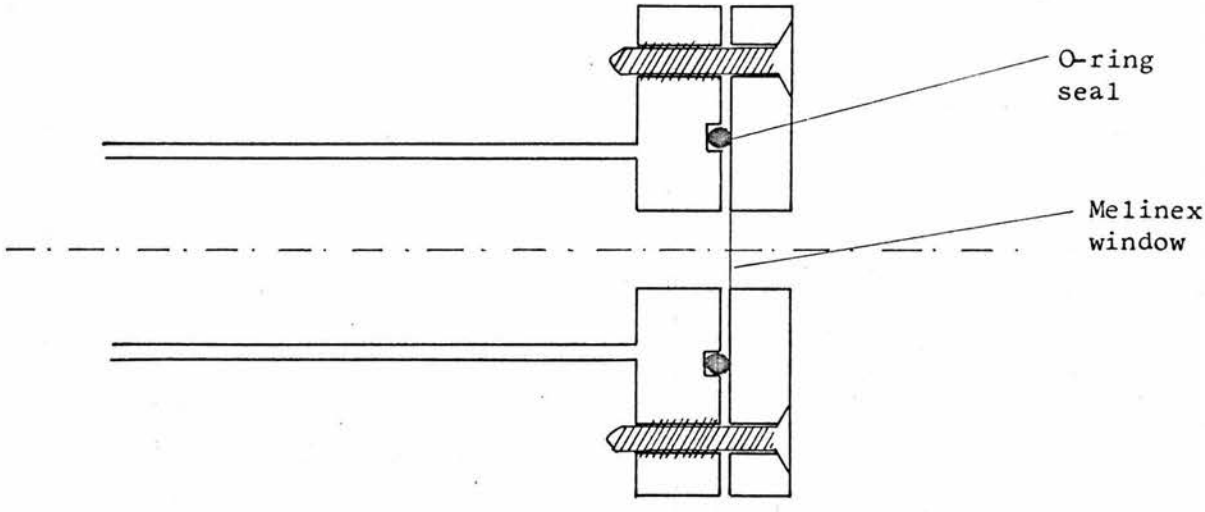

were being used. Each tube is fitted with a gas inlet and outlet pipe which can be closed off by means of a Matheson model 59 stainless steel needle valve. The design of the window assemblies is shown in figure 3.8. In both cases the window diameters were chosen to be 1 cm. The window material is 0.0254 mm Melinex film, which has the best combination of mechanical strength and X-ray transparency available. It is the need for a thin window which limits the pressures used to 3 atmospheres absolute, or less. The seals are effected by "O"rings in contact with the window film. The windows distorted appreciably under evacuation and pressurization, so that a length correction was necessary. It can be shown that a simple additive (or subtractive) constant is adequate to correct for this. The calculation of this constant is the subject of Appendix I.

By measuring this correction very precisely using a spherometer, and the overall length with undistorted windows using a travelling microscope, the percentage uncertainty in the sample length can be made insignificantly small, i.e. less than 0.05%. It was felt necessary to achieve particularly high accuracy in this measurement since any error in the length value will affect all measured mass attenuation coefficients in the same sense. By ensuring high accuracy of the length measurement, the precision of the determination rests solely on the accuracy of the $\ln(I_o/I)$ determination and the estimation of the gas density, ρ.

The accuracy to which ρ is obtainable depends on three factors; the accuracy to which the sample pressure can be measured; the accuracy to which the sample temperature can be measured; the accuracy with which the density can be specified when pressure and temperature are known with complete precision, i.e. the existing

knowledge of the P-V-T relationship of the gas in question. The first two of these fall directly under the control of the experimenter. The third can be optimised only by careful choice of gases used.

For accurate pressure measurements in the region between 0 and 2280 mm Hg (absolute) it was decided to use a simple open-ended mercury manometer. To cover the pressure range this required a U-tube with a vertical height of about 1.5 m on the side nearest the gas tube and about 2 m on the side open to the atmosphere. The use of a mercury manometer avoids the need for extensive preliminary calibration of the kind that would be required for a secondary standard pressure gauge. In practice, it proved merely necessary to make slight adjustments to the observed manometric height to allow for small differences in ambient temperature (affecting the mercury density) and the effects of surface tension. With these corrections, which never amounted to more than a small fraction of 1%, the manometer agreed on measurements of vacuum conditions with a standard Fortin barometer. The manometer readings were taken using a sliding pointer and a mirror placed behind the mercury column, thus removing parallax errors in the reading. It is a simple matter to read such a manometer to an accuracy of $\pm$ 0.5 mm on each arm, i.e. the height difference to an accuracy of $\pm$ 0.707 mm. Hence pressures above about 71 mm can be measured to better than 1% with much improved accuracy at higher pressure. In those cases where it is necessary to use low gas pressures (e.g. the low energy measurements on H_2S, HCl and A) the difficulty was overcome by taking several series of readings at slightly different pressures, thereby randomising the uncertainty in the manometer reading.

For measurements under vacuum conditions, as in the calibration of the two tubes, the pressure is measured using an Edwards model 6 Penning gauge on the vacuum tube. Since both the gas and vacuum tubes are evacuated through a common pipe the Penning gauge gives a measure of the hardness of vacuum in both. Pressures of 2×10^{-3} mm Hg were obtained using a rotary pump, and these are perfectly adequate for the experiment.

The main problem envisaged with a mercury manometer is the attenuation which one might expect to be produced by the presence of mercury vapour in the gas tube. Since the gas in the tube is in the direct presence of a reservoir of liquid mercury, it might be suggested that there would always be mercury vapour, at the saturated vapour pressure appropriate to the ambient temperature, in the gas tube. However, since the connection between the gas tube and the manometer consists of approximately 1.5 m of narrow bore (5 mm) tubing, and since the gas in the tube is regularly flushed out by evacuation and refilling, it is unlikely that the partial pressure of mercury vapour in the gas tube will reach the saturated vapour pressure, which is its maximum possible value. In the following calculation the attenuation of saturated mercury vapour is considered, and it should be borne in mind that this represents a worst possible situation which is unlikely to be realised in practice.

The saturated vapour pressure of mercury at $25^{\circ}C$ is 1.68×10^{-3} mm Hg (Kaye and Laby, 1966). If it is assumed that mercury vapour obeys the gas laws then this pressure can be related to the density of the mercury vapour by the equation:

Table 3.2 ERRORS CAUSED BY PRESENCE OF MERCURY VAPOUR IN ONE TUBE

E(keV)	$\frac{\mu}{\rho}_{air}$	μ_{air}	$\frac{\mu}{\rho}_{Hg}$	$\mu_{Hg\ vapour}$	% error: in $\frac{\mu}{\rho}$	% error: in I_0/I for 120 cm tubes
5	40.3	5.21×10^{-2}	678	1.23×10^{-5}	2.36×10^{-2}	1.48×10^{-1}
10	4.96	6.41×10^{-3}	119	2.15×10^{-6}	3.35×10^{-2}	2.58×10^{-2}
15	1.57	2.03×10^{-3}	169	3.06×10^{-6}	1.51×10^{-1}	3.67×10^{-2}
20	0.762	9.85×10^{-4}	80.5	1.45×10^{-6}	1.48×10^{-1}	1.75×10^{-2}
30	0.350	4.53×10^{-4}	28.1	5.09×10^{-7}	1.12×10^{-1}	6.11×10^{-3}

Densities: $\rho_{air} = 1.293 \times 10^{-3}$ g cm^{-3}

$\rho_{Hg\ vapour} = 1.81 \times 10^{-8}$ g cm^{-3}

Units of $\frac{\mu}{\rho}$ are cm^2/gm

" " μ " cm^{-1}

$$\rho = \frac{pM}{RT} \qquad \text{.....(3.3)}$$

where p is the s.v.p., M the molecular mass of mercury, R the gas constant per mole, and T the absolute temperature. This implies a density of 1.81×10^{-8} g cm^{-3} for mercury vapour.

The observed intensity after attenuation by a gas contaminated with saturated mercury vapour will be given by:

$$I = I_o \exp\left[-\left(\frac{\mu}{\rho} \cdot \rho \cdot x_{gas}\right) - \left(\frac{\mu}{\rho} \cdot \rho \cdot x_{Hg\ vapour}\right)\right] \qquad \text{....(3.4)}$$

$$= I_o \exp\left[-x\,(\mu_{gas} + \mu_{Hg\ vapour})\right] \qquad \text{.....(3.5)}$$

Hence the percentage error in $\frac{\mu}{\rho}$ caused by attenuation by the mercury vapour is approximately given by $100.\left[\mu_{Hg\ vapour}/\mu_{gas}\right]$; the percentage error in I_o/I for a 120 cm tube containing saturated mercury vapour is given by $100.\left[1 - \exp(-120.\mu_{Hg\ vapour})\right]$. These quantities are tabulated for several energies in the range of interest with s.t.p. air as the gas considered (see Table 3.2). The actual error caused by the presence of mercury vapour is much lower than even these figures for two reasons. Firstly, as mentioned above, the pressure of mercury vapour is unlikely to approach the s.v.p., and secondly, the mercury absorption effect is almost completely removed by the calibration of the tubes. The total mercury vapour pressure in the gas tube under evacuation will be essentially the same as the partial vapour pressure in the gas filled tube, and hence its attenuation will be constant and will be allowed for in the calibration of the tubes.

The density of the gas depends also on the temperature. As room temperature is around 300 K, the percentage error will be

Figure 3.9 THERMISTOR THERMOMETER

a) Bridge circuit

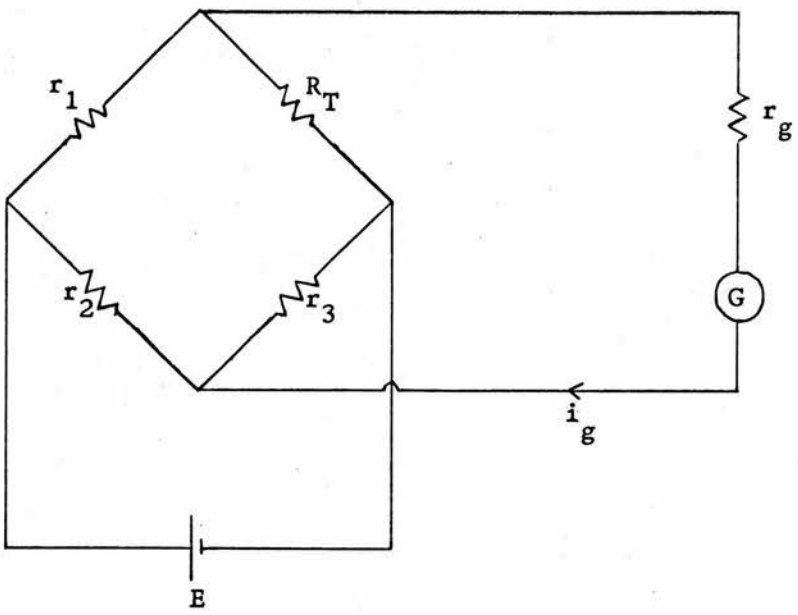

b) Low impedance 0.25 V source

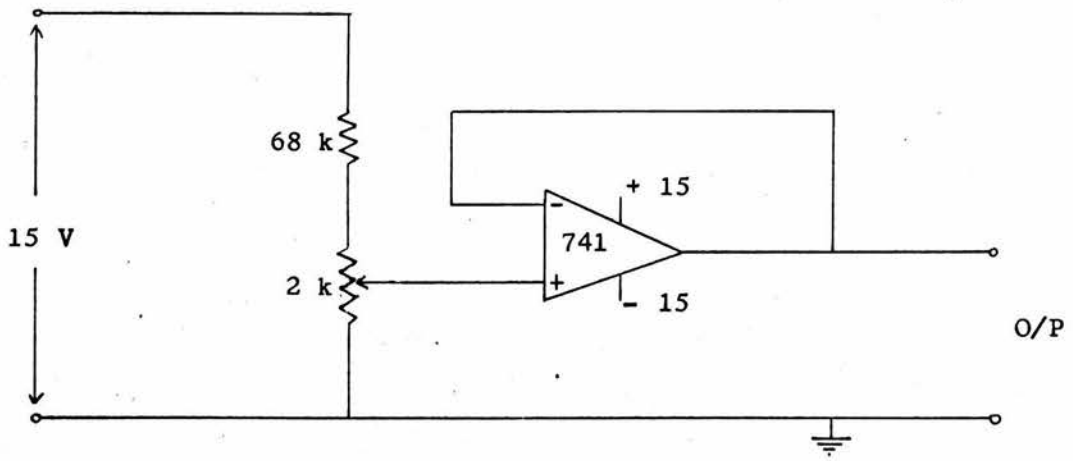

negligible if temperature can be measured to an accuracy of $\pm$ 0.1 K. This accuracy was easily achieved using a thermistor in a bridge network. Beakley (1951) has shown how it is possible to choose circuit parameters in such a way that the signal obtained from such an arrangement is a linear function of temperature near the balance point. He considers the circuit shown in figure 3.9a. The galvanometer is assumed to have no resistance, and the power supply to have no internal resistance. It is then possible to select $\frac{di_g}{dT}$, the temperature sensitivity of the galvanometer, and using this value in conjunction with the known b-factor of the thermistor (R_T = a exp (b/T) the other resistance values in the circuit may be chosen. In the experimental work the temperature sensitivity was selected to be 0.106 $\mu A\ K^{-1}$. The galvanometer used was a "Scalamp" mirror galvanometer with current sensitivity of 0.0106 $\mu A\ mm^{-1}$. Hence the temperature sensitivity is equivalent to 1 cm K^{-1}. The galvanometer had a range of $\pm$ 7 K around 293 K. The thermistor used was a type U23UD with a b-factor of 2900 K^{-1} and a measured resistance of 2147 Ω at 293 K. This led to resistance values in the bridge as follows: $r_1 = r_2 = 1490\ \Omega$; $r_3 = 2080\ \Omega$; $r_g = 17500\ \Omega$. The source voltage is 0.25 V and the power dissipation in the thermistor is then around 0.01 milliwatts. In order to obtain a 0.25 V source with internal resistance negligible compared with that of the bridge network the circuit of figure 3.9b was used. The output of a stabilised 15 V Farnell source is divided by a resistance network and the impedance is reduced to a negligible value using an op-amp with 100% feedback.

The thermistor itself was calibrated using an accurate mercury in glass thermometer. The calibration graph is shown in figure 3.10a. It was then inserted transversely across the manometer inlet arm

Figure 3.10 THERMISTOR THERMOMETER

a) Thermistor thermometer calibration

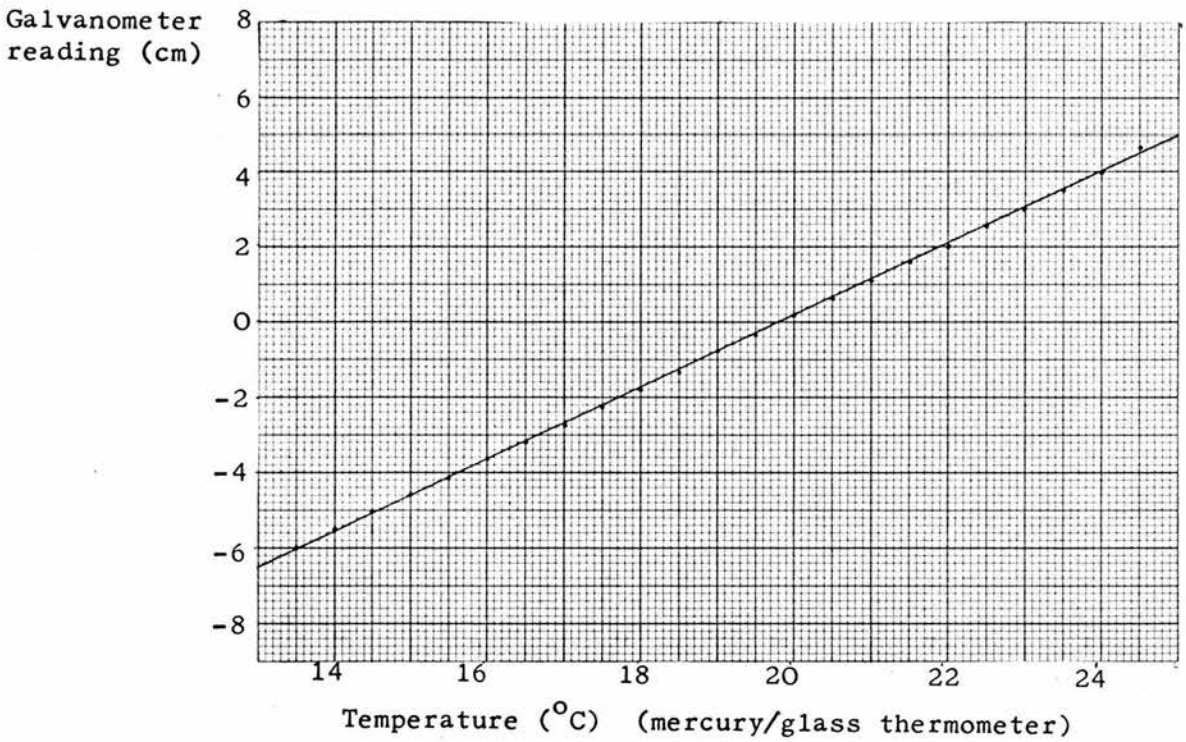

b) Location of thermistor bead

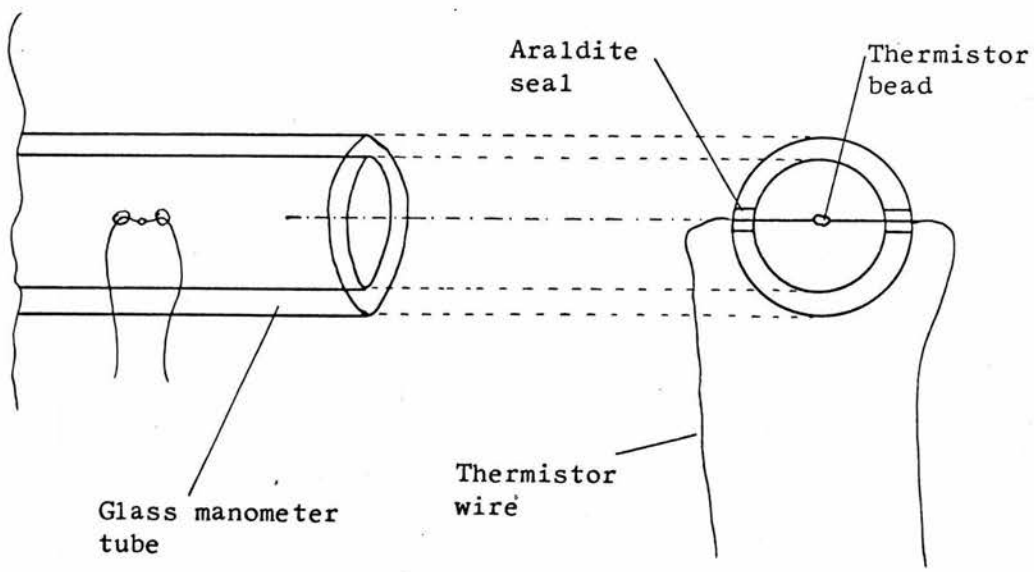

(as shown in figure 3.10b) above the maximum mercury level and the tube was sealed with Araldite resin to ensure a gas-tight joint. The thermistor bead is thus placed directly in the gas sample and is an accurate and sensitive temperature sensor.

However good our knowledge of the pressure and temperature of the gas sample there is a limitation on our knowledge of its density imposed by uncertainties in the form of the P-V-T relationship of the gas in question. All real gases deviate to a greater or lesser extent from ideality and it is necessary to consider whether in the light of such deviation it is possible to arrive at accurate values of gas densities throughout the pressure and temperature range used. The data used to calculate gas densities were taken from "Tables of Physical and Chemical Constants" by Kaye and Laby (13th edition, 1966). As well as accurate values of standard density at $0^{o}C$ and 760 mm, they also quote values of $(1 + \lambda)$, defined in the following way:-

$$1 + \lambda = \frac{p_o v_o}{p_1 v_1} \qquad \ldots\ldots (3.6)$$

where v_1 is the volume of 1 mole of a gas at 1 atmosphere pressure, p_1, and v_o is the volume at infinity small pressure p_o, the temperature being $0^{o}C$. Hence $(1 + \lambda)$ is a measure of the deviation of the gas from ideality at 1 atmosphere, assuming it to behave ideally at infinitesimal pressures. If, in addition to this, we assume that λ is a linear function of pressure up to 3 atmospheres (which for the small deviations involved is equivalent to the assumption that pv is a linear function of pressure) then it is possible to predict densities throughout the range of interest. This second assumption need not be made in the absence of experimental

Figure 3.11 DEVIATION FROM IDEAL GAS LAWS (ETHYLENE)

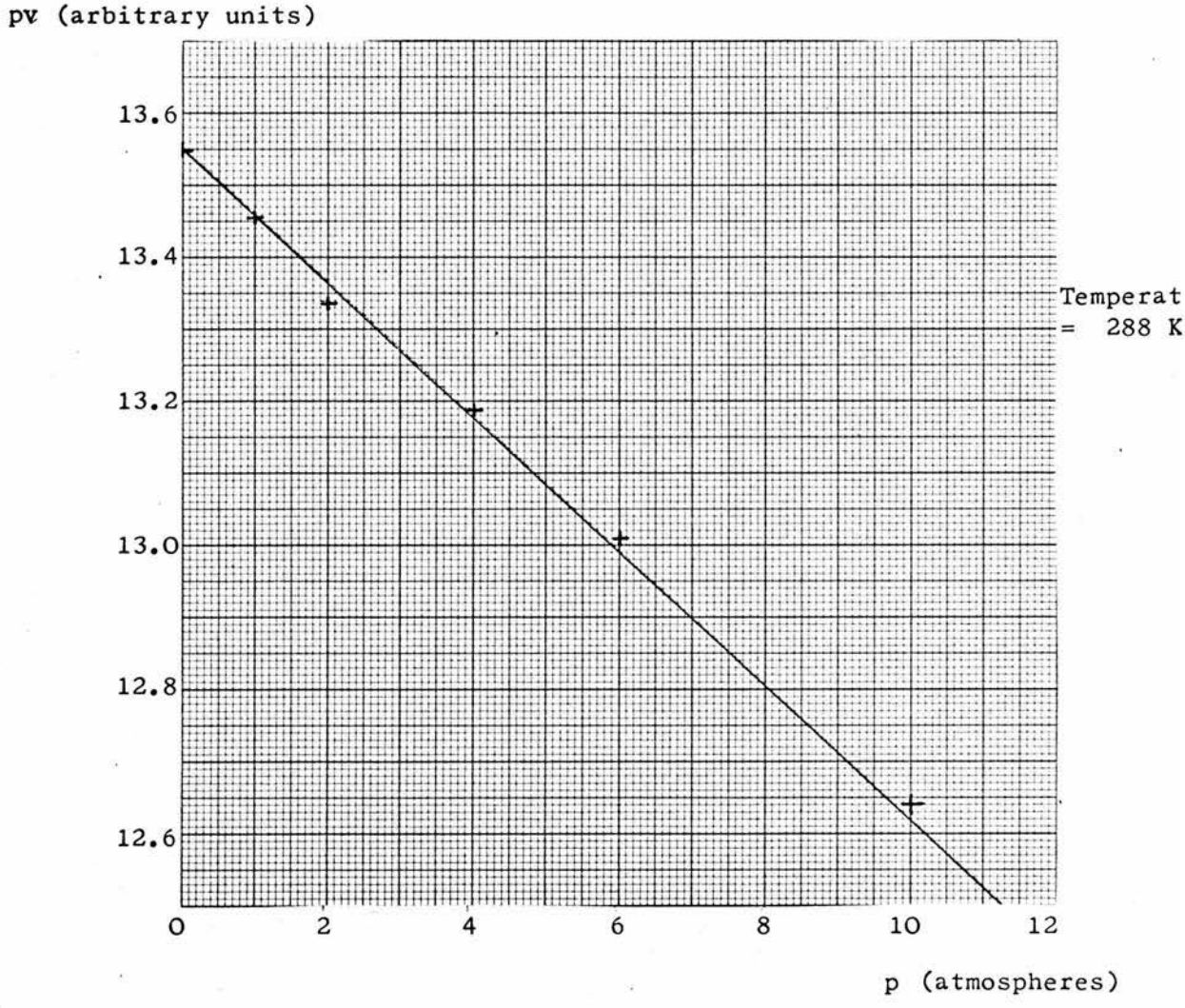

information. Using data taken from the "Matheson Gas Data Book" (1971) and from "Tables of Thermal Properties of Gases" (National Bureau of Standards Circular 564) graphs of pv against p for nitrogen, oxygen, argon, carbon dioxide, ethylene, neon and hydrogen sulphide in the pressure range from zero to 10 atmospheres can be drawn and are linear to a high degree of accuracy. For example, figure 3.11 shows one such graph. For these gases the density was calculated using values of standard density and $(1 + \lambda)$ given in "Tables of Physical and Chemical Constants". These values are expected to be accurate to better than 0.05% and will therefore contribute a very small amount to the total uncertainty. The other two gases used were carbon tetrafluoride and hydrogen chloride. For these gases there is insufficient published data to permit the assertion that pv varies linearly with p. So for these gases pressures of 1 atmosphere or less were used throughout, and λ was assumed to vary linearly in this region.

The gases used are listed in Table 3.3 together with the values of standard density, $(1 + \lambda)$, and minimum percentage purity of the samples used. All gases with minimum certified purities of less than 99.9% were analysed using a mass spectrometer. In all cases the actual sample purity was found to be better than 99.9% and in no case were any high atomic number impurities found.

In the cases of nitrogen, oxygen, neon and argon, the elementary gases were easily obtainable in a pure form suitable for attenuation studies. The actual samples used were obtained from the British Oxygen Company, the grades used being as follows: oxygen-free nitrogen; grade X oxygen; C.P. grade neon; and standard argon. All four gases show only small deviations from the perfect gas laws

and therefore present few problems in the accurate estimation of their densities.

The attenuation of air was measured to enable a check on the internal consistency of the measurements of nitrogen, oxygen and argon to be made. Either atmospheric air, dried by passage over silica gel, or compressed air supplied by B.O.C. was used.

The attenuation coefficients of carbon, fluorine, sulphur and chlorine were measured using the compounds ethylene, carbon tetrafluoride, hydrogen sulphide, and hydrogen chloride respectively. All four gases were chosen to maximise the fraction of total attenuation due to the element of interest, subject to other conditions such as availability, purity, and ideality of behaviour under compression. Ethylene was chosen as a carbon source largely on account of its available purity, which is appreciably better than that of the other paraffin and olefin gases. It departs from ideal gas behaviour by 0.7% at 1 atmosphere, but since its λ-factor is well known, the error due to compressibility is easily allowed for.

As a source of fluorine, carbon tetrafluoride offers the advantages of being inert and non-toxic, and of being obtainable at 99.7% certified purity. Its density is also better known than that of most halocarbons and its deviation from ideal behaviour is small. Fluorine accounts for around 95% of its attenuating properties, and consequently the accuracy of the determination of the attenuation coefficient of fluorine is only weakly dependent on uncertainty in the carbon component.

This same factor makes hydrogen sulphide and hydrogen chloride very convenient sources of sulphur and chlorine. Unfortunately the purity and compressibility of hydrogen sulphide is not as good as

might be desired but accurate analysis showed the sample to be purer than certified, and allowance for compressibility is easily made. Since no other gaseous source of sulphur is of comparable usefulness, hydrogen sulphide is an obvious choice. Hydrogen chloride was preferred to chlorine itself for two main reasons: it is obtainable at 99.99% certified purity compared with 99.5% for chlorine; and its deviation from ideal behaviour, though appreciable, is much less than that of chlorine.

These four gases (and carbon dioxide, which provided an internal consistency check on the carbon and oxygen values) were obtained from BDH Laboratory gases.

Specific problems encountered during work with each gas are dealt with in the discussion of results in Chapter 5.

3.3.4.2 Solids

All the preceding discussion refers to gaseous absorbers. In order to fill large gaps in the atomic number range from Z = 6 to Z = 18 it was necessary to use solid and liquid absorbers to cover the elements magnesium, aluminium, silicon and phosphorus. The problems encountered with solid and liquid absorbers are fundamentally different from those with gases.

In the energy range considered, the optimum thickness of a solid absorber varies from less than 0.1 mm at the energy of Ti Kα radiation to around 6 mm at the energy of Sn Kα radiation. Unlike gases, where the upper end of the energy range was problematical due to low absorption, solids lend themselves more easily to absorption studies at higher energies. At low energies, however, the foils required are so thin that measurement of thickness is difficult, and foil uniformity is doubtful. The effects of foil non-uniformity are considered in

Table 3.4 MAXIMUM, OPTIMUM, AND MINIMUM THICKNESSES OF ALUMINIUM REQUIRED FOR ATTENUATION STUDIES

Kα source element	Thickness (mm)		
	Maximum ($I_o/I = 20$)	Optimum ($I_o/I = 5$)	Minimum ($I_o/I = 1.5$)
Ti	0.0435	0.0234	0.00590
Cr	0.0730	0.0392	0.00991
Fe	0.118	0.0631	0.0159
Ni	0.184	0.0987	0.0249
Cu	0.227	0.122	0.0308
Zn	0.279	0.150	0.0377
Ge	0.414	0.222	0.0560
Se	0.600	0.322	0.0812
Rb	1.01	0.542	0.137
Zr	1.63	0.874	0.220
Mo	2.19	1.18	0.296
Ru	2.90	1.56	0.393
Pd	3.83	2.06	0.518
Cd	4.93	2.65	0.667
Sn	6.23	3.35	0.844

Appendix 2. It is shown that even large departures from uniform thickness result in only quite small effects on the observed attenuation coefficient.

Table 3.4 shows the thickness of aluminium required to produce maximum desirable ($I_o/I = 20$), optimum ($I_o/I = 5$), and minimum desirable ($I_o/I = 1.5$) absorption for each of the Kα radiations used, based on values of $\frac{\mu}{\rho}$ taken from the 1970 tabulation by Storm and Israel. For the data points from Cu Kα to Sn Kα the absorbers used were aluminium sheets supplied to the Hospital Physicists' Association by the National Physical Laboratory. These were made of 99.8% pure aluminium and were nominally 1.2 mm, 0.4 mm, and 0.2 mm thickness. The exact specifications given were as follows: all three types of filter had an area of 100.5 $\pm$ 0.5 mm square. The accurate values of the weight per unit area were 324 mg cm^{-2}; 107 mg cm^{-2} and 53.0 mg cm^{-2}, with estimated uncertainties of $\pm$ 1% due largely to inaccuracy in measuring the area of each filter. It is also suggested that the weight per unit area of the thickest filters is probably accurate to $\pm$ 0.5%. As regards variation of thickness over any one filter, it is stated that checks were made using a vernier micrometer and that over the central portion of the filter there was no evidence of any variation of thickness greater than the accuracy with which the reading could be made, viz. $\pm$ 0.01 mm. To improve on these specifications the area was measured using a travelling microscope. By repeating measurements of the dimensions, the uncertainty in the area can be treated as a random uncertainty, rather than a systematic one. The foils were weighed on an accurate balance. The major source of error is still the area measurement but a tolerance of $\pm$ 0.1 mm is easily attained, resulting in an uncertainty of $\pm$ 0.2%

in the weight per unit area. The accurate foil thicknesses were assessed as 323.9 mg cm^{-2}; 107.0 mg cm^{-2}; and 53.02 mg cm^{-2} with standard error of the mean of $\pm$ 0.2% with four degrees of freedom in each case. The filters were also measured by vernier micrometer to test for variation of thickness over the central area. All three types of filter were found to have a thickness variation of $\pm$ 0.0025 mm, i.e. $\pm$ 0.25% for the 1.2 mm filters; $\pm$ 0.62% for the 0.4 mm filters; and $\pm$ 1.25% for the 0.2 mm filters. In practice, the effects of this thickness variation were reduced by taking a series of measurements with different parts of the filter in the beam on each occasion. A series of ten such readings reduces the statistical uncertainty by a factor of three.

The four low energy data points required thinner aluminium absorbing foils. The material used was aluminium foil of 99.99% purity and nominal thickness of 0.025 mm, supplied by Goodfellow Metals Limited, Esher, Surrey. The accurate impurity content of the aluminium foil was as follows: Ca 0.0001%; Cu 0.0007%; Ga 0.0003%; Mg 0.001%; Si 0.001%; Na 0.0001%. No correction for any of these impurities was required. This foil was supplied as a 50 x 50 mm sample. The foil area was measured by travelling microscope and the foil weight was also determined. From these values the area density of the aluminium was determined as 6.455 $\pm$ 0.025 mm cm^{-2}. The random uncertainty in this figure is the SEOM with four degrees of freedom.

No reliable information was available for the uniformity of thickness of this foil. However, the experimental set-up used an X-ray beam of 5 mm diameter. Consequently, it was possible to sample different portions of the foil in each attenuation measurement and use

the statistical spread of the results as an estimate of the combined effects of foil non-uniformity and beam intensity fluctuation. This has the advantage of combining the uncertainty due to non-uniformity with the random uncertainties due to counting statistics. In any case, as is shown in Appendix 2, the effects of foil non-uniformity are not usually serious. Sufficient repeats were made to bring the observed total random uncertainty as expressed by the standard error of the mean, below 1% of the measured value.

In general, therefore, by measuring the foil thickness as the average of a series of readings and by measuring the attenuation of different portions of the same foil, almost all the uncertainties in the calculated attenuation coefficients of solids are random. Only uncertainties due to impurities in the attenuating samples are systematic.

The magnesium absorber used was also in the form of a foil of 99.95% pure magnesium and nominal thickness 0.02 mm, supplied by Goodfellow Metals Limited. The accurate assay of the magnesium foil impurity content was: Al 0.0005%; Cu 0.0007%; Fe 0.01%; Mn 0.005%; Si 0.01%; Na 0.0001%. A correction to observed attenuation values to allow for the iron, manganese, and silicon impurity was therefore necessary. The foil was supplied in pieces of nominal dimensions 50 x 75 mm. Each of five such pieces was weighed, and its dimensions accurately measured using a travelling microscope. The area density was measured five times for each piece. The resultant standard error of the mean was, in all cases, less than 0.5% of the measured area density. Each foil was then cut into 35 pieces each of size 10 x 10 mm. In each measurement of attenuation it was necessary to use several thicknesses of foil to approach the optimum absorption ratio. The number required varied from 3 foils

Table 3.5 IMPURITY CONTENT OF FUSED SILICA OPTICAL FLATS

OH	0.12%
H_2O	0.06%

Aluminium	0.1	ppm	Magnesium	0.1	ppm
Antimony	0.002	ppm	Manganese	< 0.01	ppm
Arsenic	0.03	ppm	Phosphorus	0.01 to 0.1	ppm
Boron	< 0.01	ppm	Potassium	< 0.001	ppm
Calcium	0.1	ppm	Sodium	0.04	ppm
Copper	0.004	ppm	Titanium	< 0.1	ppm
Iron	0.2	ppm	Zirconium	< 0.001	ppm
Lithium	< 0.05	ppm			

at Ti Kα energy to all 175 foils at the energies of Pd Kα, Cd Kα and Sn Kα. The use of multiple foils helps to improve the statistical errors introduced by thickness variation in any single foil. Random errors in the area density of the original individual foils are also reduced if pieces from two or more of the original foils are chosen to make up the composite absorber.

By using different samples from the original 50 x 75 mm foils it was possible to incorporate the fluctuations due to thickness variation into the observed variation of attenuated intensity, and by taking several repeats of these readings it was found possible to attain an overall accuracy of 1%.

To measure the attenuation coefficient of silicon, optical flats of fused silica were used. These were obtained from Pilkington Perkin-Elmer Limited, St. Asaph, Flintshire. The flats were nominally 0.5 mm thick and, as obtained, were polished to a thickness uniformity of better than 1%. The silica was better than 99.8% pure, the contaminants being shown in Table 3.5. Using these flats it was possible to measure the total attenuation coefficient of silica between 8.041 keV (Cu Kα) and 25.192 keV (Sn Kα). Below 8.041 keV the attenuation was too great for any useful results to be obtained. The area density of the flats was obtained in the same way as for foils. The area was measured by travelling microscope and the weight determined by an accurate balance. The standard error of the mean of these readings was less than 0.5% of the measured average value. For the higher energy data points, several flats were used to attenuate the beam, and the percentage uncertainty due to errors in measurement of this area density was therefore reduced. All results were corrected for impurities due to the water and OH radical content.

In all the measurements with solid absorbers a correction was applied to adjust for absorption by the air displaced by the absorber when it is in position. This correction is only around 0.1% in practice, but since it affects all results in the same sense, it is necessary to correct for it.

In the case of all solid absorbers, the apparatus layout was as shown in figure 3.3. A high degree of parallelism of the incident beam is achieved using a Soller slit assembly. A blade spacing of 1 mm is used, the blades being 2.54 cm long in the direction of the beam. The beam cross-section is defined by two aperture collimators of adjustable diameter placed before and after the absorber. The absorber is of sufficient size to intercept entirely the X-ray beam thus defined. This collimation provides adequate rejection of coherent scattered radiation and elimination of in-scattering effects. This is discussed fully in section 3.4.1.1.

3.3.4.3 Liquids

To complete the atomic number range, it was desirable to measure the attenuation of phosphorus. No suitable solid absorber exists, and the best gaseous compound, phosphine PH_3, is too toxic for safe handling in the experimental situation used, i.e. its use is dangerous outside a fume cupboard. Certain liquid compounds of phosphorus are possible absorbers. The compound chosen was tri-ethyl phosphate, $(C_2H_5)_3\ PO_4$. This is a liquid at room temperatures and is supplied by BDH Chemicals Limited at a certified minimum purity of 99.5%. This compound was chosen because its attenuation is dominated by the phosphorus content which accounts for around 66% of its total attenuation, and because it is available at a high purity. On request the manufacturers were able to state that the purity of the

Figure 3.12 LIQUID ABSORPTION CELL

Scale 2x

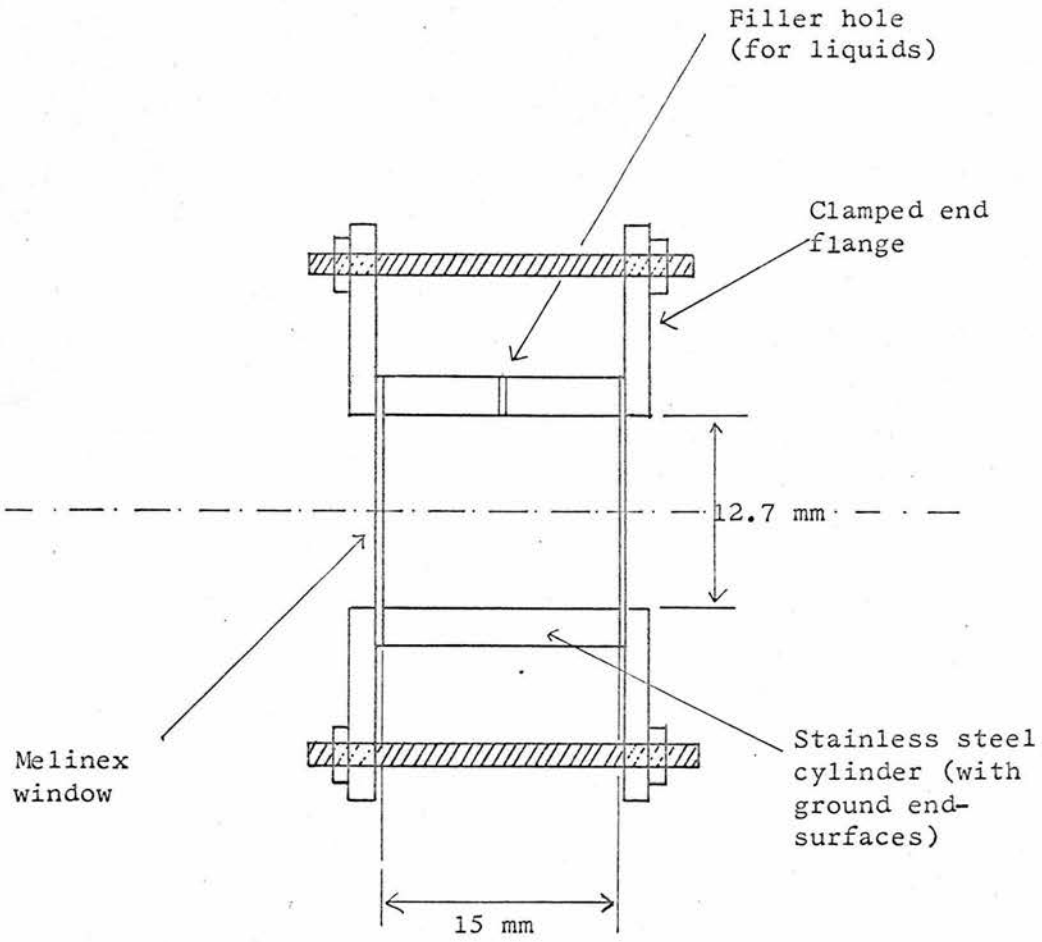

batch used was at least 99.7% with a maximum of 0.1% ethanol and 0.2% water as the only important contaminants. The density of the liquid is 1.067 - 1.069 g cm^{-3}.

To contain the liquid, a cell of accurately known dimensions was required. In order to approach an overall accuracy of around $\pm$ 1%, it was decided that the minimum length of cell usable was 5 mm. The end windows must be made of a material which is reasonably transparent to X rays and yet is sufficiently rigid that window distortion does not become problematic. It is also essential that the window is not soluble in tri-ethyl phosphate. After trying several thinner materials it was decided that 0.79 mm Perspex sheet is a suitable window material. Two sections of stainless steel tubing of 1 cm inside diameter were cut to nominal lengths of 5 mm and 15 mm and the ends were ground to a fine tolerance. The end-windows were held in pressure contact with the ground ends by means of two circular clamps to make a liquid-tight seal. A small hole in the wall of the steel cylinder permitted the liquid to be introduced using a hypodermic needle and syringe. The cell design is shown in figure 3.12. The 15 mm cell was used at energies from 21.122 keV to 25.192 keV, whilst the 5 mm cell was used from 11.210 keV to 19.235 keV. Below 11.210 keV the attenuation of the windows was so high that no useful results could be obtained.

The length of the liquid column is exactly equal to that of the stainless steel tube. Both sections of tube were measured several times using a vernier micrometer. The lengths were found to be 5.239 $\pm$ 0.005 mm and 15.185 $\pm$ 0.005 mm. The uncertainties in each case are the standard error of the mean with nine degrees of freedom.

The cell was mounted in a holder so that it could be manually removed from the beam or inserted in a reproducible position.

Figure 3.13 SINGLE-CRYSTAL SPECTROMETER

Figure 3.14 CONSISTENCY OF GONIOMETER SETTING

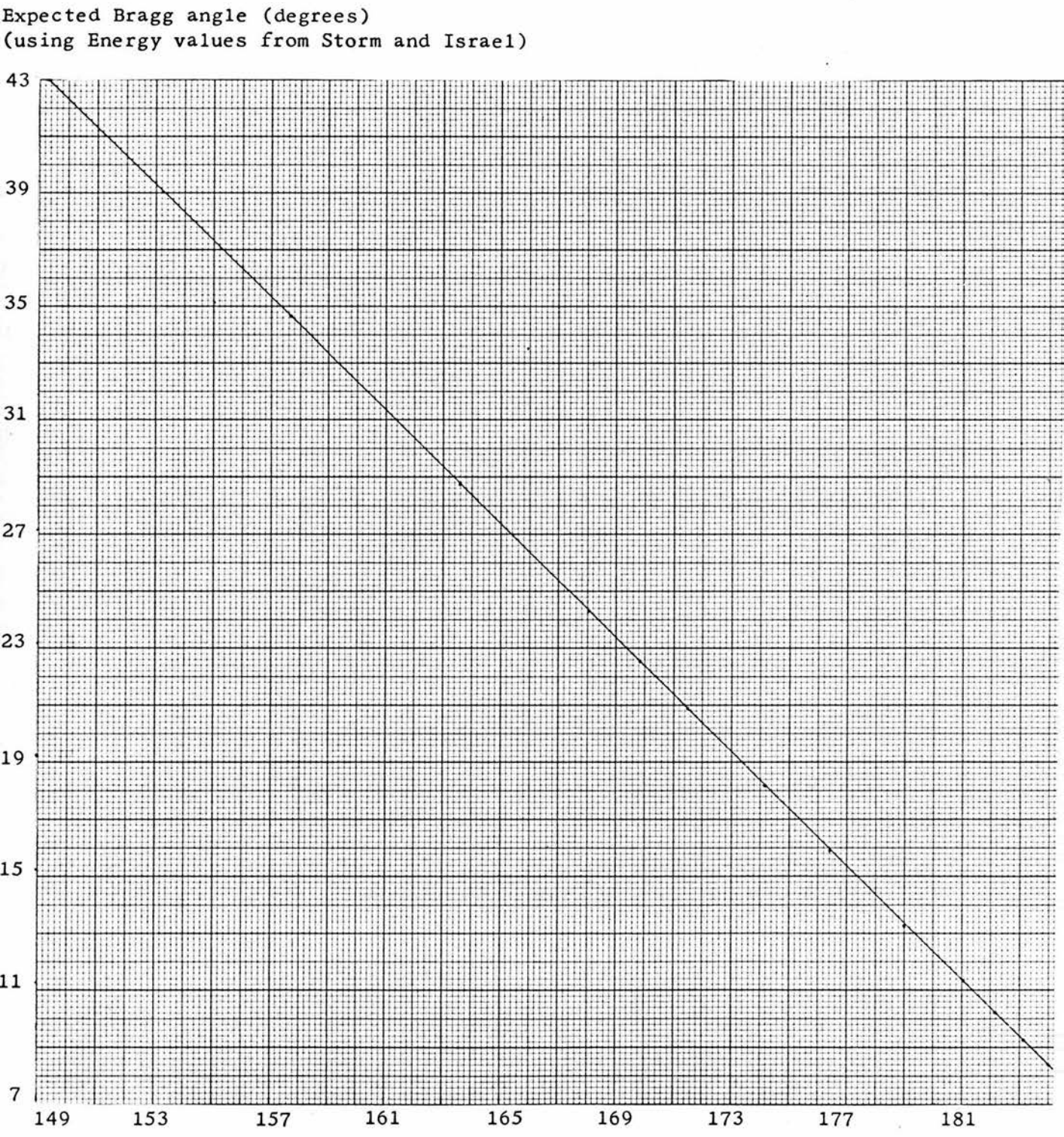

Aperture collimators before and after the cell ensured that the entire beam was intercepted by the liquid.

The apparatus lay-out was identical to that used for solid samples, which is illustrated diagrammatically in figure 3.3.

3.3.5 Spectrometer

On emerging from the absorber, the X-ray beam passes through a crystal monochromator. In the experiment a simple two-circle goniometer with a lithium fluoride crystal and Soller slit collimators was used. The spectrometer is shown in figure 3.13. Both the θ and 2θ circles were capable of fine adjustment by means of two separate worm-threads and wheels, and could be set reproducibly to 0.01° of arc. This fineness of adjustment does not permit the energy of the radiation to be specified as accurately as the values of Storm and Israel quoted in Table 3.1. The observed goniometer settings are, however, entirely consistent with these accurate values. Figure 3.14 shows a graph of the expected Bragg angle on the basis of the energy values of Table 3.1 plotted against the observed goniometer setting. The graph is linear, with a correlation coefficient of - 0.9998, which is well within the limits imposed by the fineness of adjustment available.

The crystal used was lithium fluoride which has a 2d spacing of $4.028\ \text{Å}$ for the 200 reflection. With this 2d spacing the Bragg angle varies between 43.07° for Ti $\overline{K\alpha}$ radiation and 7.02° for Sn $\overline{K\alpha}$, which is a satisfactory angular range. The crystal used was cleaved parallel to the (100) planes with an exposed (100) surface measuring 5 cm x $2\frac{1}{2}$ cm.

The collimation of the beam was achieved principally by the

Figure 3.15 SCAN OF MOLYBDENUM K-LINES

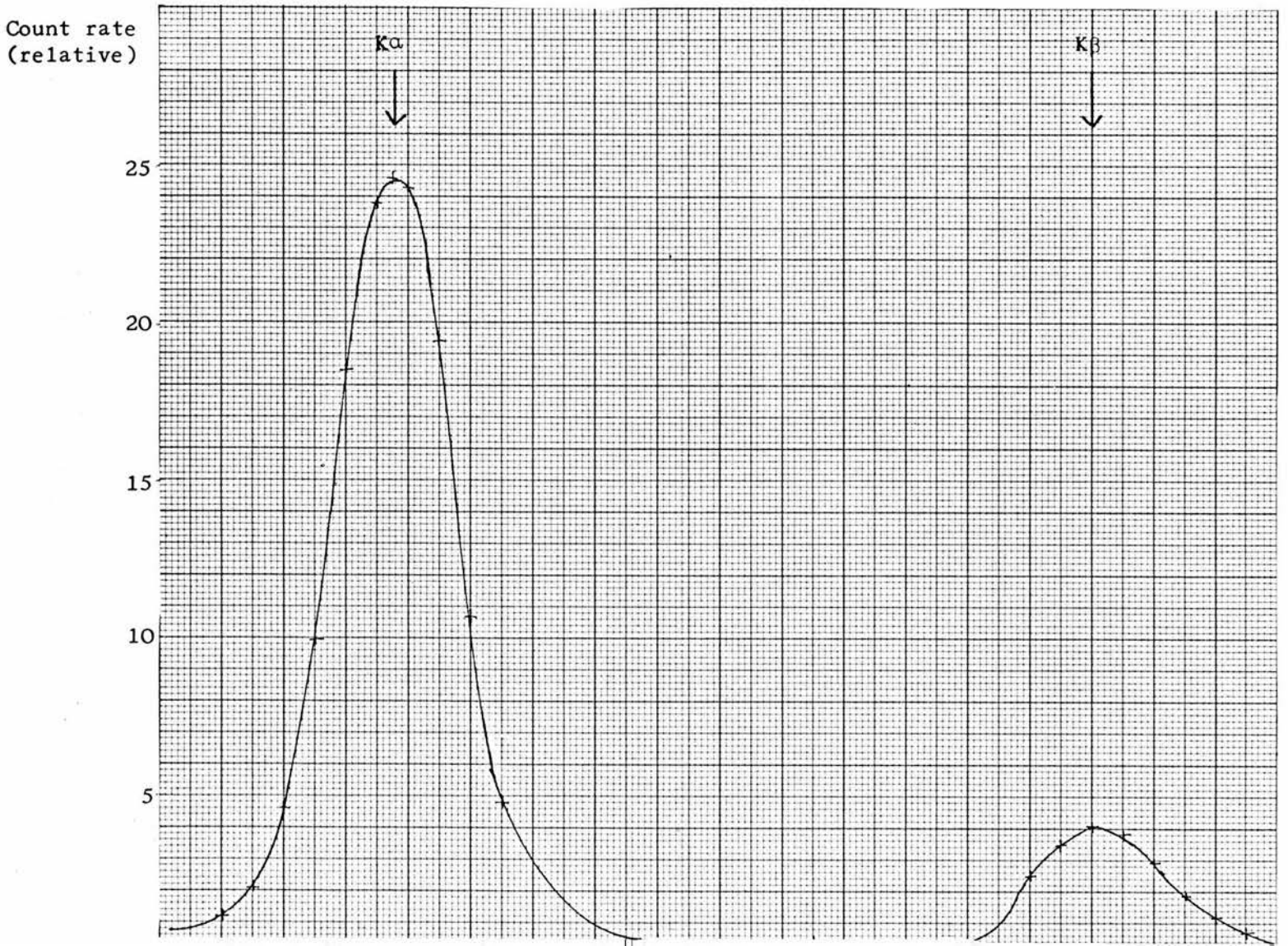

entrance collimator, which was a Soller slit assembly PW 1218/14 produced by Pye Unicam. This consists of a set of parallel blades which are 10 cm long along the X-ray path, and are arranged to present a cross-section to the X-ray beam of 1.7 cm parallel to the blade edges and 1 cm perpendicular to them. The blade spacing is 140 μm. The resolution provided by this collimator is adequate to separate Kα from Kβ peaks for all secondary fluorescent sources. The resolution of the components of the Kα peak is not, in general, possible with a single-crystal goniometer.

A secondary collimator, again of Soller slit type, was also used. This had a blade separation of 2 mm with blade length in the beam of 3 cm and effective cross-section area of 2 cm x 2 cm. The main function of this collimator was to reduce scattered incoherent radiation from the crystal and the other irradiated surfaces of the goniometer. However, its use was not crucial and it was dispensed with at low energies where low beam intensity was the main problem. Fortunately, at the larger Bragg angles involved in these cases, the scatter was also at its lowest. Conversely, the secondary slits became useful for those sources which produced the highest intensity of fluorescent radiation as a means of limiting the count-rate sufficiently to remove pulse pile-up effects in the detector.

A scan of the molybdenum K-fluorescence peak using the spectrometer is shown in figure 3.15. This was obtained by integrating the photon count observed at each angular setting as the crystal is rotated through the Kα and Kβ peaks. These peaks are easily resolved. Similar scans of titanium and tin fluorescence showed that resolution of these peaks was also achieved at the extremes of the energy range.

3.3.6 Detection System

The detector used was a sealed xenon-filled gas proportional counter (20th Century Electronics, type PX 130/Xe) with a beryllium window. The high tension supply to the counter was from a Dynatron type 1082B Power unit. The output pulses were amplified by a pulse amplifier (Dynatron type 1430A) consisting of a high impedance head amplifier and a non-overloading main amplifier stage. The amplified pulses were fed into a LABEN model 400, multichannel analyser which produced a C.R.O. display of the spectrum.

The gas proportional counter was chosen in preference to a scintillation counter largely on account of its better resolution. Zimmermann (1961) has described a method of measuring accurately the central channel and the percentage resolution of a photopeak, which lends itself easily to a computer-based analysis. Denoting channel number by x he states that for a Gaussian photopeak the channel contents y(x) will be given by:

$$y(x) = A \exp\left[-\frac{(x - x_o)^2}{2\sigma^2}\right] \qquad .....(3.7)$$

where σ is the standard deviation and x_o is the central channel.

From this it follows that one can define F(x) as:

$$F(x) = \ln \frac{y(x-1)}{y(x+1)} = \frac{2(x - x_o)}{\sigma^2} \qquad .....(3.8)$$

A graph of F(x) against x should be linear, and the central channel and resolution can be found from the intercept and slope respectively.

A programme was written for a PDP-8 computer to calculate the function F(x) for data taken from the Kα-photopeaks of the fluorescent elements used, and to carry out a regression analysis on the values

of this function in order to obtain an energy and resolution calibration of the counter. A gas proportional counter and a scintillation counter were tested. For both counters the energy calibrations (i.e. peak channel versus energy at constant amplification) were accurately linear, and the resolution calibrations (i.e. percentage resolution versus energy) were linear on a log-log scale. The resolution of the gas proportional counter was much better than that of the scintillation counter, as can be seen from the fact that whilst the resolution was found to vary as $R = 48E^{-0.51}$ for the proportional counter, the corresponding relationship for the best scintillation counter was $R = 130E^{-0.55}$ (R in percent; E in keV).

Good resolution is desirable since it provides for better rejection of higher order diffracted radiation and scatter. In any diffracting position the crystal can reflect integral multiples of the basic energy in higher order reflections. These cannot be removed by the spectrometer but may be eliminated by the detection system if the counter resolution is adequate to resolve the first order beam from the higher orders. This would not be possible at low energies with a scintillation counter.

The improved rejection of scattered background using the proportional counter arises from the fact that the observed photopeak will be entirely contained within a smaller number of channels in the multichannel analyser, i.e. the total energy window for integrating the peak is narrower. As background tends to be uniformly spread across the channels this leads to a lower percentage contribution due to background.

The availability of visual monitoring on the multichannel analyser provides an extra and useful check on the purity of the radiation being detected.

The multichannel analyser can cope with count-rates up to 6×10^4 pulses per second without distortion. In practice, the count-rates used were between 2×10^1 and 3×10^3 counts per second. It is not, however, necessary to determine the dead-time of the analyser accurately since the timer can be set to record live-time only, the dead-time of the electronics being allowed for in the total counting time. Hence, at any given timer setting, the analyser will record pulses for a total live-time equal to that specified on the timer. This does not, of course, allow for the dead-time of the counter itself, for which allowance must separately be made.

The counter dead-time was determined experimentally. The two radioactive sources used were I-125 which undergoes K-capture followed by emission of the characteristic X rays of tellurium (Te $\overline{K\alpha}$ = 27.378 keV). The two sources were counted separately and together, and a background count rate was also taken. From these count-rates the dead-time of the counter was easily calculated by a standard procedure (see for example, Snell 1962). The xenon-filled proportional counter was found to have a dead time of 1.35 ± 0.30 μs. The large percentage error arises from the fact that the experimental method relies on measuring the small difference between two large quantities - a technique which always leads to large errors. Fortunately, the error is not really significant since at a count-rate of 1000 s^{-1} it will introduce an uncertainty of only 0.035% to the count-rate; and, also, since it is the ratio of the intensities I_o and I which is to be measured, the error is further reduced as it will affect both I_o and I in the same sense.

The stability and resolution of the detection system was very satisfactory throughout the series of measurements.

3.3.7 Background levels

A low background intensity is always present in experiments of this kind. Background pulses can arise from two sources, either from electronic noise in the amplifying equipment or from diffusely scattered radiation in the room. Electronic noise sets a lower limit to the background levels obtainable. With the amplification used it was found that an average electronic background of approximately 0.01 counts per channel per second, spread uniformly across the channels, was recorded. With suitable lead shielding it was possible to reduce the total background to less than 0.05 counts per channel per second. This was achieved by placing a screen of 1.6 mm lead before and after the absorber as shown in figure 3.1. The sheets had a lateral extent of 25 cm on each side of the beam and served to screen the entire spectrometer from the radiation source. Both screens had 2 cm diameter circular apertures to permit the beam to pass. The background intensity was obtained routinely in the course of each experiment by blocking off the aperture in these screens with a sheet of 3.2 mm lead.

3.3.8 Beam intensity monitoring

In section 3.3.2, the question of the constancy of primary beam intensity was raised. Clearly, it is of importance in an experiment of this kind, that the intensity of the beam be reproducible at a given setting of the tube current and kilovoltage. The use of a beam monitoring system was considered as providing a possible means of correcting for any fluctuation in the beam intensity. In a monitoring system one wishes to observe a second beam of radiation, of a quality as closely similar as possible to that which falls on the detector but which is unaffected by the position of the absorber. If each attenuated and unattenuated intensity reading is then normalised

relative to a monitor reading, obtained simultaneously, the effects of primary beam fluctuation should be eliminated. It must, however, be remembered that the monitor reading itself will be subject to error, and hence the possibility must be considered that taking the ratio of detector counts to monitor reading will introduce a larger percentage uncertainty than exists in the detector count alone. For this reason it is necessary to choose a form of monitor which is subject to small error.

In the experimental arrangement used, it is not feasible to monitor a beam of precisely the same quality as the detector beam. To do so would necessitate using a second crystal monochromator, analysing some portion of the secondary fluorescent radiation which did not traverse the absorber. Aside from cost considerations the final beam from such an arrangement would be weak and its detection subject to statistical uncertainties of the same magnitude as those present in the detector. If such statistical uncertainties mask fluctuations due to a real variation in beam intensity, monitoring is incapable of improving the accuracy of observed intensities.

Instead it was decided to monitor a portion of the fluorescent radiation itself, since any fluctuation in the total K-radiation intensity is likely to be linearly related to the fluctuation in the $K\alpha$-radiation at the detector. The intensity of fluorescence on the transmission side of the fluorescent source at 90° to the primary beam was monitored using an ionization chamber. This receives a high radiation intensity and is not therefore likely to show high statistical fluctuation in intensity. This radiation was initially checked using an energy-dependent detector (as gas proportional counter) and its quality was found to be essentially

Figure 3.16 BEAM INTENSITY MONITORING

a) Monitor circuit

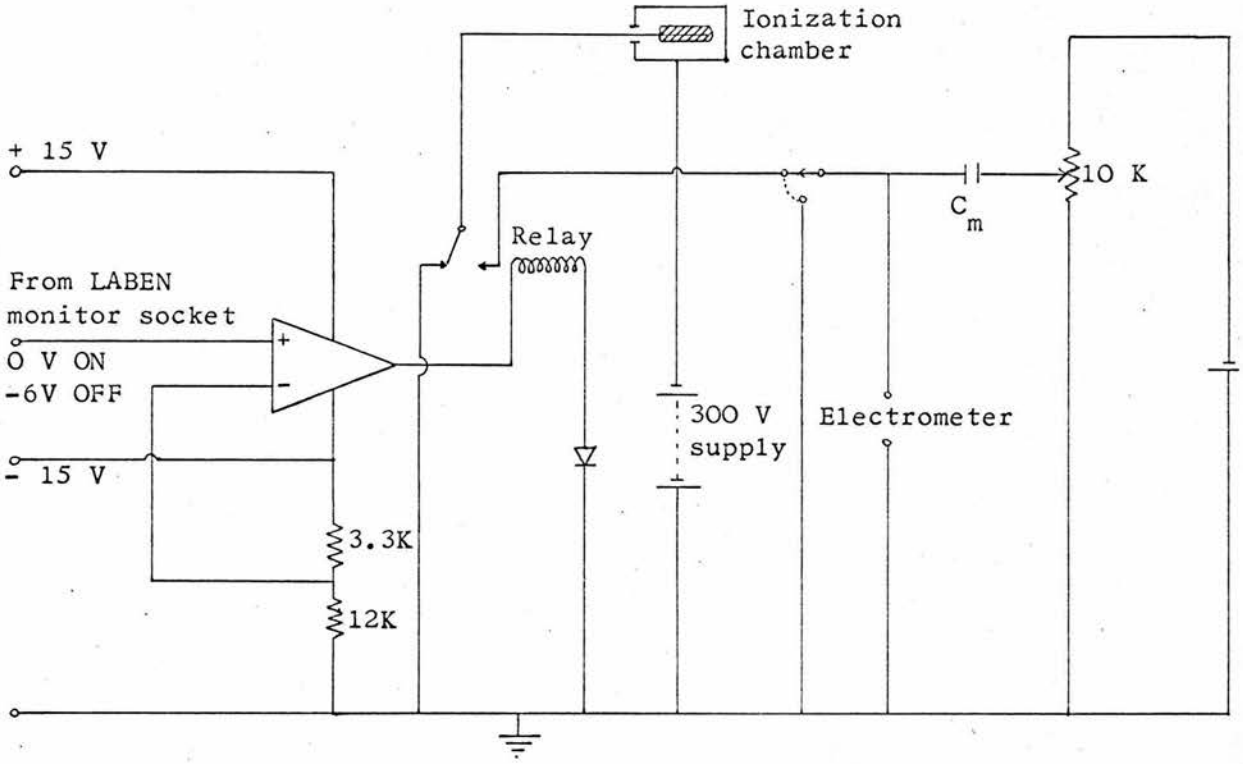

b) Apparatus layout (schematic)

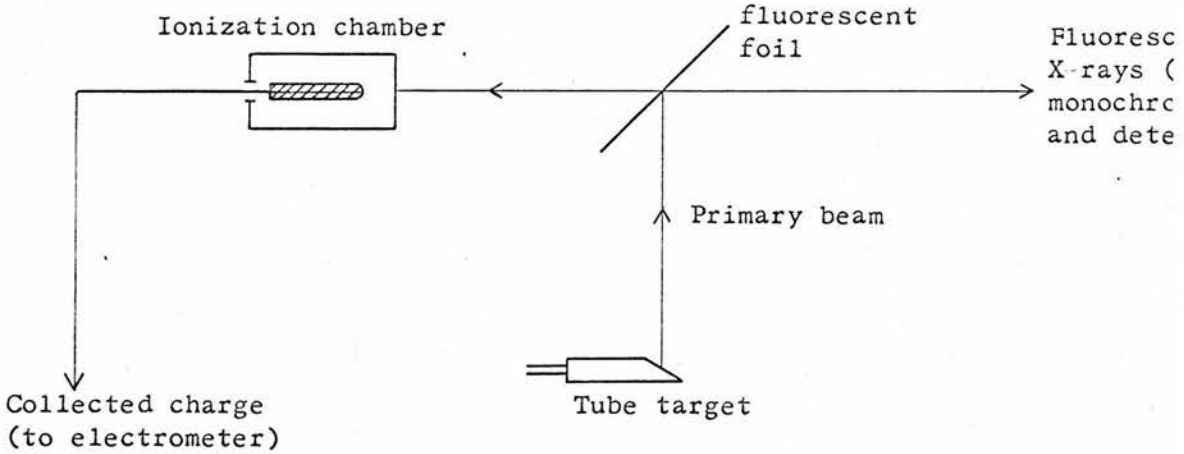

identical to that of the reflected fluorescent radiation which enters the apparatus. The monitoring circuit and a schematic diagram of the apparatus layout are shown in figure 3.16a, b. The charge collected on the chamber is integrated on the capacitor, C_m. This voltage is backed off using a decade resistance box and a stabilised 1 V source, the electrometer being used as a null detector. To test the monitoring system it is necessary to ensure that the monitor chamber and the detector are live for the same period of time. This synchronism was achieved using a relay to switch on the chamber, the relay being activated by a comparator. The input voltage which switches the comparator was a socket on the Laben model 400 multichannel analyser which sits at 0 V while counting proceeds, but drops to a fixed - 6 V level when the counter is off. As the multichannel analyser also controls the switching of the detector this system achieves the desired synchronism.

This arrangement was used to test the efficacy of the monitor experimentally. A molybdenum source was used to provide K-fluorescence radiation. Molybdenum Kα-radiation reflected from the crystal was observed by the xenon-filled proportional counter in the set-up used throughout the experiment whilst the total molybdenum K-fluorescence was observed with the ionization chamber. A series of 50 identical 40 second exposures was taken and the integrated detector counts and monitor readings were noted in each case. From these results the mean of the recorded counts and the standard error of the mean were calculated, as were the mean of the ratio of detector count to monitor reading and its standard error. The results are summarised in Table 3.6.

Table 3.6

	Detector Counts	Detector Counts / Monitor Reading
Mean	84165	9.496
Standard error of the mean	631.1	0.0605
% standard error of the mean	0.75	0.64

On the basis of Poisson statistics alone one would expect a percentage standard error of the mean of 0.35% in the detector counts. This is a purely statistical effect, independent of tube fluctuation and cannot be removed by monitoring. Since the tube fluctuations are so small that the observed standard deviation is only just over twice the minimum obtainable, the monitoring does not succeed in reducing this by an appreciable amount. In view of the problems of operating the monitor system, i.e. the extra time required per reading and the drift of the electrometer and ancillary equipment, the improvement was felt to be insufficient to justify the use of a monitor system. By concentrating on fine control of the milliampere and kilovolt meters on the tube control panel the standard deviation of the count-rate can be brought within close limits of the minimum theoretical figure.

3.4 APPARATUS DESIGN CRITERIA RECONSIDERED

The reasons governing the choice of apparatus parameters fall into three categories:-

(i) those which are necessary in order that $\frac{\mu}{\rho}$ be well-defined;

(ii) those which are necessary in order that the required precision may be attained;

(iii) those which are concerned with problems of interpretation.

3.4.1 That $\frac{\mu}{\rho}$ be well-defined

In section 3.2 there was derived a list of six criteria which must be satisfied (or from which divergence must be seen to produce a negligible effect on observed values of $\frac{\mu}{\rho}$) in order that an attenuation coefficient be well-defined.

3.4.1.1 Collimation of the beam

Good collimation of incident and detected beams is a requirement of the experiment. It is necessary to ensure that, as far as possible, no photons which undergo an interaction in the absorber are detected, and that in-scattering of photons into the beam is not a significant factor.

In the experimental arrangement used the detector collimation is good. The solid angle subtended by the detector at the absorber is governed by the effective slit system between them, i.e. the diffracting crystal. This has very good resolution in terms of energy, and will effectively prevent any incoherent scattered radiation from being detected. The collimators also provide for good rejection of coherent scattering. The rejection of fluorescence radiation originating in the absorber is also good. Considerations such as these support the placing of the absorber before the spectrometer.

In this position, however, the absorber is illuminated by a beam which is heterogeneous both in angle and energy. It must be acknowledged that a certain amount of the divergent radiation may be coherently scattered into the beam, i.e. small angle scattering out of the beam is to some extent compensated by in-scattering. The range of angle available for in-scattering is governed by the incident

slit geometry, which, in the experiment, was controlled by the entrance aperture of the absorber tubes or the fixed aperture collimators (for gaseous absorbers) and by the Soller slit assembly (for solid and liquid absorbers). In the case of the shorter gas tube the collimation is therefore provided by a 1 cm diameter circular aperture at 10 cm distance from the fluorescent foil, i.e. the collimator subtends a solid angle of approximately 0.01 steradians at the source. With the longer gas tubes, fixed aperture collimators of 5 mm diameter were used to limit the incident beam. These collimators subtend a solid angle of 0.0025 steradians at the source.

For the solid and liquid case, the incident beam is limited by a Soller slit assembly with a blade spacing of 1 mm and a blade length of 25.4 mm parallel to the beam. The effective cross-section area of the beam is also limited by an aperture of 5 mm diameter. This arrangement subtends a solid angle of less than 0.001 steradians at the source.

The differential cross-section for the Rayleigh scattering process for unpolarised X rays is:

$$\frac{d\sigma_R}{d\Omega} = \frac{r_e^2}{2}\left(1 + \cos^2\theta\right) \text{ m}^2 \text{ electron}^{-1} \qquad \text{.....(3.9)}$$

the radiation being scattered through an angle θ (r_e is the classical electron radius).

The total Rayleigh cross-section is then given by:

$$\sigma_R = \int_\Omega \frac{d\sigma_R}{d\Omega}\, d\Omega = \frac{r_e^2}{2} \int_0^\pi (1 + \cos^2\theta) \sin\theta \, d\theta \int_0^{2\pi} d\Phi$$

$$= \frac{16\pi}{3} \cdot \frac{r_e^2}{2}$$

$$\therefore \quad \frac{d\sigma_R}{d\Omega} = \frac{3\sigma_R}{16\pi}(1 + \cos^2\theta) \qquad .....(3.10)$$

The worst case being considered is that of the scattering of diffuse radiation contained within a cone, of solid angle 0.01 sr, into a collimated beam. The converse problem is easier to handle and has the same probability.

As only small angle scattering is under consideration the scattering formula (equation 3.10) can be approximated:

$$\frac{d\sigma_R}{d\Omega} = \frac{3\sigma_R}{8\pi} \qquad .....(3.11)$$

or

$$\frac{\delta\sigma_R}{\sigma_R} = \frac{3}{8\pi}\delta\Omega \qquad .....(3.12)$$

For a solid angle of 0.01 sr this gives a value of 0.12% for $\frac{\delta\sigma_R}{\sigma_R}$

The effect of in-scattering on observed total attenuation data is even less than this 0.12% figure, since over most of the energy and atomic number range of interest, the Rayleigh scattering term is only a small fraction of the whole. Its relative importance is greatest for low atomic number and high energy i.e. Sn $\overline{K\alpha}$ radiation on ethylene. For this data point Rayleigh scattering comprises 14% of the total attenuation and the magnitude of the correction calculated above on the total cross-section is then 0.017%. For all other measured data points the correction is smaller, and in most cases much smaller. A further reduction occurs since there is a high probability that coherent in-scattered photons will undergo another scattering process or be absorbed in transit through the gas sample. In-scattering can therefore be disregarded as an important source of error. This theoretical conclusion was tested experimentally (see section 5.1.7).

3.4.1.2 Monochromaticity of the beam

As the mass attenuation coefficient is a function of the radiation energy it is necessary to ensure that the observation of the attenuated and unattenuated beam intensities in any measurement be made on radiation of a single energy, or narrow band of energies. This condition is, however, less rigorous than that proposed in section 3.2. There it was stated that the incident radiation and the detected radiation should be monoenergetic and of the same energy. If, instead, the radiation used contains a wide spectrum of energies, then so long as the detection system records only that portion of the radiation whose energy falls within the narrow energy band desired, the observed ratio of attenuated and unattenuated intensities will be identical with that which would be obtained under the more demanding condition of using only pure monoenergetic radiation throughout. One important qualification of this assertion must be made, however; that it is strictly true only if both the initial and final beams are perfectly collimated. For, if not, then it is, in principle, possible for photons in the incident beam of higher energy than those being detected, to undergo a single Compton scattering event which scatters them into the detected beam. This is a similar consideration to that of small-angle coherent scattering, as discussed in the preceding section. If the detector records photons within a narrow energy band, then the number of photons "in-scattered" in this way is vanishingly small. For only a very small percentage of the photons in the imperfectly collimated and spectrally-impure incident beam will have the correct combination of energy and initial direction to make a Compton in-scattering event feasible, and even for those which have, the event has a low probability of occurrence. In view of the energy

band-width of the detection system, and the small acceptance solid-angle subtended by the entrance Soller slit at the absorber, the effect of such in-scattering can be safely disregarded. Its effect will certainly be less than that of coherent in-scattering which has been dealt with in the previous section, and shown to be negligible.

Hence, the positioning of the absorber before the monochromator, rather than after it, is desirable on all grounds except that of coherent in-scattering, which can easily be made negligible by collimation. This choice of absorber position is, therefore, entirely justifiable on theoretical grounds as well as the purely practical one of ease of construction and operation of the apparatus. Particularly with gaseous absorbers, the problems of constructing an interchange system of two 120 cm long stainless steel tubes, which would rotate with the exit collimator and proportional counter, are very substantial.

In the idealised attenuation coefficient experiment, a beam of monoenergetic radiation is proposed. Clearly this requirement cannot be met by any real apparatus. The radiation spectrum will depend on the source, collimators and detector, and can be represented by an energy "window" function $W(E - E_o)$. In the ideal case of monoenergetic radiation of energy E_o the window function becomes:

$$W(E - E_o) = \delta(E - E_o) \qquad .....(3.13)$$

where $\delta(E - E_o)$ is a Dirac δ-function.

For the real situation, let us assume that the window is more realistically represented by a Gaussian centred on E_o:

$$W(E - E_o) = \frac{1}{\sqrt{2\pi\sigma^2}} \exp\left[-\frac{(E - E_o)^2}{2\sigma^2}\right] \qquad .....(3.14)$$

The width at half-height of this Gaussian is σ so the resolving

power, R, of the spectrometer system can be defined as:

$$R = \frac{E_o}{\sigma} \qquad .....(3.15)$$

If the primary spectrum of the tube can be considered flat over that region in which $W(E - E_o)$ differs appreciably from zero then the unattenuated intensity $I_o(E_o)$ is given by:

$$I_o(E_o) = K \int_o^\infty W(E - E_o)\, dE \qquad .....(3.16)$$

where K is a constant.

With an absorber in the beam, the attenuated intensity $I(E_o)$ will be defined as:

$$I(E_o) = K \int_o^\infty T(E)W(E - E_o)\, dE \qquad .....(3.17)$$

where T(E) is the transmission function of the absorber. This can be approximated in the region between absorption edges by the relations:

$$\frac{\mu}{\rho}(E) = AE^{-3} \qquad .....(3.18)$$

and

$$T(E) = \exp\left(-\frac{\mu}{\rho} \cdot \rho x\right) \qquad .....(3.19)$$

where A is a constant factor.

The apparent mass absorption coefficient will be given by:

$$\rho x \left[\frac{\mu}{\rho}(E)\right]_{\text{apparent}} = \ln \frac{I_o}{I} = \ln \frac{\int_o^\infty W(E - E_o)\, dE}{\int_o^\infty T(E)W(E - E_o)\, dE} \qquad .....(3.20)$$

The integral can be evaluated exactly for $W(E - E_o)$ given by equation 3.13, and approximately forW as given by equation 3.14. These calculations are presented in Appendix 3.

The fractional uncertainty in $\frac{\mu}{\rho}$ introduced by imperfect monochromaticity is shown to be of the same order as R^{-2}:

$$\frac{\delta \frac{\mu}{\rho}}{\frac{\mu}{\rho}} = \sim R^{-2} \qquad \text{.....(3.21)}$$

This condition is not particularly stringent. In section 3.3.3 it was shown that for Ti $\overline{K\alpha}$ radiation an approximate resolving power of 1500 could be assigned, and for Sn $\overline{K\alpha}$, 220. These lead to percentage uncertainties in $\frac{\mu}{\rho}$ of $4.4 \times 10^{-5}\%$ and $2.1 \times 10^{-3}\%$ respectively.

This result, however, provides information only on the extent to which the attenuation coefficient is affected by impurity of the radiation spectrum. It is a separate issue to consider the effect of uncertainty in knowledge of the predominant energy E_o on observed values of $\frac{\mu}{\rho}$. Such uncertainty will not invalidate an individual measurement, but unless E_o is specified accurately any interrelation of results at different radiation energies, or comparison with the results of other workers, is impossible.

If we again assume an E^{-3} relationship:

$$\frac{\mu}{\rho} = AE^{-3} \qquad \text{.....(3.22)}$$

it easily follows that:

$$\frac{\delta \frac{\mu}{\rho}}{\frac{\mu}{\rho}} = -\frac{3\,\delta E_o}{E_o} \qquad \text{.....(3.23)}$$

Hence an uncertainty of n% in E_o will lead to a 3n% uncertainty in $\frac{\mu}{\rho}$. It is therefore of considerable interest to ensure that specified values of E_o are as accurate as possible.

As stated previously the values of $\overline{K\alpha}$ energies from Storm and Israel's 1970 publication were used. Since these are quoted to 5 significant figures it is unlikely that any error greater than 0.01% is present. However, the measured attenuation coefficients themselves can be used to detect discrepancies in the energy values

used. A graph of $\frac{\mu}{\rho}$ against E is drawn on an expanded scale; then if a systematic deviation from the best-fit line is observed for the same energy point for all absorbers, it would be reasonable to conclude that that energy value might itself be the source of the deviation. This will be discussed in conjunction with the analysis of the experimental results in Chapter 6.

3.4.1.3 Absorber homogeneity and interaction strength

In section 3.2 necessary criteria regarding the interaction strength and absorber homogeneity were stated. These were, that the quotient $\frac{\delta I}{\delta x}$ tend to a stable limit (as $\delta x \rightarrow o$) while δx is still large enough for the absorber to be regarded as homogeneous; and that the interaction be sufficiently weak that the intensity is essentially constant within a thin layer, δx, of sufficient thickness to satisfy the previous condition.

In the energy region under discussion the maximum value of the linear attenuation coefficient, μ, encountered is around 0.5 cm^{-1} for gases and around 700 cm^{-1} for solids. The corresponding values of μ^{-1} are 2 cm and 1.4×10^{-3} cm which compare with mean interatomic distances of the order of 10^{-7} cm and 10^{-8} cm for gases and solids respectively. Hence the interaction strength is such that the "mean-free path" is many orders of magnitude larger than the interatomic spacing, and the criterion of homogeneity is easily satisfied. This is the case for gaseous and liquid absorbers but may be questioned for polycrystalline solids. In this case the relevant parameter for homogeneity considerations is the crystallite dimensions rather than interatomic distances. For the materials used this is not believed likely to cause trouble, but this consideration is another reason why disordered absorbers like gases are preferable to solids with a polycrystalline structure.

3.4.2 That $\frac{\mu}{\rho}$ be measured to the required precision

The conditions that must be satisfied in order that $\frac{\mu}{\rho}$ be measured to the required precision have been mentioned in the course of section 3.3. Defining $\frac{\mu}{\rho}$ as:

$$\frac{\mu}{\rho} = \frac{1}{\rho x} \ln \frac{I_o}{I}$$

it is clearly necessary to determine $\ln \frac{I_o}{I}$, ρ, and x to sufficient precision, that $\frac{\mu}{\rho}$ be calculated to the requisite accuracy.

The precautions concerning the measurements of ρ and x have been dealt with in section 3.3.4. The accuracy of determination of $\ln \frac{I_o}{I}$ is the subject of Chapter 4. These are, however, merely considerations of experimental accuracy, and it is in order to emphasise the distinction between them and the criteria that $\frac{\mu}{\rho}$ be well-defined (section 3.4.1) that they are reiterated here.

3.4.3 Problems of interpretation of $\frac{\mu}{\rho}$

The question of small angle scattering, already considered in terms of in-scattering, also raises problems of interpretation. If one defines a scattered photon in such a way that the influence of weaker and weaker interactions is included, it is clear that the attenuation coefficient would tend to become infinitely large. It is necessary to specify in unambiguous fashion which interactions are included in the definition of total attenuation cross-section, and which are excluded. Such considerations may be regarded as hair-splitting at accuracy levels of around 1%, but they must be seen as a serious conceptual obstacle to measuring $\frac{\mu}{\rho}$ to 0.1% or better. In the present work, the total attenuation cross-section may be taken as including the photoelectric effect and Compton and Rayleigh scattering. Other long-range effects are excluded from consideration.

CHAPTER 4

O P T I M U M T H I C K N E S S O F T H E A B S O R B E R

4.1 INTRODUCTION

Several authors have previously attempted to give a theoretical analysis of the variation of accuracy of a measurement of mass attenuation coefficient with absorber thickness. One of the first to do so was Grosskurth (1934). His results, however, are derived on the basis of ionization chamber statistics and are not directly applicable to counters, where Poisson statistics may be expected to hold. More recently Bearden (1966), Heinrich (1966), and Hughes, Woodhouse and Bucklow (1968) have derived results for counters based on such statistics. Of these authors, however, only Heinrich has considered the effects of background radiation levels, and none of the three papers questions the assumption that I_o and I be recorded over identical periods of time. The following analysis shows that by dividing the time optimally between measurements of I_o and I a further improvement of performance may be anticipated, and considers the effects of background radiation on the derived results.

4.2 UNCERTAINTY IN ATTENUATION EXPERIMENTS

The mass attenuation coefficient $\frac{\mu}{\rho}$, is defined by:

$$\frac{\mu}{\rho} = \frac{1}{\rho x} \ln \frac{I_o}{I} \qquad \text{.....(4.1)}$$

In general, consider a function X

$$X = X(A, B, C, - - - - . .)$$

The mean square variation in X due to random variation in A, B, C, etc. is then given by:

$$\overline{(\delta X)^2} = \left(\frac{\partial X}{\partial A}\right)^2 \overline{(\delta A)^2} + \left(\frac{\partial X}{\partial B}\right)^2 \overline{(\delta B)^2} + \ldots \qquad \ldots\ldots(4.2)$$

Applying this to equation (4.1) gives the result:

$$\sigma_{\mu/\rho}^2 = \sigma_\rho^2 + \sigma_x^2 + \frac{1}{\left(\ln \frac{I_o}{I}\right)^2}\left(\sigma_{I_o}^2 + \sigma_I^2\right) \qquad \ldots\ldots(4.3)$$

(where the notation $\sigma_A^2 = \overline{(\delta A)^2}/A^2$ is used throughout).

$\sigma_{\mu/\rho}$ is the fractional standard error of the mean of $\frac{\mu}{\rho}$. The final term on the right-hand side of equation 4.3 is the contribution of counting statistics to the total uncertainty. It is this term whose variation with experimental conditions we wish to investigate:

$$\varepsilon^2 = \frac{1}{\left(\ln \frac{I_o}{I}\right)^2}\left(\sigma_{I_o}^2 + \sigma_I^2\right) \qquad \ldots\ldots(4.4)$$

4.2.1 Zero background level

The intensities I_o and I are defined as counts/unit time:

$$I_o = \frac{N_o}{T_o} \quad \text{and} \quad I = \frac{N}{T} \qquad \ldots\ldots(4.5)$$

Hence $\sigma_{I_o}^2 = \sigma_{N_o}^2 + \sigma_{T_o}^2$

and $\sigma_I^2 = \sigma_N^2 + \sigma_T^2$

If it can be assumed that T_o and T are measured accurately by the timer on the recording device, then the uncertainties in T_o and T are negligible, i.e. $\sigma_{T_o}^2 = \sigma_T^2 = 0$

Further, if Poisson statistics hold, the values of $\sigma_{N_o}^2$ and σ_N^2 can be obtained:

$$\sigma_{N_o}^2 = \frac{\overline{(\delta N_o)^2}}{N_o^2} = \frac{N_o}{N_o^2} = \frac{1}{N_o}$$

Similarly $\sigma_N^2 = \frac{1}{N}$

Under these conditions equation (4.4) reduces to:

$$\varepsilon^2 = \frac{1}{\left(\ln \frac{I_o}{I}\right)^2} \left(\frac{1}{N_o} + \frac{1}{N}\right) \qquad .....(4.6)$$

ε^2 is ostensibly a function of four variables; these are, however, not independent. Also, it should be noticed that some of the variables which affect ε^2 are not truly dependent on the functional relationship of equation 4.6, e.g. if the total time is doubled, (i.e. both N_o and N are doubled) then clearly ε^2 is reduced by a factor of two. So ε^2 decreases monotonically with increasing total time. It is more valuable to discover whether, for a given total time, there is an optimum way of:

(i) dividing this time between the measurement of N_o and N, and

(ii) deciding the absorption fraction $\frac{I_o}{I}$ to make ε^2 minimum.

Firstly, equation 4.6 can be expressed in terms of more useful parameters, viz. the absorption ratio R_i $(= \frac{I_o}{I})$; the ratio of counting times R_t $(= \frac{T_o}{T})$; the total time $\tau (= T_o + T)$; and the unattenuated intensity I_o. As previously pointed out, the variation of ε^2 with τ is trivial. It is also worth remarking that the quantity I_o is not under the direct control of the experimenter, but is determined by the source, and the collimator geometry.

In terms of these parameters equation 4.6 reduces to:

$$\varepsilon^2 = \frac{1 + R_t}{I_o \tau (\ln R_i)^2} \left(\frac{1}{R_t} + R_i\right) \qquad .....(4.7)$$

Figure 4.1 VARIATION OF UNCERTAINTY DUE TO COUNTING STATISTICS WITH ABSORBER THICKNESS: FIXED TIME CONDITIONS/ZERO BACKGROUND

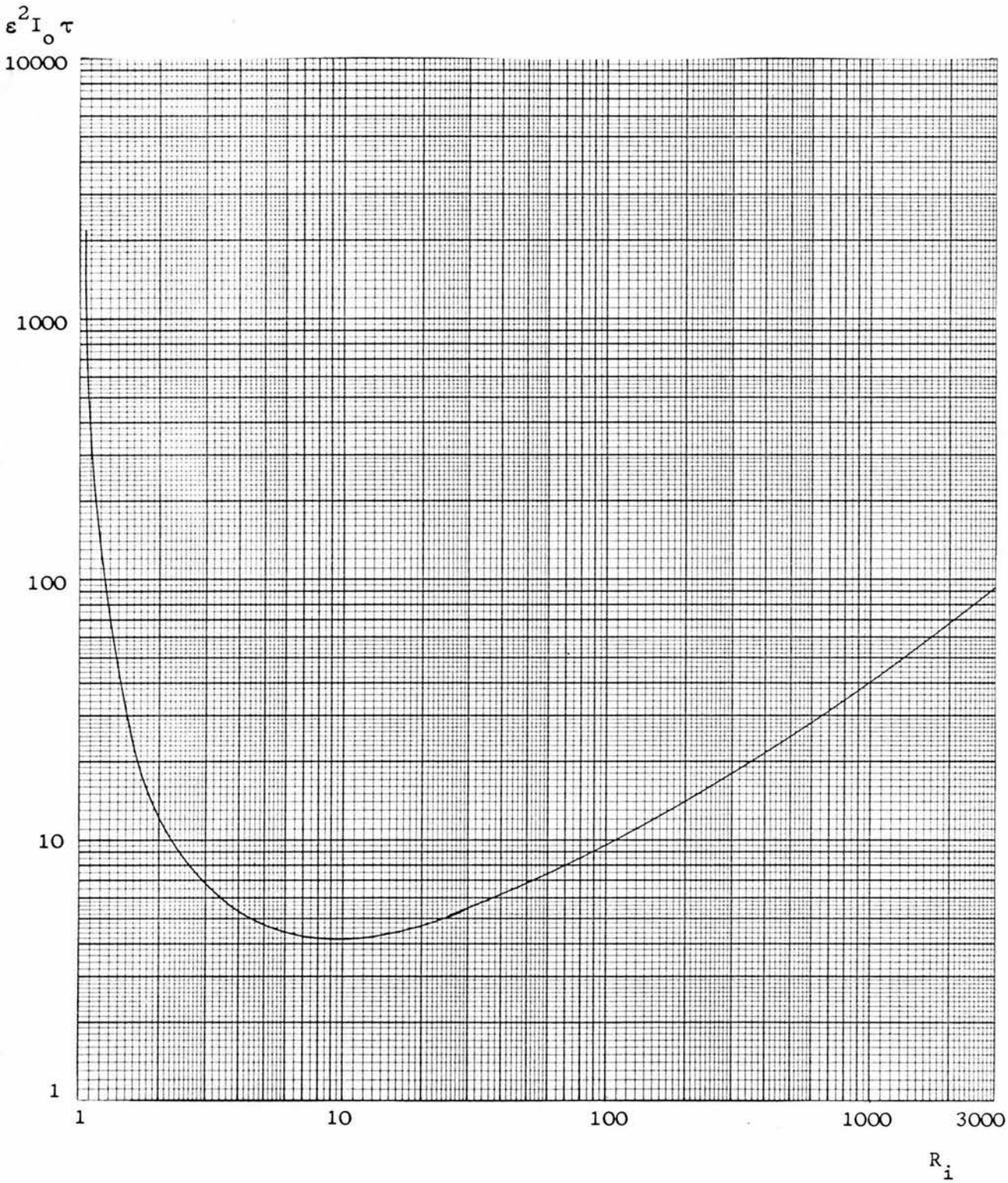

Three types of experimental conditions can be separately considered:

(i) Fixed time, in which N_o and N are counted for the same length of time;

(ii) Fixed count, in which attenuated and unattenuated beams are counted for such times that the recorded counts are the same;

(iii) No restrictions on times or counts.

4.2.1.1 Fixed time

This condition is equivalent to setting $R_t = 1$

Then

$$\varepsilon^2 = \frac{2(1 + R_i)}{I_o \tau (\ln R_i)^2} \qquad .....(4.8)$$

A graph of $\varepsilon^2 I_o \tau$ against R_i is shown in figure 4.1. The function has a minimum at $R_i = 9.19$.

This is the result quoted by Bearden (1966) and figure 4.1 is identical to the graph illustrated by Hughes, Woodhouse and Bucklow (1968).

4.2.1.2 Fixed count

Under these conditions $N_o = N$; i.e. $I_o T_o = IT$. This is equivalent to $R_t = \frac{1}{R_i}$

With this condition

$$\varepsilon^2 = \frac{2(1 + R_i)}{I_o \tau (\ln R_i)^2}$$

This is identical in form to equation 4.8 and will lead to the same result.

4.3.1.3 General case

ε^2 is defined by

$$\varepsilon^2 = \frac{1 + R_t}{I_o \tau (\ln R_i)^2} \left(\frac{1}{R_t} + R_i \right) \qquad \text{.....(4.9)}$$

In this expression, R_t is a hitherto unspecified function of R_i. We wish to find the functional relationship between R_t and R_i which will minimise ε^2 over the range of R_i.

In general terms, consider a function $f(x, y)$, where $y = y(x)$. We wish to find $y_o = y_o(x)$ such that

$$f(x, y_o(x)) \leqslant f(x, y(x)) \qquad \text{where} \quad y(x) \neq y_o(x)$$

for all x in the range $1 < x < \infty$

Consider, instead, the related problem of minimising the definite integral of $f(x, y)$ between two arbitrary limits x_1 and x_2, i.e. of minimising K where

$$K = \int_{x_1}^{x_2} f(x, y)\, dx$$

Using the calculus of variations, generalised to the case of variable end points (see, for example, Mathews and Walker (1965)) the value of K is minimum under the following conditions:

$$\frac{\partial f}{\partial y} - \frac{d}{dx} \frac{\partial f}{\partial y'} = 0$$

$$\left(\frac{\partial f}{\partial y'} \right)_{x = x_1} = \left(\frac{\partial f}{\partial y'} \right)_{x = x_2} = 0 \qquad \text{.....(4.10)}$$

In the case under consideration, f is not an explicit function of y' $(= \frac{dy}{dx})$. The conditions of equation 4.10 simplify to the single requirement

$$\frac{\partial f}{\partial y} = 0$$

or, with application to equation 4.9:

$$\left(\frac{\partial \varepsilon^2}{\partial R_t} \right)_{R_i} = 0$$

Figure 4.2 VARIATION OF UNCERTAINTY DUE TO COUNTING STATISTICS WITH ABSORBER THICKNESS: OPTIMUM DIVISION OF COUNTING TIME/ZERO BACKGROUND

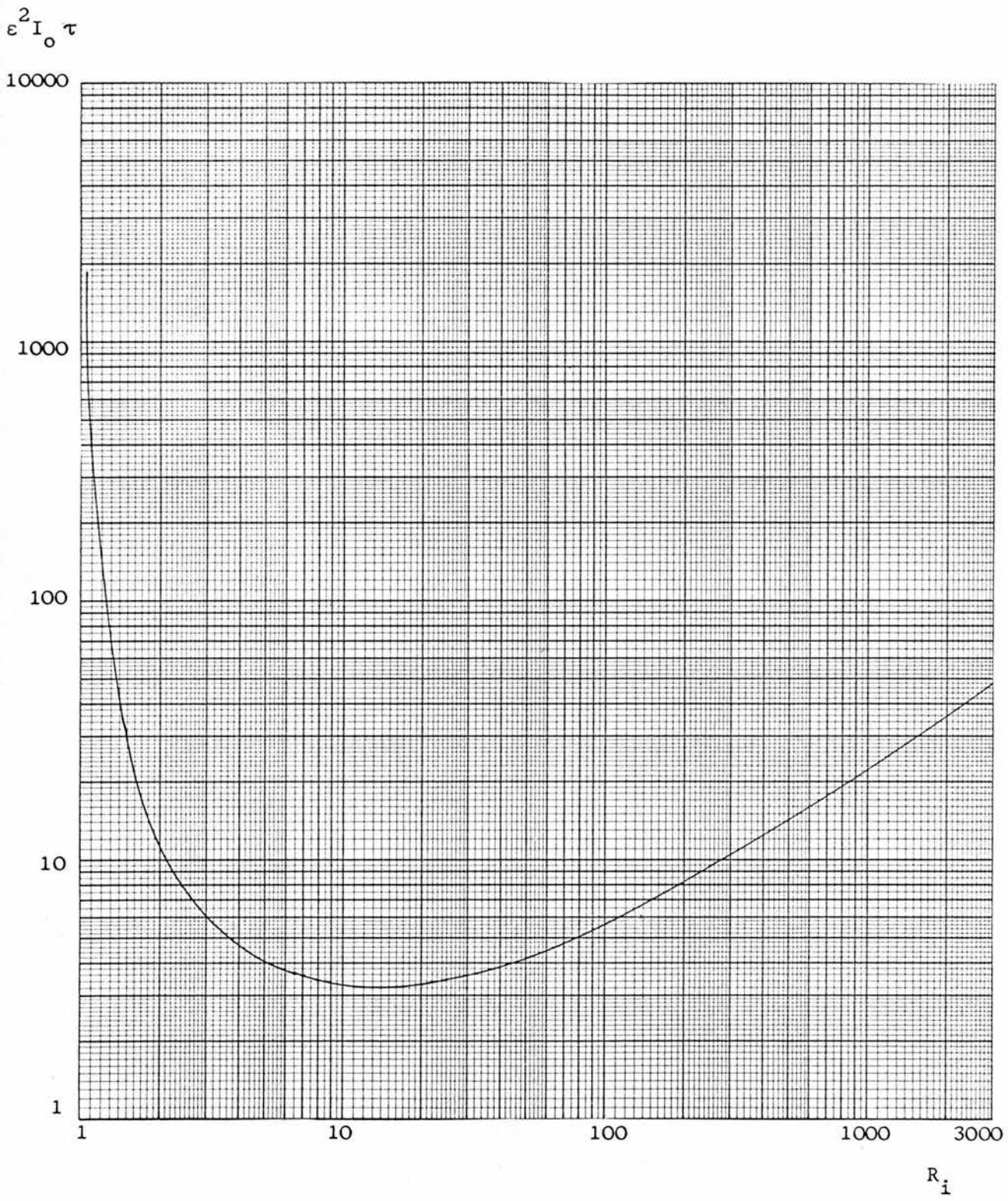

This leads to the requirement:

$$R_t = \frac{1}{\sqrt{R_i}} \qquad \ldots\ldots (4.11)$$

With this functional relationship, the integral of ε^2 between any two arbitrarily chosen values of R_i is minimum. Hence, if the function is well-behaved in the range $1 < R_i < \infty$ (which it is) the function given by equation 4.11 will lead to a minimum of ε^2 itself, at each value of R_i.

Substituting equation 4.11 into equation 4.9 it follows that

$$\varepsilon^2 = \frac{(1 + R_i^{\frac{1}{2}})^2}{I_o \tau (\ln R_i)^2} \qquad \ldots\ldots (4.12)$$

A graph of $\varepsilon^2 I_o \tau$ against R_i is shown in figure 4.2. The function has a minimum at $R_i = 12.90$. The absolute value at this minimum is less than in either the case of fixed time or fixed count.

4.2.2 Finite Background Level

The form of the graph (figure 4.2) indicates that the error rises much more rapidly as R_i tends towards unity, than as R_i becomes large. When R_i is large, however, the attenuated intensity I is small, and it may be unjustified to neglect background radiation as the preceding calculations have done. To include background in a general theory is very tedious; but fortunately, since background becomes significant only for large R_i it can be incorporated in an approximate theory which is valid at larger R_i.

Firstly, however, it is necessary to see how the preceding theory can be approximated for large R_i. Consider equation 4.6:

$$\varepsilon^2 = \frac{1}{\left(\ln \frac{I_o}{I}\right)^2} \left(\frac{1}{N_o} + \frac{1}{N}\right)$$

For large R_i, in the case of fixed time, or optimal time division, $\frac{1}{N_o} \ll \frac{1}{N}$

Hence

$$\varepsilon^2 \doteq \frac{1}{\left(\ln \frac{I_o}{I}\right)^2} \left(\frac{1}{N}\right) \qquad \ldots\ldots (4.13)$$

With the substitutions used previously this becomes:

$$\varepsilon^2 \doteq \frac{R_i (1 + R_t)}{I_o \tau (\ln R_i)^2} \qquad \ldots\ldots (4.14)$$

Incorporating background into the theory will alter equation 4.5 to:

$$I_o \doteq \frac{N_o}{T_o} \quad ; \quad I = \frac{N - N_b}{T} \quad (\text{if } N_o \gg N_b) \qquad \ldots\ldots (4.15)$$

where N_b is the number of background counts recorded in time T.

Following the steps of section 4.2.1 the result follows that:

$$\varepsilon^2 \doteq \frac{1}{\left(\ln \frac{I_o}{I}\right)^2} \left(\frac{1}{N_o} + \frac{N + N_b}{(N - N_b)^2}\right)$$

Hence, for large R_i

$$\varepsilon^2 \doteq \frac{1}{\left(\ln \frac{I_o}{I}\right)^2} \cdot \frac{N + N_b}{(N - N_b)^2} \qquad \ldots\ldots (4.16)$$

This can now be expressed in terms of I_o, τ, R_i, R_t and $R_b (= \frac{I_o}{I_b})$ After manipulation, the result is obtained that:

$$\varepsilon^2 \doteq \frac{R_i (1 + R_t)}{I_o \tau (\ln R_i)^2} \cdot \frac{R_b (R_b + R_i)}{(R_b - R_i)^2} \qquad \ldots\ldots (4.17)$$

The values of ε^2 for large R_i with and without allowance for background are then given by equations 4.14 and 4.17 respectively. By allowing for background, the uncertainty ε^2 is multiplied by a factor

Figure 4.3 VARIATION OF UNCERTAINTY DUE TO COUNTING STATISTICS WITH ABSORBER THICKNESS: OPTIMUM DIVISION OF COUNTING TIME/NON-ZERO BACKGROUND LEVELS

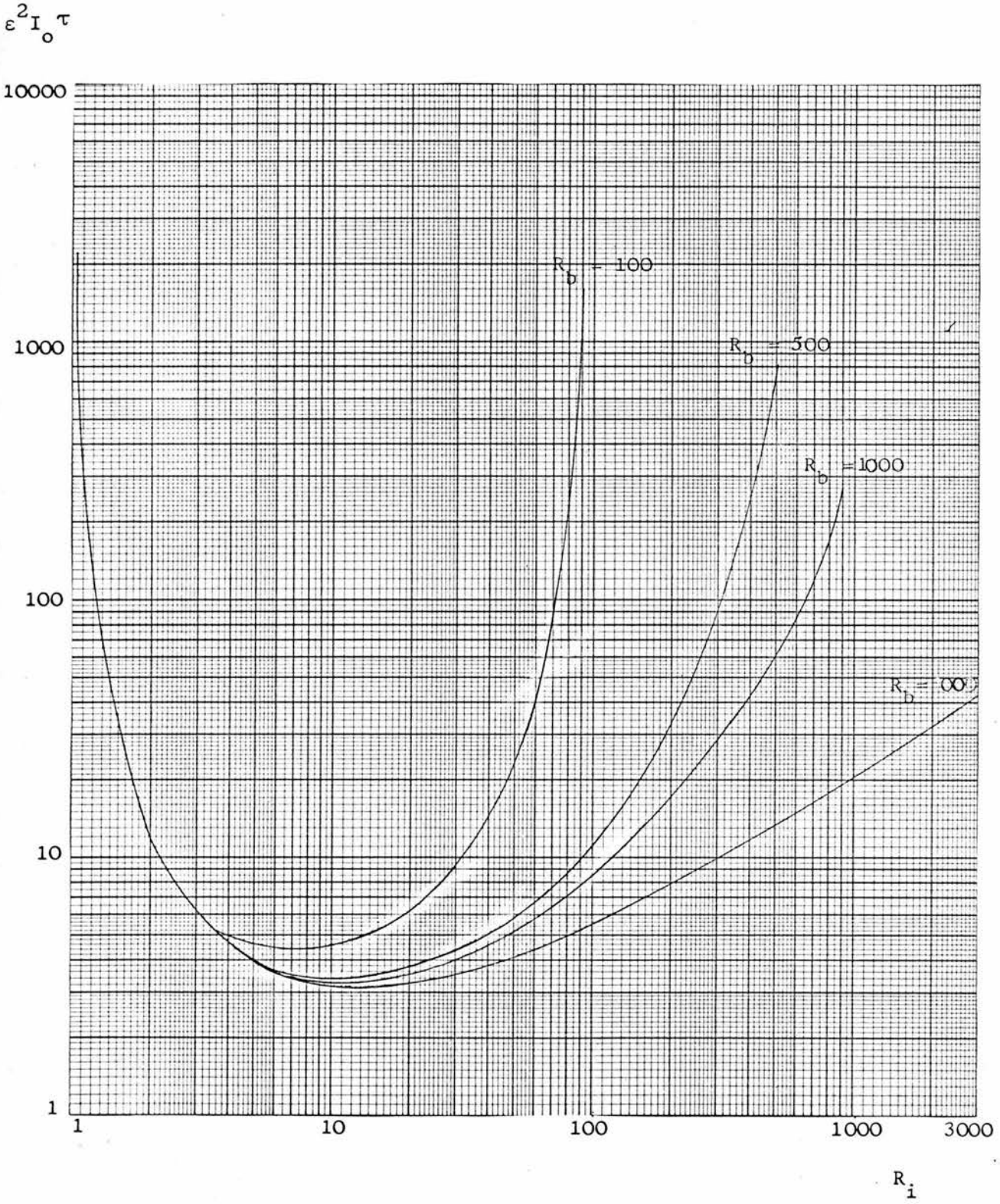

$$\frac{R_b\,(R_b + R_i)}{(R_b - R_i)^2}$$

Figure 4.3 shows graphs of $\varepsilon^2 I_o \tau$ (under optimum time ratio conditions) against R_i, with values of R_b of ∞ (no background), 1000, 500 and 100. Clearly as R_b decreases, the error rises more and more steeply with increasing R_i.

4.3 CONCLUSIONS

In the experimental work, the count-rate for the unattenuated beam lay between a minimum of 220 s^{-1} for Ti Kα and a maximum of around 3000 s^{-1} for Cu Kα and Zn Kα. The average level of background intensity was between 1 and 4 s^{-1}. For the majority of source and absorber configurations, the smallest value of R_b encountered was around 100 whilst a maximum of around 3000 was recorded. For this reason, although theory predicts best results for $R_i = 12.90$ when $R_b = \infty$, it was thought better to keep R_i in the range $5 < R_i < 8$. In practice no difficulty was experienced in obtaining a statistical accuracy (as measured by the standard error of the mean) of better than 1% from a series of ten readings of I_o and I, using values of R_i greater than 2. This arises because the minimum of the graph (figure 4.3) is a particularly shallow one. Consequently many readings were carried out with lower absorptions than might be thought desirable. The advantage of this situation is that background becomes a negligible fraction of both attenuated and unattenuated intensities and less time need be expended on measuring it accurately. At the high energy end of the range of interest, it is, however, impossible to achieve such values of R_i at manageable pressures and so much lower absorption had to be used. Around 90% of the readings were taken with $R_i \geqslant 1.5$,

Table 4.1 ATTENUATION PRODUCED BY CARBON DIOXIDE SAMPLES AT EACH Kα ENERGY

Fluorescent Element	$\frac{\mu}{\rho}$	40 μ (s.t.p.)	I_o/I			Pressure used (atmos.)
			1 atm.	2 atm.	3 atm	
Ti	54.4	4.30	73.8	-	-	$^1/4$
Cr	31.3	2.48	11.9	-	-	$\frac{1}{2}$
Fe	18.8	1.49	4.42	-	-	1
Ni	11.7	0.925	2.52	6.36	-	1
Cu	9.33	0.738	2.09	4.37	-	$1\frac{1}{2}$
Zn	7.54	0.596	1.82	3.30	5.98	$1\frac{1}{2}$
Ge	5.03	0.398	1.49	2.22	3.30	2
Se	3.44	0.272	1.31	1.72	2.26	3
Rb	2.13	0.168	1.18	1.40	1.66	3
Zr	1.32	0.104	1.11	1.23	1.37	3
Mo	1.02	0.0807	1.084	1.18	1.27	L
Ru	0.799	0.0632	1.065	1.13	1.21	L
Pd	0.643	0.0508	1.052	1.11	1.16	L
Cd	0.533	0.0421	1.043	1.088	1.13	L
Sn	0.452	0.0357	1.036	1.074	1.11	L

L = use long tube

ρ_{CO_2} = 0.00197696 g cm^{-3} at s.t.p.

and the lowest R_i used was 1.15 for ethylene at 3 atmospheres pressure using Sn Kα radiation.

For some data points higher values of R_b were unavoidable. Using Cd Kα and Sn Kα radiation with the 120 cm absorption tube, the beam strength was rather low, so that values of R_b of approximately 80 and 45 respectively were encountered. Similarly with the highly collimated beam used for measurements on solid and liquid absorbers, the beam strength for Ti Kα and Cr Kα radiation was reduced and values of R_b of 40 and 75 respectively were obtained. In all these cases the difficulty was overcome by devoting more counting time to the measurement of background than was normally the case. The final accuracies assigned to these values take into account the extra uncertainties introduced by the higher relative background.

From these results, optimum operating conditions for solid and liquid absorbers are easily calculated.

For gaseous absorbers, the results derived above were used in the following way. For each absorbing material, estimates of $\frac{\mu}{\rho}$ at each energy value used were derived from the results of Storm and Israel (1970). The expected values of R_i at 1, 2 and 3 atmospheres pressure for either the short tube (length = 40 cm), or the long tube (120 cm), were calculated. From these results it was possible to select the gas pressures, appropriate to each data point, which would yield the optimum conditions. For example Table 4.1 shows the results of such a calculation for carbon dioxide. The pressures decided upon are shown in the final column. Once the pressure has been chosen the approximate expected value of R_i can be calculated, and from this $\varepsilon^2 I_o \tau$, using the formula

$$\varepsilon^2 I_o \tau = \frac{(1 + R_i^{\frac{1}{2}})^2}{(\ln R_i)^2}$$

Table 4.2 VALUES OF $\varepsilon^2 I_o \tau$, τ(FOR I_o = 1000 s^{-1}; ε = 0.01) AND R_t, CORRESPONDING TO THE CHOSEN VALUES OF R_i FOR A CARBON DIOXIDE ABSORBER

Fluorescent Element	R_i	$\varepsilon^2 I_o \tau$	τ(sec)	R_t
Ti	2.93	6.36	63.6	0.584
Cr	3.45	5.33	53.3	0.539
Fe	4.42	4.36	43.6	0.476
Ni	2.52	7.83	78.3	0.630
Cu	3.02	6.13	61.3	0.575
Zn	2.45	8.22	82.2	0.639
Ge	2.22	9.78	97.8	0.672
Se	2.26	9.41	94.1	0.665
Rb	1.66	20.5	205	0.777
Zr	1.37	47.9	479	0.855

Using the pressures chosen for carbon dioxide in Table 4.1, the results of further calculation are shown in Table 4.2. The second column gives values of $\varepsilon^2 I_o \tau$ calculated as above. The figure in column 3 is the value of τ required to give an uncertainty $\varepsilon = 0.01$ (i.e. 1% random uncertainty in $\frac{\mu}{\rho}$ due to statistics) with an unattenuated intensity $I_o = 1000\ s^{-1}$. Finally, the fourth column shows the value of R_t which is associated with the chosen value of R_i.

The values of τ in the third column give the total counting time in seconds necessary for a single measurement of I_o and I, in order to achieve a statistical accuracy of 1% in the value of $\ln \frac{I_o}{I}$ (with $I_o = 1000\ s^{-1}$) assuming ideal Poisson statistics. It was found in practice that beam intensity fluctuations increased the expected uncertainty, but that approximately the same precision could be achieved in practice from the average of a set of five readings of I_o and I, as is ideally predicted for a single reading.

In practice, the maximum time of counting for I_o or I in a single reading was 100 seconds. From the value of τ calculated, it was possible to estimate the number of such readings required to achieve an accuracy better than 1% in the value of $\ln \frac{I_o}{I}$.

In all cases, the uncertainty was calculated for each data point on the basis of the spread of the observed results, using the procedure outlined in section 5. The theoretical results of this chapter were not relied on to estimate the accuracy of the observed results, but rather to enable the experimental conditions of each measurements to be the best possible ones, the other constraints imposed by the system being also taken into account.

CHAPTER 5

MEASUREMENT OF MASS ATTENUATION COEFFICIENTS

5.1 GASES

5.1.1 Introduction

The gases used in the experimental work fall into three classes:

(i) Elementary gases: nitrogen, oxygen, neon and argon.

(ii) Compound gases whose attenuation is mainly due to one element, and which are used to measure the mass attenuation coefficient of that element: ethylene, carbon tetrafluoride, hydrogen sulphide and hydrogen chloride.

(iii) Compound gases and mixtures used as a check on the internal consistency of other measurements: air and carbon dioxide.

However, the same experimental techniques were used to measure the attenuation of all the gases, and the calculation procedure leading to a value for the mass attenuation coefficient was also the same in all cases.

Before commencing measurements, it is necessary that the collimation system, the absorption tubes, and the diffracting crystal be aligned, so that the maximum possible intensity of radiation reaches the detector. The various pieces of apparatus are capable of being independently levelled and height adjusted. The absorption tubes are also adjustable to ensure their parallelism and accurate separation, such that they are accurately interchangeable in the beam. The alignment of the complete system was achieved optically, using a light beam and a plane mirror in the place of the crystal in the goniometer. Once this has been done,

each Kα photopeak can be located by scanning the fluorescent spectrum of each fluorescent element to find the position of maximum intensity. The reproducibility of the spectrometer setting was such that it was easily possible to re-locate these Kα photopeaks by setting the crystal at the known angle.

5.1.2 Calibration of the tubes

Before commencing the attenuation measurements proper, it is necessary to calibrate the tubes under identical conditions. Differences in transmission of the two tubes can occur due to different window transmissions, slightly different tube lengths, and the possible presence of mercury vapour in the tube to which the manometer is connected. When the short tubes are being used there is also a contribution due to slight differences in the precise tube alignment, since the end-windows of the tubes are, themselves, the apertures which limit the beam cross-section. This effect does not contribute when the long tubes are being used, since fixed apertures before and after the tubes limit the beam. The calibration ratio, therefore, is likely to differ from unity by a larger amount for the short tubes than for the long.

With the short tubes, a correction of up to $\pm$ 0.5% was sometimes required. This correction factor must be determined experimentally as a preliminary to measuring the attenuation itself. Both tubes are pumped for 30 minutes until the pressure has been brought down to rotary-pump pressure. A series of counts is taken for the same timing interval through each tube alternately. Either five or ten pairs of such readings were taken. The background count-rate, measured by placing a sheet of lead, 3.2 mm thick, in the beam, is taken at the start of the measurement and after each five readings subsequently. The transmitted count-rates are corrected for background and for counter

dead-time, and the ratio of successive measurements through the two tubes is taken, thus yielding a series of values of the calibration ratio. From this series an average value of the calibration ratio and the associated standard error of the mean (SEOM) are calculated. Calculating the SEOM from residues presupposes a normal distribution. This is a reasonable assumption since the counts recorded might be expected to follow a Poisson distribution, which for a large mean, approximates very closely to the normal distribution.

For the long tubes there are several reasons why this same technique is not practicable. Firstly, the main contributing factor to the calibration ratio for short tubes, viz. imperfect alignment, is not present. The other contributions due to length differences and mercury vapour are comparatively small. Secondly, most of the work with the long tubes is at the high energy end of the range. At these energies the attenuation of the gas samples used is well below the optimum values calculated in Chapter 4. In the majority of cases $\frac{I_o}{I}$ is less than 2.0, and for many cases it is less than 1.5 Any uncertainties in $\frac{I_o}{I}$ are multiplied several times when the logarithm is taken. Since the uncertainty in the final corrected value of $\frac{I_o}{I}$ is a compound of the uncertainties in the uncorrected value (as measured) and in the calibration ratio, it is necessary to achieve comparable precision in both measurements. Up to 70 pairs of readings are required for some data points to specify the uncorrected value of $\frac{I_o}{I}$ to the required precision. It is not an economic usage of time to take another large series of calibration readings to determine a calibration ratio which is known, from theoretical considerations, to take the value 1.0, with an uncertainty of only a very small fraction of one percent. Consequently the calibration ratio for the long tubes is considered theoretically and an upper limit placed on its possible

departure from the value 1.0.

Consider first the effect of mercury vapour. This is discussed in section 3.3.4.1. The long tube was used for energies from 11 keV upwards only. In this energy range Table 3.2 shows that for air at s.t.p. contaminated by the presence of saturated mercury vapour in one tube there will arise a percentage error of not more than 0.04% in $\frac{I_o}{I}$. The effect of the vapour is least at the high energy limit of the energy range of interest. Even allowing for the increase in this percentage uncertainty when the logarithm of the final corrected attenuation ratio is taken, the effect of mercury vapour can be safely taken to cause a reduction of less than 0.05% in the observed intensity through the gas tube.

The second factor to be considered is the slight length difference between the two tubes. The gas tube was measured as 120.08 $\pm$ 0.01 cm; the vacuum tube as 120.04 $\pm$ 0.01 cm. The ratio of lengths is 1.00033.

To combine the effects of these two sources of uncertainty, it is necessary to consider whether they lead to a random or to a systematic uncertainty in the calibration ratio. Due to mercury vapour alone, the calibration ratio can be estimated as 1.00025 $\pm$ 0.00025, the uncertainty being a systematic one, since it is a subjective assessment of the possible bounds of this uncertainty. On the other hand the length difference, considered on its own, would lead to a calibration ratio of 1.00033 with a standard error of the mean of $\pm$ 0.00014, with ν_{eff}, the effective number of degrees of freedom, being 8.

Hence, the calibration ratio used is 1.00058 with a standard error of the mean of $\pm$ 0.00014 with 8 degrees of freedom; and a total systematic uncertainty of $\pm$ 0.00025.

5.1.3 Experimental technique and calculation of results

Having dealt with the tube calibration, the measurement of the mass attenuation coefficient can proceed. The two tubes are pumped down to rotary-pump pressure. On the basis of the work presented in Chapter 4, a pressure is selected at which the measurement for the gas and energy point in question, will be made. The gas tube is then filled with gas to this pressure, and a series of alternate count-rates for transmission through the two tubes is recorded. The timing intervals are also chosen on the basis of Chapter 4. Background count-rates are determined at the beginning and after every five readings subsequently. The gas temperature and pressure are measured after half the total counts have been made. This allows sufficient time for any slight temperature fluctuations, caused by the expansion of the gas from its cylinder into the evacuated absorption tube, to have settled down.

The results are handled by a similar method to that adopted for the experimental determination of the calibration ratio, described in the previous section. All readings of attenuated and unattenuated count-rates are corrected for background and for counter dead-time. The ratios of successive attenuated and unattenuated count-rates are taken, and this yields a series of values of the uncorrected intensity ratio $\left(\frac{I_o}{I}\right)_{\text{uncorrected}}$. These are corrected by multiplying by the appropriate calibration ratio, to give a set of values of $\frac{I_o}{I}$ and $\ln \frac{I_o}{I}$. A further small correction is applied in the case of gas pressures above 1 atmosphere for the short tubes. Under these conditions the calibration ratio is determined experimentally, but the length of the gas tube filled with gas is different from that of the same tube under vacuum conditions in the calibration experiment,

due to the different sense of the window distortion.

From the final corrected values of $\frac{I_o}{I}$ and $\ln \frac{I_o}{I}$ the averages $\overline{\left(\frac{I_o}{I}\right)}$ and $\overline{\left(\ln \frac{I_o}{I}\right)}$ are calculated; their respective standard errors of the mean are $\pm$ p% and $\pm$ q% of the mean values, say. These values of SEOM depend only on the statistical spread in measured values of attenuated and unattenuated intensity; the uncertainties in the calibration ratio must also be incorporated. This is done in the following way: the percentage SEOM due to random uncertainty in calibration ratio is combined with the percentage SEOM in $\overline{\left(\frac{I_o}{I}\right)}$, by the usual law of quadrature. The resultant value is then multiplied by a factor $\frac{q}{p}$ to allow for the change in percentage uncertainty when the logarithm is taken. This gives the final SEOM due to the counting statistics. The number of degrees of freedom is calculated by the standard method, outlined in Appendix 4. If the calibration ratio also has a systematic uncertainty of $\pm$ r%, this percentage is multiplied by $\frac{q}{p}$ to give an estimate of the total systematic uncertainty in the value of $\overline{\left(\ln \frac{I_o}{I}\right)}$.

The experimental value of mass attenuation coefficient, $\frac{\mu}{\rho}$, is determined from the equation:

$$\frac{\mu}{\rho} = \frac{1}{\rho x} \ln \frac{I_o}{I}$$

The tube lengths, x, were measured by travelling microscope as described in section 3.3.4.1. The uncertainties in these lengths were randomised by repeating the measurements five times for each tube. The lengths were 39.96 $\pm$ 0.01 cm and 120.08 $\pm$ 0.01 cm for the two gas tubes, and 40.07 $\pm$ 0.01 cm and 120.04 $\pm$ 0.01 cm for the vacuum tubes. The uncertainties quoted are, in each case, the standard error of the mean, with four degress of freedom.

Uncertainties in the value of gas density, ρ, originate from three sources. Two of these are the measurement of gas pressure and

temperature, and the other is the accuracy of the available thermodynamic data. The first two are limited by the accuracy of reading of the manometer and thermometer and are therefore systematic in nature. Those arising from tabulated data can be further subdivided. The quoted values of density at s.t.p. are assumed to be the result of previous experimental work, and to be accurate to $\pm \frac{1}{2}$ unit in the last significant figure, the uncertainty being random with a very large number of degrees of freedom. The corrections for deviation from the perfect gas laws, as discussed in section 3.3.4.1 are subjectively assessed, and their contribution to uncertainty is systematic.

In summary, the magnitude of these effects is as follows:

(i) gas temperature: systematic uncertainty of $\pm$ 0.05 K

(ii) gas pressure: systematic uncertainty of $\pm$ 0.71 mm Hg

(iii) gas density at s.t.p.: random uncertainty of $\pm \frac{1}{2}$ in the final significant figure

(iv) deviations from perfect gas laws: systematic error of $\pm$ 0.05% in the predicted density.

The contribution to the total uncertainty due to impurities in the gas samples is also systematic. As stated in section 3.3.4.1 all gases were found, on analysis by mass spectrometer, to have actual purities of better than 99.9% and in no case were any high atomic number impurities found. Consequently for all gases with certified purity of 99.95% or better, it was assumed that uncertainty due to impurity could be disregarded. For the remaining gases, i.e. nitrogen, ethylene, carbon tetrafluoride and hydrogen sulphide, a percentage uncertainty of $\pm$ 0.05% in the final calculated value of mass attenuation coefficient, due to impurities in the sample, was added to the systematic

Table 5.1 SOURCES OF UNCERTAINTY IN A SINGLE READING FOR A GASEOUS ABSORBER

Uncertainty in:	Systematic or random	Approximate relative magnitude
1. Counting statistics of attenuation measurement	R	50
2. Counting statistics of calibration ratio (for short tubes)	R	50
3. Calibration ratio (for long tubes)	R + S	6 10
4. Length of absorption tube:		
Short tube	R	2.5
Long tube	R	1
5. Measurement of gas pressure: manometer reading	S	20
6. Measurement of gas temperature: thermometer reading	S	3
7. Value of gas density at s.t.p.	R	negligible
8. Correction for deviation from gas laws	S	5
9. Impurities in gas samples (for certain gases)	S	5
10. Assessment of $\overline{K\alpha}$ energies	R	3
11. Finite energy window	S	negligible
12. Experimentally determined counter dead-time	R	3
13. Coherent in-scattering (for a few high E/low Z points)	S	< 2

uncertainty.

Finally, the remaining sources of uncertainty may be summarised as follows:

(i) assessment of $\overline{K\alpha}$ energies used (section 3.4.1.2); a random uncertainty of $\pm \frac{1}{2}$ in the last significant figure on Storm and Israel's published values (1970) is assumed. This contributes a percentage uncertainty in $\frac{\mu}{\rho}$ of three times the percentage uncertainty in $\overline{K\alpha}$ energy.

(ii) the effect of a finite energy window (see section 3.4.1.2): a systematic effect but completely negligible since it is several orders of magnitude smaller than the next smallest contribution to the uncertainty.

(iii) uncertainty in the experimentally determined value of counter dead-time (section 3.3.6): a random uncertainty of not more than $\pm$ 0.03% in the value of $\frac{I_o}{I}$.

(iv) coherent in-scattering (section 3.4.1.1): no correction is applied to allow for this. The magnitude of the uncertainty resulting from in-scattering is negligible ($\ll$0.02%) at all data points except a few high energy data points for the lower atomic number elements. A small systematic uncertainty of less than 0.02% may arise at these data points.

The conclusions from this analysis of the sources of uncertainty are summarised in Table 5.1. Clearly the major sources of uncertainty are the counting statistics, the determination of the calibration ratio, and the measurement of gas pressure. Because of the large number of experimental values to be reported, it is impractical to give a complete

breakdown of the magnitudes of all the uncertainties involved in each result. Instead, the general principles, by which the uncertainty estimates were arrived at, will be stated. All contributions to the random uncertainty were assessed using the standard error of the mean for the component in question. As this uncertainty is dominated by the contributions from counting statistics and the determination of the calibration ratio, only these effects were considered in calculating the effective number of degrees of freedom, ν_{eff}.

The systematic uncertainties were combined by two different methods. Simple arithmetic addition is likely to overestimate the total uncertainty; addition by quadrature to underestimate it. Consequently the arithmetic mean of the two results is used.

In the preparation of results which follows the total random and systematic uncertainties are expressed as percentages of the quoted value of $\frac{\mu}{\rho}$. For all of these measurements the number of degrees of freedom is not sufficiently large to reduce the 95% confidence limits on the standard error of the mean to less than $\pm$ 10% of the value of the SEOM. Consequently the percentage standard error of the mean quoted is rounded upwards to two significant figures. Similarly, the quoted values of the total systematic uncertainty are rounded upwards to two significant figures (or to one significant figure in those cases where the calculated percentage systematic uncertainty is less than 0.1%).

The experimental values of mass attenuation coefficient are quoted to four significant figures, in order that rounding errors are never greater than 0.05%. Rounding errors of 0.5% which might occur in rounding to three significant figures are too large in view of the

Table 5.2 VALUES OF THE FACTOR $\frac{N_A}{M} \times 10^{-28}$ FOR CONVERTING ATTENUATION DATA FROM $m^2 kg^{-1}$ TO BARNS/ATOM

Atomic number	Chemical symbol	$\frac{N_A}{M} \times 10^{-28}$ $\frac{m^2 kg^{-1}}{b.atom^{-1}}$
6	C	0.005014
7	N	0.004300
8	O	0.003764
9	F	0.003170
10	Ne	0.002984
11	Na	0.002620
12	Mg	0.002477
13	Al	0.002232
14	Si	0.002144
15	P	0.001944
16	S	0.001878
17	Cl	0.001699
18	A	0.001508

estimated uncertainty limits on the results. The units used for mass attenuation coefficient are $m^2\ kg^{-1}$.

As shown in section 1.1, there is a linear relation between the mass attenuation coefficient and the total attenuation cross-section, for elementary absorbers.

$$\frac{\mu}{\rho}\ (m^2\ kg^{-1}) = \left(\frac{N_A}{M} \times 10^{-28}\right) \sigma_{tot}\ (\text{barns atom}^{-1})$$

where N_A is the Avogadro constant, and M the molecular mass of the element in question. Values of $\left(\frac{N_A}{M} \times 10^{-28}\right)$ for the elements from carbon to argon are listed in Table 5.2. As the values of these conversion factors are very well known all other sources of uncertainty in their values are negligible compared with the truncation error in rounding to four significant figures. The percentage uncertainties, both random and systematic, in the quoted values of σ_{tot} are identical to the percentage uncertainties in the value of $\frac{\mu}{\rho}$ at the same data point.

The random and systematic uncertainties are combined to give 99% confidence limits for each measurement. The standard error of the mean is first multiplied by the 99% value of t (from tables of the t-distribution) for the appropriate number of degrees of freedom, and the systematic error is added. These 99% confidence limits are also presented in the form of percentages of the quoted values of $\frac{\mu}{\rho}$ and σ_{tot}.

Table 5.3 NITROGEN (μ/ρ in $m^2 kg^{-1}$; σ_{tot} in barns/atom)

Kα	E(keV)	$\frac{\mu}{\rho}$	σ_{tot}	% SEOM	ν_{eff}	% Syst. unc.	% 99% conf. limit
Ti	4.508	4.209	978.8	0.89	5	0.23	3.82
Cr	5.411	2.451	569.9	0.22	5	0.17	1.06
Fe	6.400	1.460	339.5	0.55	7	0.17	2.10
Ni	7.472	0.9097	211.6	0.22	5	0.13	1.02
Cu	8.041	0.7361	171.2	0.26	7	0.13	1.04
Zn	8.631	0.5901	137.2	0.22	17	0.13	0.77
Ge	9.876	0.3919	91.14	0.30	18	0.12	0.99
Se	11.210	0.2725	63.37	0.36	12	0.12	1.22
Rb	13.375	0.1652	38.41	0.35	9	0.13	1.27
Zr	15.746	0.1071	24.91	0.84	19	0.13	2.53
Mo	17.443	0.08361	19.44	0.87	9	0.13	2.95
Ru	19.235	0.06621	15.40	0.92	19	0.13	2.75
Pd	21.122	0.05428	12.62	0.82	29	0.13	2.39
Cd	23.108	0.04522	10.52	0.87	39	0.13	2.49
Sn	25.192	0.03876	9.014	1.00	59	0.13	2.79

Table 5.4 OXYGEN (μ/ρ in $m^2 kg^{-1}$; σ_{tot} in barns/atom)

Kα	E(keV)	$\frac{\mu}{\rho}$	σ_{tot}	% SEOM	ν_{eff}	% Syst. unc.	% 99% conf. limit
Ti	4.508	6.416	1705	0.56	6	0.22	2.30
Cr	5.411	3.769	1001	0.54	7	0.22	2.11
Fe	6.400	2.237	594.4	0.39	4	0.14	1.93
Ni	7.472	1.402	372.4	0.44	7	0.14	1.68
Cu	8.041	1.126	299.1	0.24	5	0.10	1.07
Zn	8.631	0.9112	242.1	0.28	7	0.10	1.08
Ge	9.876	0.6105	162.2	0.43	17	0.10	1.35
Se	11.210	0.4180	111.0	0.57	10	0.10	1.91
Rb	13.375	0.2462	65.41	0.42	9	0.10	1.46
Zr	15.746	0.1573	41.78	0.51	9	0.10	1.75
Mo	17.443	0.1196	31.78	0.37	9	0.10	1.30
Ru	19.235	0.09366	24.88	0.90	19	0.10	2.67
Pd	21.122	0.07378	19.60	0.60	19	0.10	1.82
Cd	23.103	0.06037	16.04	0.88	29	0.10	2.53
Sn	25.192	0.05058	13.44	0.96	29	0.10	2.75

Table 5.5 NEON (μ/ρ in $m^2 kg^{-1}$; σ_{tot} in barns/atom)

Kα	E (keV)	$\frac{\mu}{\rho}$	σ_{tot}	% SEOM	ν_{eff}	% Syst. unc.	% 99% conf. limit
Ti	4.508	12.66	4243	0.42	7	0.41	1.38
Cr	5.411	7.383	2474	0.38	6	0.22	1.63
Fe	6.400	4.496	1507	0.40	5	0.22	1.83
Ni	7.472	2.799	938.1	0.54	6	0.14	2.14
Cu	8.041	2.237	749.6	0.56	7	0.14	2.10
Zn	8.631	1.854	621.2	0.36	4	0.10	1.73
Ge	9.876	1.225	410.4	0.39	5	0.10	1.67
Se	11.210	0.8396	281.4	0.69	7	0.09	2.50
Rb	13.375	0.5011	167.9	0.65	5	0.09	2.71
Zr	15.746	0.3095	103.7	0.66	14	0.09	2.05
Mo	17.443	0.2298	76.99	0.68	9	0.10	2.30
Ru	19.235	0.1734	58.13	0.78	9	0.10	3.63
Pd	21.122	0.1353	45.33	1.00	9	0.10	2.54
Cd	23.108	0.1070	35.85	0.77	9	0.10	2.60
Sn	25.192	0.08613	28.86	0.92	25	0.10	2.67

Table 5.6 ARGON (μ/ρ in $m^2 kg^{-1}$; σ_{tot} in barns/atom)

Kα	E (keV)	$\frac{\mu}{\rho}$	σ_{tot}	% SEOM	ν_{eff}	% Syst. unc.	% 99% conf limit
Ti	4.508	56.11	37210	0.74	4	0.06	3.46
Cr	5.411	35.19	23340	0.47	6	0.06	1.80
Fe	6.400	22.16	14700	0.30	7	0.06	1.11
Ni	7.472	14.35	9513	0.23	7	0.52	1.50
Cu	8.041	11.78	7811	0.33	5	0.52	1.85
Zn	8.631	9.581	6353	0.22	8	0.41	1.15
Ge	9.876	6.546	4341	0.21	15	0.29	0.91
Se	11.210	4.558	3023	0.20	15	0.24	0.83
Rb	13.375	2.747	1822	0.25	7	0.16	1.04
Zr	15.746	1.706	1132	0.29	12	0.14	1.03
Mo	17.443	1.277	846.9	0.61	12	0.14	2.01
Ru	19.235	0.9591	636.0	0.31	13	0.14	1.07
Pd	21.122	0.7216	478.5	0.51	17	0.11	1.59
Cd	23.108	0.5601	371.4	0.82	12	0.11	2.62
Sn	25.192	0.4368	289.7	0.76	17	0.11	2.31

5.1.4 Elementary Gases

Experimental values of mass attenuation coefficient and total attenuation cross-section for nitrogen, oxygen, neon and argon, together with total random and systematic uncertainties and 99% confidence limits are presented in Tables 5.3, 5.4, 5.5 and 5.6 respectively.

All values were obtained using the experimental method previously described, with the exception of the low energy values for argon. At 4.508 keV, 5.411 keV and 6.400 keV the attenuation of argon is so strong that gas pressures around 50 to 100 mm Hg are necessary for good statistical results. Using such low pressures would introduce large percentage uncertainties in the manometer reading. Consequently for these three points the measurement of attenuation was repeated several times using slightly different pressures (and temperatures) each time. This has the effect of randomising the uncertainty due to the pressure and temperature readings.

Table 5.7 ETHYLENE (μ/ρ in $m^2 kg^{-1}$)

					%	
Kα	E (keV)	$\frac{\mu}{\rho}$	% SEOM	ν_{eff}	Syst. unc.	99% conf. limit
Ti	4.508	2.188	0.67	5	0.17	2.87
Cr	5.411	1.253	0.73	7	0.17	2.73
Fe	6.400	0.7424	0.35	4	0.12	1.72
Ni	7.472	0.4675	0.43	16	0.12	1.37
Cu	8.041	0.3774	0.41	11	0.12	1.39
Zn	8.631	0.3087	0.69	18	0.12	2.10
Ge	9.876	0.2117	0.97	17	0.12	2.94
Se	11.210	0.1473	0.55	9	0.13	1.92
Rb	13.375	0.09487	0.81	9	0.13	2.76
Zr	15.746	0.06576	0.74	9	0.13	2.54
Mo	17.443	0.05322	0.81	19	0.13	2.45
Ru	19.235	0.04508	0.75	29	0.13	2.21
Pd	21.122	0.03867	0.71	39	0.13	2.05
Cd	23.108	0.03429	0.73	59	0.13	2.07
Sn	25.192	0.03119	0.67	69	0.13	1.91

Table 5.8 CARBON (μ/ρ in $m^2 kg^{-1}$; σ_{tot} in barns/atom)

						%	
Kα	E (keV)	$\frac{\mu}{\rho}$	σ_{tot}	% SEOM	ν_{eff}	Syst. unc.	99% conf limit
Ti	4.508	2.549	508.3	0.68	5	0.17	2.91
Cr	5.411	1.456	290.5	0.74	7	0.17	2.76
Fe	6.400	0.8603	171.6	0.36	4	0.12	1.78
Ni	7.472	0.5394	107.6	0.44	16	0.12	1.41
Cu	8.041	0.4342	86.60	0.42	11	0.12	1.43
Zn	8.631	0.3540	70.61	0.71	18	0.12	2.17
Ge	9.876	0.2407	48.01	1.00	17	0.12	3.02
Se	11.210	0.1656	33.02	0.59	9	0.14	2.06
Rb	13.375	0.1044	20.82	0.88	9	0.14	3.00
Zr	15.746	0.07050	14.06	0.85	11	0.14	2.78
Mo	17.443	0.05586	11.14	0.96	24	0.14	2.84
Ru	19.235	0.04644	9.261	0.94	43	0.15	2.69
Pd	21.122	0.03898	7.775	0.95	69	0.15	2.67
Cd	23.108	0.03390	6.762	1.00	115	0.15	2.77
Sn	25.192	0.03033	6.050	0.99	171	0.16	2.74

Table 5.9 CARBON TETRAFLUORIDE (μ/ρ in $m^2 kg^{-1}$)

					%	
Kα	E (keV)	$\frac{\mu}{\rho}$	% SEOM	ν_{eff}	Syst. unc.	99% conf. limit
Ti	4.508	3.029	0.29	6	0.10	1.18
Cr	5.411	4.624	0.34	7	0.44	1.63
Fe	6.400	2.791	0.18	6	0.26	0.93
Ni	7.472	1.751	0.24	7	0.21	1.05
Cu	8.041	1.405	0.30	8	0.21	1.22
Zn	8.631	1.140	0.19	7	0.17	0.84
Ge	9.876	0.7568	0.31	7	0.17	1.25
Se	11.210	0.5267	0.32	7	0.16	1.28
Rb	13.375	0.3129	0.78	7	0.16	2.89
Zr	15.746	0.1948	0.31	9	0.18	1.19
Mo	17.443	0.1476	0.53	9	0.18	1.90
Ru	19.235	0.1147	0.60	9	0.17	2.12
Pd	21.122	0.08940	0.71	9	0.17	2.48
Cd	23.108	0.07204	0.63	9	0.15	2.20
Sn	25.192	0.05876	0.83	9	0.15	2.85

Table 5.10 FLUORINE (μ/ρ in $m^2 kg^{-1}$; σ_{tot} in barns/atom)

Kα	E (keV)	$\frac{\mu}{\rho}$	σ_{tot}	% SEOM	ν_{eff}	% Syst. unc.	% 99% conf limit
Ti	4.503	8.896	2806	0.31	6	0.11	1.26
Cr	5.411	5.124	1616	0.36	7	0.46	1.80
Fe	6.400	3.096	976.7	0.19	6	0.27	0.98
Ni	7.472	1.942	612.8	0.25	7	0.22	1.15
Cu	8.041	1.558	491.5	0.32	8	0.22	1.30
Zn	8.631	1.265	399.0	0.21	7	0.18	0.92
Ge	9.876	0.8384	264.5	0.33	7	0.18	1.34
Se	11.210	0.5838	184.2	0.34	7	0.17	1.36
Rb	13.375	0.3459	109.1	0.82	7	0.17	3.04
Zr	15.746	0.2144	67.63	0.33	9	0.19	1.26
Mo	17.443	0.1621	51.14	0.56	9	0.19	2.01
Ru	19.235	0.1254	39.57	0.64	9	0.18	2.26
Pd	21.122	0.09737	30.72	0.76	9	0.19	2.66
Cd	23.108	0.07807	24.63	0.88	9	0.17	2.38
Sn	25.192	0.06325	19.95	0.90	9	0.17	3.10

Table 5.11 HYDROGEN SULPHIDE (μ/ρ in $m^2 kg^{-1}$)

					%	
Kα	E (keV)	$\frac{\mu}{\rho}$	% SEOM	ν_{eff}	Syst. unc.	99% conf. limit
Ti	4.508	43.96	0.31	5	0.10	1.35
Cr	5.411	26.71	0.23	7	0.10	0.91
Fe	6.400	16.75	0.69	8	0.10	2.42
Ni	7.472	10.79	0.55	6	0.40	2.44
Cu	8.041	8.752	0.32	7	0.38	1.50
Zn	8.631	7.147	0.39	5	0.31	1.88
Ge	9.876	4.877	0.28	8	0.24	1.18
Se	11.210	3.339	0.31	7	0.19	1.28
Rb	13.375	1.986	0.52	6	0.19	2.12
Zr	15.746	1.264	0.85	7	0.17	3.15
Mo	17.443	0.9256	0.85	7	0.17	3.15
Ru	19.235	0.6993	0.75	6	0.13	2.91
Pd	21.122	0.5258	0.83	5	0.13	3.48
Cd	23.108	0.4060	0.71	12	0.12	2.30
Sn	25.192	0.3224	0.77	16	0.12	2.37

Table 5.12 SULPHUR (μ/ρ in m^2kg^{-1}; σ_{tot} in barns/atom)

						%	
Kα	E (keV)	$\frac{\mu}{\rho}$	σ_{tot}	% SEOM	ν_{eff}	Syst. unc.	99% conf. limit
Ti	4.508	46.73	24880	0.31	5	0.10	1.35
Cr	5.411	28.39	15120	0.23	7	0.10	0.91
Fe	6.400	17.80	9479	0.69	8	0.10	2.42
Ni	7.472	11.47	6107	0.55	6	0.40	2.44
Cu	8.041	9.300	4952	0.32	7	0.38	1.50
Zn	8.631	7.594	4044	0.39	5	0.31	1.88
Ge	9.876	5.181	2759	0.28	8	0.24	1.18
Se	11.210	3.547	1888	0.31	7	0.19	1.28
Rb	13.375	2.109	1123	0.52	6	0.19	2.12
Zr	15.746	1.341	713.9	0.85	7	0.17	3.15
Mo	17.443	0.9815	522.6	0.85	7	0.17	3.15
Ru	19.235	0.7410	394.6	0.75	6	0.13	2.91
Pd	21.122	0.5566	296.4	0.83	5	0.13	3.48
Cd	23.108	0.4293	228.6	0.72	12	0.12	2.32
Sn	25.192	0.3404	181.3	0.78	16	0.12	2.40

Table 5.13 HYDROGEN CHLORIDE (μ/ρ in $m^2 kg^{-1}$)

					%	
Kα	E (keV)	$\frac{\mu}{\rho}$	% SEOM	ν_{eff}	Syst. unc.	99% conf. limit
Ti	4.503	49.31	0.46	6	0.06	1.77
Cr	5.411	30.74	0.28	5	0.06	1.19
Fe	6.400	19.41	0.30	7	0.06	1.11
Ni	7.472	12.54	0.30	7	0.43	1.48
Cu	8.041	10.30	0.34	4	0.34	1.90
Zn	8.631	8.375	0.23	6	0.29	1.33
Ge	9.876	5.757	0.37	6	0.22	1.59
Se	11.210	3.995	0.41	6	0.17	1.74
Rb	13.375	2.392	0.33	5	0.14	1.50
Zr	15.746	1.482	0.63	6	0.14	2.48
Mo	17.443	1.134	0.71	5	0.13	2.99
Ru	19.235	0.8340	0.64	5	0.13	2.71
Pd	21.122	0.6434	0.52	12	0.13	1.72
Cd	23.108	0.4988	0.65	11	0.10	2.12
Sn	25.192	0.3861	0.97	11	0.10	3.12

Table 5.14 CHLORINE (μ/ρ in $m^2 kg^{-1}$; σ_{tot} in barns/atom)

						%	
Kα	E (keV)	$\frac{\mu}{\rho}$	σ_{tot}	% SEOM	ν_{eff}	Syst. unc.	99% conf. limit
Ti	4.503	50.71	29840	0.46	6	0.06	1.77
Cr	5.411	31.61	18600	0.28	5	0.06	1.19
Fe	6.400	19.96	11750	0.30	7	0.06	1.11
Ni	7.472	12.90	7590	0.30	7	0.43	1.48
Cu	8.041	10.59	6232	0.34	4	0.34	1.90
Zn	8.631	8.611	5069	0.28	6	0.29	1.33
Ge	9.876	5.919	3484	0.37	6	0.22	1.59
Se	11.210	4.108	2418	0.41	6	0.17	1.69
Rb	13.375	2.459	1447	0.33	5	0.14	1.47
Zr	15.746	1.523	896.2	0.63	6	0.14	2.48
Mo	17.443	1.165	685.9	0.71	5	0.13	2.99
Ru	19.235	0.8566	504.2	0.64	5	0.13	2.71
Pd	21.122	0.6607	388.9	0.52	12	0.13	1.72
Cd	23.103	0.5119	301.3	0.66	11	0.10	2.15
Sn	25.192	0.3960	233.1	0.98	11	0.10	3.15

5.1.5 Compound Gases: Attenuation mainly due to one element

Experimental values of mass attenuation coefficient for ethylene, carbon tetrafluoride, hydrogen sulphide and hydrogen chloride, together with total random and systematic uncertainties and 99% confidence limits, are presented in Tables 5.7, 5.9, 5.11 and 5.13 respectively.

At 4.508 keV for carbon tetrafluoride, hydrogen sulphide and hydrogen chloride, and at 5.411 keV and 6.400 keV for hydrogen sulphide and hydrogen chloride, the attenuation is so strong that gas pressures below 100 mm Hg are required. For these points, the measurement of attenuation was repeated several times using slightly different pressures (and temperatures) each time, thereby randomising the uncertainties due to these parameters.

From these results, values of mass attenuation coefficient and total attenuation cross-section for carbon, fluorine, sulphur and chlorine were deduced. The following formulae were used:

$$\left.\begin{aligned}
\left(\frac{\mu}{\rho}\right)_{C_2H_4} &= 0.8563\left(\frac{\mu}{\rho}\right)_C + 0.1437\left(\frac{\mu}{\rho}\right)_H \\
\left(\frac{\mu}{\rho}\right)_{CF_4} &= 0.1365\left(\frac{\mu}{\rho}\right)_C + 0.8635\left(\frac{\mu}{\rho}\right)_F \\
\left(\frac{\mu}{\rho}\right)_{H_2S} &= 0.0592\left(\frac{\mu}{\rho}\right)_H + 0.9408\left(\frac{\mu}{\rho}\right)_S \\
\left(\frac{\mu}{\rho}\right)_{HCl} &= 0.0276\left(\frac{\mu}{\rho}\right)_H + 0.9724\left(\frac{\mu}{\rho}\right)_{Cl}
\end{aligned}\right\} \quad \ldots\ldots(5.1)$$

The values of these coefficients are derived from the atomic masses of the elements and any uncertainties in them are negligible relative to the rounding error.

In order to derive values of mass attenuation coefficient for carbon, sulphur and chlorine it is necessary to make use of values for the mass attenuation coefficient of hydrogen. The values published

by Storm and Israel (1970) were used. These were graphically interpolated to obtain mass attenuation coefficients at energies corresponding to the Kα energies used. Storm and Israel estimate for their data an uncertainty of 10% below 6 keV and of 3% above 6 keV. In order to estimate the uncertainties on the experimental values of mass attenuation coefficient and total attenuation cross-section it was assumed that this quoted uncertainty is the standard error of the mean with a large number of degrees of freedom. The total random and systematic uncertainties on the values of $\frac{\mu}{\rho}$ and σ_{tot} were then calculated by the usual laws of propagation of errors. The effective number of degrees of freedom was calculated using the procedure outlined in Appendix 4. At most data points the derived values depend only weakly on the value of $\left(\frac{\mu}{\rho}\right)_{hydrogen}$. At the high energy end of the range for carbon, however, the hydrogen contribution is appreciable. For these points it was necessary to obtain the mass attenuation coefficient of ethylene with a SEOM well below 1% in order that the derived value for carbon have a percentage standard error of the mean of 1% or better.

The mass attenuation coefficient of fluorine was calculated using the value for the mass attenuation coefficient of carbon as derived above. The random and systematic uncertainties and the effective number of degrees of freedom were calculated by the standard methods.

These deduced values for the mass attenuation coefficient and total attenuation cross-section of carbon, fluorine, sulphur and chlorine, together with the associated statistical parameters are presented in Tables 5.8, 5.10, 5.12 and 5.14.

Table 5.15 AIR (BY DIRECT MEASUREMENT) (μ/ρ in $m^2 kg^{-1}$)

					%	
Kα	E (keV)	$\frac{\mu}{\rho}$	% SEOM	ν_{eff}	Syst. unc.	99% conf. limit
Ti	4.508	5.409	0.38	11	0.14	1.30
Cr	5.411	3.150	0.25	14	0.14	0.89
Fe	6.400	1.900	0.19	17	0.14	0.69
Ni	7.472	1.198	0.23	8	0.11	0.89
Cu	8.041	0.9617	0.49	16	0.14	1.57
Zn	8.631	0.7754	0.30	7	0.10	1.15
Ge	9.876	0.5213	0.36	13	0.14	1.22
Se	11.210	0.3589	0.28	11	0.08	0.93
Rb	13.375	0.2174	0.25	7	0.10	0.97
Zr	15.746	0.1390	0.59	9	0.10	2.01
Mo	17.443	0.1061	0.89	9	0.10	2.99
Ru	19.235	0.08343	1.00	15	0.10	3.10
Pd	21.122	0.06738	0.94	19	0.10	2.78
Cd	23.108	0.05613	0.87	9	0.10	2.93
Sn	25.192	0.04698	1.00	29	0.10	2.86

Table 5.16 CARBON DIOXIDE (BY DIRECT MEASUREMENT) (μ/ρ in $m^2 kg^{-1}$)

					%	
Kα	E (keV)	$\frac{\mu}{\rho}$	% SEOM	ν_{eff}	Syst. unc.	99% conf. limit
Ti	4.508	5.325	0.46	7	0.39	2.00
Cr	5.411	3.116	0.37	7	0.18	1.48
Fe	6.400	1.871	0.31	7	0.14	1.23
Ni	7.472	1.170	0.45	5	0.14	1.95
Cu	8.041	0.9399	0.26	4	0.10	1.30
Zn	8.631	0.7590	0.22	6	0.10	0.92
Ge	9.876	0.5070	0.44	7	0.08	1.62
Se	11.210	0.3496	0.66	7	0.08	2.39
Rb	13.375	0.2083	0.51	9	0.10	1.76
Zr	15.746	0.1351	1.00	17	0.08	3.17
Mo	17.443	0.1022	0.51	9	0.10	1.75
Ru	19.235	0.08072	0.78	9	0.10	2.63
Pd	21.122	0.06452	0.72	9	0.10	2.44
Cd	23.108	0.05375	0.90	9	0.10	3.02
Sn	25.192	0.04556	0.80	29	0.10	2.30

Table 5.17 AIR (CALCULATED FROM EXPERIMENTAL VALUES FOR N, O, A)(μ/ρ in $m^2 kg^-$

Kα	E (keV)	$\frac{\mu}{\rho}$	% SEOM	ν_{eff}	%	
					Syst. unc.	99% conf. limit
Ti	4.508	5.386	0.57	6	0.16	2.28
Cr	5.411	3.176	0.21	14	0.26	0.89
Fe	6.400	1.906	0.34	8	0.19	1.33
Ni	7.472	1.196	0.18	12	0.14	0.69
Cu	8.041	0.9631	0.17	11	0.13	0.66
Zn	8.631	0.7798	0.15	26	0.12	0.54
Ge	9.876	0.5215	0.21	33	0.12	0.69
Se	11.210	0.3612	0.26	21	0.12	0.85
Rb	13.375	0.2171	0.24	14	0.12	0.83
Zr	15.746	0.1392	0.51	22	0.12	1.55
Mo	17.443	0.1073	0.53	10	0.11	1.78
Ru	19.235	0.08403	0.60	26	0.11	1.77
Pd	21.122	0.06736	0.53	35	0.11	1.54
Cd	23.108	0.05544	0.59	54	0.11	1.68
Sn	25.192	0.04661	0.68	77	0.11	1.91

Table 5.18 CARBON DIOXIDE (CALCULATED FROM EXPERIMENTAL VALUES FOR C, O)
(μ/ρ in $m^2 kg^{-1}$)

					%	
Kα	E (keV)	$\frac{\mu}{\rho}$	% SEQM	ν_{eff}	Syst. unc.	99% conf. limit
Ti	4.508	5.361	0.50	6	0.19	2.05
Cr	5.411	3.138	0.49	7	0.19	1.91
Fe	6.400	1.861	0.35	4	0.11	1.72
Ni	7.472	1.167	0.39	7	0.11	1.48
Cu	8.041	0.9372	0.22	5	0.10	0.99
Zn	8.631	0.7591	0.27	8	0.10	1.01
Ge	9.876	0.5096	0.40	20	0.10	1.24
Se	11.210	0.3491	0.51	10	0.10	1.71
Rb	13.375	0.2075	0.39	10	0.10	1.33
Zr	15.746	0.1336	0.46	10	0.10	1.55
Mo	17.443	0.1022	0.35	12	0.10	1.17
Ru	19.235	0.08077	0.78	20	0.09	2.31
Pd	21.122	0.06428	0.53	22	0.09	1.58
Cd	23.108	0.05315	0.75	32	0.09	2.15
Sn	25.192	0.04505	0.80	32	0.09	2.28

5.1.6 Checks on Internal Consistency

Experimental values of mass attenuation coefficient for air and carbon dioxide, together with total random and systematic uncertainties and 99% confidence limits, are presented in Tables 5.15 and 5.16. These were measured, using samples of air and carbon dioxide, by the experimental technique described above.

However it is also possible to calculate values of mass attenuation coefficient, with the associated statistical parameters, for air from the values for nitrogen, oxygen and argon presented in Tables 5.3, 5.4 and 5.6; and for carbon dioxide from the values for carbon and oxygen presented in Tables 5.8 and 5.4. This calculation was carried out and the results are shown in Tables 5.17 and 5.18. The following formulae were used:

$$\left.\begin{aligned}\left(\frac{\mu}{\rho}\right)_{air} &= 0.7556\left(\frac{\mu}{\rho}\right)_N + 0.2316\left(\frac{\mu}{\rho}\right)_O + 0.01283\left(\frac{\mu}{\rho}\right)_A \\ \left(\frac{\mu}{\rho}\right)_{CO_2} &= 0.2729\left(\frac{\mu}{\rho}\right)_C + 0.7271\left(\frac{\mu}{\rho}\right)_O\end{aligned}\right\} \quad \ldots\ldots(5.2)$$

The coefficients used for the composition of air are taken from Kaye and Laby (1966).

As a check on the consistency of measurements carried out over a period of time, the two sets of results for air and carbon dioxide were tested to establish whether the results obtained by the two methods were significantly different, bearing in mind the uncertainties associated with each value. The t-test was used. This test can be used to verify or reject the hypothesis that two observed results come from the same population. Only the random uncertainties are used in this test, but if the difference between means is not significant in this case, then it will certainly not be significant once systematic

Table 5.19 AIR: COMPARISON OF TWO RESULTS (μ/ρ in $m^2 kg^{-1}$)

		Measured directly			Deduced from N/O/A Measurements					
Kα	E (keV)	$\frac{\mu}{\rho}$	% SEOM	ν_{eff}	$\frac{\mu}{\rho}$	% SEOM	ν_{eff}	t^2_m	ν	$t^2_{95\%}$
Ti	4.508	5.409	0.38	11	5.386	0.57	6	0.39	11	4.7
Cr	5.411	3.150	0.25	14	3.176	0.21	14	6.35	27	4.2
Fe	6.400	1.900	0.19	17	1.906	0.34	8	0.65	13	4.7
Ni	7.472	1.198	0.23	8	1.196	0.18	12	0.03	16	4.5
Cu	8.041	0.9617	0.49	16	0.9681	0.17	11	1.64	19	4.4
Zn	8.631	0.7754	0.30	7	0.7798	0.15	26	2.86	10	5.0
Ge	9.876	0.5213	0.36	13	0.5215	0.21	33	0.01	22	4.3
Se	11.210	0.3589	0.28	11	0.3612	0.26	21	2.80	27	4.2
Rb	13.375	0.2174	0.25	7	0.2171	0.24	14	0.16	18	4.4
Zr	15.746	0.1390	0.59	9	0.1392	0.51	22	0.03	22	4.3
Mo	17.443	0.1061	0.89	9	0.1073	0.53	10	1.19	14	4.6
Ru	19.235	0.08343	1.00	15	0.08403	0.60	26	0.37	25	4.2
Pd	21.122	0.06733	0.94	19	0.06736	0.53	35	0.00	31	4.2
Cd	23.103	0.05613	0.87	9	0.05544	0.59	54	1.38	18	4.4
Sn	25.192	0.04698	1.00	29	0.04661	0.68	77	0.43	56	4.0

Table 5.20 CARBON DIOXIDE: COMPARISON OF TWO RESULTS (μ/ρ in $m^2 kg^{-1}$)

		Measured directly			Deduced from C/O Measurements					
Kα	E (keV)	$\frac{\mu}{\rho}$	% SEOM	ν_{eff}	$\frac{\mu}{\rho}$	% SEOM	ν_{eff}	t^2_m	ν	$t^2_{95\%}$
Ti	4.508	5.325	0.46	7	5.361	0.50	6	0.98	12	4.8
Cr	5.411	3.116	0.37	7	3.138	0.49	7	1.31	12	4.8
Fe	6.400	1.871	0.31	7	1.861	0.35	4	1.31	9	5.1
Ni	7.472	1.170	0.45	5	1.167	0.39	7	0.19	10	5.0
Cu	8.041	0.9399	0.26	4	0.9372	0.22	5	0.71	8	5.3
Zn	8.631	0.7590	0.22	6	0.7591	0.27	8	0.00	13	4.7
Ge	9.876	0.5070	0.44	7	0.5096	0.40	20	0.77	18	4.4
Se	11.210	0.3496	0.66	7	0.3491	0.51	10	0.03	14	4.6
Rb	13.375	0.2083	0.51	9	0.2075	0.39	10	0.36	17	4.5
Zr	15.746	0.1351	1.00	17	0.1336	0.46	10	0.93	22	4.3
Mo	17.443	0.1022	0.51	9	0.1022	0.35	12	0.00	16	4.5
Ru	19.235	0.08072	0.78	9	0.08077	0.78	20	0.00	24	4.3
Pd	21.122	0.06452	0.72	9	0.06428	0.53	22	0.17	19	4.4
Cd	23.108	0.05375	0.90	9	0.05315	0.75	32	0.92	22	4.3
Sn	25.192	0.04556	0.80	29	0.04505	0.80	32	0.99	60	4.0

errors are included.

If the two values obtained are x_1 and x_2 with standard errors of the mean of S_1 and S_2, with effective number of degrees of freedom ν_1 and ν_2 respectively then it can be shown that

$$t_m = \frac{|x_1 - x_2|}{\left(S_1^2 + S_2^2\right)^{\frac{1}{2}}}$$

is distributed according to the t-distribution with ν degrees of freedom, given by

$$\nu = \frac{\left(S_1^2 + S_2^2\right)^2}{S_1^4/\nu_1 + S_2^4/\nu_2}$$

The value of t_m^2 was compared with the 95% value of t^2 obtained from statistical tables. If the calculated value of t_m^2 is the smaller, then such a difference between the means could arise by chance more often than once in twenty times on the basis of the data available.

The results of this test for air and carbon dioxide are shown in Table 5.19 and 5.20. In only one case out of thirty (air at 5.411 keV) is t_m^2 larger than $t_{95\%}^2$, and in this particular case t_m^2 is smaller than $t_{99\%}^2$.

Hence the differences observed are believed to be notsignificant, and the results obtained are consistent.

This result indicates that the long-term stability and reproducibility of the measuring system is good.

Table 5.21 EXPERIMENTAL TEST FOR IN-SCATTERING

			With normal aperture			With reduced aperture					
Kα	E(keV)	Absorber	μ/ρ (m^2kg^{-1})	% SEOM	ν_{eff}	μ/ρ (m^2kg^{-1})	% SEOM	ν_{eff}	t_m^2	ν	$t^2_{95\%}$
Ni	7.472	Air	1.198	0.23	8	1.201	0.54	5	0.18	6	6.0
Zr	15.746	Argon	1.706	0.29	12	1.721	0.89	5	2.03	7	5.6
Sn	25.192	Argon	0.4368	0.76	17	0.4337	1.31	5	0.22	8	5.3

5.1.7 Investigation of in-scattering

In section 3.4.1.1 the possibility of some scattered photons being counted by the detector was considered, and rejected on theoretical grounds. During the measurement it was decided to check this conclusion experimentally. To do this a smaller aperture was placed before the entrance window of the gas tube to reduce the angle subtended at the fluorescent source by the entrance aperture of the gas tube. Using this reduced aperture three mass attenuation coefficients were measured using energy values at the low, medium and high regions of the range. Air was used at the energy of Ni $\overline{K\alpha}$ radiation and argon at Zr $\overline{K\alpha}$ and Sn $\overline{K\alpha}$. The results thus obtained were compared with those obtained with the normal aperture using the t-test as described in the previous section. The results are presented in Table 5.21.

From this it is clear that there is no evidence that the results using a smaller entrance aperture are significantly different from those with the normal aperture. This, therefore, provides experimental verification for the theoretical conclusions of section 3.4.1.1.

5.2 SOLIDS

The experimental procedure for measuring the mass attenuation coefficient for a solid absorber is simpler than that for gases. The solid samples used were mounted in a holder which could be manually inserted in the X-ray beam or removed from it. The samples themselves were of sufficient area to intercept completely the X-ray beam.

At each energy used, alternate readings of transmitted intensity with the absorber in and out of the beam were taken. Background count-rates were measured before the experiment and after each five readings subsequently. In the lower energy region using a silica absorber this procedure had to be modified slightly. Here the attenuation was very great even using the thinnest available silica sample. More time was devoted to measurement of background, and readings were taken in groups of three, measuring alternately the unattenuated, attenuated, and background count-rates. By either technique a series of values of $\ln \frac{I_o}{I}$, corrected for background, is obtained. A second small correction is made for air displaced out of the beam by the presence of the solid sample, i.e. for attenuation by an air column of thickness equal to that of the solid.

From the resultant corrected values of $\ln \frac{I_o}{I}$, the average $\left(\ln \frac{I_o}{I}\right)$, and the standard error of the mean, are calculated. The other contributions to total uncertainty are different for each solid sample used.

5.2.1 Magnesium

All of the sources of uncertainty are dealt with in section

Table 5.22 MAGNESIUM (μ/ρ in $m^2 kg^{-1}$; σ_{tot} in barns/atom)

Kα	E (keV)	$\frac{\mu}{\rho}$	σ_{tot}	% SEOM	ν_{eff}	% Syst. unc.	% 99% conf. limit
Ti	4.508	21.63	8732	0.48	10	0.11	1.63
Cr	5.411	12.86	5192	0.56	9	0.11	1.93
Fe	6.400	7.922	3198	0.44	8	0.11	1.59
Ni	7.472	5.048	2038	0.25	16	0.10	0.83
Cu	8.041	4.032	1628	0.21	14	0.10	0.73
Zn	8.631	3.270	1320	0.30	9	0.10	1.08
Ge	9.876	2.204	889.8	0.45	7	0.10	1.68
Se	11.210	1.496	604.0	0.37	8	0.10	1.34
Rb	13.375	0.8832	358.6	0.23	9	0.10	0.85
Zr	15.746	0.5485	221.4	0.39	13	0.10	1.27
Mo	17.443	0.4061	163.9	0.57	12	0.10	1.84
Ru	19.235	0.3087	124.6	0.76	11	0.10	2.46
Pd	21.122	0.2288	92.37	0.52	4	0.10	2.49
Cd	23.108	0.1791	72.31	0.51	4	0.10	2.45
Sn	25.192	0.1416	57.19	0.26	5	0.10	1.15

3.3.4.2. The area density of each individual magnesium foil, as measured, has a standard error of the mean of $\pm$ 0.5%. At all energy points, however, the magnesium absorber consisted of a composite sample containing several foils. The area density is therefore assumed to contribute an uncertainty of $\pm \frac{0.5}{\sqrt{n}}$ % to the random error, where n is the number of foils in the absorber. The SEOM of each individual foil has 4 degrees of freedom. Hence the SEOM for the composite sample will have 4 n degrees of freedom, as each foil contributes equally to the total uncertainty. The total random uncertainty is obtained by combining the contributions from counting statistics and from the area density measurement.

The systematic uncertainty is made up of contributions due to possible variations in thickness of the foils and to impurities in the sample. Allowing for the effects of sampling different parts of the foil, and for the conclusions of Appendix 2, an upper bound of $\pm$ 0.1% is allowed for thickness variation of a single foil. For a composite sample this reduces to $\pm \frac{0.1}{\sqrt{n}}$ %. An uncertainty of 0.1% is also allowed for impurities in the foil. Since corrections were applied for the iron, manganese and silicon impurities, the other trace contaminants are unlikely to contribute more than 0.1% uncertainty.

Experimental values for mass attenuation coefficient and total attenuation cross-section for magnesium, together with total random and systematic uncertainties and 99% confidence limits, are presented in Table 5.22.

Table 5.23 ALUMINIUM (μ/ρ in $m^2 kg^{-1}$; σ_{tot} in barns/atom)

Kα	E (keV)	$\frac{\mu}{\rho}$	σ_{tot}	% SEOM	ν_{eff}	% Syst. unc.	% 99% conf limit
Ti	4.508	25.54	11440	0.84	7	0.10	3.04
Cr	5.411	15.36	6884	0.59	16	0.07	1.79
Fe	6.400	9.392	4208	0.47	9	0.07	1.60
Ni	7.472	6.130	2746	0.36	9	0.05	1.22
Cu	8.041	5.004	2242	0.51	12	0.20	1.76
Zn	8.631	4.052	1815	0.46	12	0.20	1.61
Ge	9.876	2.723	1220	0.44	12	0.20	1.55
Se	11.210	1.874	839.6	0.58	6	0.20	2.35
Rb	13.375	1.102	493.9	0.24	9	0.20	0.98
Zr	15.746	0.6828	305.9	0.36	7	0.20	1.46
Mo	17.443	0.5041	225.9	0.26	7	0.20	1.12
Ru	19.235	0.3781	169.4	0.40	7	0.20	1.60
Pd	21.122	0.2898	129.8	0.28	8	0.20	1.14
Cd	23.108	0.2253	100.9	0.30	8	0.20	1.21
Sn	25.192	0.1770	79.31	0.41	6	0.20	1.72

5.2.2. Aluminium

As stated in section 3.3.4.2 the measurements on aluminium from 8.041 keV to 25.192 keV were made on samples supplied by the National Physical Laboratory, whilst those from 4.508 keV to 7.472 keV were made on thinner foils. The methods used for both types of sample were identical and the uncertainties in counting statistics were obtained from the results in the usual way. Other contributions to random and systematic uncertainty were different for the two samples.

For the thin foils, the area density was accurately measured and the standard error on the mean for this quantity was $\pm$ 0.4% with four degrees of freedom. If a sample consists of n such foils, the SEOM will be $\pm \frac{0.4}{\sqrt{n}}$ % with 4n degrees of freedom.

The systematic uncertainty was estimated as $\pm \frac{0.1}{\sqrt{n}}$ % for possible thickness variation. The impurity levels are so low that they contribute a negligible uncertainty.

For the larger aluminium sheets there is a random uncertainty of $\pm$ 0.2% on the area density, with four degrees of freedom. In cases where several sheets are used to make up an attenuating sample the total random uncertainty in area density and its associated number of degrees of freedom were calculated by the standard method (see Appendix 4).

As regards systematic uncertainties, the contribution for thickness variation of a single sheet is negligible. The measured upper bound of such variation is $\pm$ 0.0025 mm which, for the thinnest sheet, represents a percentage variation of $\pm$ 1.25%. From Appendix 3 this is shown to have a very small effect on measured attenuation coefficients. However an uncertainty of $\pm$ 0.2% for impurities is allowed.

Experimental values for mass attenuation coefficient and total

Table 5.24 SILICON DIOXIDE (μ/ρ in $m^2 kg^{-1}$)

Kα	E (keV)	$\frac{\mu}{\rho}$	% SEOM	ν_{eff}	Syst. unc.	99% conf. limit %
Cu	8.041	3.511	0.57	8	0.17	2.09
Zn	8.631	2.828	0.52	6	0.17	2.10
Ge	9.876	1.930	0.58	8	0.17	2.12
Se	11.210	1.322	0.61	9	0.17	2.15
Rb	13.375	0.7808	0.68	10	0.17	2.33
Zr	15.746	0.4826	0.77	7	0.14	2.34
Mo	17.443	0.3627	0.33	15	0.14	1.11
Ru	19.235	0.2759	0.60	7	0.14	2.24
Pd	21.122	0.2120	0.39	9	0.13	1.40
Cd	23.103	0.1639	0.71	6	0.13	2.76
Sn	25.192	0.1302	0.56	6	0.13	2.21

Table 5.25 SILICON (μ/ρ in $m^2 kg^{-1}$; σ_{tot} in barns/atom)

Kα	E (keV)	$\frac{\mu}{\rho}$	σ_{tot}	% SEOM	ν_{eff}	% Syst. unc.	% 99% conf limit
Cu	8.041	6.228	2905	0.69	8	0.21	2.53
Zn	8.631	5.012	2338	0.63	6	0.21	2.55
Ge	9.876	3.433	1601	0.70	8	0.21	2.56
Se	11.210	2.352	1097	0.74	9	0.21	2.62
Rb	13.375	1.390	648.3	0.82	10	0.21	2.81
Zr	15.746	0.8533	398.0	0.94	7	0.18	3.47
Mo	17.443	0.6397	298.4	0.41	16	0.18	1.38
Ru	19.235	0.4836	225.5	0.75	8	0.18	2.70
Pd	21.122	0.3694	172.3	0.50	10	0.16	1.75
Cd	23.108	0.2820	131.5	0.91	6	0.16	3.54
Sn	25.192	0.2210	103.1	0.76	7	0.16	2.82

attenuation cross-section for aluminium, together with the associated statistical parameters, are presented in Table 5.23.

5.2.3 Silicon Dioxide

The samples used were 0.5 mm slides of fused silica. Because of the high attenuation, it proved impossible to obtain any results below 8.041 keV. The experimental method adopted was that used for the metallic foils. In addition to random uncertainty arising from counting statistics, there is a contribution of $\pm \frac{0.5}{\sqrt{n}}$ % from the area density measurement, with 4 n degrees of freedom, where n is the number of slides making up the absorber.

The measured values of mass attenuation coefficient were corrected for a water content of 0.06% and OH content of 0.12%. However, an uncertainty of 0.1% to allow for impurities was added to an uncertainty of $\pm \frac{0.1}{\sqrt{n}}$ % for possible thickness variation to make up the total systematic uncertainty.

Experimental values of mass attenuation coefficient for silica, together with total random and systematic uncertainties and 99% confidence limits are presented in Table 5.24.

From these results the mass attenuation coefficient and total attenuation cross-section for silicon were calculated. The assumed composition was

$$\left(\frac{\mu}{\rho}\right)_{SiO_2} = 0.4674 \left(\frac{\mu}{\rho}\right)_{Si} + 0.5326 \left(\frac{\mu}{\rho}\right)_{O}$$

The values of $\left(\frac{\mu}{\rho}\right)_{O}$ used were those shown in Table 5.4. The total random and systematic uncertainties and the effective number of degrees of freedom were calculated from the values for silica and oxygen in the standard way.

The deduced values of mass attenuation coefficient and total attenuation cross-section for silicon together with these statistical parameters are shown in Table 5.25.

5.3 LIQUIDS

The experimental procedure for liquid measurements was similar to that for solids. An absorber consisting of two sheets of 0.79 mm Perspex, identical to the liquid cell windows, was made up. The "unattenuated" intensity was measured on the X-ray beam transmitted by this absorber. The attenuated beam was measured on transmission through the cell i.e. two windows plus the liquid sample. The ratio of these two intensities, corrected for background, is a direct measure of the attenuation due to the liquid alone. Alternate readings of unattenuated and attenuated intensity are taken. Background is measured at the beginning and after every five subsequent readings. At the lower energies used the background count-rate was determined after each pair of attenuated and unattenuated count-rates. From these results a series of values of $\ln \frac{I_o}{I}$ was obtained, and hence the mean value $\overline{\left(\ln \frac{I_o}{I}\right)}$ and its standard error of the mean were calculated.

Other contributions to the total random uncertainty come from the measurement of sample thickness and the value of liquid density used. For the former, a standard error of the mean of $\pm$ 0.1% with nine degrees of freedom was assumed, whilst for the latter a SEOM of 0.2%. with a very large number of degrees of freedom was used.

A contribution of $\pm$ 0.1% to the systematic uncertainty to allow for uncorrected impurities was made. Impurity levels of 0.1% ethanol and 0.2% water were corrected for, but even these maximum impurity levels result in only a 0.1% change in the value for tri-ethyl phosphate. Consequently an uncertainty of $\pm$ 0.1% is believed adequate. However, the main source of systematic uncertainty is due to window distortion.

Table 5.26 WATER: CHECK ON LIQUID CELL LENGTH

		Measured on water			Deduced from O/H values					
Kα	E (keV)	$\frac{\mu}{\rho}$ (m^2kg^{-1})	% SEOM	ν_{eff}	$\frac{\mu}{\rho}$ (m^2kg^{-1})	% SEOM	ν_{eff}	t_m^2	ν	$t^2_{95\%}$
Rb	13.375	0.2248	0.37	10	0.2229	0.42	9	3.88	18	4.4
Mo	15.746	0.1096	0.34	10	0.1103	0.38	9	3.14	18	4.4

Table 5.27 TRIETHYL PHOSPHATE (μ/ρ in $m^2 kg^{-1}$)

					%	
Kα	E (keV)	$\frac{\mu}{\rho}$	% SEOM	ν_{eff}	Syst. unc.	99% conf. limit
Se	11.210	0.7194	0.54	13	0.58	2.21
Rb	13.375	0.4253	0.33	29	0.58	1.49
Zr	15.746	0.2660	0.66	5	0.58	3.24
Mo	17.443	0.1986	0.43	7	0.58	2.09
Ru	19.235	0.1531	0.57	6	0.58	2.69
Pd	21.122	0.1202	0.41	10	0.27	1.57
Cd	23.103	0.09581	0.39	9	0.27	1.54
Sn	25.192	0.07843	0.44	7	0.27	1.81

Table 5.28 PHOSPHORUS (μ/ρ in $m^2 kg^{-1}$; σ_{tot} in barns/atom)

						%	
Kα	E (keV)	$\frac{\mu}{\rho}$	σ_{tot}	% SEOM	ν_{eff}	Syst. unc.	99% conf limit
Se	11.210	2.953	1519	0.30	14	0.86	3.24
Rb	13.375	1.731	890.4	0.51	36	0.87	2.26
Zr	15.746	1.057	543.7	1.00	5	0.90	4.93
Mo	17.443	0.7773	399.9	0.68	8	0.91	3.19
Ru	19.235	0.5808	298.7	0.96	8	0.94	4.17
Pd	21.122	0.4458	229.3	0.72	14	0.45	2.60
Cd	23.108	0.3420	175.9	0.77	18	0.47	2.69
Sn	25.192	0.2685	138.1	0.91	14	0.49	3.20

Even a small distortion of 0.05 mm will result in a 1% error when using a 5 mm liquid sample. The bounds of systematic uncertainty due to such distortion were estimated as $\pm$ 0.5% for the 5 mm cell and $\pm$ 0.17% for the 15 mm cell.

As an experimental check on these uncertainty values for liquid measurements one measurement on water was made using each cell. The result can be compared with the expected value on the basis of experimental results for oxygen and the hydrogen values of Storm and Israel (1970) using a t-test. The results of such a test are shown in Table 5.26. Neither pair of results shows a significant difference at the 95% significance level. This increases confidence that the postulated values of the various contributions to the total uncertainty have not been underestimated.

Experimental values of mass attenuation coefficient for tri-ethyl phosphate together with total random and systematic uncertainties and 99% confidence limits are shown in Table 5.27.

From these results, values for phosphorus may be deduced. The formula used was:

$$\left(\frac{\mu}{\rho}\right)_{(C_2H_5)_3PO_4} = 0.3956\left(\frac{\mu}{\rho}\right)_C + 0.0830\left(\frac{\mu}{\rho}\right)_H + 0.1700\left(\frac{\mu}{\rho}\right)_P + 0.3513\left(\frac{\mu}{\rho}\right)_O$$

Values of mass attenuation coefficient for carbon and oxygen and values of total uncertainties were taken from Tables 5.8 and 5.4, respectively. Storm and Israel's values for hydrogen were used, and a percentage standard error of the mean of $\pm$ 3% with a large number of degrees of freedom was assumed.

The deduced values of mass attenuation coefficient and total attenuation cross-section for phosphorus together with total random and systematic uncertainties and 99% confidence limits are shown in Table 5.28.

CHAPTER 6

TOTAL ATTENUATION CROSS-SECTION, PHOTOELECTRIC CROSS-SECTION AND THEIR VARIATION WITH ENERGY

6.1 EXPERIMENTAL VALUES OF PHOTOELECTRIC CROSS-SECTION

From the experimental values of total attenuation cross-section presented in the previous chapter, it is a simple matter to deduce values of the photoelectric cross-section. The total cross-section is a sum of three separate effects, the photoelectric effect, Compton (or incoherent) scattering, and Rayleigh (or coherent) scattering.

$$\sigma_{tot} = \tau_{pe} + \sigma_{C}^{bd} + \sigma_{R} \qquad \ldots\ldots (6.1)$$

In calculating the photoelectric cross-section τ_{pe}, values of the incoherent scattering cross-section σ_{C}^{bd}, and the coherent scattering cross-section σ_{R}, taken from Storm and Israel (1970) were used. The uncertainty in the deduced values of τ_{pe} is therefore no longer completely within the control of the experimenter, but depends on the uncertainty associated with the tabulated values of the scattering cross-sections. Storm and Israel estimate an uncertainty of $\pm$ 3% on their values of σ_{C}^{bd} and σ_{R} separately. In deriving the uncertainties on the quoted values of τ_{pe} it was assumed that both σ_{C}^{bd} and σ_{R} had random uncertainties corresponding to a percentage standard error of the mean of $\pm$ 3% with a large number of degrees of freedom. This may well overestimate the uncertainty especially as the sum $(\sigma_{C}^{bd} + \sigma_{R})$ is usually more precise than the individual components considered separately.

The values of the scattering cross-section tabulated by Storm and

Table 6.1 PHOTOELECTRIC CROSS-SECTION, τ_{pe} (barns/atom)

Kα	E (keV)	C	N	O	F	Ne	Mg	Al	Si	P	S	Cl	A
Ti	4.508	493.2	964.4	1685	2773	4206	8681	11390	-	-	24800	29750	37100
Cr	5.411	281.7	557.5	983.6	1592	2443	5148	6833	-	-	15040	18520	23240
Fe	6.400	163.8	328.7	579.4	956.3	1480	3159	4164	-	-	9416	11680	14610
Ni	7.472	100.6	202.1	359.2	595.3	915.1	2004	2707	-	-	6051	7526	9447
Cu	8.041	79.35	162.1	286.8	475.0	723.2	1597	2205	2863	-	4899	6182	7745
Zn	8.631	64.20	128.6	230.6	383.7	601.2	1291	1781	2299	-	3994	5012	6291
Ge	9.876	41.98	83.26	151.8	251.1	392.8	864.3	1190	1566	-	2714	3434	4285
Se	11.210	27.29	55.92	101.6	172.1	265.8	581.3	812.8	1067	1484	1848	2374	2972
Rb	13.375	15.57	31.57	57.05	98.37	154.7	339.2	471.3	622.8	861.0	1089	1410	1780
Zr	15.746	9.100	18.74	34.16	58.33	92.28	204.9	286.7	376.4	519.0	685.6	864.2	1096
Mo	17.443	6.420	13.54	24.59	42.56	66.37	148.8	208.2	278.9	377.4	497.6	657.2	814.1
Ru	19.235	4.761	9.800	18.01	31.40	48.05	110.7	153.3	207.8	278.1	372.0	477.6	606.5
Pd	21.122	3.456	7.210	13.10	22.98	35.76	79.57	115.1	155.9	210.4	276.5	365.0	452.4
Cd	23.103	2.562	5.350	9.750	17.13	26.62	60.72	87.04	116.2	158.4	210.4	279.6	349.3
Sn	25.192	1.920	3.994	7.330	12.78	20.02	46.12	66.14	88.65	122.0	163.6	213.2	267.2

Table 6.2 PHOTOELECTRIC CROSS-SECTION: PERCENTAGE STANDARD ERROR OF THE MEAN

Kα	E (keV)	C	N	O	F	Ne	Mg	Al	Si	P	S	Cl	A
Ti	4.508	0.70	0.90	0.57	0.31	0.42	0.48	0.84	-	-	0.31	0.46	0.74
Cr	5.411	0.77	0.23	0.55	0.38	0.39	0.57	0.59	-	-	0.23	0.28	0.47
Fe	6.400	0.39	0.57	0.41	0.20	0.41	0.45	0.43	-	-	0.69	0.30	0.30
Ni	7.472	0.49	0.25	0.46	0.27	0.56	0.26	0.37	-	-	0.56	0.30	0.28
Cu	8.041	0.49	0.30	0.27	0.34	0.58	0.22	0.52	0.70	-	0.32	0.34	0.33
Zn	8.631	0.31	0.28	0.32	0.24	0.38	0.31	0.47	0.64	-	0.40	0.28	0.22
Ge	9.876	1.18	0.39	0.48	0.37	0.42	0.47	0.46	0.72	-	0.29	0.38	0.22
Se	11.210	0.84	0.50	0.65	0.40	0.74	0.40	0.60	0.76	0.82	0.32	0.42	0.21
Rb	13.375	1.38	0.63	0.57	0.94	0.73	0.28	0.28	0.86	0.53	0.54	0.35	0.26
Zr	15.746	1.77	1.32	0.73	0.51	0.79	0.46	0.41	1.00	1.05	0.89	0.66	0.31
Mo	17.443	2.34	1.57	0.79	0.80	0.86	0.67	0.34	0.47	0.73	0.90	0.75	0.64
Ru	19.235	2.83	1.92	1.49	0.98	1.04	0.90	0.50	0.84	1.04	0.81	0.69	0.34
Pd	21.122	3.64	2.21	1.41	1.25	1.39	0.69	0.42	0.60	0.81	0.90	0.57	0.55
Cd	23.103	4.76	2.31	2.04	1.58	1.27	0.73	0.40	1.07	0.89	0.80	0.73	0.89
Sn	25.192	6.14	3.72	2.55	1.88	1.63	0.60	0.65	0.95	1.07	0.89	1.09	0.84

Table 6.3 RANDOM UNCERTAINTY ON τ_{pe}: EFFECTIVE NUMBER OF DEGREES OF FREEDOM

Kα	E (keV)	C	N	O	F	Ne	Mg	Al	Si	P	S	Cl	A
Ti	4.503	5	5	6	6	7	10	7	-	-	5	6	4
Cr	5.411	7	5	7	7	6	9	16	-	-	7	5	6
Fe	6.400	4	7	4	7	5	8	9	-	-	8	7	7
Ni	7.472	19	7	7	8	6	17	9	-	-	6	7	7
Cu	8.041	14	10	6	9	7	15	12	8	-	7	4	5
Zn	8.631	20	33	9	9	4	9	12	6	-	5	6	8
Ge	9.876	19	34	21	8	5	7	12	8	-	8	6	15
Se	11.210	17	26	12	9	7	9	6	9	14	7	6	16
Rb	13.375	17	42	18	7	5	15	13	10	37	6	5	7
Zr	15.746	36	37	22	28	17	18	9	7	5	7	6	13
Mo	17.443	92	22	65	17	12	15	14	20	8	7	5	12
Ru	19.235	>200	58	30	19	13	13	11	8	8	6	5	16
Pd	21.122	>200	163	115	20	12	6	24	13	15	5	13	19
Cd	23.193	>200	>200	114	22	20	8	30	6	20	13	12	12
Sn	25.192	>200	>200	131	28	57	61	18	9	16	18	11	18

Table 6.4 PHOTOELECTRIC CROSS-SECTION: PERCENTAGE TOTAL SYSTEMATIC UNCERTAINTY

Kα	E (keV)	C	N	O	F	Ne	Mg	Al	Si	P	S	Cl	A
Ti	4.508	0.18	0.24	0.23	0.11	0.42	0.11	0.10	-	-	0.10	0.06	0.06
Cr	5.411	0.19	0.18	0.23	0.47	0.23	0.11	0.07	-	-	0.10	0.06	0.06
Fe	6.400	0.14	0.19	0.16	0.28	0.23	0.12	0.07	-	-	0.10	0.06	0.06
Ni	7.472	0.16	0.16	0.16	0.24	0.15	0.11	0.06	-	-	0.41	0.44	0.53
Cu	8.041	0.17	0.16	0.13	0.24	0.15	0.11	0.21	0.22	-	0.39	0.35	0.53
Zn	8.631	0.19	0.17	0.14	0.21	0.12	0.11	0.21	0.22	-	0.32	0.30	0.42
Ge	9.876	0.23	0.18	0.16	0.22	0.12	0.12	0.22	0.22	-	0.25	0.23	0.30
Se	11.210	0.31	0.22	0.19	0.23	0.13	0.13	0.22	0.23	0.89	0.21	0.18	0.25
Rb	13.375	0.46	0.32	0.27	0.28	0.16	0.16	0.24	0.24	0.92	0.22	0.16	0.18
Zr	15.746	0.71	0.46	0.41	0.38	0.21	0.20	0.27	0.23	0.97	0.22	0.18	0.17
Mo	17.443	0.96	0.60	0.54	0.46	0.27	0.25	0.30	0.25	1.00	0.24	0.19	0.18
Ru	19.235	1.27	0.79	0.71	0.56	0.35	0.31	0.34	0.28	1.06	0.24	0.21	0.20
Pd	21.122	1.71	1.03	0.95	0.73	0.44	0.40	0.39	0.30	0.56	0.28	0.24	0.20
Cd	23.108	2.27	1.37	1.26	0.91	0.57	0.50	0.46	0.35	0.62	0.33	0.25	0.23
										0.69	0.39	0.31	0.27

Figure 6.1 VARIATION OF PHOTOELECTRIC CROSS-SECTION, τ_{pe} WITH ENERGY FOR CARBON, OXYGEN, NEON, ALUMINIUM, SULPHUR AND ARGON

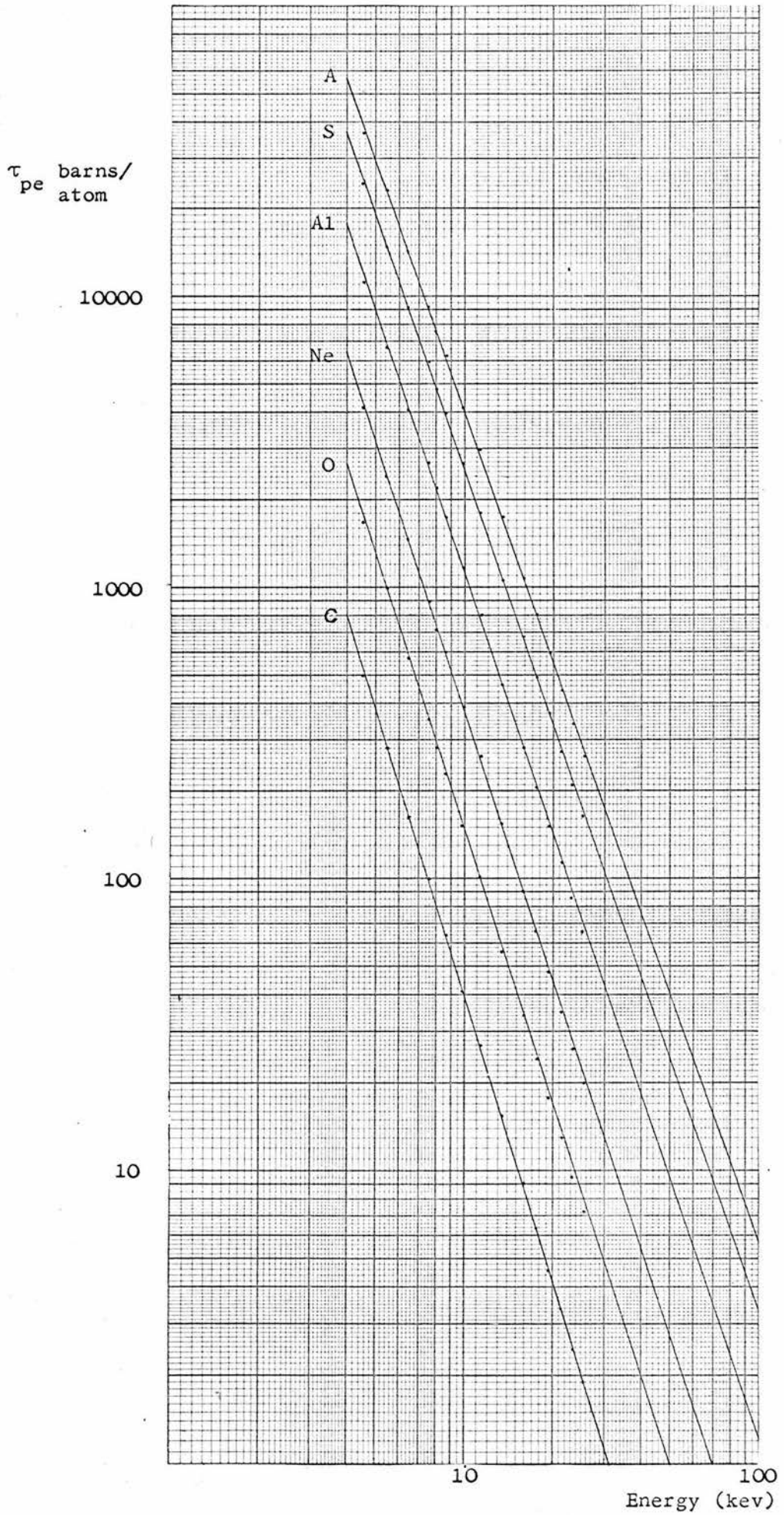

Table 6.5 COEFFICIENTS OF LINEAR REGRESSION FIT (ON LOG-LOG SCALES) TO OBSERVED PHOTOELECTRIC CROSS-SECTION AND ENERGY DATA

$\tau_{pe} = AE^{b}$

Attenuating element	A	b	Correlation coefficient
C	66960	-3.2337	-0.9999
N	123800	-3.1947	-0.9999
O	208200	-3.1665	-0.9999
F	315000	-3.1207	-0.9999
Ne	474500	-3.1088	-0.9999
Mg	918000	-3.0563	-0.9998
Al	1123000	-3.0065	-0.9998
Si	1619000	-3.0349	-0.9999
P	2586000	-3.0884	-0.9999
S	2182000	-2.9352	-0.9998
Cl	2469000	-2.8872	-0.9998
A	3090000	-2.8866	-0.9998

Israel correspond to integral values of incident photon energy. These were interpolated graphically to obtain values at the energies used in the measurements. The accuracy to which this can be done depends on the fineness of scale division on the graphs. A contribution due to this limit of reading was added to the systematic uncertainty in τ_{pe}.

Values of photoelectric cross-section, τ_{pe}, are presented in Table 6.1. The percentage standard error of the mean, its associated effective number of degrees of freedom, and the percentage systematic uncertainty are shown in Tables 6.2, 6.3 and 6.4 respectively.

From these tables it can be seen that over most of the range the percentage standard error of the mean is still less than 1%, as is the percentage systematic uncertainty. An appreciable increase in the uncertainties arises at higher energies for the lowest atomic number elements. This is not surprising since at these points, scattering is the major contribution to total cross-section.

6.2 LINEAR REGRESSION

In section 2.3 semi-empirical work on mass attenuation coefficients and total attenuation cross-sections was discussed. Many workers have shown that the relationship between log E and log τ_{pe} is linear to a high degree of accuracy.

Figure 6.1 shows the variation of τ_{pe} with E for C, O, Ne, Al, S and A using the results of Table 6.1. Clearly the relationship between these parameters on a log-log scale is almost linear. The coefficients of a linear regression fit to the experimental data are shown in Table 6.5, together with the correlation coefficient for the fit. However, it is now well-known that although the log of the photoelectric cross-section

Figure 6.2 VARIATION WITH ENERGY OF δ (EQUATION 6.3) FOR OXYGEN

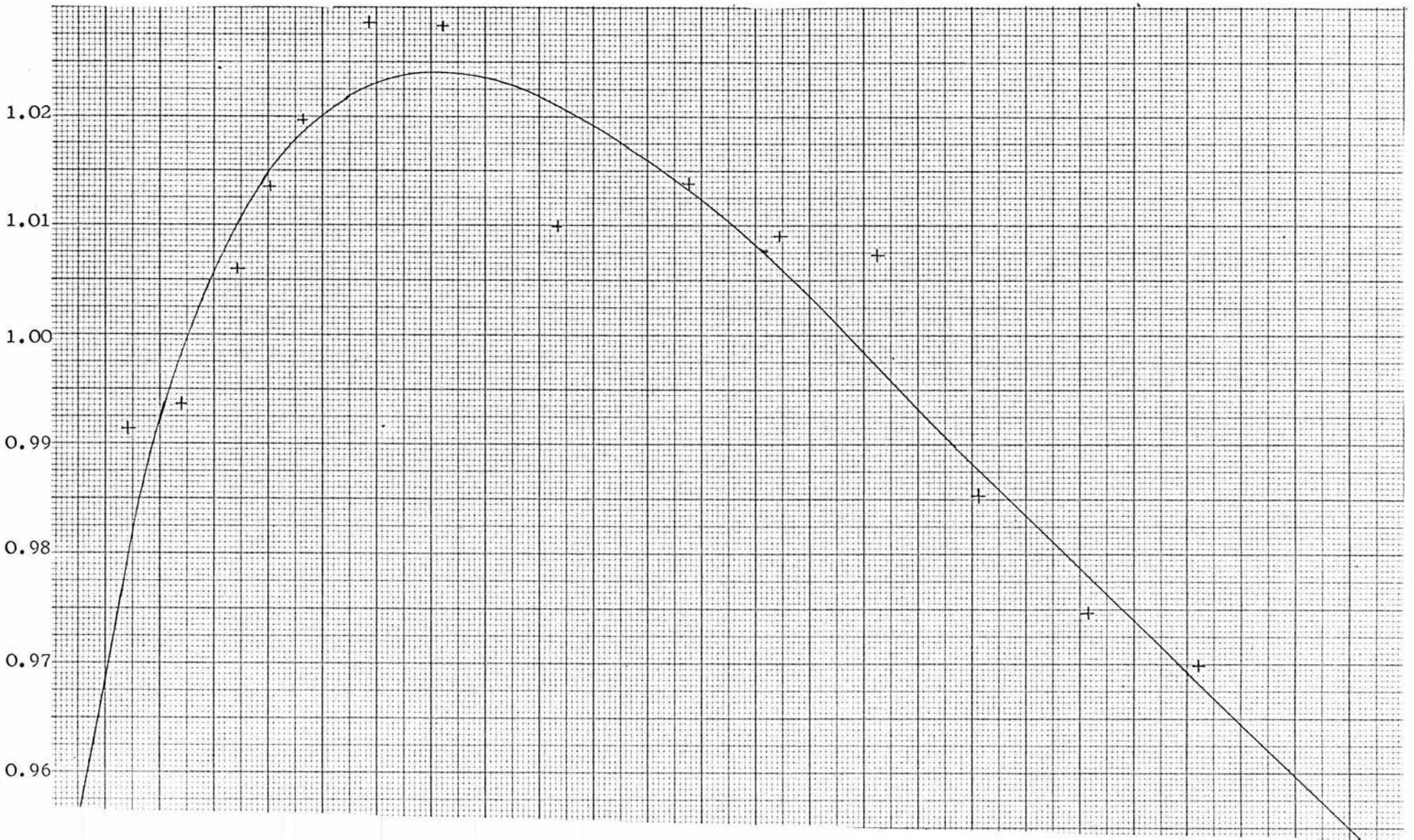

Figure 6.4 VARIATION WITH ENERGY OF δ(EQUATION 6.3) FOR ARGON

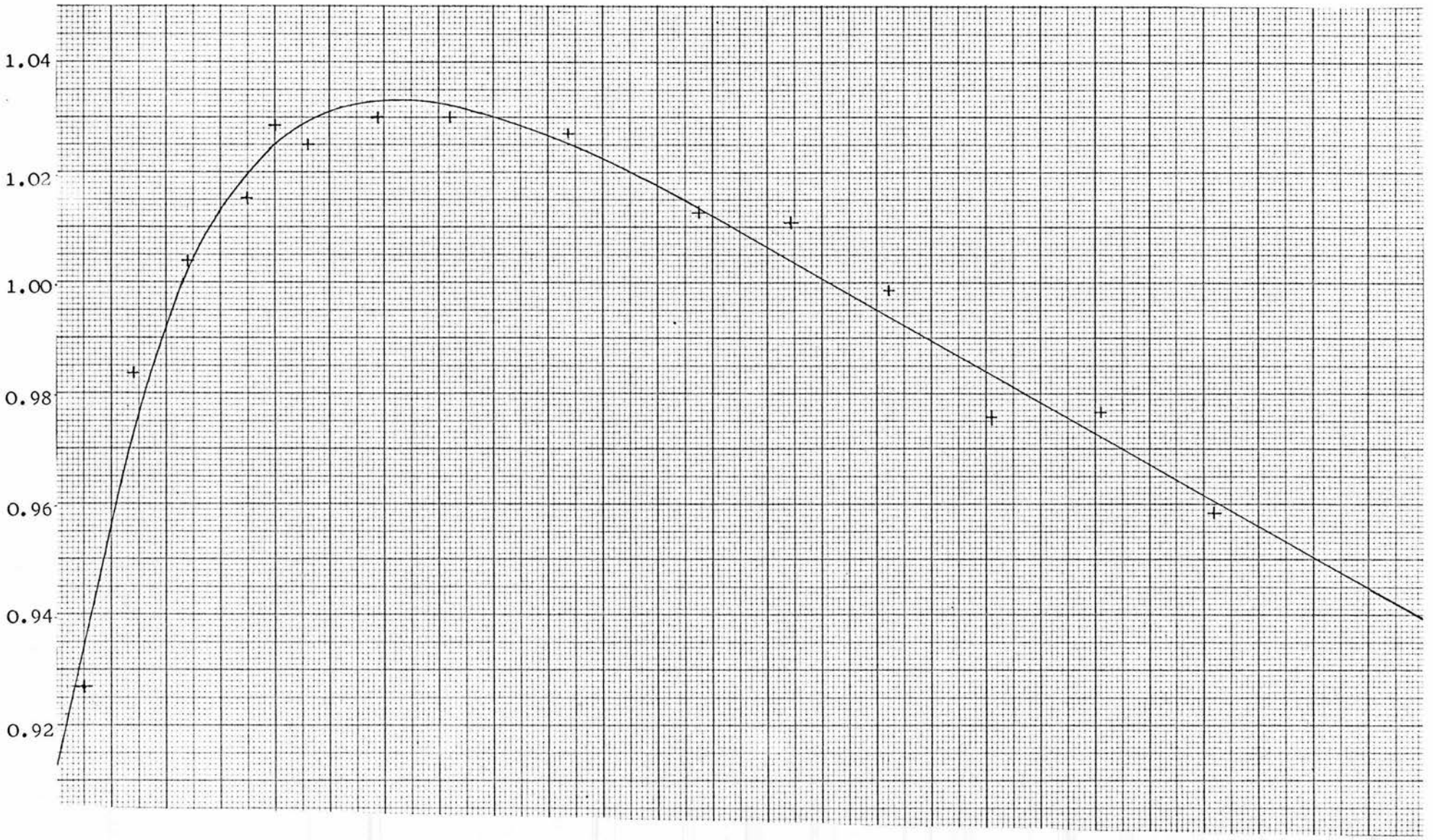

varies almost linearly with log E in the region between absorption edges, it takes a lower value than that predicted from linear behaviour at energies just above the absorption edge. This is reflected in figure 6.1 by a tendency for the experimental points to be rather lower than the best-fit line at the low energy end. This tendency is most marked for the higher atomic number materials, since the lowest energy used (4.508 keV) is much closer to the K-edge than in the case of the lower atomic number elements. In general, however, a plot on log-log axes is not a particularly sensitive test of the experimental data.

A much more sensitive test was applied. Using a PDP-12 computer, a linear regression fit for $\ln \tau_{pe}$ with $\ln E$ was obtained:

$$\ln \tau_{pe} = a + b \ln E \qquad \ldots\ldots(6.2)$$

Using the two best-fit parameters a and b, the predicted values $(\tau_{pe})_{predicted}$, were calculated. The deviations, δ, from the straight-line are given by:

$$\delta = (\tau_{pe})_{experimental} \Big/ (\tau_{pe})_{predicted} \qquad \ldots\ldots(6.3)$$

A graph of δ against Energy is then drawn. Figures 6.2, 6.3 and 6.4 show such graphs for oxygen, aluminium and argon respectively. Similar graphs were obtained for all the elements used. The smooth behaviour of the very sensitive parameter, δ, on all these graphs is good evidence for the reliability of the measured data. The trend shown by these deviations also indicates the expected decrease in τ_{pe}, relative to linear behaviour, as the K-edge is approached.

6.3 SMOOTHING AND INTERPOLATION OF PHOTOELECTRIC CROSS-SECTION DATA:

The work described above provides further indication that, at the level of accuracy required, a linear fit on log-log axes is inadequate to describe the relationship between τ_{pe} and energy, or to interpolate τ_{pe} at intermediate energy values. Consider for example the sign of the deviation of $(\ln \tau_{pe})_{oxygen}$ from the best-fit straight line:

\- - - + + + + + + + + + - - -

The pattern of these deviations shows that a straight-line is unable to describe the relationship adequately.

A higher-order fit is required. Clearly a compromise must be found. For if too low an order of polynomial fit is used it will be an inadequate fit to the data, whilst if the fit is of too high an order no smoothing of the results will be achieved. A cubic polynomial was chosen to fit the relationship of $\ln \tau_{pe}$ and $\ln E$:

$$\ln \tau_{pe} = \sum_{i=0}^{3} C_i (\ln E)^i \qquad .....(6.4)$$

This is the order of fitting which has been used by McMaster et al. (1969) and Veigele et al. (1971) in their compilation work. The sign of the deviation of $(\ln \tau_{pe})_{oxygen}$ from the best-fit cubic is:

\- + - - - + + + - + + + - - +

This is much more like the random arrangement of deviations expected and suggests that the level of fitting is adequate.

The experimental values of photoelectric cross-section for all the elements used were fitted to a cubic polynomial of the form of equation 6.4 using a curve-fitting routine available from the Edinburgh

Table 6.6 CUBIC-FIT COEFFICIENTS FOR LN τ_{pe} /LN E CURVE FITTING

Element	C_o	C_1	C_2	C_3
C	10.8327	-3.02389	-0.0214286	-0.00597454
N	11.2975	-2.80492	-0.0905506	0.00257002
O	11.7734	-2.74711	-0.0910907	0.00106096
F	12.7722	-3.47063	0.235715	-0.0439051
Ne	12.9900	-3.25081	0.166515	-0.0369001
Mg	13.0588	-2.42438	-0.160546	0.00786803
Al	12.9147	-1.93926	-0.336985	0.0310278
Si	14.4133	-3.39317	0.220523	-0.0380660
P	13.1703	-1.30676	-0.658478	0.0305336
S	13.7704	-2.07261	-0.270371	0.0245366
Cl	13.6404	-1.72015	-0.387025	0.0389175
A	13.8830	-1.76300	-0.360370	0.0341723

Regional Computing Centre. The values for the coefficients C_i (i = 0, 1, 2, 3) are shown in Table 6.6.

Using these cubic-fit coefficients it is possible to obtain smoothed values of τ_{pe} at the Kα energies used, or to interpolate at different energies. Extrapolation beyond the limits of the energy range is likely to be much less reliable than interpolation.

As a result of the smoothing procedure, many of the uncertainties which were systematic as regards their effect on a single experimental value are now randomised and reduced. For example the systematic uncertainties in the gas measurements due to pressure and temperature readings, and those in the solid measurements due to variation in sample thickness, are randomised, since their effects are likely to affect different values in different senses. In fact the only important effects which remain systematic are those due to sample impurity, and deviations from the ideal gas laws (in the case of gaseous absorbers).

The value of the random uncertainty on smoothed or interpolated results can be calculated from the scatter of the experimental points about the cubic best-fit curve. The theoretical basis of this is discussed in general terms in Appendix 5. The results of this appendix relate to the particular situation in question as follows: the experimental work provides a set of pairs of values of photoelectric cross-section τ_{pe} and energy E, ($(\tau_{pe})_i$, E_i). The logarithm of both variables is taken to give a series of co-ordinate pairs ($(\ln \tau_{pe})_i$; $(\ln E)_i$). These points are then fitted to a cubic polynomial. This enables $\ln \tau_{pe}$ to be expressed as a function of ln E, or, simply as a function of E.

The residuals, v_i^2, (i.e. the squares of the differences between

the experimental value and that predicted by the cubic curve) are summed. A measure of the variance of the original individual values of $\ln \tau_{pe}$ is given by σ^2, where

$$\sigma^2 = \frac{\sum v_i^2}{n - 4} \qquad \ldots\ldots (6.5)$$

n being the number of experimental values.

Using this value of σ^2, the variance of a predicted value of $\ln \tau_{pe}$ at any value of energy E can be predicted. As $\ln \tau_{pe}$ itself is a function of energy E it is to be expected that var $\left[\ln \tau_{pe}\right]$ will also be energy dependent. The situation is analogous to that of equation A5.13. The independent variable x in that equation is replaced by the independent variable ln E in the present situation. $(\ln E)_i$ (i = 1 to n) correspond to the n values of energy at which measurements were made, and $\overline{\ln E}$ is the mean of these values of ln E. The dependent variable u(x) of equation A5.13 is here replaced by the dependent variable $\ln \tau_{pe}$, which is a function of ln E, and hence of E. The variance in the predicted value of $\ln \tau_{pe}$ at any energy value E is given by:

$$\text{var}\left[\ln \tau_{pe}(E)\right] = \frac{\sigma^2}{n}\left[1 + (\ln E - \overline{\ln E})^2 \frac{n}{\sum_i \left((\ln E_i) - \overline{\ln E}\right)^2}\right] \qquad \ldots\ldots (6.6)$$

From the variance of $\ln \tau_{pe}$, the variance of τ_{pe} can be calculated. Consider the law of propagation of error, applied to the functional relationship

$$y = \exp(x) \qquad \ldots\ldots (6.7)$$

Then $\overline{\delta y^2} = \left(\frac{dy}{dx}\right)^2 \overline{\delta x^2}$

Table 6.7 UNCERTAINTIES IN SMOOTHED/INTERPOLATED VALUES OF PHOTOELECTRIC CROSS-SECTION

		as percentage	
Attenuating element	SEOM	Systematic uncertainty	99% confidence limits
C	0.41	0.10	1.17
N	0.31	0.08	0.87
O	0.34	0.05	0.92
F	0.30	0.10	0.87
Ne	0.35	0.05	0.95
Mg	0.41	0.10	1.16
Al	0.36	0.05	0.98
Si	0.47	0.10	1.31
P	0.26	0.10	0.80
S	0.37	0.08	1.03
Cl	0.44	0.05	1.20
A	0.29	0.05	0.80

$$= \left[\exp(x)\right]^2 \overline{\delta x^2}$$

So $$\frac{\overline{\delta y^2}}{y^2} = \overline{\delta x^2} \qquad \ldots\ldots (6.8)$$

Hence since $\tau_{pe} = \exp(\ln \tau_{pe})$

it follows that $$\frac{\overline{\delta \tau_{pe}^2}}{\tau_{pe}^2} = \overline{\delta (\ln \tau_{pe})^2} \qquad \ldots\ldots (6.9)$$

i.e. the fractional variance of τ_{pe} is equal to the actual variance in $\ln \tau_{pe}$.

From the form of equation 6.6 it is clear that the variance of $\ln \tau_{pe}$, and hence of τ_{pe}, is a function of energy. In view of the approximations already used in applying the theory of linear regression fitting to the case of a cubic fit it would be unjustified to apply equation 6.6 rigorously. Instead the maximum value within the range, of the bracketed term, will be used, and the same variance associated with all points of the energy domain. This should overestimate the uncertainty.

Using equations 6.6 and 6.9 values for the standard error of the mean for smoothed or predicted values of photoelectric cross-section using a cubic polynomial are calculated from observed residues. The results are shown in Table 6.7. The percentage standard error of the mean is quoted; the effective number of degrees of freedom is assumed large. The total percentage systematic uncertainties shown are those due to impurities and deviations from ideal gas laws only, since the other effects are randomised in the smoothing process.

Table 6.8 SMOOTHED VALUES OF PHOTOELECTRIC CROSS-SECTION τ_{pe} (barns/atom)

Kα	E (keV)	C	N	O	F	Ne	Mg	Al	Si	P	S	Cl	A
Ti	4.508	497.8	969.8	1692	2781	4215	8698	11340	-	-	24840	29890	37340
Cr	5.411	280.7	553.2	973.1	1592	2436	5144	6830	-	-	15040	18400	23000
Fe	6.400	165.2	328.7	582.2	954.4	1470	3151	4239	-	-	9398	11640	14580
Ni	7.472	101.1	202.6	360.9	594.9	921.0	1993	2708	-	-	6051	7571	9487
Cu	8.041	80.00	160.8	287.3	475.3	737.2	1601	2134	2860	-	4902	6157	7720
Zn	8.631	63.80	123.6	230.4	382.7	594.3	1295	1772	2317	-	3995	5037	6318
Ge	9.876	41.41	83.92	151.0	252.9	393.6	862.0	1187	1551	-	2699	3424	4298
Se	11.210	27.52	56.03	101.2	170.9	266.4	585.7	810.4	1063	1434	1860	2373	2980
Rb	13.375	15.52	31.79	57.68	98.60	153.8	340.0	473.5	625.0	860.4	1102	1415	1778
Zr	15.746	9.107	18.75	34.15	58.94	91.95	204.5	286.6	381.1	518.7	676.2	873.9	1097
Mo	17.443	6.507	13.44	24.53	42.54	66.35	148.3	208.8	278.8	377.7	496.9	644.6	808.9
Ru	19.235	4.712	9.766	17.85	31.07	48.43	108.9	154.0	206.3	279.1	369.7	481.5	603.7
Pd	21.122	3.455	7.185	13.15	22.94	35.73	80.90	115.0	154.4	209.2	278.4	363.9	455.8
Cd	23.103	2.562	5.345	9.792	17.09	26.61	60.72	86.74	116.6	158.8	211.8	278.0	347.7
-	25.139	1.920	4.019	7.368	12.85	19.99	46.03	66.13	88.88	122.0	162.8	214.5	268.0

Table 6.9 INTERPOLATED PHOTOELECTRIC CROSS-SECTIONS, τ_{pe} (barns/atom)

E(keV)	C	N	O	F	Ne	Mg	Al	Si	P	S	Cl	A
4	723.1	1397	2423	4011	6034	12210	15700	-	-	34300	40770	50390
5	359.8	705.8	1237	2026	3039	6463	8519	-	-	18710	22730	28410
6	202.6	401.3	709.7	1162	1786	3808	5098	-	-	11270	13900	17390
7	124.4	248.5	441.7	726.1	1122	2419	3274	-	-	7290	9085	11380
8	81.31	163.4	292.0	482.8	748.7	1626	2217	2904	-	4974	6247	7832
9	55.80	112.7	202.1	336.5	523.1	1142	1565	2046	-	3538	4470	5608
10	39.78	80.66	145.2	243.4	378.8	829.9	1143	1495	-	2602	3304	4147
12	22.08	45.05	81.52	138.4	215.7	475.2	659.2	866.3	1203	1521	1946	2444
15	10.68	21.95	39.93	68.73	107.2	238.0	332.9	441.7	603.0	782.2	1009	1267
20	4.141	8.595	15.72	27.39	42.68	96.23	136.3	182.9	247.5	328.5	428.5	537.1
25	1.970	4.122	7.556	13.18	20.50	47.18	67.74	91.06	124.9	166.6	219.5	274.2

Smoothed values of photoelectric cross-section at the fifteen energy points used are tabulated in Table 6.8. Interpolated values at a selection of integral energies are shown in Table 6.9. The uncertainties associated with all these values are those stated in Table 6.7.

6.4 SMOOTHING AND INTERPOLATION OF TOTAL ATTENUATION CROSS-SECTION DATA

It might now be supposed that the easy way to re-synthesise smoothed values of total attenuation cross-section would be to add the scattering contribution back on to the smoothed photoelectric cross-sections derived above. However, because of the 3% uncertainty associated with the scattering data this procedure can result in values of σ_{tot} which have larger uncertainties than the original measured values as presented in Chapter 5. In general terms, the uncertainty associated with a final value of σ_{tot} arrived at by subtracting the scattering contribution from a measured value, smoothing the resultant photoelectric cross-section, and re-adding the same scattering contribution is not straight forward to calculate. Clearly since the same numerical value of the scattering term is firstly subtracted and then re-added, the uncertainties involved in these two operations are not independent, and the normal rules for combining independent uncertainties are invalid.

Consider a measured total cross-section T from which a scattering cross-section S is subtracted to leave a photoelectric cross-section P. This is then smoothed to give a final photoelectric cross-section P_f. Finally the scattering is added again and the resultant value of the total cross-section is T_f.

Table 6.10 A HYPOTHETICAL EXAMPLE SHOWING HOW SMOOTHED σ_{tot} VALUES DERIVED VIA τ_{pe} CAN BE LESS ACCURATE THAN UNSMOOTHED VALUES

Variable	True value	Measured value	Uncertainty	Actual er
T	100	100.5	$\pm$ 1.0	+ 0.5
S	50	51.0	$\pm$ 1.5	+ 1.0
P(= T - S)	50	49.5	$\pm$ 1.8	- 0.5
P_f	50	49.8	$\pm$ 0.4	- 0.2
T_f(= P_f + S)	100	100.8	$\pm$ 1.0	+ 0.8

Table 6.11 CUBIC-FIT COEFFICIENTS FOR LN σ_{tot}/LN E CURVE FITTING

Element	C_o	C_1	C_2	C_3
C	9.07725	-0.117237	-1.63132	0.300014
N	9.56238	-0.0411333	-1.55448	0.266433
O	10.2122	-0.308131	-1.35233	0.221306
F	11.4510	-1.44082	-0.793568	0.132426
Ne	11.8148	-1.45704	-0.735530	0.116017
Mg	12.5462	-1.62814	-0.570144	0.0798676
Al	12.4831	-1.27077	-0.680182	0.0913124
Si	13.0976	-1.71556	-0.494462	0.0661637
P	12.2190	-0.115059	-1.16435	0.154863
S	13.5612	-1.75023	-0.435781	0.0540207
Cl	13.4812	-1.46918	-0.518934	0.0630565
A	13.7504	-1.55247	-0.471403	0.0546040

Table 6.12 UNCERTAINTIES IN SMOOTHED/INTERPOLATED VALUES OF TOTAL ATTENUATION CROSS-SECTION

		as percentage	
Attenuating element	SEOM	Systematic uncertainty	99% confidence limits
C	0.34	0.10	0.98
N	0.19	0.08	0.56
O	0.34	0.05	0.92
F	0.30	0.10	0.87
Ne	0.40	0.05	1.08
Mg	0.32	0.10	0.92
Al	0.34	0.05	0.94
Si	0.41	0.10	1.15
P	0.24	0.10	0.72
S	0.33	0.08	0.94
Cl	0.35	0.05	0.96
A	0.24	0.05	0.67

Then clearly $$P = T - S \qquad \ldots\ldots (6.10)$$

$$\delta P = \left(\frac{\partial P}{\partial T}\right)_S \delta T + \left(\frac{\partial P}{\partial S}\right)_T \delta S$$

$$= \delta T - \delta S \qquad \ldots\ldots (6.11)$$

After smoothing, the uncertainty in P_f is given by δP_f. Let us postulate that smoothing reduces the magnitude of δP, i.e.

$$\delta P_f = \alpha \delta P$$

$$\text{where } |\alpha| < 1 \qquad \ldots\ldots (6.12)$$

Then since

$$T_f = P_f + S$$

$$\delta T_f = \delta P_f + \delta S$$

$$= \alpha \delta P + \delta S$$

$$= \alpha \delta T + (1 - \alpha)\, \delta S \qquad \ldots\ldots (6.13)$$

Equation 6.13 is now squared and the average is taken.

Since T and S are independent ($\overline{\delta T\, \delta S} = 0$) it follows that:

$$\overline{\delta T_f^2} = \alpha^2\, \overline{\delta T^2} + (1 - \alpha)^2\, \overline{\delta S^2} \qquad \ldots\ldots (6.14$$

Hence if the uncertainty in the scattering term is comparable with that in the original measured total cross-section, this procedure will fail to improve that uncertainty. To illustrate this by a hypothetical example consider the situation shown in Table 6.10.

In view of this, better results will be achieved by fitting the measured values of total attenuation cross-section to a polynomial on log-log scales and proceeding by the same method as was used to smooth the photoelectric cross-section data. Table 6.11 shows values of the cubic-fit coefficients for fitting $\ln \sigma_{tot}$ to $\ln E$. The uncertainties associated with smoothed and interpolated values of σ_{tot} were calculated as described for the case of photoelectric data in section 6.3. The results are presented in Table 6.12. Smoothed values of σ_{tot} at the

Table 6.13 SMOOTHED VALUES OF TOTAL ATTENUATION CROSS-SECTION, σ_{tot} (barns/atom)

Kα	E (keV)	C	N	O	F	Ne	Mg	Al	Si	P	S	Cl	A
Ti	4.508	505.7	977.8	1701	2791	4226	8728	11370	-	-	24880	29950	37430
Cr	5.411	290.3	569.0	996.6	1625	2481	5199	6891	-	-	15120	18480	23110
Fe	6.400	173.7	341.6	601.3	981.4	1507	3198	4292	-	-	9473	11720	14670
Ni	7.472	108.2	212.6	375.0	614.4	946.9	2029	2749	-	-	6112	7634	9562
Cu	8.041	86.64	169.9	299.7	492.1	759.2	1633	2221	2899	-	4956	6216	7788
Zn	8.631	70.12	137.0	241.4	397.4	613.4	1323	1806	2358	-	4045	5091	6381
Ge	9.876	47.30	91.43	160.5	265.1	409.1	886.0	1215	1588	-	2742	3472	4353
Se	11.210	33.13	63.08	109.9	181.8	280.0	607.0	835.5	1094	1519	1898	2415	3028
Rb	13.375	23.79	38.40	65.30	108.5	166.1	358.6	495.5	650.0	889.6	1134	1452	1819
Zr	15.746	14.05	24.97	41.30	68.24	103.5	221.1	306.2	402.3	543.5	703.9	905.8	1133
Mo	17.443	11.24	19.40	31.85	51.42	77.35	163.6	226.9	298.1	400.2	522.1	673.8	841.3
Ru	19.235	9.245	15.46	24.83	39.50	58.87	123.0	170.7	224.2	299.7	392.6	508.0	633.0
Pd	21.122	7.814	12.62	19.78	30.90	45.58	93.86	130.3	171.0	228.1	299.1	388.0	482.3
Cd	23.103	6.772	10.54	16.08	24.58	35.84	72.57	100.8	132.1	176.2	230.6	299.3	371.6
Sn	25.192	6.011	8.993	13.33	19.86	28.60	56.84	78.97	103.2	138.1	179.8	234.3	289.4

Table 6.14 INTERPOLATED TOTAL ATTENUATION CROSS-SECTIONS, σ_{tot} (barns/atom)

E(keV)	C	N	O	F	Ne	Mg	Al	Si	P	S	Cl	A
4	719.8	1377	2335	3949	5946	12160	15640	-	-	34240	40750	50910
5	370.1	720.8	1259	2056	3128	6515	8576	-	-	18780	22820	28520
6	211.8	416.0	731.0	1192	1826	3858	5155	-	-	11350	13980	17490
7	132.0	259.7	457.7	743.6	1152	2459	3319	-	-	7356	9154	11460
8	87.98	172.6	304.4	499.8	771.0	1658	2254	2942	-	5030	6306	7901
9	61.96	120.7	212.6	350.3	540.8	1169	1597	2086	-	3586	4522	5668
10	45.64	88.11	154.6	255.4	394.0	853.6	1171	1531	-	2644	3350	4201
12	27.56	51.92	89.97	148.8	228.7	495.4	683.0	894.8	1236	1556	1986	2489
15	15.71	28.29	47.72	78.21	119.0	255.2	353.2	463.9	629.0	811.2	1042	1305
20	8.600	14.18	22.56	35.63	52.88	109.9	152.5	200.2	267.3	350.5	454.0	565.1
25	6.070	9.112	13.55	20.24	29.17	58.08	80.69	105.5	141.1	183.8	239.5	295.9

$\overline{K\alpha}$ energies used, and interpolated values at integral energies are shown in Tables 6.13 and 6.14 respectively.

It is worth commenting on the fact that the compilations of McMaster et al. (1969) and Veigele (1971) which are based on experimental data use the procedure of subtracting scatter from σ_{tot}, smoothing the resultant τ_{pe} values, and adding the scatter again. The conclusions drawn above suggest that this method may not be an advantageous one over much of the energy range they consider.

6.5 TEST OF RADIATION SOURCES AND $\overline{K\alpha}$ ENERGY VALUES

It has been stated previously (section 3.4.1.2) that the experimental results themselves would provide a check on the values assumed for the $\overline{K\alpha}$ energies, and on the purity of the radiation sources. Graphs such as those presented in figures 6.2, 6.3 and 6.4 are very sensitive tests of the experimental results. If, in fact, any one source is emitting radiation of a markedly higher or lower energy than that used in calculation, then this would be reflected by a tendency for the data obtained with this source to be systematically higher or lower than the smoothed value at this energy for all absorbers. In Table 6.15a the sign of the deviation of the observed value from the smoothed value is shown for all the measured photoelectric cross-sections. " + " indicates that the measured value is higher than the final smoothed value; " - " indicates the measured value to be lower. In a few cases (shown as " O ") there was no difference between measured and smoothed results, to four significant figures. Those cases where the deviation of the measured value from the smoothed value was greater than 1% are circled. Qualitatively this table shows no evidence of erroneous energy values. The evidence can also be assessed quantitatively. The observed

Table 6.15 EXPERIMENTAL TESTING OF ENERGY VALUES USED

a)

Kα	C	N	O	F	Ne	Mg	Al	Si	P	S	Cl	A
Ti	+	−	−	−	−	−	+			−	−	−
Cr	+	+	+	−	+	+	+			0	+	(+)
Fe	−	0	−	+	+	+	(−)			+	+	+
Ni	−	−	−	+	−	+	−			0	−	−
Cu	−	+	−	−	(−)	−	+	+		−	+	+
Zn	+	0	+	+	(+)	−	+	−		−	−	−
Ge	(+)	−	+	−	−	+	+	+		+	+	−
Se	−	−	+	+	−	−	+	+	0	−	+	−
Rb	+	−	(−)	−	+	−	−	−	+	−	−	+
Zr	−	−	+	(−)	+	+	+	(−)	+	(+)	(−)	−
Mo	(−)	+	+	+	+	+	−	+	−	+	(+)	+
Ru	(+)	+	+	(+)	−	+	−	+	−	+	−	+
Pd	0	+	−	+	+	(−)	+	+	+	−	+	−
Cd	0	+	−	+	+	0	+	−	−	−	+	+
Sn	0	−	+	−	+	+	+	−	0	+	−	−

b)

Radiation source	Expected	Observed	χ^2	$\chi^2_{95\%}$
Ti	5 : 5	2 : 8	2.5	3.84
Cr	5 : 5	8.5 : 1.5	3.6	3.84
Fe	5 : 5	6.5 : 3.5	0.4	3.84
Ni	5 : 5	2.5 : 7.5	1.6	3.84
Cu	5.5 : 5.5	5 : 6	0.0	3.84
Zn	5.5 : 5.5	5.5 : 5.5	0.0	3.84
Ge	5.5 : 5.5	7 : 4	0.4	3.84
Se	6 : 6	5.5 : 6.5	0.0	3.84
Rb	6 : 6	4 : 8	0.8	3.84
Zr	6 : 6	6 : 6	0.0	3.84
Mo	6 : 6	9 : 3	2.1	3.84
Ru	6 : 6	8 : 4	0.8	3.84
Pd	6 : 6	7.5 : 4.5	0.5	3.84
Cd	6 : 6	7 : 5	0.1	3.84
Sn	6 : 6	6 : 6	0.0	3.84

split between + and - for each radiation source can be compared with the null hypothesis that the number of pluses should equal the number of minuses, using a χ^2 test. Those cases where measured and smoothed values are equal were taken to contribute $\frac{1}{2}$ to each category. In calculating χ^2, Yates' correction for one degree of freedom was also applied. The results of this test are shown in Table 6.15b. For no element is there any evidence of irregularity in the distribution of these deviations at the 5% significance level.

It can therefore be assumed that the sources used were pure and that the energy values are correct, since no evidence to the contrary is provided.

CHAPTER 7

VARIATION OF PHOTOELECTRIC CROSS-SECTION WITH ATOMIC NUMBER

7.1 INTRODUCTION

Until recently it has been generally assumed that not only was the photoelectric cross-section, τ_{pe}, a smooth function of energy in the regions between absorption edges, but also a smooth function of absorber atomic number, again insofar as no absorption edge effects are involved. Departures from such behaviour were only to be expected at very low photon energies where energy differences in electronic orbitals from one element to the next become of comparable size to the incident photon energy itself. Recently, however, this assumption of a smooth relationship between photoelectric cross-section and atomic number has been called into question. Refinements in the theory of the photoelectric effect have indicated that certain irregularities or "bumps" might be expected in a graph of τ_{pe} against atomic number, Z. This has been proposed by McGuire (1968) and by Manson and Cooper (1968). These irregularities are predicted even at photon energies appreciably greater than the energy differences between orbitals. They reflect rather the fact that although a continuous function like energy might have a smooth relationship with τ_{pe}, the discrete variable, Z, does not behave in such a simple fashion.

No attempt to provide experimental evidence for or against this hypothesis has yet been made, and no existing data set by a single experimenter (i.e. data obtained in such a way that any systematic difference between experimenters is eliminated) is sufficiently

Figure 7.1 VARIATION WITH ATOMIC NUMBER OF THE RATIO (τ_{pe} measured): (τ_{pe} predicted by linear regression)

a) 5 keV

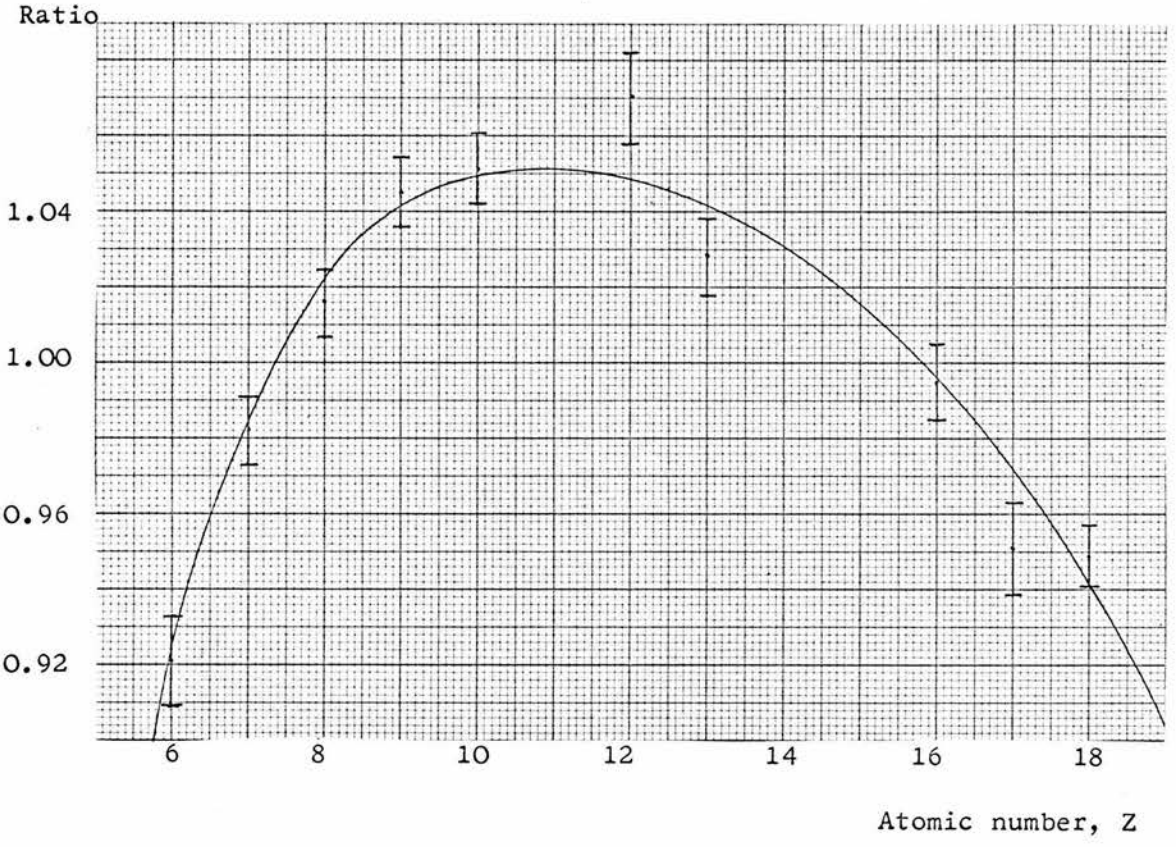

b) 10 keV

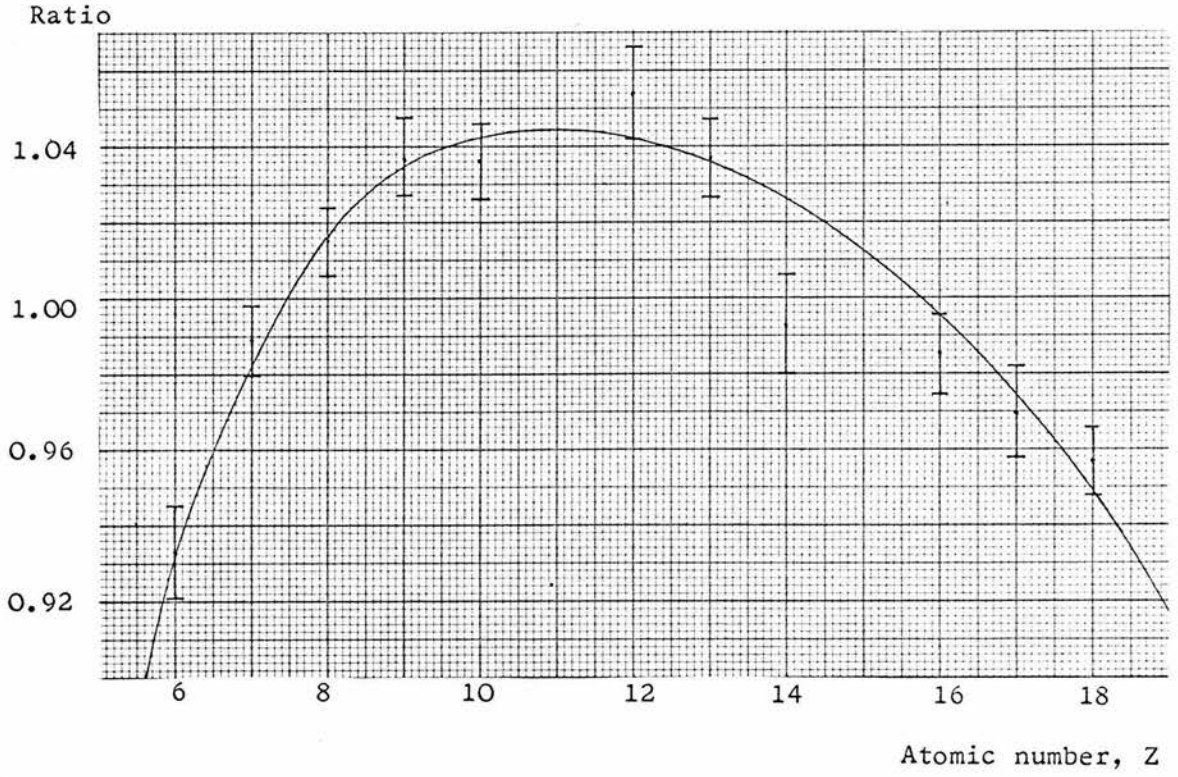

Figure 7.1 (CONTINUED)

c) 15 keV

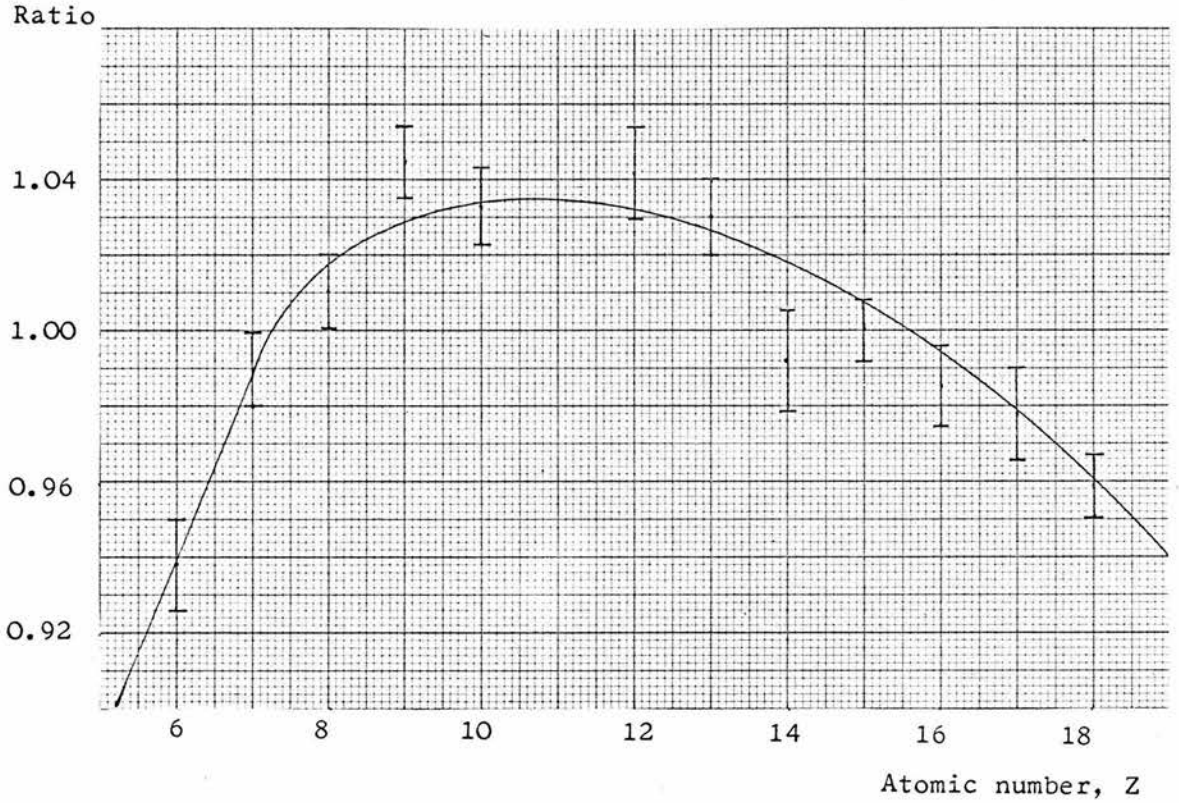

d) 20 keV

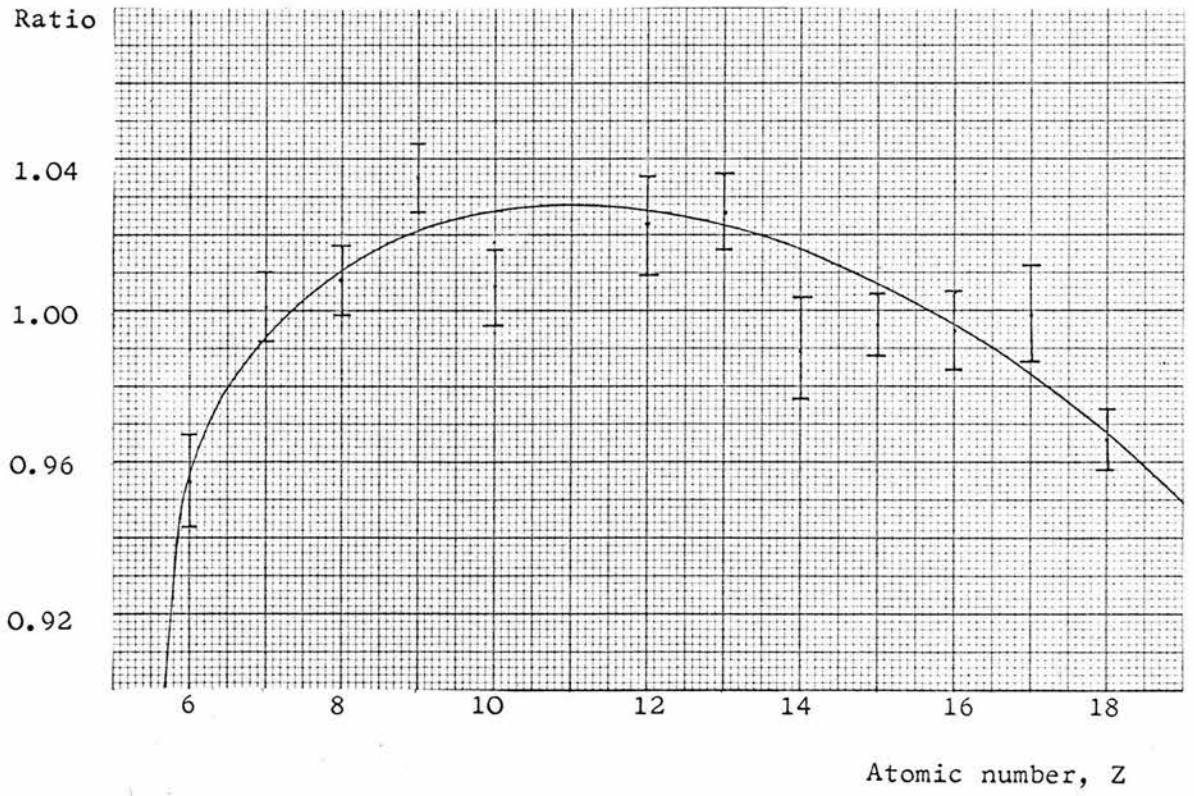

comprehensive in terms of its energy and atomic number range to provide such evidence. The data presented in the previous Chapter, however, can be used to investigate these hypothetical irregularities.

7.2 EVIDENCE FOR IRREGULARITIES IN THE LN τ_{pe}/LN Z RELATIONSHIP

To display small irregularities in the relationship between τ_{pe} and atomic number, a sensitive method of handling the data is required. The technique adopted was similar to that described in the previous Chapter for investigating the finer details of the energy dependence of the photoelectric cross-section. Use is made of the fact that to a first approximation the graph of ln τ_{pe} against ln Z is linear. Using the smoothed values of photoelectric cross-section, linear regression fits of ln τ_{pe} against ln Z at a selection of integral energy values throughout the range were obtained. The ratio of the observed photoelectric cross-section to the predicted value from this linear fit was plotted, as ordinate, against atomic number. This has the effect of greatly expanding the vertical scale. The graphs obtained in this way for photon energies of 5, 10, 15 and 20 keV are shown in figures 7.1a, b, c, d respectively. The error bars shown on these graphs represent the 99% confidence limits as presented in Table 6.7. All these graphs indicate that with the accuracy indicated for each point, no smooth function can be fitted to the data. It would therefore appear that at a precision corresponding to a 99% confidence limit of around 1% of the value of τ_{pe}, irregularities in the τ_{pe}/Z relationship of the type predicted by theory, may be observed experimentally. It is of interest to compare the graphs of figure 7.1 with graphs obtained by the same technique from the published data of Storm and Israel (1970), which is based on the theoretical work

Figure 7.2 VARIATION WITH ATOMIC NUMBER OF THE RATIO (τ_{pe} quoted): (τ_{pe} predicted by linear regression) FOR STORM AND ISRAEL'S DATA

a) 5 keV

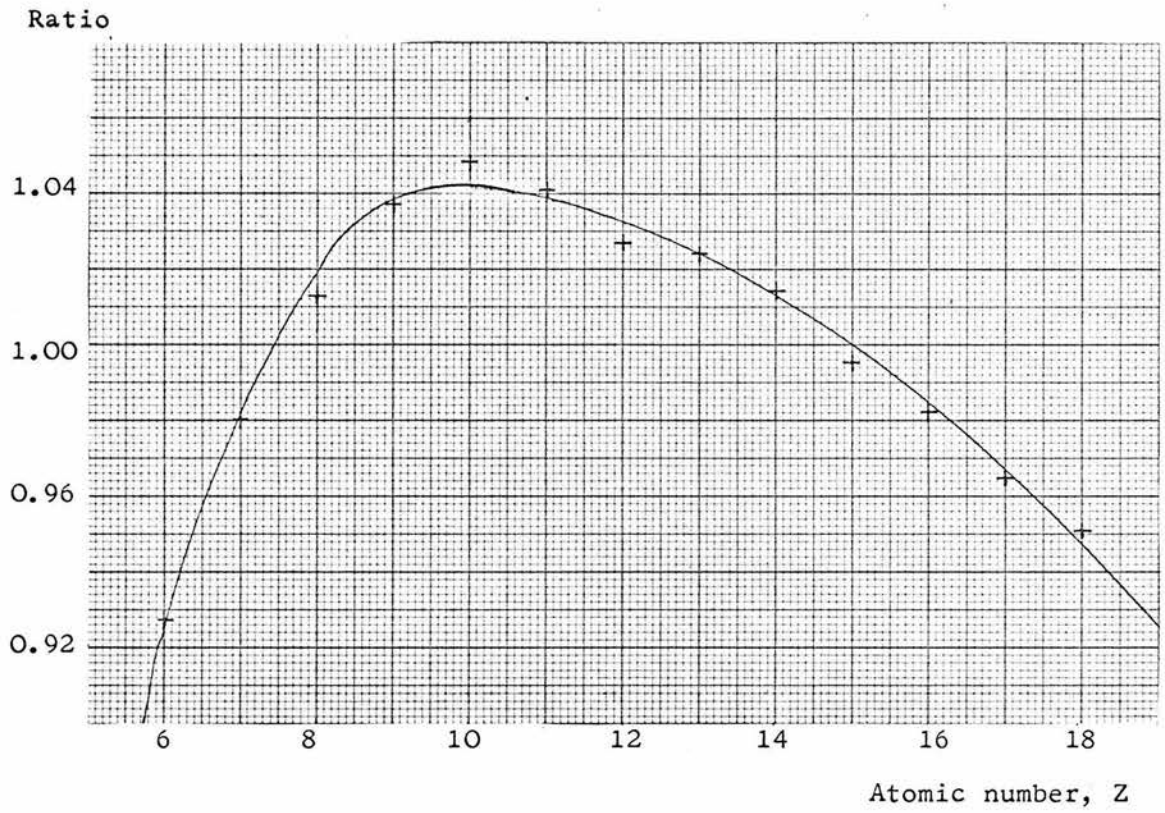

b) 10 keV

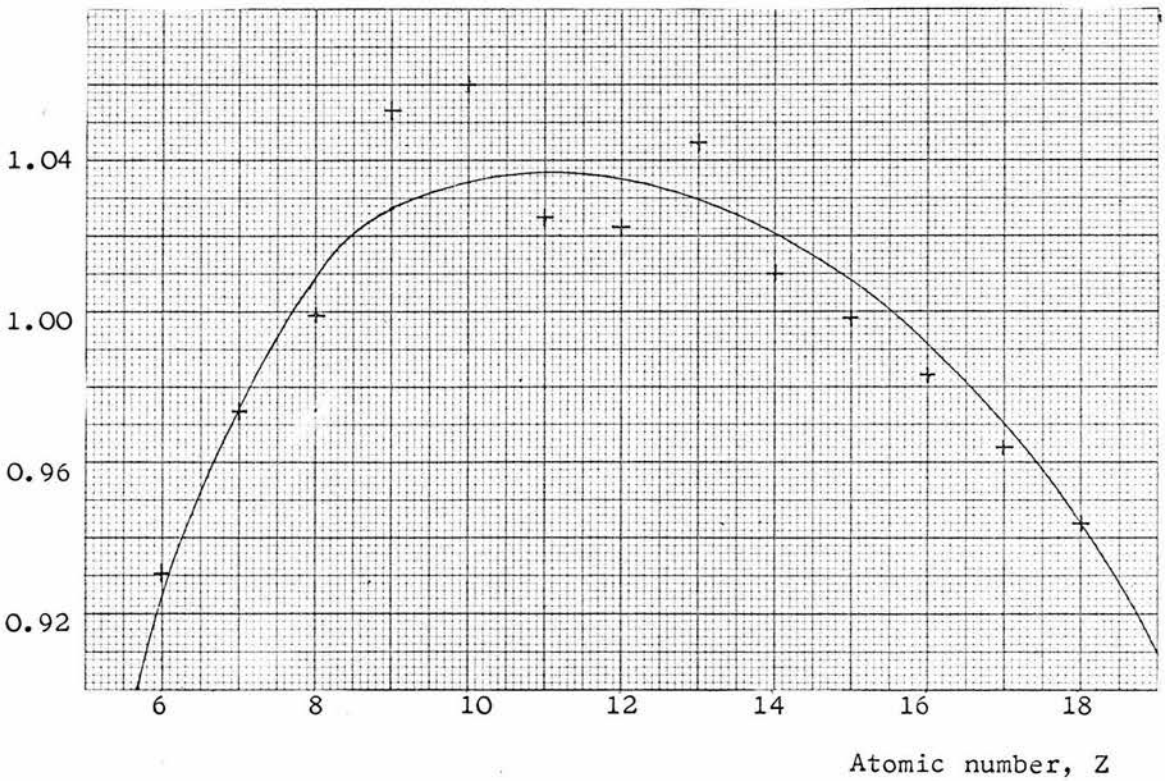

Figure 7.3 VARIATION WITH ATOMIC NUMBER OF THE RATIO (τ_{pe} quoted): (τ_{pe} predicted by linear regression) FOR McGUIRE'S DATA

Energy = 4.13 keV (3 Å)

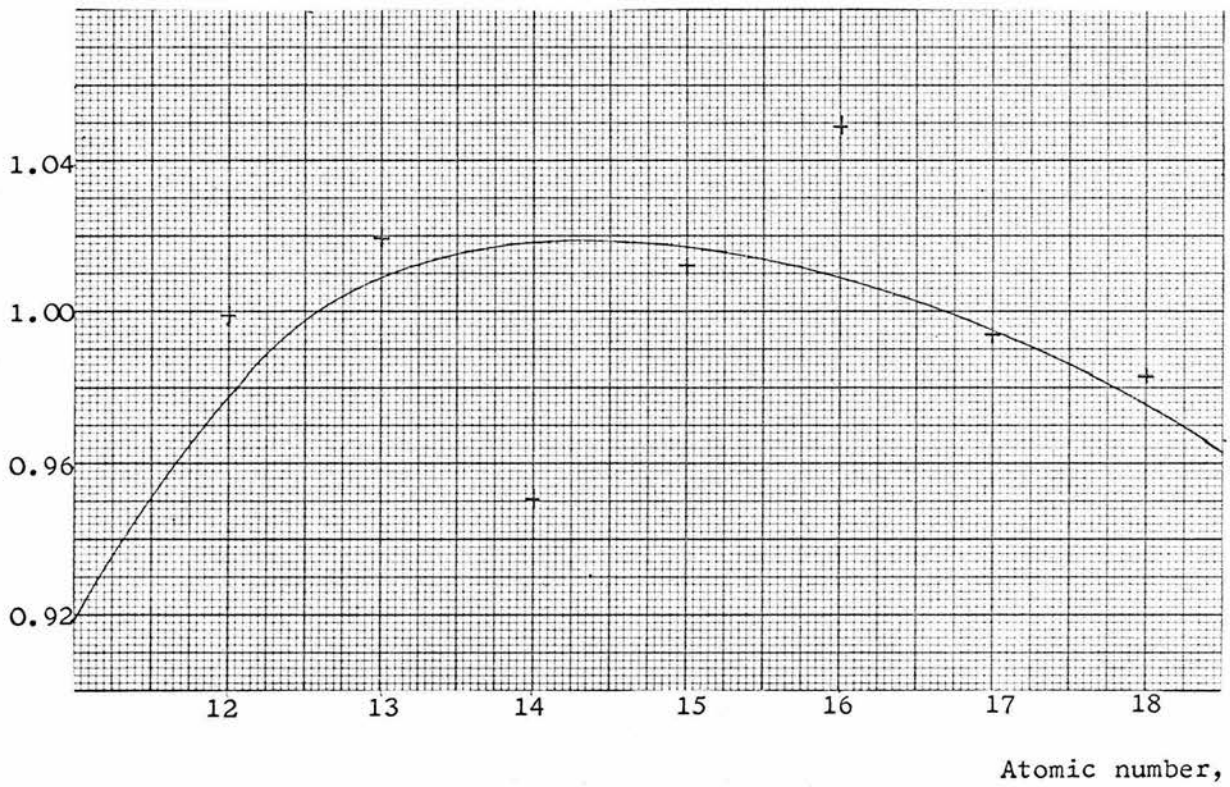

of Brysk and Zerby (1968); and also from the published results of McGuire (1968) who draws attention to these irregularities in the relationship. Figure 7.2a, b shows the result of treating Storm and Israel's data at 5 and 10 keV and figure 7.3 is derived from McGuire's published results at 4.13 keV (3 Å) for Z = 12 to 18. Both these data sets indicate fluctuations of the same type as those shown by the experimental data. It is more difficult to assess quantitatively the observed fluctuations in the experimental results relative to those shown by Storm and Israel and by McGuire, for the uncertainties in data from both these sources are not precisely known. It is likely, in fact, that at the accuracy claimed by the authors, the irregularities observed in the τ_{pe}/Z relation for Storm and Israel's data are not significant, especially at 5 keV. McGuire's data at 4.13 keV, however, show wider variation such that the low point at Z = 14 and the high point at Z = 16 are probably significant. This corresponds well to the observed tendency for Z = 14 to be a low point in the experimental results at 10, 15, 20 keV; a high point at Z = 16 is also observed in the experimental results at 5 keV.

There is therefore experimental verification of the theoretical prediction that the relationship of $\ln \tau_{pe}$ with $\ln Z$ at constant energy is not a smooth one.

7.3 INTERPOLATION TO OTHER ATOMIC NUMBERS

As a result of these conclusions it is not possible to interpolate experimental data to other atomic numbers with the same confidence as for interpolation to intermediate energies. The irregularities observed are not, however, of such a size as to render any attempts at interpolation invalid. The uncertainties associated with results

Table 7.1 SMOOTHED VALUES OF τ_{pe} (barns/atom) FOR SODIUM, SILICON AND PHOSPHORUS

E (keV)	Na	Si	P
4	8719	20330	26920
5	4541	11230	14640
6	2651	6738	8310
7	1675	4319	5606
8	1122	-	3335
9	736.1	-	2761
10	570.5	-	2020
12	325.8	-	-
15	162.6	-	-
20	65.25	-	-
25	31.68	-	-

Table 7.2 CUBIC FIT COEFFICIENTS FOR $\ln \tau_{pe}/\ln E$ CURVE FITTING

Element	C_o	C_1	C_2	C_3
Na	13.0303	-2.32595	-0.0011783	-0.01397220
Si	13.1261	-1.80474	-0.417227	0.04564460
P	13.6635	-2.23574	-0.160595	0.0054277

obtained from such a procedure would be expected to be adequately assessed by assigning a 99% confidence limit of $\pm$ 3% to any interpolated value. Interpolated results with this degree of accuracy are none the less useful, for in the energy and atomic number range considered in this work interpolation across atomic number permits values of photoelectric cross-section for sodium at all energies, and for silicon and phosphorus at the lower energies, to be obtained. Direct experimental evidence with better accuracy than $\pm$ 3% (99% confidence limits) would be very difficult to obtain.

Interpolated values were calculated using a linear regression fit of the $\ln \tau_{pe}/\ln Z$ data, and correcting the result obtained using a correction factor derived from a graph such as those shown in figure 7.1, making use of the correction factors for the neighbouring elements. The values obtained in this way were then smoothed against energy using a cubic-fit on log-log scales to yield the final result. The results of this work for sodium, silicon and phosphorus are shown in Table 7.1. The coefficients of this energy fit are shown in Table 7.2 and enable interpolation at other energies to be carried out. This gives a second set of cubic-fit coefficients for silicon and phosphorus (see Table 6.6). It must therefore be emphasised that the values quoted in Table 6.6 for these two elements are likely to lead to better interpolated values within the energy ranges which they cover, i.e. 8 to 25 keV for silicon; 11 to 25 keV for phosphorus. It is only to obtain interpolated results at energies down to 4 keV for these two elements that the coefficients of Table 7.2 should be used, and the reliability of these results is not so good. For sodium, however, the coefficients of Table 7.2 provide the only available means of interpolation.

Total attenuation cross-section values for sodium and the low

Table 7.3 SMOOTHED VALUES OF σ_{tot} (barns/atom) FOR SODIUM, SILICON AND PHOSPHORUS

E (keV)	Na	Si	P
4	3730	20360	26960
5	4603	11360	14730
6	2693	6303	8381
7	1709	4369	5752
8	1147	-	3931
9	806.8	-	2801
10	583.8	-	2065
12	342.0	-	-
15	177.2	-	-
20	77.44	-	-
25	41.69	-	-

Table 7.4 CUBIC FIT COEFFICIENTS FOR $\ln \sigma_{tot}$/$\ln$ E CURVE FITTING

Element	C_o	C_1	C_2	C_3
Na	12.3772	-1.77477	-0.555584	0.03462150
Si	12.3589	-1.37073	-0.649652	0.03831700
P	13.4572	-1.94759	-0.343386	0.03938030

energy values for silicon and phosphorus may be obtained by adding the scattering cross-sections of Storm and Israel. These are shown in Table 7.3. Cubic fitting can again be carried out as described above, and the coefficients are shown in Table 7.4. The same comments as regards reliability of these results apply to the case of total cross-section.

7.4 CRITICISM OF COMPILED DATA

The data presented in most compilations of photon interaction cross-sections is derived from the available experimental values smoothed and interpolated to other energies and atomic numbers. Although it must be admitted that this is the only course open for some of the "difficult" elements (e.g. Na, K, Ca, etc.) limitations of this procedure should be recognised. In the compilation of Veigele et al. (1971) the smoothing against atomic number is probably given too much weight. McMaster et al. (1969) rely more heavily on smoothing with energy and their results are probably, therefore, rather better. In any case for compilations with an estimated uncertainty of $\pm$ 3%, if this uncertainty is to be understood as one standard error of the mean, then the irregularities of Z-fitting should not prove detrimental at this lower accuracy level. For precise work, however, interpolation with Z is a less reliable technique than might ideally be desired.

Table 8.1 COMPARISON OF TOTAL ATTENUATION CROSS-SECTIONS PUBLISHED BY DESLATTES, σ_D, WITH MEASURED VALUES σ_M

	Mg			Al		
E(keV)	σ_D	σ_M	% diff	σ_D	σ_M	% diff
3.047	1588	1629	2.50	2252	2216	-1.62
3.904	1184	1206	1.82	1662	1648	-0.85
9.885	860.8	883.6	1.56	1214	1212	-0.21
11.22	594.0	605.4	1.88	840.6	833.3	-0.88
12.49	430.1	439.7	2.18	610.8	606.7	-0.68
13.39	350.2	357.4	2.01	501.1	493.8	-1.48
14.96	253.6	257.2	1.40	362.0	356.0	-1.68
15.77	217.3	220.1	1.27	-	304.8	-
17.48	161.1	162.6	0.92	228.6	225.5	-1.38
17.67	156.6	157.6	0.63	221.7	218.5	-1.47
19.61	115.1	116.3	1.03	163.4	161.4	-1.27
20.21	105.7	106.6	0.84	149.7	147.9	-1.19
22.16	81.89	81.79	-0.12	115.7	113.6	-1.82
23.22	71.48	71.58	0.14	101.1	99.41	-1.72
24.94	58.63	58.47	-0.27	82.98	81.23	-2.16
25.27	56.98	56.35	-1.12	79.71	78.29	-1.82

CHAPTER 8

C O N C L U S I O N S

8.1 COMPARISONS WITH OTHER EXPERIMENTAL WORK

Although no other single data set covers the entire range of this investigation, there are several other sets of results with which certain of the experimental values can be compared. Perhaps the most important of these are the measurements on magnesium and aluminium by Deslattes (1959). These formed part of a programme in which accurate mass attenuation coefficients for a range of metals were obtained, and which is probably regarded as the most reliable data set in the literature. In order to compare the two sets of results it was necessary to interpolate the measured total attenuation cross-sections at the energies used by Deslattes. This was done using the cubic-fit coefficients of Table 6.11. Table 8.1 shows these interpolated results, together with Deslattes' published results and the percentage difference between the two sets. These differences are compatible with the estimates of accuracy already given, assigning a comparable accuracy to Deslattes' work. However, there appears to be a systematic difference between the results of Deslattes and of this work, in that the present values are higher for magnesium, except above 20 keV, whilst those for aluminium are all lower than Deslattes. The very fact that the differences are positive for one element and negative for the other rules out certain possible explanations. For example it is unlikely that any uncorrected defect in the radiation sources or the detection system would produce effects in different senses for different absorbers. The source of the observed differences is more likely

Table 8.2 COMPARISON OF TOTAL ATTENUATION CROSS-SECTIONS PUBLISHED BY HUGHES, WOODHOUSE AND BUCKLOW, σ_{HWB}, WITH MEASURED VALUES, σ_M

Attenuating material: Aluminium

E(keV)	σ_{HWB}	σ_M	% diff
4.511	12000	11350	-5.73
5.415	7180	6877	-4.41
6.405	4470	4282	-4.39
7.479	2830	2742	-3.21
8.041	2270	2221	-2.21
9.444	1420	1386	-2.45
10.84	918.0	922.7	0.51

to lie with the absorbers themselves. It is possible that some uncertainty in the measurement of density per unit area might affect all values for any given element in the same sense. It is most unlikely, however, that this could produce an error of 1%. A more likely explanation is absorber impurity, which is outside the direct control of the experimenter. It is impossible to assess whether uncorrected impurities in the foils used by Deslattes could have arisen. On the basis of certified purities of the films used in this experimental work it would seem that no error of the required magnitude could be present. In low atomic number materials like magnesium and aluminium most impurities will necessarily be of higher atomic number and these will tend to raise the observed attenuation. This would suggest that the present results on aluminium may be preferable to those of Deslattes. The only simple impurity effect which might have reduced Deslattes' values for magnesium is oxidation of the surface layer - an effect which would be more noticeable at low energies, and would be supported by the observed results. These suggestions are, however, merely speculative and the more impressive feature of the comparison of Deslattes' results with those measured here is the excellent agreement shown.

Another set of accurate results on aluminium is that of Hughes, Woodhouse and Bucklow (1968). A similar comparison between interpolated results and their published figures is shown in Table 8.2. The agreement, while not so good as with Deslattes, is within a few percent above 7 keV. These results of Hughes et al. appear to become increasingly rather high as the photon energy decreases.

The only experimental data set enabling a comparison to be made across the atomic number range is that of Bearden (1966). These are

Table 8.3 COMPARISON OF TOTAL ATTENUATION CROSS-SECTIONS PUBLISHED BY BEARDEN, σ_B, WITH MEASURED VALUES, σ_M

a) Carbon

E (keV)	σ_B	σ_M	% diff
4.511	499	504.7	1.13
5.415	303	290.2	-4.41
6.404	175	173.4	-0.92
8.048	86.3	86.41	0.13

b) Nitrogen

4.511	1030	975.9	-5.54
5.415	535	567.7	-3.05
6.404	350	341.0	-2.64
8.048	170	169.5	-0.29

c) Oxygen

4.511	1840	1693	-8.36
5.415	1000	904.4	-9.61
6.404	672	600.2	-11.96
8.048	314	298.9	-5.05

d) Neon

4.511	4360	4218	-3.37
5.415	2550	2475	-3.03
6.404	1500	1504	0.27
8.048	737	757.2	2.67

e) Aluminium

4.511	10900	11350	3.96
5.415	6670	6877	3.01
6.404	4140	4234	3.36
8.048	2310	2215	-4.29
10.000	1340	1171	-14.43
12.500	605	605.3	0.05
15.000	360	353.2	-1.93
20.000	153	152.5	-0.33
25.000	83.3	80.69	-3.23

f) Argon

4.511	44200	37360	-18.31
5.415	28000	23070	-21.37
6.404	13200	14640	-24.32
8.048	7330	7769	-0.79

Table 8.4 PERCENTAGE DIFFERENCE BETWEEN INTERPOLATED EXPERIMENTAL VALUES OF TOTAL ATTENUATION CROSS-SECTION AND COMPILATION DATA: $\left(\frac{\sigma_{expt} - \sigma_{compilation}}{\sigma_{expt}} \times 100\right)$

a) Storm and Israel (1970)

E (keV)	C	N	O	F	Ne	Mg	Al	Si	P	S	Cl	A
4	-4.33	-3.35	-3.56	-0.23	-0.91	1.32	-2.94			1.37	-1.60	1.00
5	-2.67	-1.23	-0.37	-0.19	-0.06	4.37	0.77			2.02	-0.35	1.12
6	-1.93	-0.96	-0.55	0.17	-0.77	4.35	1.65			1.32	-0.14	1.66
8	1.57	2.67	0.79	-0.34	-1.56	3.50	1.95	-0.61		1.19	0.73	1.66
10	0.74	1.71	1.63	-1.41	-2.23	3.00	-0.77	-1.24		0.15	0.30	0.98
15	0.70	1.38	1.09	2.31	0.00	2.04	1.19	-1.96	0.43	-0.19	1.15	0.38
20	-0.23	1.27	0.71	2.05	0.34	0.32	0.33	-1.90	-1.38	-0.14	1.10	0.02

b) McMaster et al. (1969)

E (keV)	C	N	O	F	Ne	Mg	Al	Si	P	S	Cl	A
4	-3.22	-5.08	-3.77	-4.71	-0.10	-2.71	-5.32			0.18	-1.96	-2.83
5	0.05	-0.35	0.00	-3.55	1.31	-1.96	-3.43			0.48	-2.41	-2.35
6	1.42	0.84	1.37	-3.10	1.86	-1.63	-2.25			0.53	-2.86	-2.12
8	2.86	2.20	2.17	-2.23	2.30	-1.15	-1.33	-5.17		0.60	-3.44	-1.76
10	4.21	3.13	2.65	-1.17	2.69	-0.54	-0.94	-4.83		0.64	-3.53	-1.40
15	5.60	5.16	4.32	1.38	4.03	1.14	-0.06	-3.21	-1.05	1.32	-2.69	-0.23
20	4.00	4.30	4.03	2.93	4.12	2.00	0.59	-1.65	-1.12	1.97	-1.12	0.90

c) I.C.R.U. Report 17 (1970)

E (keV)	C	N	O	F	Ne	Mg	Al	Si	P	S	Cl	A
4	-4.46	-0.09	1.03			6.33	0.33			1.25		-2.90
5	-2.93	1.27	3.14			6.43	3.35			2.46		0.02
6	-0.76	2.17	3.60			5.09	3.53			2.42		1.04
8	0.43	2.72	2.25			2.36	0.61			-0.34		0.12
	1.62	2.61	1.02			0.68	-0.62			-1.70		-1.34
									-0.50	-1.09		-1.12

compared in Table 8.3. With the exceptions of oxygen and argon where Bearden's results seem strangely low, the agreement is within a few percent. On the whole, however, Bearden's results look less reliable than either those of Hughes et al. or Deslattes.

8.2 COMPARISON WITH COMPILED DATA SETS

A more searching comparison can be made between the measured experimental data and that published in the major compilations. For the purposes of this comparison, the total cross-section was used, rather than the photoelectric cross-section, which depends on the use of published scattering data. The compilations chosen for comparison were those of Storm and Israel (1970) and McMaster et al. (1969), as well as the data published in the report of the International Commission on Radiation Units and Measurements, I.C.R.U. Report 17, (1970). These are, respectively, the best theoretical set, the best experimentally-based set, and the set most widely used in medical applications. Fortunately, all three of these reports quote attenuation data at the same set of energy values. The experimental results were interpolated at 4, 5, 6, 8, 10, 15 and 20 keV using the coefficients of the cubic-fit as given in Table 6.11. The percentage difference between the interpolated experimental value, σ_{expt}, and the quoted value in the compilation, $\sigma_{compilation}$, was calculated:

$$\% \text{ difference} = \frac{\sigma_{expt} - \sigma_{compilation}}{\sigma_{expt}} \times 100$$

The values of this percentage difference for each of the three compilations are shown in Table 8.4a, b, c. The extent of agreement across the range is very good, especially with Storm and Israel's

values. The results are also entirely compatible with those of McMaster et al. bearing in mind the estimated uncertainty of $\pm$ 3% on McMaster's data. In fact it would appear that both Storm and Israel, and McMaster et al. are reliable to a better accuracy than $\pm$ 3% as one standard error of the mean. With a few exceptions, a figure of $\pm$ 3% as a 99% confidence limit could be accepted. It is also of interest to note that for magnesium, where McMaster's data lean heavily on accurate experimental work like that of Deslattes, the agreement with the measured data is better than Storm and Israel; for aluminium, where the same situation obtains, the agreement is comparable in both tabulations. On the other hand for silicon, where there is a dearth of experimental values for McMaster to use, agreement with Storm and Israel is much better. This pattern suggests several conclusions. Firstly it implies that the limiting factor on work such as that of McMaster and his co-workers is the availability of experimental data, and emphasises the need for more accurate experimental work, if a real improvement in the state of knowledge of attenuation coefficients is sought. Secondly it indicates that in the region where much accurate experimental work is available the measured values are in very good agreement and thus lends increased confidence to the results obtained in regions where previous experimental work is scanty or non-existent.

Apart from its magnesium values, the I.C.R.U. report is in substantial agreement with this experiment. The level of agreement with it, however, gives no reason to suppose that it is to any measurable extent an improvement on Storm and Israel.

The excellent agreement with Storm and Israel's data is an indication of the reliability of the modern theoretical techniques.

This agreement over a wide range of energy and atomic number provides very strong support for the theoretical predictions. By thus increasing confidence in these theoretical values, the present experimental programme has, therefore, value which goes beyond the scope in energy and wavelength of the actual measurements themselves. For by providing strong evidence to support the theoretical findings of Storm and Israel, it lends confidence to the entire published results of their compilation over a much wider energy and atomic number range.

8.3 A PROPOSED SET OF "BEST" VALUES

In conclusion it seems desirable to propose a set of experimental values of total attenuation cross-section and photoelectric cross-section which may be relied upon to a better level of accuracy than any existing publication within the range of energy and atomic number considered. This might serve to reduce the present confusion in which several compiled data-sets compete for recognition as the "best" set.

The following is proposed:

a) In the energy region from 4 to 25 keV for C, N, O, F, Ne, Mg, Al, S, Cl, A (and from 8 to 25 keV for Si and from 11 to 25 keV for P) the recommended values of total attenuation cross-section are shown in Tables 6.13 and 6.14. The associated uncertainties are given in detail in Table 6.12 and may be regarded as corresponding roughly to a 99% confidence limit of $\pm$ 1% for all elements. Interpolated values at other energies within the range may be obtained using the coefficients shown in Table 6.11.

b) The corresponding values of photoelectric cross-section are presented in Tables 6.8 and 6.9. The 99% confidence limits are of approximately the same magnitude as those for the total

cross-sections. Interpolated values at other energies within the range may be obtained using the coefficients shown in Table 6.6.

c) Total attenuation cross-sections for Na from 4 to 25 keV, for Si from 4 to 8 keV, and for P from 4 to 11 keV are shown in Table 7.3. The estimated 99% confidence limits on these results are $\pm$ 3% of the values quoted. Interpolated values at other energies within these ranges may be obtained using the coefficients shown in Table 7.4.

d) Photoelectric cross-sections for Na from 4 to 25 keV, for Si from 4 to 8 keV and for P from 4 to 11 keV are shown in Table 7.1. The estimated 99% confidence limits on these results are $\pm$ 3% of the values quoted. Interpolated values at other energies within these ranges may be obtained using the coefficients shown in Table 7.2.

These results are believed to have a better accuracy and internal consistency within this energy range than any other experimental, theoretical or compiled data set available.

Figure A1.1

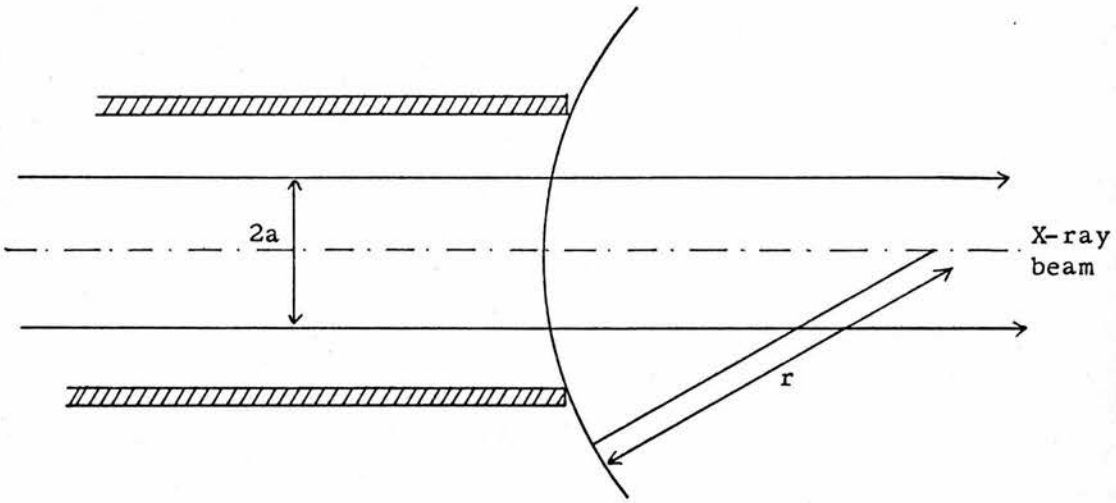

Figure A1.2

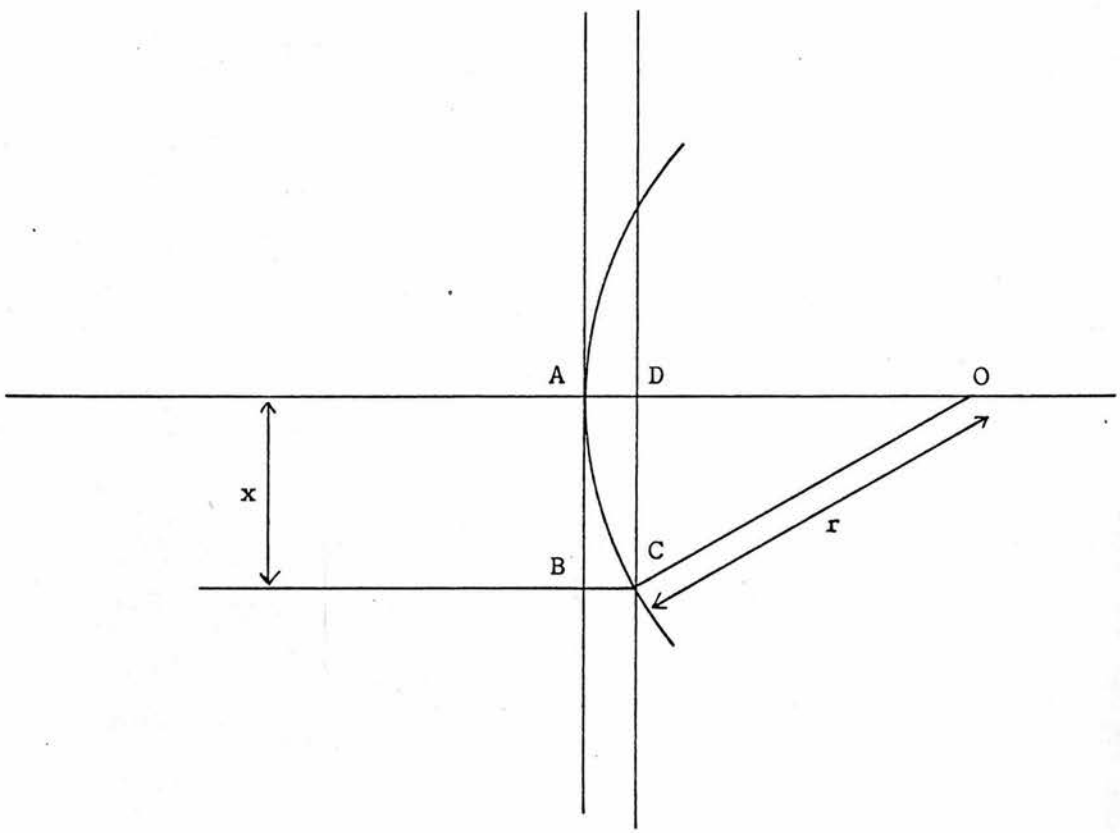

APPENDIX 1

LENGTH CORRECTION TO ACCOUNT FOR DISTORTION UNDER PRESSURE OF THE GASEOUS ABSORBER TUBE WINDOWS

When a pressure difference arises across the "Melinex" windows of the gas absorber tubes, these thin windows will distort. The distortion may be assumed uniform, i.e. the window assumes the form of a part of a spherical surface with radius of curvature r. The window geometry is shown in figure A1.1.

For simplicity, the X-ray beam is considered to be a collimated beam of circular cross-section with a cross-section diameter 2a.

The rays within this beam do not pass through identical thicknesses of absorber, due to the curvature of the window, but in the case illustrated, where the pressure outside is greater than inside, the parts of the beam nearer the axis are less strongly absorbed than those at the outer limits of the beam. Let us consider that the length of the absorbing column is measured along the axis, and calculate the correction required to allow for window curvature.

Referring to the notation of figure A1.2: rays at distance x from the axis must pass through an extra distance BC, within the absorber

$$
\begin{aligned}
BC = AD &= AO - OD \\
&= r - \left(r^2 - x^2\right)^{\frac{1}{2}} \\
&= r - r\left(1 - \frac{x^2}{r^2}\right)^{\frac{1}{2}} \\
&= r - r\left(1 - \frac{x^2}{2r^2} + \frac{x^4}{8r^4} \quad \ldots\ldots\right) \\
&= \frac{x^2}{2r} - \frac{x^4}{8r^3} \quad \ldots\ldots
\end{aligned}
$$

For a well-collimated beam and a slightly curved window

$$BC \doteq \frac{x^2}{2r} \qquad \ldots\ldots \text{(A1.1)}$$

A portion dI_o of the incident beam passes through an annulus at radius x:

$$dI_o = I_o \frac{2\pi x\, dx}{\pi a^2} = \frac{2x\, dx}{a^2} I_o$$

The transmitted intensity is given approximately by:

$$dI = \frac{2x\, dx}{a^2} I_o \exp\left(-\frac{\mu x^2}{2r}\right) \qquad \ldots\ldots \text{(A1.2)}$$

$$I = \frac{2I_o}{a^2} \int_o^a x \exp\left(-\frac{\mu x^2}{2r}\right) dx$$

$$= \frac{2I_o r}{\mu a^2}\left[1 - \exp\left(-\frac{\mu a^2}{2r}\right)\right] \qquad \ldots\ldots \text{(A1.3)}$$

The same attenuation could have been achieved by an extra thickness, t , of absorber, distributed uniformly across the beam. t is defined by:

$$I = I_o \exp(-\mu t) = \frac{2I_o r}{\mu a^2}\left[1 - \exp\left(-\frac{\mu a^2}{2r}\right)\right] \qquad \ldots\ldots \text{(A1.4)}$$

For small t

$$I_o(1 - \mu t) \doteq \frac{2I_o r}{\mu a^2}\left[\frac{\mu a^2}{2r} - \frac{\mu^2 a^4}{8r^2}\right]$$

$$= I_o\left[1 - \frac{\mu a^2}{4r}\right]$$

So $$t \doteq \frac{a^2}{4r} \qquad \ldots\ldots \text{(A1.5)}$$

Hence the tube length, measured along the axis, should be corrected by the addition of an extra length equal to $a^2/4r$ for each window, i.e. by $a^2/2r$.

This is simply equal to the linear distortion at the axis of one window, i.e. the centre of the window moves through a distance of $a^2/2r$ due to the pressure difference. This can therefore be easily measured and the length correction made.

APPENDIX 2

ERRORS IN MEASUREMENT OF MASS-ATTENUATION COEFFICIENTS FOR SOLID ABSORBERS DUE TO ABSORBER NON-UNIFORMITY

One source of error in experimentally determined mass attenuation coefficients using thin solid absorbers is non-uniformity of the absorber. It is of value to consider how serious the effects of such non-uniformity are on the experimental values obtained.

Consider an absorber of average thickness T. The deviation from this average thickness at any point $\underline{r}$ on the absorber is $t(\underline{r})$, $\underline{r}$ being a 2-dimensional position vector.

Then
$$\int_S t(\underline{r})\, d\underline{r}^2 = 0 \qquad \ldots\ldots \text{(A2.1)}$$

Transmission through an element of the absorber at position $\underline{r}$ is given by

$$dI = \frac{I_o\, d\underline{r}^2}{\int_S d\underline{r}^2} \exp\left[-\frac{\mu}{\rho} \cdot \rho \cdot (T + t(\underline{r}))\right]$$

So
$$I = \frac{I_o}{\int_S d\underline{r}^2} \int_S \exp\left[-\frac{\mu}{\rho} \cdot \rho \cdot (T + t(\underline{r}))\right] d\underline{r}^2$$

$$= \frac{I_o}{\int_S d\underline{r}^2} \exp\left(-\frac{\mu}{\rho} \cdot \rho \cdot T\right) \int_S \exp\left(-\frac{\mu}{\rho} \cdot \rho \cdot t(\underline{r})\right) d\underline{r}^2$$

$\ldots\ldots$ (A2.2)

The integral term can then be expanded as a polynomial series. Expanding to the 2nd order term and applying equation A2.1 produces the result:

$$I \doteq I_o \exp\left(-\frac{\mu}{\rho} \cdot \rho \cdot T\right)\left[1 + \frac{\left(\frac{\mu}{\rho} \cdot \rho\right)^2}{2} \frac{\int_S t^2(\underline{r})\, dr^2}{\int_S d\underline{r}^2}\right] \quad \ldots\ldots \text{(A2.3)}$$

The term $\dfrac{\int_S t^2(\underline{r})\, d\underline{r}^2}{\int_S d\underline{r}^2}$ gives the expectation value of $t^2(\underline{r})$ over the surface, i.e. it is the mean square deviation in thickness. This quantity may be denoted by ε^2.

So equation A2.4 reduces to

$$I \doteq I_o \exp\left(-\frac{\mu}{\rho} \cdot \rho \cdot T\right)\left(1 + \frac{\left(\frac{\mu}{\rho}\ \rho\right)^2 \varepsilon^2}{2}\right) \quad \ldots\ldots \text{(A2.4)}$$

In the case of no thickness deviation, the observed intensity is I' where

$$I' = I_o \exp\left(-\frac{\mu}{\rho} \cdot \rho \cdot T\right)$$

Then

$$\frac{\delta\left(I/I_o\right)}{\left(I/I_o\right)} = \frac{I' - I}{I'}$$

$$= \frac{\left(\frac{\mu}{\rho}\ \rho\right)^2 \varepsilon^2}{2} \quad \ldots\ldots \text{(A2.5)}$$

By the normal law of propagation of error, the fractional error in $\frac{\mu}{\rho}$ follows from this:

$$\frac{\delta\left(\frac{\mu}{\rho}\right)}{\left(\frac{\mu}{\rho}\right)} = \frac{\delta\left(I/I_o\right)}{\left(I/I_o\right)} \cdot \frac{1}{\ln\left(I/I_o\right)}$$

$$\doteq \frac{\left(\frac{\mu}{\rho} \cdot \rho \cdot T\right)}{2} \cdot \left(\frac{\varepsilon}{T}\right)^2 \quad \ldots\ldots \text{(A2.6)}$$

Under optimum conditions, T is chosen such that $I_o/I \doteq 5$. Hence $\left(\frac{\mu}{\rho} \cdot \rho \cdot T\right) \doteq 1.6$. Using this value the fractional error in $\frac{\mu}{\rho}$ becomes

$$\frac{\delta\left(\frac{\mu}{\rho}\right)}{\left(\frac{\mu}{\rho}\right)} \quad \doteq \quad 0.8 \left(\frac{\varepsilon}{T}\right)^2 \qquad \ldots\ldots \text{(A2.7)}$$

Hence an r.m.s. deviation from average thickness of 10%, which is larger than that expected of any of the foils used, would result in an error of only 0.8% in the measured value of $\frac{\mu}{\rho}$.

APPENDIX 3

EFFECT ON ATTENUATION COEFFICIENT OF A FINITE ENERGY WINDOW

Using the notation of section 3.4.1.2 the apparent attenuation coefficient due to an energy window $W(E - E_o)$ is given (as in equation 3.20) by:

$$\rho x \left[\frac{\mu}{\rho} (E_o) \right]_{\text{apparent}} = \ln \frac{\int_0^\infty W(E - E_o)\, dE}{\int_0^\infty T(E)\, W(E - E_o)\, dE} \qquad \ldots\ldots \text{(A3.1)}$$

The further assumptions are made that $T(E) = \exp\left(- \frac{\mu}{\rho} \cdot \rho x \right)$ and that $\frac{\mu}{\rho}(E) = AE^{-3}$ (where A is a constant).

In the ideal situation $W(E - E_o)$ is a Dirac δ-function:

$$W(E - E_o) = \delta(E - E_o) \qquad \ldots\ldots \text{(A3.2)}$$

The integrals of A3.1 may then be performed easily as follows:

Numerator: $$\int_0^\infty W(E - E_o)\, dE = \int_0^\infty \delta(E - E_o)\, dE = 1$$

Denominator: $$\int_0^\infty T(E)\, W(E - E_o)\, dE = \int_0^\infty T(E)\, \delta(E - E_o)\, dE$$

$$= T(E_o)$$

$$= \exp\left(- \frac{\mu}{\rho} (E_o) \cdot \rho x \right)$$

Hence A3.1 reduces to:

$$\rho x \cdot \left[\frac{\mu}{\rho} (E_o) \right]_{\text{apparent}} = \rho x \cdot \frac{\mu}{\rho} (E_o) \qquad \ldots\ldots \text{(A3.3)}$$

That is, the apparent value of $\frac{\mu}{\rho}$ is the precise value at energy E_o .

This may be contrasted with the result obtained when the window takes the more realistic form of a Gaussian centred on E_o:

$$W(E - E_o) = \frac{1}{\sqrt{2\pi\sigma^2}} \exp\left[- \frac{(E - E_o)^2}{2\sigma^2} \right] \qquad \ldots\ldots \text{(A3.4)}$$

Consider then the integrals of equation A3.1:

$$\text{Numerator:} \quad \int_o^\infty W(E - E_o)\, dE = \frac{1}{\sqrt{2\pi\sigma^2}} \int_o^\infty \exp\left[- \frac{(E - E_o)^2}{2\sigma^2} \right] dE$$

$$= 1$$

$$\text{Denominator:} \quad I = \int_o^\infty T(E)\, W(E - E_o)\, dE$$

$$= \frac{1}{\sqrt{2\pi\sigma^2}} \int_o^\infty \exp\,(-A\rho x E^{-3}) \exp\left[- \frac{(E - E_o)^2}{2\sigma^2} \right] dE$$

$$\Rightarrow \quad I \doteq \frac{1}{\sqrt{2\pi\sigma^2}} \int_{-\infty}^\infty \exp\,(-A\rho x E^{-3}) \exp\left[- \frac{(E - E_o)^2}{2\sigma^2} \right] dE$$

$$\text{if } E_o \gg \sigma \qquad \ldots\ldots \text{(A3.5)}$$

This integral cannot be performed analytically, but under certain conditions, can be evaluated by an approximation:

The function $\exp\,(-A\rho x E^{-3})$ is expanded in a Taylor series about the point $E = E_o$

$$\text{i.e. } f(E) = f(E_o) + (E - E_o)\, f'(E_o) + \frac{(E - E_o)^2}{2}\, f''(E_o) \ldots$$

$$\text{Hence } \exp\,(-A\rho x E^{-3}) = \exp\,(-A\rho x E_o^{-3}) \left[1 + K_1.(E - E_o) + K_2.(E - E_o)^2 \ldots \right]$$

$$\ldots\ldots \text{(A3.6)}$$

$$\left.\begin{aligned} \text{where } K_1 &= 3\,A\rho x E_o^{-4} \\ \text{and } K_2 &= 9\,(A\rho x)^2\,E_o^{-8} - 12\,A\rho x E_o^{-5} \end{aligned}\right\}$$

The integral of A3.5 then becomes:

$$I \doteq \frac{1}{\sqrt{2\pi\sigma^2}}\,\exp\,(-A\rho x E_o^{-3}) \int_{-\infty}^{\infty} dE\,\exp\left[-\frac{(E-E_o)^2}{2\sigma^2}\right]\left[1 + K_1(E-E_o) + K_2\,(E-E_o)^2\right]$$

$$= \exp\,(-A\rho x E_o^{-3})\left[1 + \tfrac{1}{2}\,K_2\,\sigma^2\right] \qquad \ldots\ldots \text{(A3.7)}$$

Substituting this into equation A3.1 we have:

$$\rho x\left[\frac{\mu}{\rho}(E_o)\right]_{\text{apparent}} = A\rho x E_o^{-3} - \ln\left[1 + \tfrac{1}{2}\,K_2\,\sigma^2\right]$$

$$= \rho x\,\frac{\mu}{\rho}(E_o) - \ln\left[1 + \tfrac{1}{2}\,K_2\,\sigma^2\right] \qquad \ldots\ldots \text{(A3.8)}$$

$$\text{Hence } \rho x\left[\left[\frac{\mu}{\rho}(E_o)\right]_{\text{apparent}} - \frac{\mu}{\rho}(E_o)\right] = -\ln\left[1 + \tfrac{1}{2}\,K_2\,\sigma^2\right]$$

$$\doteq -\tfrac{1}{2}\,K_2\,\sigma^2 \quad (\text{if } \tfrac{1}{2}\,K_2\,\sigma^2 \ll 1)$$

The difference between the apparent and precise values of $\frac{\mu}{\rho}$ at energy E_o is then given by $\delta\frac{\mu}{\rho}(E_o)$ where:

$$\delta\frac{\mu}{\rho}(E_o) = -\frac{K_2\sigma^2}{2\rho x}$$

$$= \frac{\sigma^2}{2\rho x}\left[\frac{12\,A\rho x}{E_o^{5}} - \frac{9(A\rho x)^2}{E_o^{8}}\right]$$

$$= \frac{\sigma^2}{E_o^{2}}\left[\frac{6A}{E_o^{3}} - \frac{9\,A\rho x \,.\, A}{2\,E_o^{6}}\right] \qquad \ldots\ldots \text{(A3.9)}$$

Therefore $$\frac{\delta \frac{\mu}{\rho}(E_o)}{\frac{\mu}{\rho}(E_o)} = \frac{\sigma^2}{E_o^2}\left[6 - \frac{9\,\rho x\,\frac{\mu}{\rho}(E_o)}{2}\right] \qquad \text{..... (A3.10)}$$

The term $\left[6 - \frac{9}{2}\,\frac{\mu}{\rho}(E_o)\,\rho x\right]$ is of order unity throughout the experiment. Hence the fractional error in $\frac{\mu}{\rho}$ at energy E_o is of the same order of magnitude as the inverse second power of the resolution, R, defined as:

$$R = \frac{E_o}{\sigma} \qquad \text{..... (A3.11)}$$

i.e. $$\frac{\delta \frac{\mu}{\rho}(E_o)}{\frac{\mu}{\rho}(E_o)} \sim R^{-2}$$

APPENDIX 4

CALCULATION OF EFFECTIVE NUMBER OF DEGREES OF FREEDOM FOR DERIVED RESULTS

If a physical quantity is measured n times yielding values x_i (i = 1 to n) then the mean, $\bar{x}$, and standard deviation, σ_x, are defined as:

$$\bar{x} = \frac{\sum_{i=1}^{n} x_i}{n} \qquad \text{.....(A4.1)}$$

$$\sigma_x^2 = \frac{1}{n-1} \sum_{i=1}^{n} (x_i - \bar{x})^2$$

assuming the variable x_i to be normally distributed.

The mean itself is a more reliable estimate of the population mean than any individual measurement. The standard error of the mean is defined as:

$$\sigma_{\bar{x}}^2 = \frac{1}{n(n-1)} \sum_{i=1}^{n} (x_i - \bar{x})^2 \qquad \text{.....(A4.2)}$$

Both σ_x and $\sigma_{\bar{x}}$ are said to have (n - 1) degrees of freedom, one degree being lost in calculating $\bar{x}$.

If x is a function of independent variables a, b, c, ...

$$x = x(a, b, c, ...)$$

it can easily be shown that

$$\sigma_x^2 = \left(\frac{\partial x}{\partial a}\right)^2 \sigma_a^2 + \left(\frac{\partial x}{\partial b}\right)^2 \sigma_b^2 \qquad \text{.....(A4.3)}$$

The same relationship holds for the standard error of the mean

$$\sigma_{\bar{x}}^2 = \left(\frac{\partial \bar{x}}{\partial \bar{a}}\right)^2 \sigma_{\bar{a}}^2 + \left(\frac{\partial \bar{x}}{\partial \bar{b}}\right)^2 \sigma_{\bar{b}}^2 \qquad \text{.....(A4.4)}$$

$$= \sum_{i = a, b, \ldots} a_i$$

where $\alpha_i = \left(\frac{\partial \bar{x}}{\partial \bar{i}}\right)^2 \sigma_{\bar{i}}^2$

It can be shown that for a quantity derived from several separate measurements, the effective number of degrees of freedom, ν_{eff}, is given by:

$$\frac{1}{\nu_{eff}} = \sum_i \frac{C_i^2}{\nu_i}$$

where $C_i = \frac{\alpha_i}{\sum_i \alpha_i}$ ..... (A4.5)

Hence C_i is the fractional contribution to the total random uncertainty due to the i^{th} component. As ν_{eff} calculated from equation A4.5 will be usually non-integral, it must be rounded downwards to the next integer.

APPENDIX 5

UNCERTAINTY IN PREDICTED VALUES FROM A CUBIC FIT

A5.1 INTRODUCTION

In Chapter 6, the relationship between experimental values of photoelectric cross-section and energy is discussed. The functional relationship between these parameters can be adequately described by a cubic polynomial on a log-log scale. It is necessary to consider the uncertainty associated with predictions from this fitted polynomial.

To discuss this problem rigorously would involve an extremely complex statistical analysis, but estimates of the uncertainty can be arrived at by a somewhat simpler technique. This involves a consideration of the same problem for the case of a straight-line fit to the experimental data. The approach outlined here follows that of Guest (1961). The results of this approach can then be generalised to cover the case of cubic, rather than linear, fitting.

A5.2 LINEAR REGRESSION

In its most thorough form, the linear regression method permits the assignation of different weights to the experimental points according to their relative precisions. Since, however, the standard deviation of the standard error of the mean is a large fraction of the SEOM (except when the associated number of degrees of freedom is large) it is felt that it would be unjustified to assign different weights to the experimental data in this case. Consequently all points are given equal weighting.

We wish to find a fitted regression curve:

$$u(x) = b_o + b_1 x \qquad \ldots\ldots \text{(A5.1)}$$

such that we minimise $\sum_i \left(y_i - u(x_i)\right)^2$

i.e. $$\sum_i \left(y_i - b_o - b_1 x_i\right)^2$$

This implies the two conditions:

$$\left.\begin{aligned} \sum_i \left(y_i - b_o - b_1 x_i\right) &= 0 \\ \sum_i x_i \left(y_i - b_o - b_1 x_i\right) &= 0 \end{aligned}\right\} \quad \ldots\ldots \text{(A5.2)}$$

Solving these simultaneous equations gives:

$$\left.\begin{aligned} b_1 &= \frac{n \sum_i x_i y_i - \sum_i x_i \sum_i y_i}{D} \\ b_o &= \frac{\sum_i x_i^2 \sum_i y_i - \sum_i x_i \sum_i x_i y_i}{D} \\ \text{where } D &= n \sum_i x_i^2 - \left(\sum_i x_i\right)^2 \end{aligned}\right\} \quad \ldots\ldots \text{(A5.3)}$$

To develop this approach, it is convenient to move the origin of x to lie at the mean value $\bar{x}$. This leaves the slope b_1 unchanged but alters the constant term.

So we define

$$a = x - \bar{x} = x - \frac{\sum_i x_i}{n}$$

The fitted regression line is $u_1(a) = a_o + a_1 a$ ..... (A5.4)

Since this must be identical with the regression line defined by equation A5.1 it follows that

$$b_o + b_1 x \equiv a_o + a_1 a = a_o + a_o\left(x - \frac{\sum_i x_i}{n}\right) \quad \ldots\ldots \text{(A5.5)}$$

This implies $b_1 = a_1$ and $b_o = a_o - a_1\left(\frac{\sum_i x_i}{n}\right)$ ..... (A5.6)

Under this transformation equation A5.3 reduces to:

$$\left.\begin{aligned} a_1 &= \frac{\sum_i \alpha_i y_i}{\sum_i \alpha_i^2} \\ a_o &= \frac{\sum_i y_i}{n} \\ D &= n \sum_i \alpha_i^2 \end{aligned}\right\} \quad \text{..... (A5.7)}$$

A5.3 STANDARD DEVIATION OF THE ESTIMATES

To simplify the notation, the variance of the individual values y_i is denoted by σ^2

i.e. $\text{var } y_i = \sigma^2$ ..... (A5.8)

The choice of equal weights for the points implies that σ^2 is constant for all y_i .

Also, the following statistical results are assumed:

$$\left.\begin{aligned} \text{var } ay &= a^2 \text{ var } y \\ \text{var } (a + b) &= \text{var } a + \text{var } b + 2 \text{ cov } (a, b) \end{aligned}\right\} \text{..... (A5.9)}$$

Then $\text{var } a_1 = \text{var}\left(\frac{\sum_i \alpha_i y_i}{\sum_i \alpha_i^2}\right)$

$$= \frac{\sum_i \alpha_i^2 \text{ var } y_i}{\left(\sum_i \alpha_i^2\right)^2}$$

$$= \frac{\sigma^2}{\sum_i \alpha_i^2} \quad \text{..... (A5.10)}$$

and $\text{var } a_o = \text{var}\left(\frac{\sum_i y_i}{n}\right)$

$$= \frac{\sum_i \text{var } y_i}{n^2}$$

$$= \frac{\sigma^2}{n} \qquad \ldots\ldots \text{(A5.11)}$$

Finally, for the fitted value itself:

$$\text{var } \left(u_1(\alpha) \right) = \text{var } (a_o + a_1 \alpha)$$

$$= \text{var } a_o + \alpha^2 \text{ var } a_1 + 2\, \alpha \text{ cov } (a_o, a_1)$$

It can easily be shown that $\text{cov } (a_o, a_1 \alpha) = 0$

Hence $$\text{var } \left(u_1(\alpha) \right) = \text{var } a_o + \alpha^2 \text{ var } a_1$$

$$= \frac{\sigma^2}{n} \left[1 + \frac{n\alpha^2}{\sum_i \alpha_i^2} \right] \qquad \ldots\ldots \text{(A5.12)}$$

In terms of the original variables this becomes:

$$\text{var } \left(u(x) \right) = \frac{\sigma^2}{n} \left[1 + \frac{(x - \bar{x})^2 \, n}{\sum_i (x_i - \bar{x})^2} \right] \ldots\ldots \text{(A5.13)}$$

Usually σ^2 is not a given quantity but is derived from the data itself, using the residuals. The residuals, v_i, are:

$$v_i = y_i - u(x_i) = y_i - a_o - a_1 \alpha_i \qquad \ldots\ldots \text{(A5.14)}$$

Clearly the expectation value of v_i is zero. However the expectation value of v_i^2 is given by:

$$E(v_i^2) = \text{var } v_i = \text{var } y_i + \text{var } a_o + \alpha_i^2 \text{ var } a_1$$
$$- 2 \text{ cov}(y_i, a_o) - 2\alpha_i \text{ cov } (y_i, a_1)$$
$$+ 2\, \alpha_i \text{ cov}(a_o, a_1)$$

This can be shown to simplify to yield the final result:

$$E(v_i^2) = \text{var } y_i - \text{var } a_o - a_i^2 \text{ var } a_1$$

$$= \sigma^2 \left(1 - \frac{1}{n} - \frac{a_i^2}{\sum_i a_i^2} \right)$$

So $$E(\sum_i v_i^2) = \sigma^2 (n - 2)$$

Hence $$s^2 = \frac{\sum_i v_i^2}{n - 2} \qquad \ldots\ldots \text{(A5.15)}$$

is an unbiased estimate of σ^2 . This is the expected result since the sum of residuals from a linear fit will have (n - 2) degrees of freedom.

A5.4 GENERALISATION TO CUBIC FITTING

It would involve much heavy algebra to repeat the above analysis for a cubic fit. However, since the photoelectric cross-section data fitted by a cubic polynomial on a log-log scale can be fitted to a reasonable degree of accuracy by a straight line, the method used above may be generalised to deal with the case of a higher order polynomial. The method adopted is as follows.

a) The sum of residuals $\sum_i v_i^2$ is calculated from the data by directly calculating the differences between the initial data points and the predicted values from the cubic fit.

b) σ^2 is estimated by the quotient $\sum_i v_i^2/(n - 4)$. The denominator (n - 4) is chosen since cubic fitting removes four degrees of freedom.

c) Using this value of σ^2 , the variance at any value of x is estimated from equation A5.13 :

$$\text{var}\left(u(x)\right) = \frac{\sigma^2}{n}\left[1 + (x - \bar{x})^2 \frac{n}{\sum_i (x_i - \bar{x})^2}\right]$$

ACKNOWLEDGEMENTS

The work described in this thesis was financed by a Graduate Research Scholarship for which I am indebted to the Faculty of Medicine of the University of Edinburgh.

I should also like to thank Professor J. R. Greening for his supervision and encouragement throughout the project.

My thanks are also due to:

The members of staff, both academic and technical, of the Department of Medical Physics and my fellow research students for their assistance and interest. I might particularly mention Dr. J. Law with whom I had many helpful discussions, particularly in the early stages of the work.

The workshop staff of the Department of Medical Physics, both at the Royal Infirmary and the Western General Hospital who constructed various pieces of the apparatus.

Mr. J. Davidson, Department of Medicine, and Mr. J. White, Department of Anaesthetics, in the Royal Infirmary, whose advice enabled me not only to develop the gas-handling system, but also to do so in safety.

Dr. C. A. Beevers, Mr. G. Thomas and Mr. J. Broom of the Department of Chemistry, University of Edinburgh, for carrying out X-ray fluorescence analysis of the tri-ethyl phosphate sample, mass spectrographic analyses of the gas samples, and for the glass-blowing work involved in the making of the manometer, respectively.

REFERENCES

ALLEN, S. J. M. Phys. Rev. 27, 266, 1926.

ALLING, W. R. and JOHNSON, W. R. Phys. Rev. 139, A 1050, 1965.

ALLISON, J. W. Austral. J. Phys. 14, 443, 1961.

BARKLA, C. G. and SADLER, C. A. Phil. Mag. 17, 739, 1909.

BEAKLEY, W. R. J. Scient. Instrum. 28, 176, 1951.

BEARDEN, A. J. Bull. Am. Phys. Soc. 4, 66, 1959.

BEARDEN, A. J. J. appl. Phys. 37, 1681, 1966.

BERGER, R. T. Rad. Res. 15, 1, 1961.

BETHE, H. A. and SALPETER, E. E. in Flügge, S. (Ed.) "Encyclopaedia of Physics" Vol. XXXV Berlin/Göttingen/Heidelberg Springer, 1957. pp. 381-409.

BEWILOGUA, L. Physik. Z. 32, 740, 1931.

BIERMANN, H. H. Ann. Phys. 26, 740, 1936.

BRAGG, W. H. and BRAGG, W. L. Proc. Roy. Soc. 88, 428, 1913.

BRAGG, W. H. and PIERCE, S. E. Phil. Mag. 28, 626, 1914.

de BROGLIE, L. J. de Phys. et Rad. 3, 33, 1922.

BROWN, R. T. Phys. Rev. A1, 1342, 1970.

BROWN, R. T. Phys. Rev. A2, 614, 1970.

BRYSK, H. and ZERBY, C. D. Union Carbide Corp. Report UCC/DSSD-299, 1967

BRYSK, H. and ZERBY, C. D. Phys. Rev. 171, 292, 1968.

CALLISEN, F. Zeit f. Physik, 107, 15, 1937.

CHIPMAN, D. R. J. appl. Phys. 26, 1387, 1955.

CHIPMAN, D. R. and JENNINGS, L. D. Phys. Rev. 132, 728, 1963.

COLVERT, W. Phys. Rev. 36, 1619, 1930.

COMPTON, A. H. Phys. Rev. 14, 247, 1919.

COOPER, M. J. Acta. Cryst. 18, 813, 1965.

CROMER, D. T. J. chem. Phys. 50, 4857, 1969.

CROMER, D. T. Unpublished data given to Storm and Israel, 1970.

CROMER, D. T., LARSON, A. C. and WABER, J. T. Acta. Cryst. 17, 1044, 1964.

CROMER, D. T. and MANN, J. B. J. chem. Phys. 47, 1892, 1967.

CROMER, D. T. and WABER, J. T. Acta. Cryst. 18, 104, 1965.

CROWTHER, J. A. and ORTON, L. H. H. Phil. Mag. 10, 329, 1930.

CROWTHER, J. A. and ORTON, L. H. H. Phil. Mag. 13, 505, 1932.

DAVISSON, C. M. in Siegbahn, K. (Ed.) "Alpha-, Beta-, and Gamma-Spectroscopy" Vol. I. Ch. 2, and App. 1. Amsterdam: North Holland Publ. 1965.

DESLATTES, R. D. AFOSR Report No. TN-58-784, 1958.

DESLATTES, R. D. Acta. Cryst. A25, 89, 1969.

EHRENFRIED, C. E. and DODDS, D. E. AFSWC - TN-59-33, 1960.

ERBER, T. Annals of Physics. 8, 435, 1959.

ERGUN, S. and TIENSUU, V. J. appl. Phys. 29, 946, 1958.

FORSSNER, T. Arkiv. f. Fysik, 35, 477, 1968.

FREEMAN, A. J. Acta Cryst. 12, 919, 1959.

FRIEDRICH, W., KNIPPING, P. and von LAUE, M. Ber. bayer. Akad. Wiss. 303, 1912.

GAVRILA, M. Phys. Rev. 113, 514, 1959.

GAVRILA, M. Phys. Rev. 124, 1132, 1961.

GRODSTEIN, G. National Bureau of Standards Report No. 583, 1957.

GROSSKURTH, K. Ann. Phys. 20, 197, 1934.

GUEST, P. G. "Numerical Methods of Curve Fitting", C.U.P., 1961.

HALL, A. W. and RICE, M. Phys. Rev. 8, 326, 1916.

HALL, H. Phys. Rev. 45, 620, 1934.

HALL, H. and SULLIVAN, E. C. Phys. Rev. 152, 4, 1966.

HANSEN, H. Ann. Phys. 35, 584, 1939.

HANSON, H. P., HERMAN, F., LEA, J. D. and SKILLMAN, S. Acta Cryst. 17, 1040, 1964.

HEINRICH, K. F. J. in McKinley, Heinrich and Wittry (Eds.) "The Electron Microprobe", New York: Wiley, 1966, pp. 296-377.

HEISENBERG, W. Physik. Z. 32, 737, 1931.

HERMAN, F. and SKILLMAN, S. "Atomic Structure Calculations": Englewood Cliffs, N.J.: Prentice-Hall Inc., 1963.

HEWLETT, C. W. Phys. Rev. 17, 284, 1921.

HILSENRATH, J. H. "Tables of Thermal Properties of Gases", National Bureau of Standards Report No. 564, 1955.

HOPKINS, J. I. J. appl. Phys. 30, 185, 1959.

HUBBELL, J. H. National Bureau of Standards Report No. NSRDS-NBS 29, 1969.

HUBBELL, J. H. Atomic Data, Vol. 3, No. 3, 1971.

HUGHES, G. D., WOODHOUSE, J. B. and BUCKLOW, I. A. J. Phys. D. 1, 695, 1968.

HULME, H. R., MC.DOUGALL, J., BUCKINGHAM, R. A., and FOWLER, R. H. Proc. Roy. Soc. (London) A149, 131, 1935.

HULTBERG, S., NAGEL, B. and OLSSON, P. Arkiv. f. Fysik, 20, 555, 1961.

HULTBERG, S., NAGEL, B. and OLSSON, P. Arkiv. f. Fysik, 38, 1, 1968.

INTERNATIONAL COMMISSION ON RADIOLOGICAL UNITS AND MEASUREMENTS. I.C.R.U. Report No. 17, 1970.

KAYE, G. W. C. and LABY, T. H. "Tables of Physical and Chemical Constants", 13th ed.: Longmans 1966.

KRAMERS, H. A. Phil. Mag. 46, 836, 1923.

KÜSTNER, H. Zeit. f. Physik, 70, 324, 1931.

LEROUX, J. Adv. in X-ray Analysis, 5, 153, 1961.

LIBERMAN, D., WABER, J. T. and CROMER, D. T. Phys. Rev. 137, A27, 1965

LUBLIN, P., CUKOR, P. and JAWOROWSKI, P. J. Adv. in X-ray Analysis, 13, 632, 1970.

MC.CRARY, J. H., LOONEY, L. D. and ATWATER, H. F. J. appl. Phys. A1, 3570, 1970.

MC.CRARY, J. H., LOONEY, L. D., CONSTANTEN, C. D. and ATWATER, H. F. Phys. Rev. A2, 2489, 1970.

MC.CRARY, J. H., PLASSMANN, E. H., PUCKETT, J. M., CONNER, A. L. and ZIMMERMAN, G. W. Phys. Rev. 153, 307, 1967.

MC.GINNIES, R. T. National Bureau of Standards. Supplement to Report No. 583, 1959.

MC.GUIRE, E. J. Phys. Rev. 175, 20, 1968.

MC.MASTER, W. H., del GRANDE, N. K., MALLETT, J. H. and HUBBELL, J. H. University of California, Report UCRL-50174, Rev. 1, 1969.

MANN, J. B. J. chem. Phys. 46, 1646, 1967.

MANSON, S. T. and COOPER, J. W. Phys. Rev. 165, 126, 1968.

MATESE, J. J. and JOHNSON, W. R. Phys. Rev. 140, A1 1965.

"MATHESON gas data book" 5th ed., Matheson Gas Products, 1971.

MATHEWS, J. and WALKER, R. L. "Mathematical Methods of Physics", pp. 304-315, Benjamin, 1965.

MILBERT, M. E. and BRAILSFORD, A. D. Acta Cryst. 11, 672, 1958.

NAGEL, B. C. H. Arkiv. f. Fysik. 18, 1, 1961.

OWEN, E. A. Proc. Roy. Soc. 94, 510, 1918.

PRATT, R. H. Phys. Rev. 117, 1017, 1960.

PRATT, R. H. Phys. Rev. 119, 1619, 1960.

PRATT, R. H., LEVEE, R. D., PEXTON, R. L. and ARON, W. Phys. Rev. 134, A898, 1964.

RAKAVY, G. and RON, A. Phys. Rev. 159, 50, 1967.

RÖNTGEN, W. C. Nature, 53, 274, 1896.

SAUTER, F. Ann. Physik, 9, 217, 1931.

SAUTER, F. Ann. Physik, 11, 454, 1931.

SCHMICKLEY, R. D. and PRATT, R. H. Phys. Rev. 164, 104, 1967.

SNELL, A. H. (Ed.) "Nuclear Instruments and their uses" p. 364ff.: Wiley, 1962.

SPENCER, R. G. Phys. Rev. 39, 178, 1932.

STOBBE, M. Ann. Physik, 7, 661, 1930.

STORM, E. and ISRAEL, H. I. University of California, Los Alamos Report LA- 3753, 1967.

STORM, E. and ISRAEL, H. I. Nuclear Data Tables, A7, 565, 1970.

THOMSON, SIR J. J. and THOMSON, G. P. "Conduction of Electricity through Gases" 3rd ed. Vol. II, C.U.P., 1933.

VEIGELE, W. J. Kaman Sciences Corporation Report KN-71-431(R), 1971.

VICTOREEN, J. A. J. appl. Phys. 14, 95, 1943.

VICTOREEN, J. A. J. appl. Phys. 19, 855, 1948.

VICTOREEN, J. A. J. appl. Phys. 20, 1141, 1949.

WHITE, G. R. National Bureau of Standards Report No. 1003, 1952.

WOERNLE, B. Ann. Phys. 5, 475, 1930.

WREDE, W. Ann. Phys. 36, 681, 1939.

WUILLEUMIER, F. Thesis. University of Paris, 1969.

ZIMMERMANN, W. Rev. scient. Instrum. 32, 1063, 1961.